Properties of Micro- and Nanostructured PA66/PPE Polymer Blends

Von der Fakultät für Ingenieurwissenschaften
der Universität Bayreuth
zur Erlangung der Würde
Doktor-Ingenieur (Dr.-Ing.)
genehmigte Dissertation

von
M.Sc. Alper Aksit
aus
Stuttgart

Erstgutachter:	*Professor Dr.-Ing. Holger Ruckdäschel*
Zweitgutachter:	*Professor Dr. Martin Weber*
Tag der mündlichen Prüfung:	*13. November 2023*

Lehrstuhl für Polymere Werkstoffe
Universität Bayreuth
2023

Kurzzusammenfassung

Die Herstellung von Polymerblends beweist sich als probates Mittel, um Eigenschaften von Kunststoffwerkstoffen für unterschiedlichste Anwendungen maßzuschneidern. Styrol-Maleinsäureanhydrid- (SMA-) Copolymere wurden zur Kompatibilisierung von Polyamid 66 / Poly(2,6-dimethyl-1,4-phenylenether) Blends (PA66 / PPE) verwendet. Drei SMAs mit unterschiedlichem MA-Gehalt wurden zunächst einzeln in PA66 und PPE untersucht. Keines der SMAs zeigte eine Mischbarkeit in PA66. In PPE wurde jedoch vollständige Mischbarkeit für das SMA8 nachgewiesen. Die Reaktivität der SMAs mit PA66 wurde durch rheologische Messungen bewertet, wobei höhere MA-Gehalte zu einem größeren Anteil an gepfropften SMA-g-PA66 Copolymeren führten (SMA24 > SMA8 > SMA4). Für PA66 / PPE / SMA Blends wurde ein maximaler PPE-Gehalt bei gleichzeitigem Erhalt der Tröpfchen-Morphologie angestrebt und mit 50:50 m/m PA66 / PPE vordefiniert. Die drei SMAs variierten von 1,25 bis 10 Gew.-% in ihren Einsatzkonzentrationen. Die Mischungen wurden in einem zweistufigen Prozess hergestellt, wobei erst PA66 mit SMA gemischt und dann PPE hinzugefügt wurde.

Mit zunehmendem MA-Gehalt wurden morphologische Veränderungen ausgeprägter. Während SMA4 – unabhängig von der Einsatzmenge – immer eine Tröpfchen-Morphologie aufwies, zeigte SMA8 eine intermediäre Übergangsphase (DCT). SMA24 zeigte hingegen eine vollständige Co-Kontinuität bei 10 Gew.-%. Nanoskalige Domänen innerhalb der PA66-Phase wurden in allen SMA-haltigen ternären Blends vorgefunden. Der Größenbereich reichte von 10 – 160 nm und nahm mit zunehmender MA-Konzentration ab. Für SMA8 wurden jedoch außergewöhnlich große Domänen nachgewiesen, welche auf die Ausbildung einer Nanoemulsionen hinweist. Diese Emulsion besteht aus PPE Tröpfchen, welche mit SMA8-g-PA66-Copolymermizellen umgeben sind. In Zugversuchen erzielten jeweils Blends mit 10 Gew.-% SMA die besten Ergebnisse, wobei SMA8 ein außergewöhnlich gutes Dehnungsverhalten (5 %) erzeugte. Dies wurde durch eine starke Grenzflächenaktivität des SMA8 mit einer ausgeprägten Fähigkeit zur Rissüberbrückung ermöglicht, welche durch ausgedehnte Fibrillen an den Grenzflächen visualisiert wurde.

Das SMA8 wurde ausgewählt, um verschiedene Mischungsverhältnisse von PA66 und PPE (60:40 und 40:60 m/m) zu untersuchen. Die Tröpfchenmorphologie von PA66 / PPE Blends im Verhältnis 60:40 m/m wurde durch die Zugabe von SMA8 nicht beeinflusst. Bei 40:60 m/m konnte ab 7,5 Gew.-% hingegen eine Co-Kontinuität festgestellt werden. In beiden Blends wurden erneut Nanoemulsionen gefunden, die in ihrer Größe variierten, wobei die größten Nanodomänen bei 40:60 PA66 / PPE mit 10 Gew.-% SMA8 auftraten. Das Mischungsverhältnis erwies sich auch im Hinblick auf die Zugeigenschaften als entscheidend, wobei ein höherer PA66-Anteil stets vorteilhafter war. Zudem führte ein Anteil von 10 Gew.-% SMA8 hinsichtlich der mechanischen Kennwerte immer zu den besten Ergebnissen.

PA66 / PPE Blends aller Mischungsverhältnisse, mit und ohne 10 Gew.-% SMA8, wurden in Zugversuchen und Ermüdungsrissausbreitungstests (FCP) untersucht. Von besonderem Interesse war dabei, das Eigenschaftsprofil in Abhängigkeit des Feuchtegehalts der Proben darzustellen. Die Anwesenheit von SMA8 hat sowohl im Zugversuch als auch im FCP zu einer Leistungssteigerung geführt. Im FCP konnte die Zugabe von SMA8 die negativen Auswirkungen anwesender Feuchtigkeit vollständig ausgleichen.

Short Summary

Blending of polymers has revealed a strong potential in tailoring plastic material properties for different applications. Styrene-maleic anhydride (SMA) type copolymers have been used to compatibilize polyamide 66 / poly(2,6-dimethyl-1,4-phenylene ether) (PA66 / PPE) blends. Three different SMAs, varying by MA content and molecular structure, were first incorporated into PA66 and PPE individually. While none of the SMAs were miscible with PA66, one was fully miscible in PPE (SMA8). The reactivity of SMAs with PA66 was evaluated by oscillatory rheological measurements, where higher MA contents lead to greater extent of grafted SMA-g-PA66 copolymers (SMA24 > SMA8 > SMA4). For ternary PA66 / PPE / SMA systems, a maximum PPE content at a stable droplet-sea morphology was fixed as 50:50 w/w PA66 / PPE, while the three SMAs were varied in their concentrations from 1.25 to 10 wt%. The blend production followed a two-step processing, blending PA66 with SMA first, followed by addition of PPE.

Morphological changes have been found to be more pronounced with increasing MA content. While SMA4 retained a droplet-sea morphology for all concentrations, SMA8 revealed a starting dispersed-to-co-continuous transition (DCT). SMA24 surpassed the DCT to have full co-continuity at 10 wt%. In all SMA containing ternary blends, nano-sized domains in the PA66 have been found, being attributed to (un-)reacted SMA. The size range varied from 10 – 160 nm, decreasing with increasing MA concentration, *i.e.* reactivity. In case of SMA8 however, enlarged domains were found, proving the formation of nano-emulsions of PPE droplets, covered by SMA8-g-PA66 copolymer micelles. All SMAs performed best in tensile tests at a content of 10 wt%, while SMA8 overperformed with an exceptional strain behavior (5%). This performance was enabled by a strong interfacial activity of the SMA8 with a strong crack bridging capability, proven by extensive fibrillations at the blend interfaces upon fracture.

The SMA 8 has been chosen to be part further investigations, where different PA66 / PPE blend ratios (60:40 and 40:60 w/w) were evaluated. The morphology of 60:40 w/w PA66 / PPE blend ratios were unaffected by the addition of SMA8, even at 10 wt. With a PPE majority, the blend underwent a transition already at 5 wt% to finally become co-continuous from 7.5 wt%. In both blends, again nano-emulsions were found, varying in size with the largest found in 40:60 w/w PA66 / PPE at 10 wt% SMA8. The blend ratio was also found crucial in terms of tensile properties, wherein a higher PA66 amount was beneficial over a PPE majority in both, binary PA66 / PPE and ternary blend with 10 wt% SMA8. The mechanical properties of ternary blends with SMA8 were best at 10 wt% of compatibilizer, regardless of the blend ratio.

PA66 / PPE blends with(out) 10 wt% SMA8 at all three blend ratios have been tested in tensile and dynamic fatigue crack propagation (FCP) tests. The property profile in dependence of humidity was of special interest. The presence of SMA8 resulted in improved properties in both tensile and FCP test. Upon cyclic loading, SMA8 was capable to fully compensate the detrimental effect of humidity in the blend materials.

Acknowledgment

I would like to express my sincere appreciation to Professor Dr.-Ing. Volker Altstädt, not only for supervising the thesis but also for the numerous discussions, assistance, and endless encouragement. Through him, I learned what it means to have a mentor. In the years of working together, I have been able to take away a lot for my professional as well as private future.

I thank Professor Dr.-Ing. Holger Ruckdäschel for his support after having left the department and for the primary revision of this thesis. At the same time, I want to thank Professor Dr. Martin Weber for the secondary revision. I always enjoyed our fruitful discussions on polymer blends during our numerous lunches at the university.

I would like to deeply thank the company Ensinger GmbH for their support and generous provision of raw materials. In particular, I would like to single out Dr. Michael Möller. Our direct and candid communication led to a very efficient and pleasant cooperation, which I always appreciated. I am also grateful to him for reviewing this work. I also want to thank Ardy Doelen from Polyscope B.V. for the generous supply of the compatibilizers and technical discussions.

I would like to express my gratitude to all department members for their endless support. I thank Sebastian Gröschel for the introduction to polymer processing and his eternal patience with me. Ute Kuhn is thanked for the thermal-mechanical measurements and also for all the valuable exchanges on scientific and private topics. I would like to thank Andreas Mainz and Alexander Brückner for the mechanical tests and the discussions on the evaluation of results. Anne Lang and Annika Pfaffenberger have my thanks for the numerous microscopy pictures. Furthermore, I would like to thank Kerstin Mosig, Theresa Adelhardt, Dr. Bärbel Tenhunen and Milena Korczyk for always having my back.

This work would not have been possible without all the students and assistants. For their active support, I especially thank Teresa Menzel, Nico Geis, and Eduardo Szpoganicz da Silva, who have built the cornerstones of my work.

I have to express my gratitude to my former office colleague Dr.-Ing. Tobias Bubmann for the endless discussions on polymer blends and the many fun moments that made my everyday life at the department more appreciable.

I thank my family for their never-ending efforts to support my academic and personal development.

Finally, I thank my wife and former colleague, Dr.-Ing. Merve Aksit, from the bottom of my heart. We have shared sorrows and joys, and this is what has given me the stamina I own today. Our shared goals have carried us to where we are and will continue to do so in the future.

Table of content

Kurzzusammenfassung ..... **I**
Short Summary ..... **II**
Acknowledgment ..... **III**
Table of content ..... **IV**
Abbreviations ..... **VI**
Symbols ..... **VII**
1 Introduction and motivation **1**
2 State of the art **5**
2.1 Polymer blends 5
2.1.1 Thermodynamics 6
2.1.2 Morphology of immiscible polymer blends 8
2.2 Compatibilization of polymer blends 14
2.3 Mechanical behavior of polymer blends 21
2.3.1 Deformation mechanisms in polymer blends 22
2.3.2 Fracture mechanics of polymer blends 25
2.3.3 Measuring toughness 27
2.3.4 Fatigue crack propagation (da/dN) 28
2.3.5 Effect of humidity 31
2.3.6 Summary 33
3 Aims and approaches **34**
4 Materials **39**
4.1 Blend components 39
4.2 SMA compatibilizers 39
5 Experimental methods **42**
5.1 Blend production 42
5.2 Characterization methods 43
5.2.1 Rheological characterization 43
5.2.2 Morphological characterization 43
5.2.3 Thermo-mechanical characterization 44
5.2.4 Mechanical characterization 45
6 Results **46**
6.1 Characterization of neat blends and compatibilizer interactions 46

6.1.1 PA66 / PPE: the reference blend system....46
6.1.2 Compatibilizer interactions with neat PA66 and neat PPE....50
6.1.3 Blending sequence of ternary PA66 / PPE / SMA blends....57
6.1.4 Summary....59
6.2 Influence of SMA type on PA66 / PPE blends....60
6.2.1 Influence on morphology....61
6.2.2 Influence on mechanical behavior under quasi-static load....70
6.2.3 Summary....76
6.3 Influence of blend ratio on PA66 / PPE / SMA8 blends....79
6.3.1 Influence on morphology....80
6.3.2 Influence on mechanical behavior under quasi-static load....84
6.3.3 Summary....91
6.4 Influence of humidity on PA66 / PPE / SMA8 Blends....94
6.4.1 Influence on mechanical behavior under quasi-static load (tensile)....95
6.4.2 Influence on mechanical behavior under dynamic load (FCP)....97
6.4.3 Summary....122
7 Summary....125
8 Zusammenfassung....127
9 Outlook....130
10 Bibliography....132
11 Other sources....154

Abbreviations

PPE	Poly (2,6-dimethyl-1,4-phenylene ether)
PA66	Polyamide 66
SMA	Styrene-maleic anhydride copolymer
MA	Maleic anhydride
PA6	Polyamide 6
low-M_w	Low-molecular weight
JPs	Janus particles
NPs	Nanoparticles
CA	Citric acid
PS	Polystyrene
GMA	Glycidyl methacrylate
PBT	Polybutylene terephthalate
PET	Polyethylene terephthalate
PC	Polycarbonate
SAN	Styrene-acrylonitrile copolymer
ABS	Acrylonitrile-butadiene-styrene copolymer
PMMA	Polymethyl methacrylate
DSC	Differential scanning calorimetry
SEM	Scanning electron microscopy
TEM	Transmission electron microscopy
HIPS	High-impact polystyrene
LEFM	Linear elastic fracture mechanics
FCP	Fatigue crack propagation test
CT	Compact tension specimen
H_2O	Water
SEC	Size exclusion chromatography
RI	Refractive index
$CHCl_3$	Chloroform
TDS	Technical data sheet
DMA	Dynamic mechanical analysis
w/w	Weight for weight
DCT	dispersed-to-co-continuous transition

Symbols

ΔG_{mix}	Change in Gibbs free energy of mixing
ΔH_{mix}	Change in mixing enthalpy
ΔS_{mix}	Change in mixing entropy
T	Temperature
ϕ_i	Volume concentration of polymer i
R	Ideal gas constant
v_r	Reference volume
v_{total}	Total volume
r_i	Number of chain segments in polymer i
χ_{ij}	Flory-Huggins interaction parameter for polymer i and j
γ_{AB}	Interfacial tension between polymer A and B
η_r	Viscosity ratio
$\eta_{A,B}$	Viscosity of polymer A and B
η_d	Viscosity of dispersed phase
η_m	Viscosity of matrix phase
Ca	Capillary number
Ca_{crit}	Critical capillary number
Ca^*	Reduced capillary number
$\dot{\gamma}$	Deformation rate
d	Diameter
x	Phase transition border
M_w	Weight-averaged molecular weight
T_g	Glass transition temperature
M_e	Entanglement molecular weight
v_e	Entanglement density
C_∞	Chain stiffness
da/dN	Fatigue crack propagation
K_I	Stress intensity factor for mode I
K_{Ic}	Critical stress intensity factor in mode I
ΔK	Amplitude of the stress intensity factor
ΔK_{th}	Threshold amplitude of the stress intensity factor
ΔK_{max}	Maximum amplitude of the stress intensity factor
C	Material constant
m	Slope of the Paris-Erogan linear dependency regime
ΔK_{cf}	Critical amplitude of the stress intensity factor for unstable crack growth
D	Molar mass dispersity
AN	Acid number
rpm	Rotations per minute
$tan\ \delta$	Loss factor
K_{max}	Maximum stress intensity
K_{min}	Minimum stress intensity
R	Minimum to maximum load ratio
ω	Frequency applied in shear rheology
η^*	Complex shear viscosity

σ_M	Tensile strength
σ_Y	Yield strength
ε_B	Elongation at break
E	Young's modulus
U_T	Tensile toughness
v	Poisson's ratio

1 Introduction and motivation

The development and design of advanced materials is inevitably connected to the multifunctionality of the desired products. An innovative material is expected to fulfill the same or even higher requirements compared to the predecessor product, while ideally keeping the complexity of the product formulation and process technology at a similar or lower level. In this regard, preferred properties of an existing material need to be tailored by structural modifications of the material nature at macro- to micro- or even nano-scale. In terms of polymeric materials, the typical structure modifications might include the use of foamed materials or the manufacturing of (nano) composites or blends. These modifications are critical success factors for the production of high-performance materials.

Nanostructured materials have been focused in industrial and academic research within the last decades due to their potential for obtaining multifunctional products [1–6]. They are made by either combining a polymer with nano-scaled particles as it is described by nanocomposites [7–12] or by blending at least two polymers and forming nanometer-sized domains when immiscible polymers are used (nano blends) [13–17]. Given by the small structure sizes and thus high volume–to–surface–ratios, outstanding enhancements in material properties such as electrical conductivity or toughness have been reported [18–20]. In contrast to nanocomposites, nanostructured polymer mixtures are somewhat challenging to produce as strong internal or external forces must be applied to overcome undesired effects, such as coalescence [21–24]. Block copolymer-based self-assemblies [25–29] or solvent-mediated assemblies [30–33] have been proposed as very efficient methods to generate well-defined polymeric nanostructures. Due to their complex synthesis and higher manufacturing costs, only very few examples were implemented commercially, such as styrene-butadiene-styrene and polypropylene-polyethylene block copolymers [34–38].

Industrially relevant processing techniques, such as melt blending, are commonly used for recent developments. Melt blending is a continuous process with almost no investment costs as existing infrastructure can be used. A significant drawback of the mentioned method is the lack of material design freedom at a molecular level. This is an outcome of only a few available parameters for tuning the resulting material properties, such as screw configuration and specific

energy input, influenced by the rotation speed and shear or elongational forces being applied. This challenge can be overcome by internally stimulating the polymer mixture to create nanostructures, mainly by adding processing aids, such as emulsifying agents [39]. There is an extensive body of academic publications regarding the morphology control of polymer blends via melt mixing [40–47]. However, the research studies in this field are limited due to the challenges in obtaining nanostructured polymer blends with significantly enhanced mechanical and thermal properties. Therefore, more detailed studies correlating the morphological changes of the resulting polymer material performance are highly important.

One example of a commercial and multifunctional material is an insulation profile used as thermal break for modern metal window and door systems. It is applied within modern window and door frames made of aluminum as a barrier material to reduce the heat loss in buildings, visualized as orange structures in Figure 1.

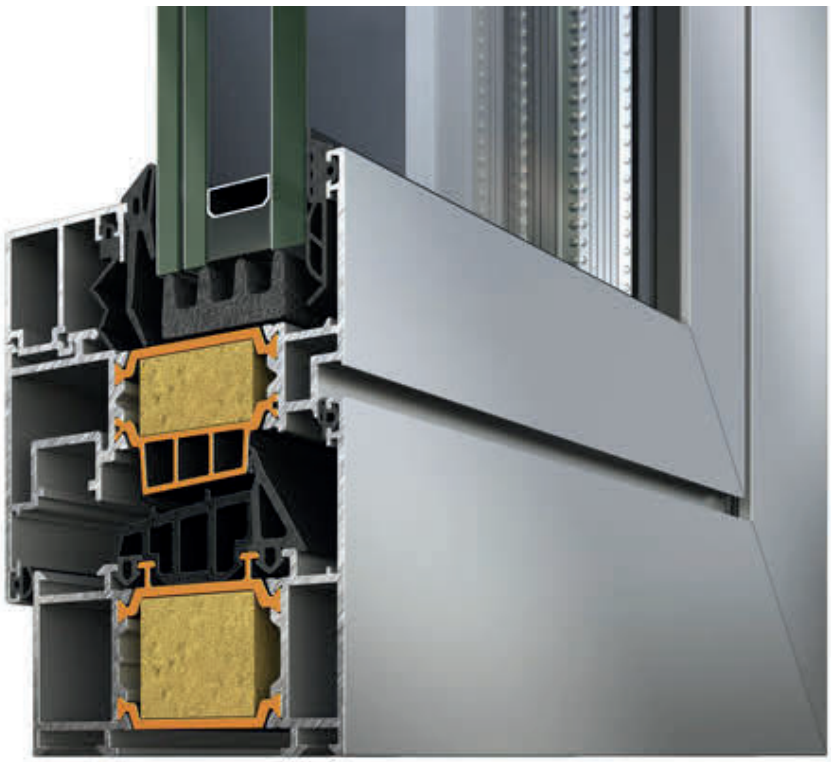

Figure 1 Thermal breaks (orange) inserted in aluminum window frames [a].

Thermal breaks are expected to feature high tensile strength, resistance to fatigue crack propagation and dimensional stability, good chemical resistance, high heat resistance, good paintability, and low thermal conductivity. For this specific application, a blend consisting of poly (2,6-dimethyl-1,4-phenylene ether) (PPE) and polyamide 66 (PA66) has been commercialized successfully [b]. Blending mentioned polymers allows overcoming the deficits of the individual polymers. PPE, having high heat resistance, low thermal conductivity, low water uptake, and thus good dimensional stability, reveals poor processability, low chemical resistance, and a lack of paintability. PA66, with its good paintability, excellent processability, and good solvent resistance, unfortunately possesses high water uptake, a strong tendency to warpage, and low heat stability. Besides all the synergism, the immiscibility of the components has to account for the system's drawbacks, leading to a microstructure with disadvantageous properties. Such undesired morphologies cause a vulnerability to mechanical stresses, as weak spots are found at the interfaces. Hence, compatibilizers are used to improve the microstructure and mechanical performance of the immiscible blend.

An extensive body of literature regarding the compatibilization of PA / PPE blends shows that reactive compatibilization is applied predominantly [48–55]. The compatibilizers – frequently functionalized polystyrenes – are usually synthesized by modification of an existing polymer either in solution or in molten state and subsequently added to the immiscible blend. Such polymer-analogous conversions are often cost-intensive, hence not preferred for industrial applications. One commercially available type of compatibilizer for PA / PPE blends is styrene-maleic anhydride copolymer (SMA). The synthesis is a straightforward method where maleic anhydride (MA) monomers are often added to the reactor during the styrene polymerization, thus representing a ready-made compatibilizer without requiring further processing. The intensive studies on the compatibilizing efficiency of SMA for polyamide 6 (PA6) / PPE blends show great potential for enhancing the resulting blends' mechanical performance [56–58]. The improvements were attributed to an optimized morphology at micro-scale, yet the understanding of apparent micromechanical phenomena is still missing. Also, the knowledge transfer to PA66-based PPE blends has not been considered so far, revealing a highly interesting scientific gap and demanding more detailed considerations.

To address this, within this thesis, PA66 / PPE blends will be compatibilized with various types and contents of SMA to identify their potential as efficient compatibilizers. The efficiency is mainly evaluated by characterizing the resulting mechanical properties under static and dynamic stresses, performed via tensile and fatigue crack propagation tests (FCP). The mechanical performance will not only be investigated in a dry state but also in a humid state to understand the behavior under more realistic conditions.

2 State of the art

This chapter aims to provide a theoretical background regarding the general polymer blend theory, including the morphology evolution, the compatibilization mechanisms. Emphasis is put on the physicochemical compatibilization, wherein SMA copolymers are discussed in detail. Additionally, previous studies regarding the deformation behavior of blends under static and dynamic loading will be reviewed and correlated to the micromechanical fracture characteristics.

2.1 Polymer blends

Within the last decades, reports of new polymer findings have stagnated [59]. In contrast, the blending of polymers has become very popular [60–64], whereby an almost limitless number of polymer combinations give rise to novel materials with multifunctional properties. The facile production, low investment costs, and short development cycles are key factors for the successful commercial use of blend systems. A new set of properties can be achieved by combining available ‘standard’ polymers. As most polymer combinations appear to be immiscible when blended, controlling their micro- and nanostructure becomes crucial to achieving the required performance within a desired application. This control is considered as the most crucial know-how in the production of polymer blends.

Among many parameters, material composition and processing conditions have been found most crucial for influencing the final properties of multiphase materials. Material composition involves the blend proportion, interfacial tension, viscosity, and elasticity ratio. Relevant processing conditions are usually described by mixing intensity, temperature, time, and the type of applied forces [65–67]. To understand the complex relations between these parameters and the resulting blend properties better, the fundamentals of polymer blends will be discussed.

2.1.1 Thermodynamics

Polymer blends are generally described as a physical mixture consisting of at least two non-identical homo- or copolymers [68]. Depending on the chemical nature of each polymer, blends are categorized into three sections: miscible, partially miscible, and immiscible. Upon mixing of two polymers, the latter case is found for the majority of blend systems, expressed by phase separation at micro or macro-scale. Miscible blends show a homogeneous structure with no distinct phases visible, whereas partially miscible blends combine heterogeneous structures with single-phased regions [68].

Besides qualitative information about the miscibility of a polymer mixture, the degree of miscibility can be expressed by the change of Gibbs free energy of mixing, ΔG_{mix}, as given in Equation 1 [69,70]. Herein, ΔH_{mix} is the change in mixing enthalpy, T is temperature, and ΔS_{mix} represents the change in mixing entropy.

$$\Delta G_{mix} = \Delta H_{mix} - T \cdot \Delta S_{mix} \tag{1}$$

Generally, a negative ΔG_{mix} value represents a (partially) miscible blend. To further specify the type of miscibility, one has to consider the second derivative of ΔG_{mix} in respect of the polymer volume concentration (ϕ_i), as shown in Equations 2 and 3. For a fully-miscible system, the following expression has to be fulfilled.

$$\frac{\partial^2 \Delta G_{mix}}{\partial \phi_i^2} > 0 \tag{2}$$

In case of partial miscibility, the second derivative of ΔG_{mix} is negative at certain blend ratios.

$$\frac{\partial^2 \Delta G_{mix}}{\partial \phi_i^2} < 0 \tag{3}$$

A phase separated, thus immiscible blend is given for strictly positive values of ΔG_{mix}.

Flory-Huggins theory

As ΔG_{mix} cannot be determined directly, Flory and Huggins estimated the free energy by thermodynamical modeling [71,72]. Up to now, it is the most commonly applied model. For

describing ΔS_{mix}, they considered a spatially limited lattice, wherein all interactions happen within this lattice. Furthermore, it was assumed that both polymers consist of equal cell sizes, where each polymer segment is in the size of one cell and is connected by flexible chains, as seen in Figure 2.

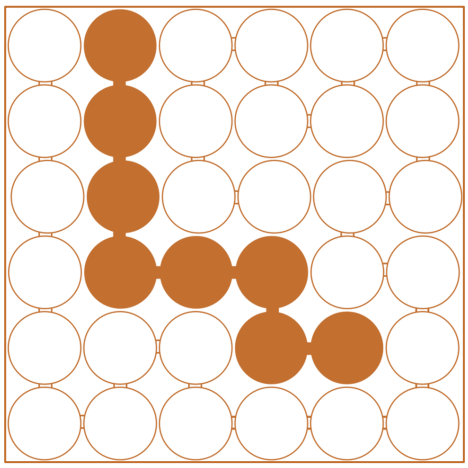

Figure 2 Flory-Huggins lattice model applied for a mixture of two polymer chains. Reproduced from [73].

For the calculation of ΔH_{mix}, molecular interactions between the two polymer chains, such as dipole, ionic, or van der Waals' forces, are relevant. These interactions cause a change in enthalpy, thus the system's internal energy. To determine the ΔG_{mix} of a polymer mixture of polymers A and B, Equation 1 was specified as follows [74]:

$$\frac{\Delta G_{mix}}{R \cdot T \cdot (v_{total}/v_r)} = \chi_{AB} \cdot \phi_A \cdot \phi_B + \left(\frac{\phi_A}{r_A} \cdot ln\phi_A + \frac{\phi_B}{r_B} \cdot ln\phi_B\right) \quad (4)$$

where R: ideal gas constant, T: absolute temperature, v_{total}, v_r: total and reference volume, $r_{A,B}$: number of polymer chain segments in polymer A and B, $\phi_{A,B}$: volume content of polymer A and B, χ_{AB}: Flory-Huggins interaction parameter for polymer A and B.

Commercially relevant polymers usually have molecular weights far above 1 kg/mol. Thus, the contribution of entropy in Equation 4 becomes negligible. As a result, a closer look has to be

taken at the enthalpy term. The Flory-Huggins interaction parameter, χ_{ij}, describes temperature-dependent, solid-state interactions between two polymers, which contributes most to determining the miscibility of two polymers (Equation 4). Therefore, a positive or negative χ_{ij} most often results in an immiscible or miscible blend system, respectively.

2.1.2 Morphology of immiscible polymer blends

The morphology mainly dictates the final blend properties, thus the molecular orientation of one polymer phase with respect to the second polymer phase. This orientation is affected by various parameters, such as processing conditions, viscosity ratio, interfacial tension, and blend composition. Furthermore, the effect of coalescence should not be ignored, as it coexists with deformation and breakup processes while melt-mixing. The most frequently observed morphologies are shown in Figure 3.

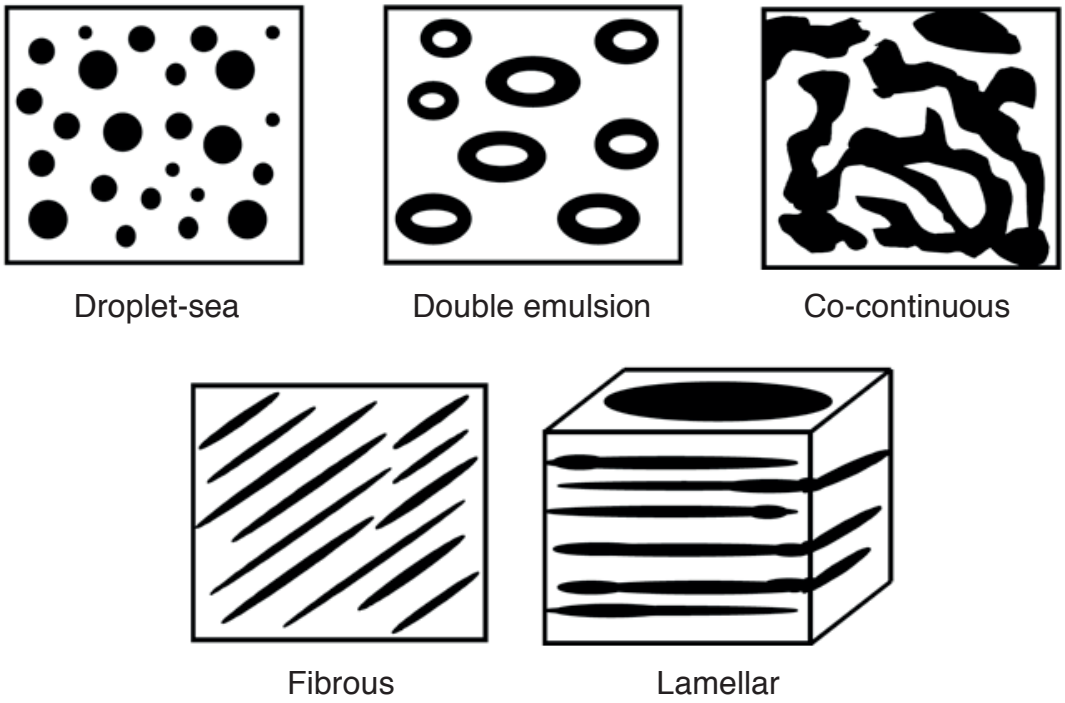

Figure 3 Schematic overview of morphologies usually obtained by melt processing of immiscible polymer blends [61,75,76]

For each morphology, specific properties are either supported or contradicted; therefore, it is crucial to control the morphology of a blend depending on the desired application. For an effective toughening, a droplet-sea or double emulsion are ideal candidates [46,77,78], whereas good barrier properties are instead achieved with a lamellar morphology [79,80]. Whenever an anisotropy of the relevant property (*e.g.,* electrical conductivity) is expected, a co-continuous morphology is considered the most suitable [81–83].

2.1.2.1 Influence of rheology

During melt mixing of two polymers, the morphology evolution mainly depends on the applied forces within the extruder (given by the screw design) and its intensity, the viscosities of the polymers and their ratio, their interfacial tension, and the initial form (*e.g.,* granulate, powder or pellet) of the polymers before melting. All mentioned parameters can be summarized within (micro-) rheological considerations, which will be discussed in this section.

Interfacial tension

For a given flow field, the interfacial tension (γ_{AB}) between two polymers A and B has an opposite effect on the deformation and breakup of the molten phases [84,85]. If a finely structured morphology is aimed, γ_{AB} should be set as low as possible [86,87]. γ_{AB} is mainly estimated after measuring the individual surface tensions of each component [88] or by application of Palierne's model at shear rheological measurements [89]. For the first case, two different equations are primarily used for an estimation: the harmonic-mean equation (Eq. 5) and the geometric-mean equation (Eq. 6).

$$\gamma_{AB} = \gamma_A + \gamma_B - 4\left(\frac{\gamma_A^d * \gamma_B^d}{\gamma_A^d + \gamma_B^d} + \frac{\gamma_A^p * \gamma_B^p}{\gamma_A^p + \gamma_B^p}\right) \tag{5}$$

$$\gamma_{AB} = \gamma_A + \gamma_B - 2\left(\sqrt{\gamma_A^d * \gamma_B^d} + \sqrt{\gamma_A^p * \gamma_B^p}\right) \tag{6}$$

where $\gamma_{A,B}$ are the surface tensions of component A or B, $\gamma_{A,B}{}^d$ and $\gamma_{A,B}{}^p$ are the dispersive and polar contributions of the surface tension of component A or B, respectively.

Viscosity ratio

The viscosity ratio (η_r) is defined as the quotient of polymer A and B viscosity (η_A and η_B), as seen in Equation 7 [90]. For droplet-sea morphologies, the dispersed phase (droplet) is usually placed as the numerator, whereas the matrix polymer (sea) is set as the denominator.

$$\eta_r = \frac{\eta_A}{\eta_B} = \frac{\eta_d}{\eta_m} \tag{7}$$

With an increasing η_r, the dispersed phase deformation is difficult. For values of $\eta_r > 3.8$, a deformation of the dispersed polymer may not even be possible under simple shear flow [74,91,92].

Processing conditions

Besides the processing temperature and material throughput, several parameters, such as elongational or shear flow and the deformation rate (for elongational or shear stress) play an important role in controlling the morphology. A correlation of the mentioned conditions was set by Grace [85] as follows (Eq. 8):

$$Ca = \frac{\eta_m \cdot \dot{\gamma} \cdot d}{\gamma_{AB}} \tag{8}$$

where Ca: capillary number, $\dot{\gamma}$: deformation rate in shear or elongational flow, and d: diameter of droplets (dispersed phase).

All values, apart from $\dot{\gamma}$, are simply determined by experimental methods. Latter is usually estimated using the specific energy input during the extrusion process or by simulations and modeling. Still, determining the exact proportions of shear and elongational flow in twin-screw extruders remains challenging.

The relation between Ca and η_r was visualized by Grace as depicted in Figure 4 [85].

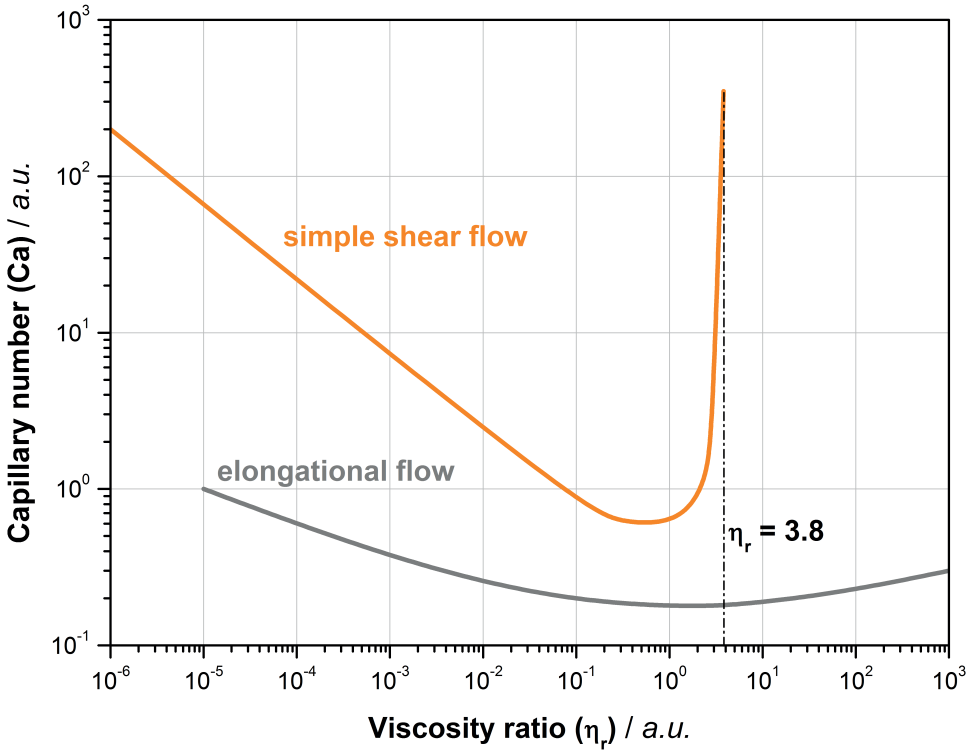

Figure 4 *Ca* as a function of η_r in shear and elongational flow. Orange and gray lines represent the critical capillary numbers (Ca_{crit}) for shear and elongational flow respectively [85].

The orange and gray lines represent the critical capillary numbers (Ca_{crit}) which must be overcome to enable droplet breakup. It becomes evident that elongational flow is more effective than shear flow over the complete range of η_r. For simple shear flow, Ca_{crit} converges to infinity at a η_r of 3.8, limiting a good dispersion. Independent of the apparent flow type, four distinct regions are proposed by Utracki and Shi [91] by applying the reduced capillary number (Ca^*) given in Equation 9:

$$Ca^* = \frac{Ca}{Ca_{crit}} \tag{9}$$

- $Ca^* < 0.1$: No droplet deformation.
- $0.1 < Ca^* < 1$: Droplet deformation takes place, yet no breakup.
- $1 < Ca^* < 2$: Droplet deform and split into two droplets.
- $Ca^* > 2$: Droplet deforms into a stable filament.

To further evaluate the droplet breakup mechanisms, this consideration has to be supported by the η_r. Harrats et al. [80] proposed four different droplet breakup mechanisms under shear flow conditions, as shown in Figure 5.

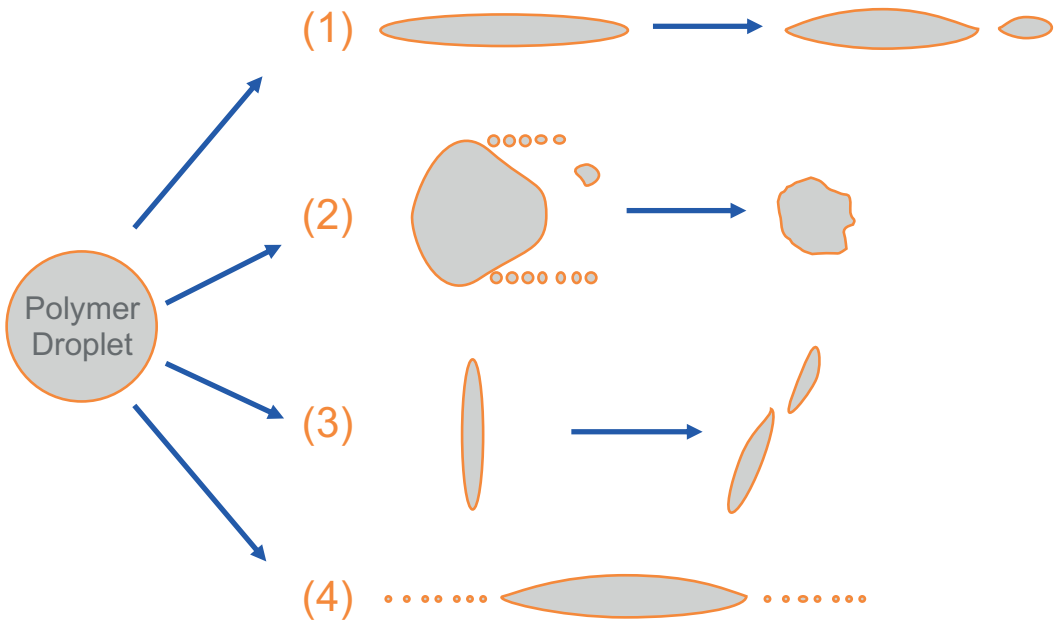

Figure 5 Droplet breakup mechanisms under simple shear flow (flow direction from left to right) with (1) sheet formation and breakup, (2) surface erosion, (3) perpendicular stretching and breakup and (4) tip streaming [80].

(1) $0.05 < \eta_r < 9$: Sheet formation parallel to flow direction followed by a breakup.
(2) $0.05 < \eta_r < 60$: Slow erosions on the surface due to very high droplet viscosity.
(3) $\eta_r \sim 7.5$: Stretching perpendicular to flow followed by a breakup.
(4) $0.05 < \eta_r < 3$: Very high matrix viscosity enables tip streaming (very small domains).

All these factors require high experimental and calculatory efforts to describe occurring morphological phenomena qualitatively. Nevertheless, this fundamental knowledge is essential for understanding the morphology formation when blending immiscible polymers. It is noteworthy that all considerations up to this point are independent of the blend composition.

2.1.2.2 Influence of blend ratio

The most convenient method to alter the blend morphology is provided by changing the blend ratio of a given system. When neglecting any external stimuli, two primary morphologies are observed for a binary blend depending on the blend composition: (1) Droplet-sea (binodal decomposition), and (2) Co-continuous morphology (spinodal decomposition), illustrated in Figure 6.

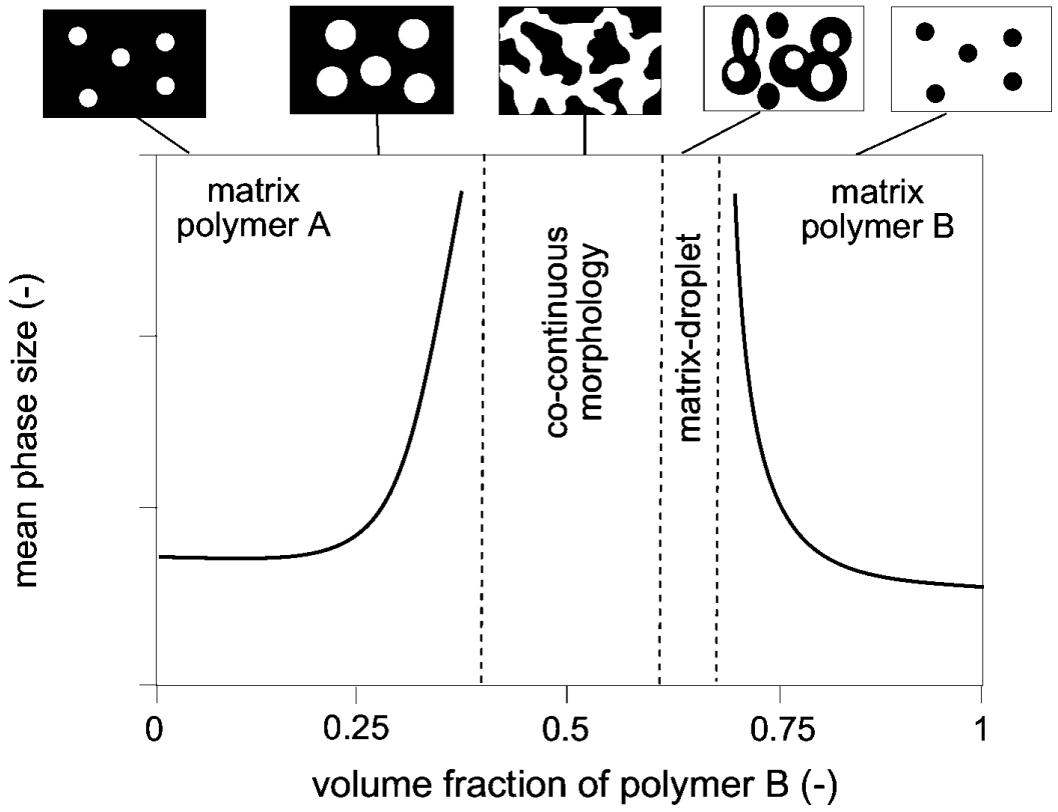

Figure 6 Schematic representation of the blend morphology as a function of polymer volume fraction in a binary system [93].

For small fractions of polymer B, polymer A forms the matrix phase having relatively small polymer B domains. With increasing polymer B content, the domain sizes increase to a certain extent, where a morphology shift becomes evident at 50 vol%. A further increase results in another phase transition to an inversed droplet-sea structure, in which polymer B is the matrix

polymer, having polymer A domains distributed. Each of the three morphology windows might vary in width or position on the x-axis, depending on the η_r of the blend partners.

A quantitative description of the apparent morphology and the phase transition borders were proposed by Jordhamo et al. [94], as given in Equation 10.

$$x = \frac{\phi_A}{\phi_B} \cdot \frac{\eta_B}{\eta_A} \tag{10}$$

The following three conditions are defined for this relation:

- $x > 1$: Polymer A matrix / polymer B droplets.
- $x \approx 1$: Polymer A continuous / polymer B continuous.
- $x < 1$: Polymer A droplets / polymer B matrix.

Other models, considering additional parameters and circumstances, were reported by several other authors [95–97]. Throughout all models mentioned, the less viscous polymer is described to form the matrix phase even for blend ratios with a minority of mentioned polymer.

2.2 Compatibilization of polymer blends

Aside from the morphology, interfacial properties play a significant role in immiscible polymer blends. Due to the strong tendency of phase separation, blends usually consist of very weak and thin interfaces. Because of this lack of interaction, the mixture reveals poor resistance against mechanical stresses, thus showing brittle failure, especially at the interfaces. Additionally, coarsening of the dispersed phases by coalescence [75,98] or Ostwald ripening [91,99] are observed in the molten state, leading to a heterogeneous domain size distribution, hence showing unpredictable properties once solidified [100]. As most compounds are re-processed after a first compounding and granulation process, the stability of the apparent morphology is not guaranteed. At any time, a second melting process, *e.g.*, injection molding, might change the morphology in an undesired manner.

To overcome the mentioned drawbacks and to have superior control of the blend morphology and thus mechanical properties, so-called compatibilizers are used. These materials provide a particular interfacial activity, simultaneously enabling interaction with both blend partners. The compatibilizer content in polymer blends typically varies from 0.1 to 10 wt% [101]. Concentrations up to 20 wt% are also found, which technically cannot be considered an additive anymore [102,103]. A schematic representation of the droplet formation is depicted in Figure 7 [76].

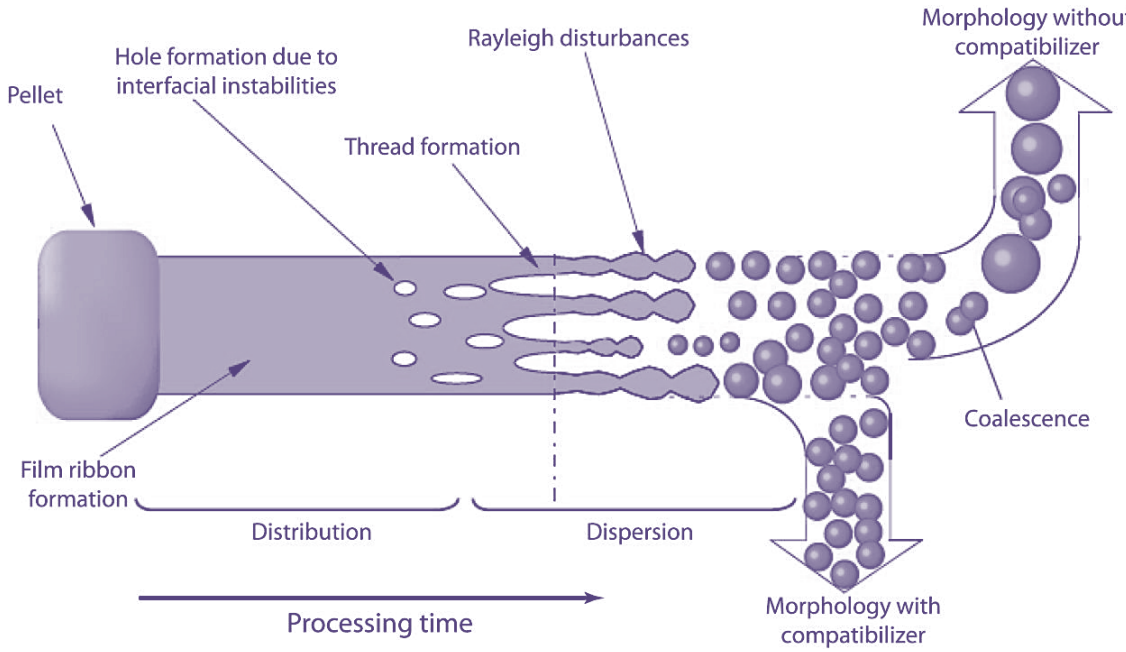

Figure 7 Effect of compatibilization on the mechanism of morphology development in immiscible polymer blends [104].

As mentioned, a compatibilizer leads to a greatly improved, more homogeneous morphology with decreased domain sizes and narrower distribution. In general, it is expected that effective compatibilization covers three main aspects [105–108]:

- Reduction of the interfacial tension.
- Hindrance of coalescence in a sterical, electrostatic or electrosteric manner.
- Providing interfacial adhesion / increasing the interface thickness.

To achieve this control, diverse compatibilizer types were used: (1) Unreactive (block / graft) copolymers [105,109,110], (2) Low molecular weight (low-M_w) reactive molecules [111–115], (3) Reactive copolymers [116–118], (4) Catalysts [119,120], (5) Inorganic nanoparticles [49,121–123] and (6) Janus-type hybrid particles (JPs) [108,123–127]. Latter two are multifunctional compatibilizers, as they combine the compatibilizing effect with additional improvements in toughness [126,128], electrical conductivity [81,129,130] or barrier properties [131,132]. The mentioned compatibilizers can be classified into three fundamental working principles: physical, chemical, and physicochemical compatibilization, as seen in Figure 8. Other compatibilization principles, such as catalyst-assisted transesterification [133], chemical / mechanical degradation [134] or specific interaction-based methods [106,135,136] will not be discussed in detail, yet are mentioned here for the sake of completeness.

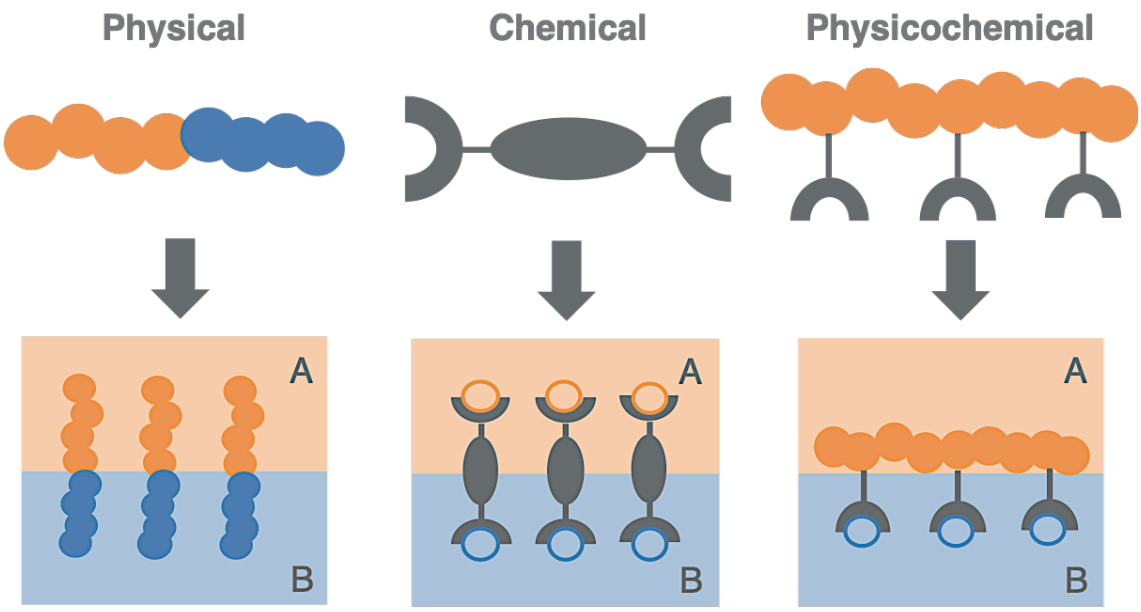

Figure 8 Schematic depiction of the three compatibilization principles. Orange and blue chains represent polymeric chains, whereas the gray semicircular arches represent reactive moieties.

Physical compatibilization

Physical compatibilization contains any type of unreactive compatibilizer, such as block and graft copolymers, nanoparticles (NPs), or JPs having an emulsifying effect to reduce domain sizes effectively [137–139]. In the case of copolymers and JPs, each part's chemical affinity (miscibility) to one of the blend partners is the driving force to diffuse selectively to the interface of the blend. Yet, much effort is needed for the synthesis and purification, which has a noticeable impact on the final material price [126,140]. Once the compatibilizer is ready for use, all components can be combined in a simple one-step compounding process. In the case of the NPs, a selective localization is provided by a tailored surface energy, which neither matches the surface energy of polymer A nor polymer B. Thus, the diffusion of the NPs to the interface is inevitable [141,142]. For this reason, the NPs usually require surface treatment to tailor the surface energy with respect to the blend polymers [130,143–145].

Compatibilizers in this category reduce the interfacial tension and inhibit coalescence by steric hindrance. However, the interfacial adhesion is not necessarily improved to a satisfactory level as no covalent bonds are formed. Additionally, such tailor-made copolymers might come at a significantly higher material price in comparison to the blend polymers, needing careful economical evaluations.

Chemical compatibilization

The chemical compatibilization includes multifunctional low-M_w molecules, which mostly react in a two-step manner. In the first step, polymer A is modified with the multifunctional molecule by a polymer-analogous conversion, preferably via melt-grafting [55,146–148]. The (partially) modified polymer A acts as the compatibilizer when blended with polymer B [52,149]. The described steps may be performed by a two-step processing [150] or simultaneously within a single blending process [115,151,152]. Simple and readily available base chemicals, such as MA or citric acid (CA), and molecules with glycidyl ether (‘epoxides’) or oxazoline moieties are frequently found as ideal modifier candidates.

Chemical-type compatibilizers form covalent bonds with both blend partners and fulfill all the requirements by reducing interfacial tension, inhibiting coalescence, and increasing interfacial adhesion. One major disadvantage is the unselective reaction between the blend polymers

featuring no control on the resulting product. Another drawback that needs to be mentioned is the difficulty of handling the mostly hazardous low-M_w substances, having irritant, corrosive, or even toxic properties [153–155].

Physicochemical compatibilization

The combinatory approach of physicochemical compatibilization allows using reactive copolymers to benefit from both methods (physical and chemical compatibilization). While one part of the compatibilizer enables physical entangling with one blend partner, the other part undergoes covalent bonding with the other blend partner. Most frequently used examples are polystyrene (PS)-co-glycidyl methacrylate (GMA) used for PPE / polybutylene terephthalate (PBT) blends [156], polyethylene-co-GMA for polyethylene terephthalate (PET) / polycarbonate (PC) blends [157], styrene-acrylonitrile (SAN)-co-MA used for PA / acrylonitrile-butadiene-styrene copolymer (ABS) blends [158–160], or SMA used for PA6 / PS [161–163] and PA66 / PPE [164]. Using copolymer compatibilizers gives rise to mainly branched topologies consisting of the compatibilizer itself grafted by the reactive polymer used in the blend system.

Besides their excellent compatibilization, physicochemical compatibilizers are also easy to handle (mostly granular and dust-free products) and commercially available in various modifications, making them particularly interesting for typical melt-mixing processes.

Styrene-maleic anhydride (SMA) copolymers as blend compatibilizers

Similar to PS, SMA copolymers are synthesized by radical polymerization, leading to linear copolymers with a mainly random distribution of the monomers whenever styrene is the majority [165]. By shifting the monomer concentrations to a molar ratio of 1:1, an SMA with an alternating structure can be obtained [165,166]. The general chemical structural formula of a random SMA is shown in Figure 9.

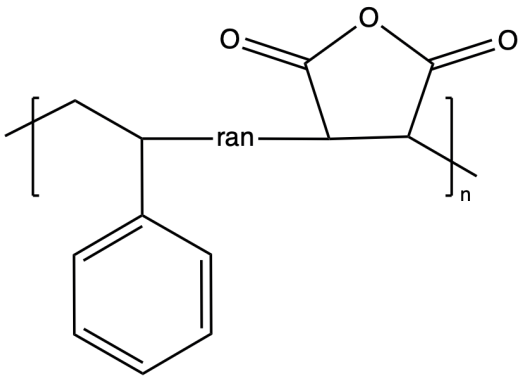

Figure 9 General chemical structural formula of a random SMA copolymer.

SMA has been reported to be miscible or at least compatible with various polymers, such as SAN [167,168], polymethyl methacrylate (PMMA) [64,168], ABS [169], PS [56,167], and PPE [170,171]. Besides the physical affinity, the availability of the very reactive anhydride moieties enables a covalent link to condensation polymers containing carboxylic acids or amines. Commercial SMAs have been used to compatibilize blends consisting of polypropylene / polyvinylidene fluoride [172], ABS / PMMA [173], PS / thermoplastic polyurethane [174], PS / PET [175], ABS / PBT [176], PA6 / ABS [177–179], PA6 / PS [162,163,180,181], PA6 / PPE [182–187], PA66 / PS [146] or PA66 / PPE [164].

SMA as a compatibilizer for PA / PPE blends

PA-based blends have been predominantly investigated in the literature. The main focus of early-stage work was to prove the formation of graft polymers between PA and SMA, and to indicate successful compatibilization by morphological analysis. The successful grafting formation was qualitatively described by rheological measurements [188] and solvent extraction methods [77,188]. Quantitative descriptions were provided via Fourier-transformed infrared spectroscopy [182,187] or titration [55]. The miscibility of SMA with the other blend partner (*e.g.*, ABS, PS, PPE) has been chiefly verified by thermal analysis, such as differential scanning calorimetry (DSC) [167,170] or by optical methods, such as optical or electron microscopy [167,171]. For PPE / SMA blends, it was found that SMAs with a maximum MA content of 8 wt% reveal complete miscibility [56,187]. SMAs with higher MA concentrations appear immiscible in PPE due to an exceeded polarity of the copolymer [186]. The

morphological changes upon compatibilization of PA / PPE blends were visualized by scanning electron microscopy (SEM) [183,184,189] or transmission electron microscopy (TEM) [58,190]. In almost all cases, SMA copolymers did show a reduction of the mean diameter of the dispersed phase, which is believed to indicate successful compatibilization [164].

Concerning PA6 / PPE blends, the effect of MA content in SMA on the final properties has been discussed controversially. While most of the literature is limited to SMA with MA contents of 8 wt% or lower, only very few investigate SMA types with MA contents higher than 10 wt% (immiscible in PPE) [186]. Based on this fact, it is impossible to generate a clear opinion on the effect of the MA content on the properties of PA / PPE blends. Dedecker and Groeninckx [182] compared two types of SMA used in PA6 / PPE (70 wt% PA6) with 2 and 8 wt% MA, namely SMA2 and SMA8, respectively. They stated that besides a higher reactivity of SMA8, higher interfacial activity was found as the miscibility of SMA8 in PPE is very close to the limit. Additionally, smaller PPE domain sizes and thus a larger interfacial area was located at 5 wt% SMA8 content compared to the same amount of SMA2.

Another study comparing two different SMAs with 2 and 17 wt% concluded that the immiscible SMA (SMA17) is less efficient in the size reduction of PA6 domains in a blend consisting of (PPE/PS) / PA6 with 25 wt% PA6 [56]. The location of the SMA was not visualized in any of these two studies. Furthermore, in another investigation, an immiscible SMA (21.8 wt% MA) was used to compatibilize a PA6 / PPE blend with a ratio of 70:30 w/w [186]. The workgroup reported a significant PPE droplet size reduction from 3.42 µm to 0.56 µm upon adding 10 wt% SMA. They attributed an improved morphology to the interfacial activity of the given SMA, expressed by sub-micron-sized residues at the blend interfaces.

Regarding PA66 / PPE blends, few studies exist in the literature, such as in [52,65,191,192]. The lower melting temperature, reactivity, and cost were benefits of choosing PA6 as a more suitable polymer material. However, higher thermal stability, higher modulus, and a slightly lower humidity / water uptake are good arguments for using PA66 as an alternative blend partner. Interestingly, until 2021, only chemical compatibilization was used to improve the material properties of PA66 / PPE blends in academic literature, where PPE was modified by reactive extrusion first and then reactively coupled to the PA66 [51,65,152,193].

In terms of physicochemical compatibilization, two studies can be found [164,194]. In the first, Zhang *et al.* [194] used self-made high-impact polystyrene (HIPS)-g-MAH compatibilizers analogously to the previously mentioned PPE-g-MAH methodology. In the second study, Kim *et al.* [164] used SMA as a compatibilizer. Here, an SMA with 7 wt% MA could reduce the domain sizes of miscible PPE / HIPS within a PA66 / (PPE / HIPS) blend at 20 wt% content. Further related studies with SMA compatibilized PA66 / PPE blends are only published by the author of this work [195,196].

In summary, SMA copolymers have been widely used to enhance the morphological and mechanical properties of a diversity of polymer blends. A fast reaction between anhydride and amine moieties, enabling a conventional compounding process, made SMA very attractive for PA-based blends, such as PA6 / PS or PA6 / PPE. For PA6 / PPE, a multitude of publications are found. However, only a small number of them describe the location of SMA corresponding to the MA content. Furthermore, a systematic study comparing miscible and immiscible type SMAs' mechanical performance is missing completely. Recently, PA66 / PPE blends have been gaining more attraction. Therefore, a systematic study and a deep understanding of the influence of the SMA type (miscible / immiscible in PPE), the SMA content, and the blend ratio of PA66 / PPE are highly of interest.

2.3 Mechanical behavior of polymer blends

The mechanical performance of polymer blends is strongly influenced by a variety of material-based preconditions, such as blend miscibility, blend morphology, and the contribution of the individual blend components [107]. For miscible blends (single-phase blends), the mechanical properties can be tuned linearly [74,111]. In the case of an immiscible blend (multiphase blend), the interfacial adhesion, *i.e.*, a good stress transfer at the interfaces, is believed to be a critical parameter in determining the mechanical characteristics of the blend [74,197,198]. Compatibilizers must be located at the blend interface for a decent stress transfer. However, adding a third component increases the system's complexity even further.

Within this section, firstly, an overview of general deformation mechanisms of polymer blends will be shown, followed by a brief introduction to fatigue crack propagation measurements,

which is a powerful tool for the description of micromechanical phenomena of the material. Lastly, the effect of humidity on the mechanical performance of polymer blends will be discussed since PAs lead to a drastic change in the properties upon water / humidity uptake [199].

2.3.1 Deformation mechanisms in polymer blends

When a polymeric material is exposed to mechanical loading, elastic deformation occurs up to a certain extent, followed by plastic deformation as soon as a particular stress limit (elasticity limit) is surpassed. For uncompatibilized multiphase blends, a weak interface serves as a predetermined breaking point, where limited adhesion can be provided to transfer the applied stress from one phase to the other. In such a case, only a low degree of decohesion in coexistence with interfacial friction is described as main energy dissipation mechanisms [74,200]. Compatibilization guarantees an efficient stress transfer with a robust interfacial interaction. Characteristic polymer material properties, such as chain flexibility, crystallinity, entanglement density, and bonding strength, govern the deformation mechanisms [80,201,202]. In terms of test conditions, parameters affecting the deformation mechanisms include loading mode (static or dynamic), type of stress (pulling, bending, compressing, among others), deformation speed, specimen size and shape, and temperature [148,203,204].

Observing a polymer specimen under load, the deformation appears like a homogeneous process at a macroscopic scale. However, at the microscopic level, polymer deformation is governed by various mechanisms; thus, a heterogeneous process becomes evident. Three main types of micro-scale deformations have been established in literature: (A) crazes, (B) shear bands, and (C) deformation zones [202]. Crazes, also named “pseudo-cracks” or “micro-cracks”, consist of strongly localized bands of plastically deformed polymer, always oriented normal to the direction of maximum (tensile) stress. Crazes are likely to appear within amorphous phases of polymers (also in semi-crystalline polymers) undergoing a multi-step process, including (1) void nucleation and fibril formation, (2) craze propagation, (3) fibril thickening, and (4) fibril fracture, which is extensively discussed in the literature [205–210]. One such craze comprises multiple fibrils in a diameter range of 5 – 15 nm, highly oriented in the loading direction, as depicted in Figure 10.

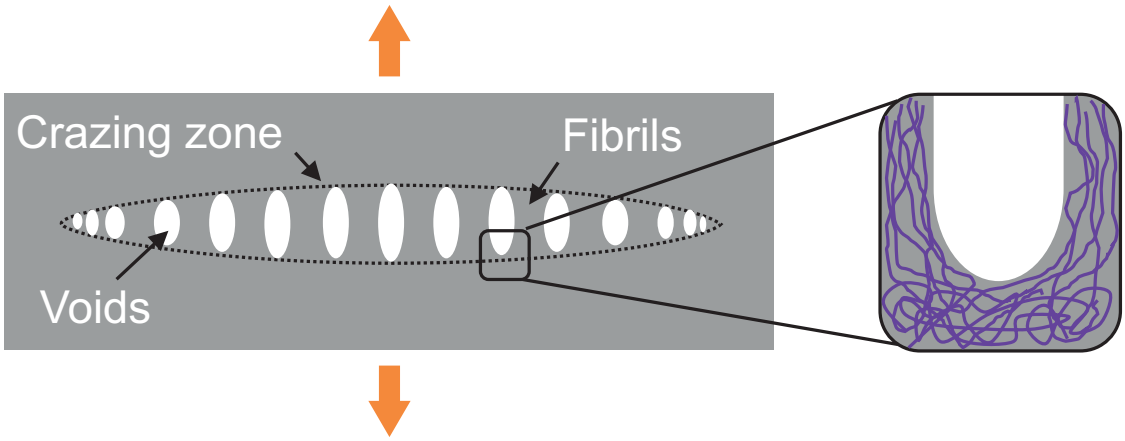

Figure 10 Schematic representation of a craze growing perpendicular to the stress. The polymer chains arrange around a void (fibrillation and orientation) [211].

Between the fibrils, elongated voids can exist with diameters up to 50 nm, which undergo growth and coalescence simultaneously until a micro-crack is formed once the fibrils rupture. Crazing is a highly desired mechanism for energy dissipation typically found in rubber-toughened brittle polymers (PS, SAN, or PMMA) [212–215].

In contrast to the highly-localized crazes, shear bands may also occur diffusely. Localized bands are oriented approximately 45° to the stress direction. Thicker shear bands usually consist of multiple thin shear bands given in spatial proximity and appear in a more diffuse structure with a width of around 100 nm. Shear banding does not include the formation of voids and thus exhibits a deformation without a change in volume (displacement of matter) [216]. Macroscopically, shear bands appear as crossed patterns mainly localized at necking or cold-drawing zones [202]. Deformation zones are usually created by the coalescence of a significant number of shear bands resulting in a diffuse deformation area, growing perpendicular to the direction of stress, the same as for crazes [202,217]. The stress needed to initiate crazing or shear-induced yielding mainly depends on the measurement temperature relative to the polymers' glass transition temperature (T_g). However, a general assumption is not readily available since many molecular factors influence the resistance to craze or yield. In general, a higher M_w results in greater resistance to deformation. Nevertheless, the predominant deformation mechanism of a polymer depends on its entanglement molecular weight (M_e), entanglement density (ν_e), and molecular mobility, *i.e.*, chain stiffness (C_∞).

Polymers, such as PS, SAN, and PMMA, mainly fail via crazing (low craze stress), as they possess a rather high M_e and low v_e. In contrast, PPE and PC have very low M_e, a very high v_e, and a relatively low C_∞, with which both are keen to fail by yielding (very high craze stress) [218]. An overview of various polymers, their M_e, v_e, and favored deformation structures are given in Table 1.

Table 1 Entanglement molecular weight (M_e), entanglement density (v_e), chain stiffness (C_∞), and characteristic deformation behavior of various thermoplastic polymers in the amorphous state [219].

Type of Polymer	**M_e** [g/mol]	**v_e** [10^{13} chains / μm^{-3}]	**C_∞** [a.u.]	**Deformation mechanism**
PS	18 700	3.4	10.8	fibrillated crazes
SAN	11 600	5.6	10.6	homogeneous and fibrillated crazing
PMMA	9 200	7.7	8.2	homogeneous and fibrillated crazing
PPE	3 620	17.8	3.2	shear bands and deformation zones
PC	1 790	40.5	2.4	shear bands and deformation zones
PA6	2 480	26.2	6.2	complex
PA66	1 990	32.3	6.1	complex

All mentioned deformation mechanisms apply to amorphous polymers or structures without orientation. The deformation of semi-crystalline polymers appears more complex as they include three additional modes: (1) lamellae stack rotation, (2) interlamellar separation, and (3) interlamellar slip [220–222]. While interlamellar separation is only found under specific circumstances (stress perpendicular to the lamellar surface), interlamellar slip is frequently observed for measurements above T_g of the materials, involving shear of amorphous phases located between individual lamellae. Lamellae stack rotation occurs whenever a further deformation of the amorphous phase is exhausted. Once all lamellae stacks are oriented, crystallographic slip mechanisms take place.

Applying stress to polymers causes inelastic deformation once the elasticity limit is exceeded. At the same time, there is a competition between craze formation and shear yielding or even a combination of both. v_e and C_∞ define which of the both mechanisms are predominant.

Polymers with low v_e and high C_∞ show crazing and are classified as brittle polymers. In contrast, polymers with high v_e and low C_∞ deform under shear yielding and are categorized as (pseudo-) ductile polymers [74,218]. Semi-crystalline polymers undergo more complex deformation structures; once the amorphous phases are under maximum stress, forcing the crystalline sections to deform. Upon blending of two polymers, especially when combining a semi-crystalline and an amorphous species, for instance, PA66 and PPE, the interactions at the interface provide further complexity to the system [52]. Sue and Yee [223] investigated the deformation behavior of a commercial PA66 / PPE blend (Noryl® GTX 910) under tensile loading. The authors showed that the material deforms under a substantial volume increase upon exceeding the yielding point of the blend (> 40 MPa), indicating a strong void formation. As described before, a change in volume upon loading is characteristic for a crazing mechanism, which TEM micrographs given by the authors also support. In general, the deformation of PPE and PA66 is mainly governed by shear banding and large deformation zones allowing extensive yielding and necking. However, it was also found that strong craze formations root in the PPE domains. This unexpected crazing is attributed to a styrene-based copolymer used as a toughener for PPE, also contributing to the overall energy consumption before rupture. Similar results by Hobbs and Dekkers [224] also support the complex fracture behavior of mentioned blends under tensile stress. Interestingly, the literature has not reported SMA compatibilized PA66 / PPE blends concerning micro-mechanical deformation mechanisms.

2.3.2 Fracture mechanics of polymer blends

A further extension of the above-mentioned micro-mechanical deformation mechanisms leads to the formation of micro-cracks, followed by coalescence to macroscopic cracks resulting in an ultimate macroscopic fracture of the materials. Defects in the form of (micro-) cracks or other artifacts are known to initiate a brittle fracture behavior even in polymers considered as ductile polymers. This pseudo-ductile behavior is also described as “notch-sensitivity”, which is found in many thermoplastic polymers, such as PA, PET, or PC [225,226]. However, brittle failure is undesired; hence, much effort is put into introducing ductility to materials to prevent an easy propagation of cracks. The ability of a material to resist fracture is called “toughness” and is described as the energy absorption or dissipation during deformation before failure.

To increase the toughness of the polymeric material, two different paths are commonly followed: (1) initiation of many localized events of energy absorption to inhibit the crack formation and (2) reducing the speed of crack propagation or even stopping it [223,227,228]. Path 1 may include the addition of small and hard particles or fibers to enable multiple micro-cracking, void formation, or ductile particles to initiate multiple sites for craze or shear band formation [229–231]. Another efficient way is using soft nanoparticles to create nano-voids and extensive matrix yielding between the single nano-domains [128,232,233]. Path 2 involves either stiff or soft particles. In the case of stiff particles, such as glass fibers or silicon dioxide, the crack encounters a higher strength area, where mainly crack deflection occurs, as a cohesive failure of the stiff particles is not possible [234–236]. The good bonding between the polymer and the stiff particles increases the toughness tremendously. Using soft (rubber-like) particles, the crack is desired to propagate to an area of higher ductility, where crack tip blunting and maybe even crack stop occurs [237,238]. An overview of possible mechanisms to enhance the toughness of a polymer (blend) is given in Figure 11.

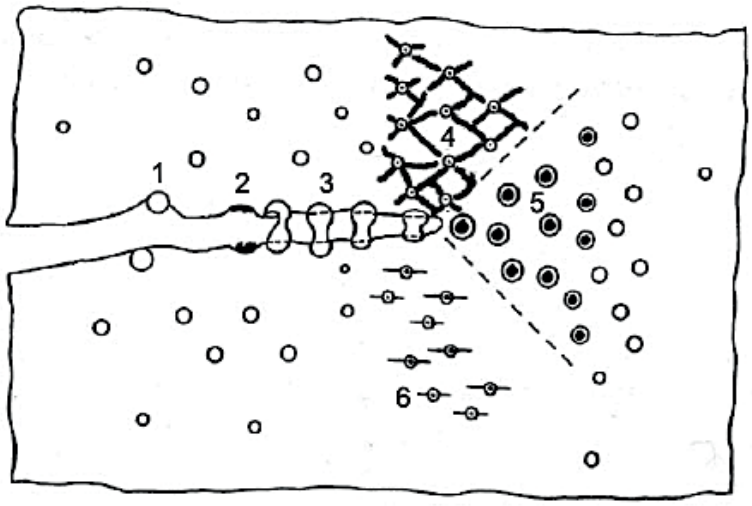

Figure 11 Mechanisms for crack-tip shielding to enhance the toughness of polymer (blends): (1) crack deflection, (2) cohesive failure, (3) bridging of dispersed phase, (4) shear banding zone, (5) (rubber) particle cavitation and void growth, (6) craze formation and micro-cracking by dispersed phase. Reproduced from [197].

Regarding polymer blends, ideally, one blend partner has an intrinsic toughness to improve the less ductile blend partner [239]. Nevertheless, it must be considered that the blend interface is the most critical region as it may be the weakest spot in the system to facilitate crack propagation readily. Concerning PA-based blends, the toughness was increased by simply coupling both polymers via reactive extrusion [77,240], using compatibilizers as a third component [241–243] or by using the latter with very soft segments to increase the interfacial bonding and making use of one of the mentioned toughening approaches [128,244].

2.3.3 Measuring toughness

The toughness of a polymer is mainly evaluated by applying tensile or impact tests (impact energy), whereby the latter has been reported most frequently [205,245]. In polymer blends, a higher toughness is related to a stronger interface between the immiscible phases [115,246]. However, the mentioned methods assume a flawless specimen without defects and may not be sufficient to predict their resistance to deformation in the presence of defects. This behavior is simulated by the introduction of a defined notch and a sharp crack before the measurement. Notched impact tests are commonly used for polymer blends as a straightforward method [247,248]. Nevertheless, more complex but even more descriptive and precise techniques have been developed by applying fracture toughness (static) and fatigue crack propagation (dynamic) tests. Both include a defined notch and a naturally sharp crack introduced before the measurement, giving information about the stress needed for the critical failure of the polymer (static) and the speed of crack propagation (dynamic).

2.3.4 Fatigue crack propagation (da/dN)

The fatigue crack propagation test (FCP) is one of the most sensitive methods for describing a cracked material's lifetime in combination with evaluating apparent micro-mechanical deformation and fracture mechanisms [249]. Regarding polymer blends, it is the most powerful test to investigate the degree of interfacial interactions. The fundamentals of this method reside within the theory of linear-elastic fracture mechanics (LEFM), which is only valid for a brittle fracture type under tensile loading, considering very small plastic zones [250,251]. An essential measure for the apparent stresses located at the crack tip is the so-called stress intensity factor (K_I) [250]. The index "*I*" describes the mode of applied crack loading, which in this case is opening, and thus the tensile load. The most significant measure within the K-concept is named critical stress intensity factor (K_{Ic}), also called fracture toughness, describing the upper stress limit, where an unstable crack growth is initiated. Unstable crack growth is defined as no additional energy is required for the crack to grow along the material, resulting in fatal failure. To understand the crack propagation behavior under stable conditions ($K_I < K_{Ic}$), cyclic loads are applied as described by Hertzberg and Manson [252]. Within the scope of this thesis, the FCP characteristics are investigated by evaluating the crack growth rate (da/dN) as a function of the stress intensity factor amplitude (ΔK). By doing this, the FCP behavior can be defined over multiple decades of growth rates, ranging from 1 nm / cycle to 1 mm / cycle. One key parameter of dynamic tests is the frequency, which was shown to have a significant influence on the response of the tested material [253] and thus, should be chosen carefully. This work applies 10 cycles per second, which is a typical value applied for (fiber-reinforced) polymeric materials [234,239,254], as found for thermal breaks mounted in aluminum window frames. Compact tension (CT) shaped specimens are most frequently used to evaluate the FCP performance, shown in Figure 12a, together with a typical double-logarithmic plot of *da/dN versus* ΔK in Figure 12b. The scheme consists of two characteristic curves, both showing three distinct regimes, representing a rigid polymer (black) and a semi-rigid polymer (grey). The measurement starts from low ΔK values and is subsequently increased until the end of the measurement, where ΔK shows a dramatic increase.

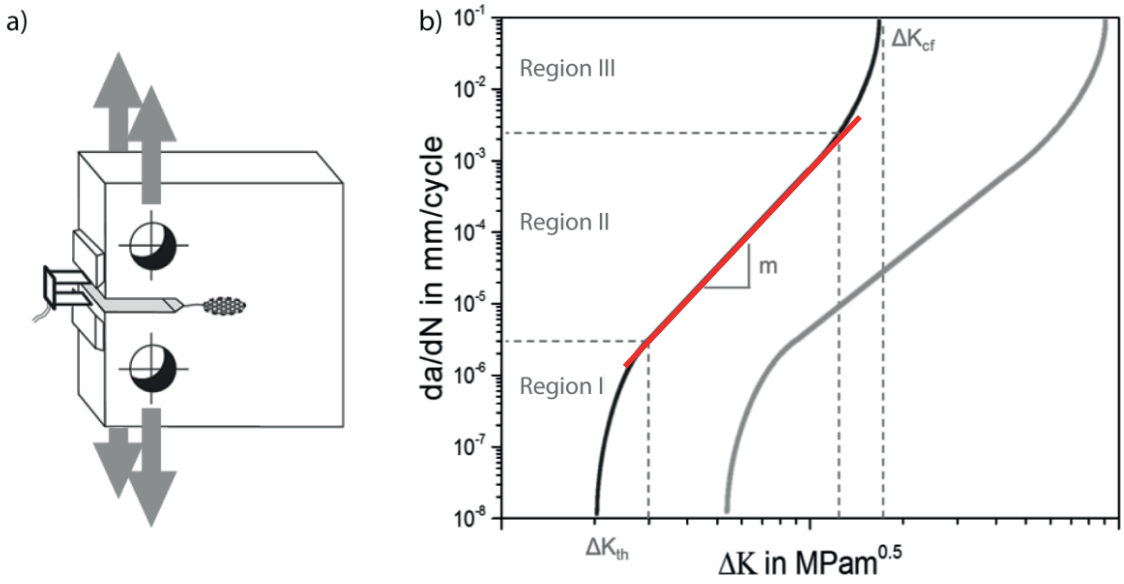

Figure 12 Schematic illustration of (a) compact tension (CT) specimen with a propagated crack under mode I load, and (b) double-logarithmic *da/dN – ΔK* plot with the typical data curvature (grey curve shows an improved FCP behavior). Reproduced from [255].

The first region (Region I) is known as crack propagation initiation. The threshold ΔK (ΔK_{th}) is the most important value describing the minimum stress intensity needed to initiate a crack growth. Below this value, propagation of the crack is not possible. Passing this region, a linear relationship can be found in Region II, also known as the Paris-Erdogan region. This region represents the range of stable crack growth, which can be mathematically described by the Paris-Erdogan equation [256], as given in Equation 11, where C and m are material coefficients influenced by measurement environment, frequency, temperature, and stress ratio.

$$\frac{da}{dN} = C \cdot \Delta K^m \tag{11}$$

Upon double-logarithmic plotting, the slope of the linear region (m) is calculated from the dependency shown in Equation 12.

$$log\frac{da}{dN} = \log C + m \cdot log\Delta K \tag{12}$$

The slope can be seen as a relative measure describing the degree of crack propagation resistance. In region III, an unstable crack growth regime is reached, where the crack propagates with the speed of sound once a critical ΔK (ΔK_{cf}) is reached [257].

The FCP test was first developed to investigate metals, followed by ceramic materials and later polymers. However, up to now, mostly thermoset polymers have been tested as they easily fulfill the requirements of plain-strain deformation within LEFM theory as proposed by Irwin [250]. Thermoplastic polymers were also studied later, where Hertzberg is considered a pioneer as an extensive list of publications can be found [253–255]. Detailed descriptions of all fundamental relationships and definitions of test parameters have been systematically reported in the literature [253,261].

One should note that microscopic analysis of the fracture surface is crucial after FCP testing to reveal the full potential of this method. By doing so, micro-mechanical deformation and fracture mechanisms can be used to explain the obtained results.

FCP tests have been proven as a great tool to investigate the fatigue behavior of (reinforced) homopolymers [228,235,262]. Nonetheless, only a few studies can be found in the literature regarding polymer blends, identifying the importance of interfacial interactions, such as SAN / PMMA [254], PS / polyethylene [263], PC / ABS [264] and PPE / SAN [265], for fatigue behavior. Surprisingly, one of the very first publications reporting FCP data for immiscible blends was based on PA blends, including a commercial PA66 / PPE blend (Noryl® GTX 900) [266]. The workgroup compared a PA66 homopolymer with the Noryl® GTX 900 and found significantly worsened FCP behavior for the blend system. It was claimed that the interfacial interaction between PA66 and PPE is the weakest spot during fracture and thus must be strengthened appropriately. Adding a rubber-toughened PA (7 wt%) to Noryl® GTX 900 improved the values noticeably, leading to a lower slope in Region II and a higher ΔK_{cf} value compared to one of the neat PA66. The primary deformation mechanism was identified as craze coalescence for PA66 alone. As PA66 was the matrix phase upon blending with rubbers or PPE, a change of deformation mechanisms could not be reported. This fact shows that the matrix phase predefines deformation and fracture characteristics. Another PA-based blend studied was PA6 / ABS, which was varied in the blend ratio (70:30 and 30:70 w/w). These two blends were then compared under subsequent compatibilization with an MA-

modified SAN (2 wt% MA) [158]. The authors exhibited that a blend ratio of 70:30 w/w, where PA6 represents the majority phase, is beneficial for all mechanical tests, including static and dynamic loading. Uncompatibilized blends featured a significant deterioration in mechanical performance due to the lack of interfacial interaction. Upon addition of the compatibilizer, noticeable improvements were achieved, being very pronounced for static mechanical tests. In the FCP test, the compatibilizer (up to 2 wt%) shifted the curve further right, expressed by a lower slope and higher ΔK_{cf}, indicating a stronger interface. The improvement is associated with an enlargement of the total interfacial area since a size reduction of PA6 domains was observed by adding the compatibilizer, creating a higher number of interaction sites during fracture.

In summary, many critical factors influencing mechanical deformation and fracture behaviors of polymer blends have been identified. All applied methods underline the importance of the apparent blend morphology and the intrinsic properties of the matrix polymer since it predefines the main type of deformation and fracture. Nevertheless, it is also emphasized on the degree of interfacial interaction between two polymers, as it represents the weakest spot in the system, urging for stabilization by compatibilization. The effect of compatibilization was mainly evaluated by tensile and impact testing for defect-free specimens. For the mechanical properties with a given defect, K_{Ic} and FCP were applied, whereas considerably more research studies are found in the literature for the first method. This thesis will use the latter approach to fill this gap and understand the effect of SMA compatibilizers in PA66 / PPE blends.

2.3.5 Effect of humidity

Many polymers are known to undergo specific interactions with water (H_2O), such as being either water-soluble, water-swellable, or hygroscopic and thus being likely to "store" H_2O inside their free volume [267]. For the latter group of polymers, the absorption of H_2O strongly influences their overall properties, such as thermal, electrical, and mechanical properties [268,269]. Hygroscopic polymers usually exhibit polar structures within the backbone or are capable of hydrogen-bonding, such as epoxides, PAs and polyesters. Latter two polymers absorb H_2O being located within the amorphous phase [270,271]. The H_2O molecules weaken the inter-chain hydrogen bonding of the amide groups in the PA chains by a bridging

mechanism, acting as a plasticizing agent and increasing the molecular mobility of the polymer chains. At a macroscopical scale, the mechanical performance is altered from hard-brittle to a more elastic-ductile behavior. It is reported that upon H_2O uptake, Young's modulus, tensile strength, and hardness of PA are reduced with increasing H_2O content [199].

In contrast, increased elongation under tensile stress and impact resistance are shown [272–274]. In terms of fracture resistance, the effect of moisture on PA6 was studied by Bretz et al. [275]. The researchers reported a very little parallel shift to faster crack growth for 1 wt% H_2O, whereas an H_2O content of 2.5 wt% surprisingly improved the FCP behavior, albeit not very pronounced. A fully saturated PA6 (8.5 wt% H_2O) resulted in faster crack growth with a significantly lower ΔK_{th}. The variation of FCP behavior was attributed to the theory of "loosely" and "tightly" bound H_2O [270,276]. It is stated that up to 2 wt% H_2O uptake, a decrease in T_g is very pronounced, whereas higher H_2O contents result in only little changes. The drastic decline is associated with the absorbed H_2O, interrupting hydrogen bonding between the polymer chains by building bridges. As mentioned above, higher molecular mobility is achieved once H_2O is introduced in the amorphous phase. This leads to an improved packing of the polymer chains given by a decreased specific volume of the tightly-bound water, meaning that H_2O contents exceeding 2 wt% are loosely-bound and act as a plasticizer. They summarize that tightly-bound H_2O facilitates a sufficient degree of localized deformations to induce crack blunting, thus improving the FCP behavior.

On the contrary, loosely-bound H_2O significantly reduces the resistance to crack growth by providing a high degree of chain mobility. In the case of polymer blends, more specifically PA / PPE (Ultranyl® KR 4520, BASF), only one study was found to address the effect of humidity on the viscoelastic properties, measured by dynamic-mechanical analysis (DMA) [192].

The authors describe that upon H_2O uptake, a significant change in the T_g and the storage or loss modulus gets apparent. However, they summarize that the changes in the blend with PPE are less detrimental than in neat PA66. As thermal breaks and other products made from PA66 / PPE blends encounter various weather conditions throughout their lifetime, they are exposed to daily-changing moisture levels. To easily compare the materials used in this work, the mechanical properties will be given in a dehydrated state (< 0.2 wt% H_2O). In the case of

tensile and FCP behavior, the effect of humidity (conditioned state: ~ 1 wt%) will also be investigated for selected samples to get a more realistic insight into the material's performance at ambient conditions.

2.3.6 Summary

Finally, it may be concluded that the morphology evolution of a polymer blend is mainly influenced by the viscosity ratio (η_r) and can also be tuned by adjusting the weight ratio of both polymers. For PA / PPE blends, the η_r is very large; thus, PPE is likely to form the dispersed phase even for contents higher than 50 wt%. As PA and PPE are immiscible upon blending, compatibilization must be applied to increase the interfacial interactions and mechanical performance. Besides polymer modifications and subsequent blending, copolymers, such as SMA as a third component, have been very effective in PA6 / PPE blends. However, a detailed analysis of the morphology on nano-scale is missing, only focusing on the ability of domain size reduction of the dispersed phase.

Regarding PA66 / PPE blends, SMA copolymers were only used as ordinary compatibilizers to elevate general properties (SMA with a fixed amount and MA concentration) and thus, not discussing the effect of various SMA types or contents on the morphology, rheology, or mechanical properties at all. The investigation of latter properties especially lacks a systematic approach, not allowing a proper structure-property relationship between the blend polymers and the compatibilizers. In detail, the effect of SMA copolymers on static (tensile) and dynamic (FCP) mechanical properties has not been studied for PA66 / PPE blends in the literature yet. Finally, even knowing the sensitivity of PAs to humidity, only one study has been found to address the effect of moisture on the change of PA / PPE blend (here PA66) properties. Consequently, no research studies in the literature are available concerning mechanical performance, such as in tensile and FCP tests, under dry and humid conditions.

3 Aims and approaches

SMA copolymers have been identified to have great prospects to compatibilize immiscible PA-based blends. Acting as physicochemical compatibilizers, they have the potential to chemically link to one polymer (PA) while being physically miscible with the other blend partner. This pseudo-amphiphilicity was proven to be suitable to enhance the properties of PA-based blends with PS, PPE, or ABS [177,184,277]. **The main objective of this thesis is to understand the influence of the SMA copolymer constituents regarding structure-property relationships for SMA compatibilized PA66 / PPE blends at different blend ratios. From these relationships, the optimal blend composition for maximum improvement in the performance of SMA compatibilized PA66 / PPE should be identified.**

Despite its broad use in PA6 / PPE blends, SMA was not investigated for PA66 / PPE blends up to now, making this constellation highly interesting to study in detail, especially from the viewpoint of the industrial relevance of this blend material. PA66 / PPE blends in particular are used for the manufacturing of thermal insulation bars (thermal breaks) in modern aluminum window frames. These bars are strongly contributing to the respectful use of energy and resources. Related to the mentioned application, this work emphasizes the structural analysis of PA66 / PPE / SMA blends at micro- and nano-scale and on their (micro-) mechanical properties. Apart from static testing in tensile mode, the most sensitive test (fatigue crack growth) to understand the effect of compatibilizers on the interfacial strength of a blend will be performed to investigate the interfacial interactions in detail. **Various SMA types and concentrations** will be used to obtain a **fundamental understanding of the reactivity and miscibility of the SMAs** and to **correlate this knowledge to the resulting rheological, morphological, and mechanical changes**, thus **establishing structure-property relationships from nano- to macroscopic scale**.

For the current work, the following sub-aims are derived:

1) **Understanding the interaction of various SMA types in neat PA66 and neat PPE.** Different SMA types, varying in their MA content and molecular composition, will be blended individually with neat PA66 and neat PPE to evaluate their miscibility in PPE and their reactivity with PA66. The aim is to understand in which phase the different SMAs are most likely to reside upon blending.

   Hypothesis 1: SMA8 will provide the best compromise between miscibility in PPE and reactivity with PA66.

   Hypothesis 2: The blend processing sequence will influence the localization at the interface and the mechanical properties, subsequently.

2) **Establishing fundamental correlations between the SMA interactions and the morphological and mechanical properties of the ternary PA66 / PPE / SMA blends at a constant PA / PPE ratio of 50:50 w/w.** After understanding the interactions with the individual blend polymers and finding the optimal processing sequence, the influence of the SMAs on the morphology and static mechanical properties is evaluated. For a given PA66 / PPE blend ratio (50:50 w/w), various SMA amounts will be used to find an optimum range and to identify the best-performing SMA type. Detailed analysis of the fracture surfaces will support the evaluation of the performance under static loading.

   Hypothesis 1: The alteration of morphology will be more pronounced with increasing MA content of the respective SMA.

   Hypothesis 2: The mechanical properties of the blends will improve with SMA miscibility in PPE and with increasing SMA amount.

3) **Understanding the role of PA / PPE blend ratio on the evolution of the morphology and quasi-static mechanical properties.** Choosing the best performing SMA, its effect will be investigated under varying PA66 / PPE blend ratios at 40:60 and 60:40 w/w. Also, here, it will be emphasized on the morphological changes and the static mechanical properties (tensile) to finally find the most suitable SMA amount for all blend ratios.

   Hypothesis 1: The mechanical properties of the blends are mainly determined by the PA66 content, increasing at higher ratios of PA66.

   Hypothesis 2: The degree of interaction of SMA8 with PA66 / PPE blends will be maximized with increasing PPE ratio, leading to greatest relative changes in mechanical properties compared to the binary systems.

4) **Gaining a deeper understanding of selected blends in the quality of the interphase between the blend components by fatigue crack propagation (FCP) experiments. Evaluating the relevance of humidity and controlled conditioning on the performance of the interphase.** Finding the optimum SMA amount, the mechanical properties under dynamic loading, *i.e.,* FCP tests, will be investigated on dry specimens. A correlation between the toughness in a quasi-static tensile test and the toughness obtained from FCP experiments will be established. The differences in the results for the FCP tests will be described by a detailed analysis of the fracture surfaces, thus identifying the apparent fracture and deformation mechanisms. As PA66 is hygroscopic, an investigation of conditioned samples is inevitable. After controlled conditioning of the blends, the same mechanical tests will be performed to reveal differences in the blends in dry state. The mechanistic changes after different sample conditioning will also be evaluated by analysis of the fracture surfaces.

   Hypothesis 1: A co-continuous morphology will be superior over droplet-sea structures.

   Hypothesis 2: The presence of SMA will improve toughness and compensate possible detrimental effects of increased humidity in the blends.

A conceptual overview and guide of the thesis is given in Figure 13. In Chapter 6.1, the interactions between the individual blend components will be analyzed. It will mainly be emphasized the properties of the used SMAs, such as miscibility in PPE and reactivity with PA66. In Chapter 6.2, the influence of SMA type in PA66 / PPE blends (50:50 w/w) will be revealed concerning rheological, morphological, and mechanical properties. An optimum SMA type will be chosen for further studies. In Chapter 6.3, the optimum SMA content will be identified for various PA66 / PPE blend ratios (40:60 and 60:40 w/w). Again, the morphological and mechanical properties will be investigated to determine the optimum SMA amount. In Chapter 6.4, the FCP properties of the optimized ternary blends at various PA / PPE blend ratios (40:60, 50:50, and 60:40 w/w) will be evaluated. Also, the influence of humidity will be investigated for quasi-static (tensile) and dynamic (FCP) testing after sample conditioning. All mechanical tests will be further analyzed by post-test fractography.

The contents of Chapters 6.1, 6.2, and 6.3 are partially published by the author within two peer-reviewed articles. As the articles are licensed under open access (CC BY 4.0), permission to reprint any text and figures is given upon citation, where applicable.

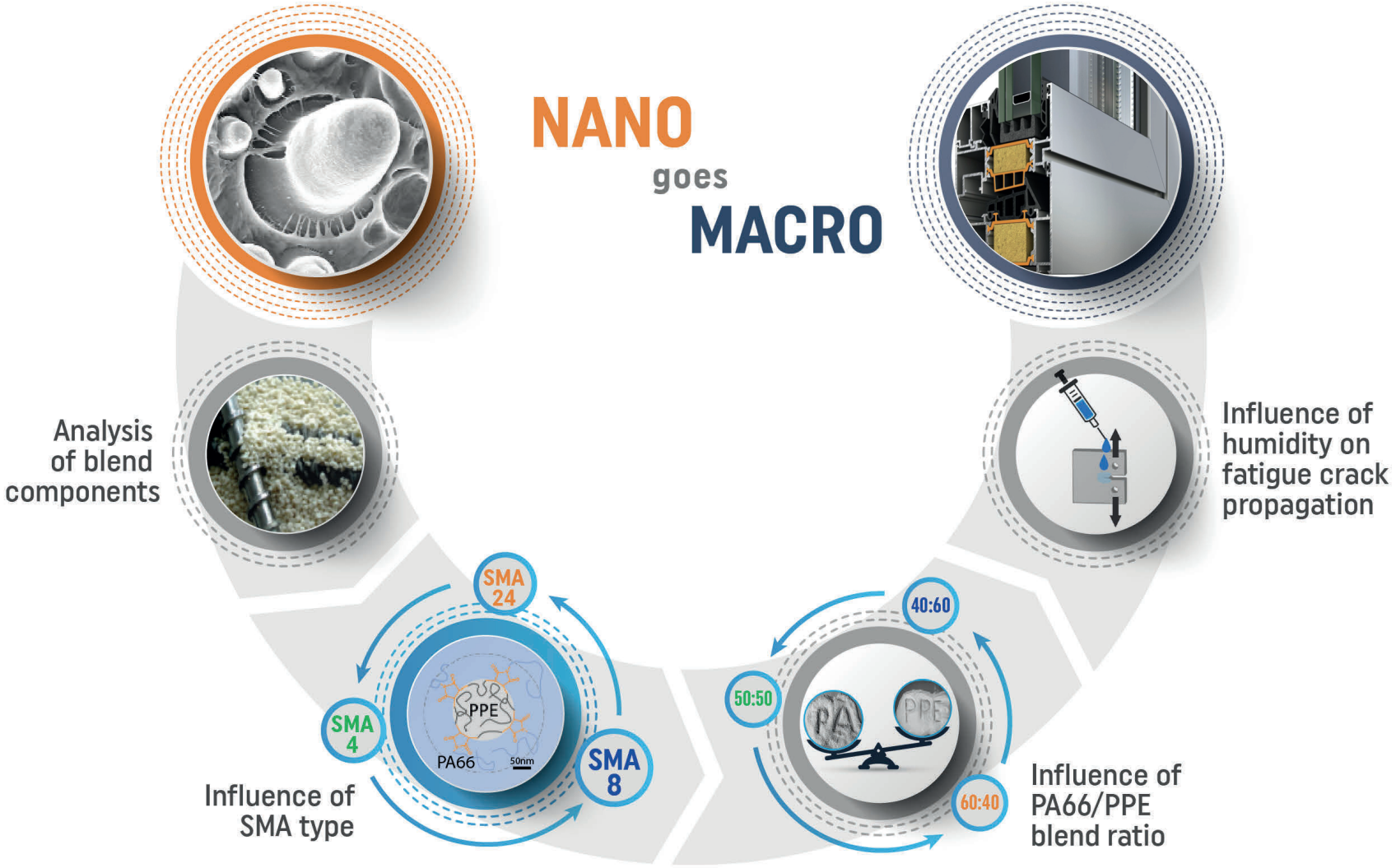

Figure 13 Graphical abstract of the thesis summarizing the sub-aims and chapters in the results section.

4 Materials

4.1 Blend components

The commercially available extrusion grade PA66 was obtained as granulates from BASF SE, Ludwigshafen, Germany (Ultramid® A27E), with a relative viscosity of 2.62 – 2.83 and viscosity number of 142 – 158 ml/g (ISO 307). The weight-averaged molecular weight M_w = 60.2 kg/mol with the corresponding molar mass dispersity D = 1.74 was determined by size-exclusion chromatography (SEC). Hexafluoroisopropanol has been used as an eluent at a flow rate of 0.5 ml/min (columns at 23 °C), together with a refractive index (RI) detector and a narrowly distributed PMMA standard for calibration.

Commercial grade OH-functional PPE (Xyron® S202A) with a viscosity number of 41 ml/g was obtained as a powder from Asahi Kasei Europe GmbH, Düsseldorf, Germany. The M_w = 36.8 kg/mol and D = 1.98 were also determined by SEC with chloroform ($CHCl_3$) as eluent at a flow rate of 0.5 ml/min (columns at 23 °C) using an RI detector and narrowly distributed PS standard for calibration. This reactor-grade PPE is free of additives, such as PS or styrene-(ethylene/butylene)-styrene copolymer. Mentioned polymers are usually added to ease processability or to increase toughness.

It is noteworthy that no processing aids, such as antioxidants or thermal stabilizers, were added to the blends at any stage of processing.

4.2 SMA compatibilizers

The commercial copolymers are usually offered with varying M_w and MA concentrations; however, no commercial copolymers were found to have varying M_w at constant MA concentration or *vice versa*. The MA concentration is calculated after determining the acid number (AN) by titration according to ASTM D3644, as shown in Equation 13.

$$MA\ concentration\ [\%] = \frac{AN\ [mgKOH/g]}{12.47} \tag{13}$$

SMA24

A granular shaped SMA with an AN of 300 mgKOH/g, M_w = 120 kg/mol and T_g = 150 °C was acquired by INEOS Styrolution, Frankfurt, Germany (Lustran® SMA 245) [c]. The MA concentration is calculated as 24 wt%. The chemical structure is depicted in Figure 9.

SMA8

A granulated SMA with an intermediate AN concentration of 104 mgKOH/g (MA concentration = 8.3 wt%) was provided by Polyscope B.V., Geleen, Netherlands (XIBOND® 120) [d]. The T_g and M_w are given as 120 °C and 245 kg/mol, respectively. The chemical structure is depicted in Figure 9.

SMA4

SMA4 (XIBOND® 315) is a copolymer containing an unknown amount of N-phenyl maleimide as a third monomer, with the chemical structure shown in Figure 14. It was received by Polyscope B.V., Geleen, Netherlands [e]. Besides the AN of 57 mgKOH/g (4.6 wt% MA), the powder material has an M_w of 155 kg/mol and a T_g of 180 °C. Given the bulkier substituent in the N-phenyl maleimide monomer, a higher chain stiffness is achieved, and thus a higher T_g and heat stability.

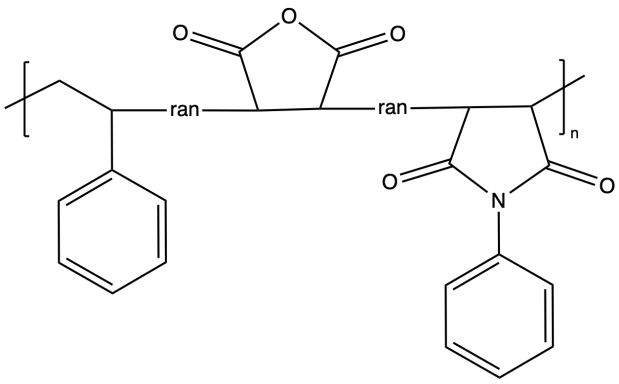

Figure 14 General chemical structural formula of a random SMA copolymer with N-phenyl maleimide co-monomer.

A summary of all considered materials and their abbreviations are given in Table 2.

Table 2 Material overview and abbreviations.

Material	Abbreviation
Ultramid® A27E	PA66
Xyron® S202A	PPE
SMA 245	SMA24
XIBOND® 120	SMA8
XIBOND® 315	SMA4

5 Experimental methods

5.1 Blend production

Melt processing

A co-rotating twin-screw extruder (ZSK 26MCC, Coperion GmbH, Stuttgart, Germany) with a screw diameter of 25 mm and a length to diameter ratio of 44 (length = 1100 mm) was used to perform melt blending of the polymers. The applied screw design and temperatures in °*C* along the barrel are illustrated in Figure 15.

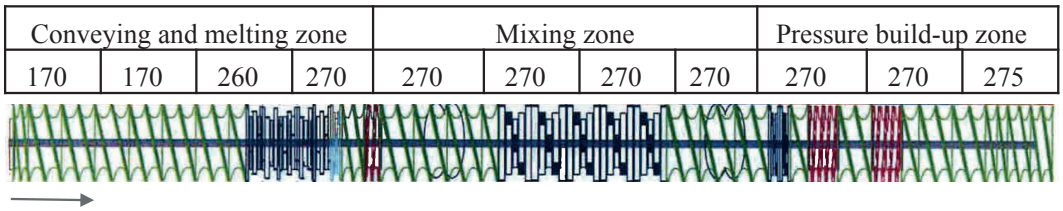

Figure 15 Screw configuration and barrel temperatures [°*C*] of the twin-screw extruder used for blend production.

A screw speed of 300 *rpm* and a feeding rate of 10 kg/h was kept constant for all compounding processes. After an approximate residence time of 90 s, the strands were water-cooled and pelletized. All polymers were introduced via the main feeder. An atmospheric and vacuum-assisted degassing was placed at 550 mm and 825 mm, respectively.

Sample preparation

All specimens were prepared by an injection molding unit (Arburg Allrounder 470H 1000-170, Arburg GmbH, Loßburg, Germany) with a screw diameter of 25 mm. Prior to injection molding, all granules were dried in an industrial dryer at 80 °C overnight. A dynamic pressure of 80 bar, an injection speed of 80 cm^3/s, and a holding pressure of 1000 bar was applied. A nozzle and mold temperature of 290 °C and 100 °C were selected, respectively.

5.2 Characterization methods

5.2.1 Rheological characterization

Rheological properties were investigated by a stress-controlled dynamic-mechanical rheometer (RDA III, Rheometrics Scientific, Piscataway, USA) under a nitrogen atmosphere applying a plate-plate geometry. Disc-shaped samples with a diameter of 25 mm and a thickness of 1 mm were used for the measurements. Complex viscosities of the blends were measured at 270 °C as a function of frequency within the range of 0.1 – 500 rad s^{-1} and a strain of 10 %. All specimens were dried overnight at 80 °C under vacuum to exclude the effect of hydrolysis.

5.2.2 Morphological characterization

Transmission electron microscopy (TEM)

For morphological analysis, a TEM Zeiss EM922 OMEGA (Zeiss NTS GmbH, Oberkochen, Germany) was used at an acceleration voltage of 200 kV. Tensile test specimens were used to prepare ultrathin sections (~ 60 nm) using an ultra-microtome (Leica EM UC7, Leica Microsystems GmbH, Wetzlar, Germany). For contrast enhancement, staining was implemented by using ruthenium tetroxide for 15 min, giving the PPE and SMA phases a darker appearance.

Number-averaged domain size distributions were calculated from at least 50 individual domains with the help of the software “ImageJ”. In this analysis, the largest diameter of each domain was considered, assuming that all droplets are circular and were cut at a point revealing their maximum diameters.

Field-emission scanning electron microscopy (FESEM)

Field-emission scanning electron microscopy (FESEM) Zeiss LEO 1530 (Zeiss NTS GmbH, Oberkochen, Germany) was conducted at an acceleration voltage of 3 kV for the characterization of the fracture surfaces after tensile and da/dN testing. Representative tensile bars and compact tension (CT) specimens, with the values closest to the average were sputtered with a platinum layer (1.3– 2 nm thickness) prior to analysis.

5.2.3 Thermo-mechanical characterization

Differential scanning calorimetry (DSC)

T_g of the neat PPE, SMA, and binary blends of PPE and SMA was determined by a Mettler Toledo DSC 1 (Mettler Toledo, Giessen, Germany) device. The method consists of a heating–cooling–heating cycle under a nitrogen atmosphere from 25 to 300 °C at the scanning rate of 10 K min^{-1}. The values of the second heating cycle were evaluated to calculate the T_g following ISO 11357-2, using the center temperature. Two measurements for each material were applied to increase the precision of the results.

Dynamic mechanical analysis (DMA)

Thermo-mechanical properties were characterized using a Gabo Eplexor® 500N (NETZSCH-Gerätebau GmbH; Selb, Germany) DMA. During heating from 25–250 °C (2 K/min), oscillatory stress (2.5 MPa) was applied at the frequency of 1 Hz in tensile mode. Loss factor (*tan* δ) signals were considered for interpreting the results, where occurring glass transitions appear as peaks. Each material was measured three times to minimize experimental errors. The T_g values were reported as an average of three *tan* δ peak values. Before testing, all specimens were dried overnight at 80 °C under vacuum to reduce the effect of hydrolysis.

5.2.4 Mechanical characterization

Tensile testing

Young's modulus, tensile strength, elongation at break, and tensile toughness data were obtained by using a universal testing machine (Zwick Z020, ZwickRoell GmbH & Co. KG, Ulm, Germany) equipped with an extensometer. All measurements were performed according to ISO 527-2, using 1A-type specimens. Young's modulus was determined at a pulling speed of 1 mm/min, whereas other characteristic values were measured at a crosshead speed of 50 mm/min. Average values from a minimum number of 10 samples are reported.

For measurements under dry conditions, all specimens were dried overnight at 80 °C under vacuum and vacuum sealed to exclude humidity (≤ 0.2 wt%). Conditioned samples were prepared by accelerated conditioning according to DIN EN ISO 1110. The samples were placed in a cabinet for seven days at a constant climate of 70 °C and 62 % relative humidity. The specimens were vacuum sealed to maintain the humidity level upon testing.

Fatigue crack propagation behavior (FCP)

The FCP behavior, described as fatigue crack growth rate da/dN as a function of stress intensity factor ΔK, was determined based on ISO 15850/ASTM E647 using a servo-hydraulic testing machine (IST Hydro Pulse MHF) from Schenck, Germany. This method was described by Herzberg and Manson [252] and explained in more detail in [261]. CT specimens with a thickness of 4 mm were exposed to dynamic loading (frequency = 10 Hz) in tension-tension mode. The amplitude of the sinusoidally applied stress intensity factor ($\Delta K = K_{max} - K_{min}$) was constantly increased with increasing crack length. The minimum to maximum load ratio, R ($R = K_{min} / K_{max}$), was set as 0.1. A naturally sharp pre-crack was introduced into the V-notched specimen by a razor blade. With the help of a crack opening displacement gauge (632.13F-20, MTS Sensor Technology GmbH & Co. KG, Germany) fixed to the specimen Fig. 11a, the crack length was measured *via* the Compliance method as described by Saxena and Huduk [278]. The quasi-continuously measured compliance is translated into the crack propagation rate, plotted as a function of ΔK, as shown in Figure 11b. Each measurement was repeated at least four times to minimize the experimental errors. The most representative curve will be selected to be displayed in the relevant results section.

6 Results

6.1 Characterization of neat blends and compatibilizer interactions

This chapter gives a basic understanding of the properties of the individual blend components in more simple binary systems, such as the reference blend PA66 / PPE, and also the particular SMA types in binary mixtures with neat PA66 (PA66 / SMA) and with neat PPE (PPE / SMA). Herein, interfacial activity of the SMA types will be investigated before the interactions in the more complex ternary blend systems (PA66 / PPE / SMA) are being evaluated. Following that, the production process (blending sequence) of the ternary blends will be investigated and finally determined for the next chapters.

6.1.1 PA66 / PPE: the reference blend system

The binary PA66 / PPE blend represents the reference system and is the starting point for this material development, wherein fundamental properties and interactions must be determined first. Talking about blend structures, questions regarding the miscibility, rheological properties, and morphology need to be answered.

As PA66 / PPE blends are known to be immiscible, thus phases separate when mixed, it is crucial to define the blend morphology by considering the individual polymer viscosities and the resulting blend ratio (η_r). Determining the complex viscosities (η^*) of the particular blend components at relevant processing temperatures, η_r can be calculated according to Equation 7. It is of interest to know that η_r might vary depending on the considered frequency (ω), as each polymer shows an altering response for varying shear forces. The η^* of neat PA66 and neat PPE, together with their η_r and the blend viscosity at 50:50 w/w, are shown in Figure 16.

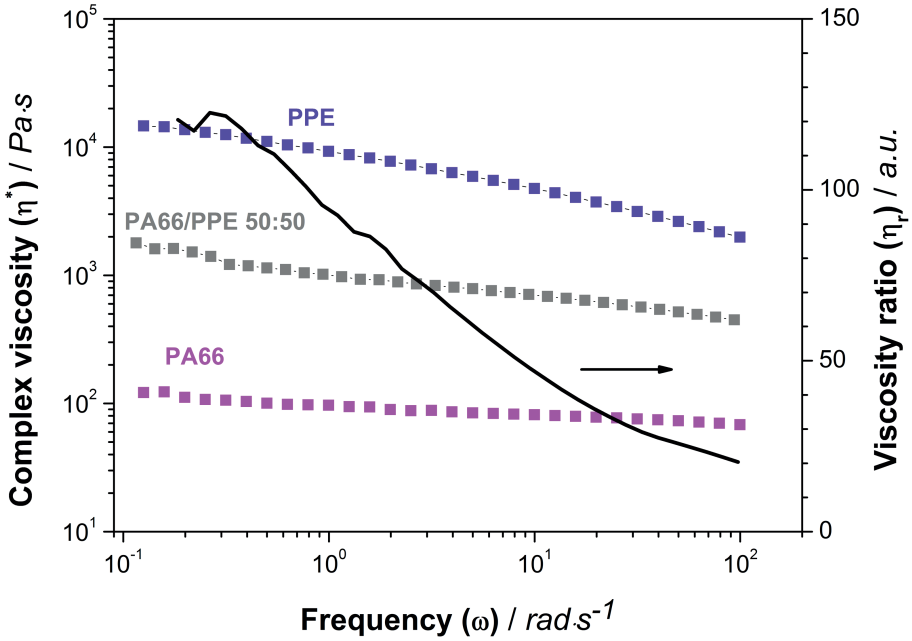

Figure 16 Complex shear viscosity (η^*) of neat PPE (purple), neat PA66 (magenta), binary PA66 / PPE 50:50 w/w (grey) and blend ratio (η_r) calculated by Equation 7 (black line).

The results reveal a significantly lower viscosity for PA66 than PPE throughout the full spectrum of ω. As the viscosity of PPE declines faster than that of PA66 for higher ω, η_r respectively drops to be lowest at the maximum frequency of 500 rad/s [65]. The blend viscosity of the binary PA66 / PPE (50:50 w/w) ranges between the individual components, however, residing closer to the PPE, thus being mainly influenced by PPE. With a lowered viscosity of the blend, processability *via* extrusion or injection molding is enabled at milder conditions. Typical shear rates for extrusion processes are reported to be between 50 – 500 s^{-1}, yet strongly depend on the extruder scale, screw design, and applied parameters [65,121,279].

The frequency-dependent ratios (extracted from Figure 16) are given in Table 3. Provided by the very high η_r between PPE and PA66, the less-viscous PA66 will form the matrix for a broad range of blend ratios [187,280].

Table 3 Selected, frequency (ω) dependent viscosity ratios (η_r) of PA66 and PPE calculated according to Equation 7.

Frequency (ω) [rad/s]	**0.1**	**1**	**10**	**100**
Viscosity ratio (η_r) [a.u.]	120	96	58	29

A phase inversion model for immiscible blends possessing a large viscosity mismatch was proposed by Utracki [95] as shown in Equation 14.

$$\eta_r = \frac{\eta_{PPE}}{\eta_{PA66}} = \left(\frac{\phi_m - \phi_{PA66}}{\phi_m - \phi_{PPE}}\right)^{[\eta]*\phi_m} \tag{14}$$

Where ϕ_m is the maximum volume packing and $[\eta]$ is the intrinsic viscosity, both given as 0.84 and 1.9 (for spherical domains in a matrix), respectively [95]. Considering a η_r of 29 and solving Equation 14 for the phase inversion point, a volume fraction of 76.7 and 23.3 vol% results for PPE and PA66, which translates to 75.4 and 24.6 wt% under regard to the individual bulk densities, respectively. This information allows us to estimate that PPE will only form the matrix once its amount exceeds 75.4 wt%. Below this, both polymers will either be in co-continuous state or PA66 will form the matrix. As the model of Utracki is only limited to a phase inversion, where one polymer is not forming the matrix anymore, further information is required to describe the blend ratio-dependent morphology in such blends. Micrographs of binary PA66 / PPE blends at different blend ratios, ranging from 70:30 to 20:80 w/w, are given in Figure 17.

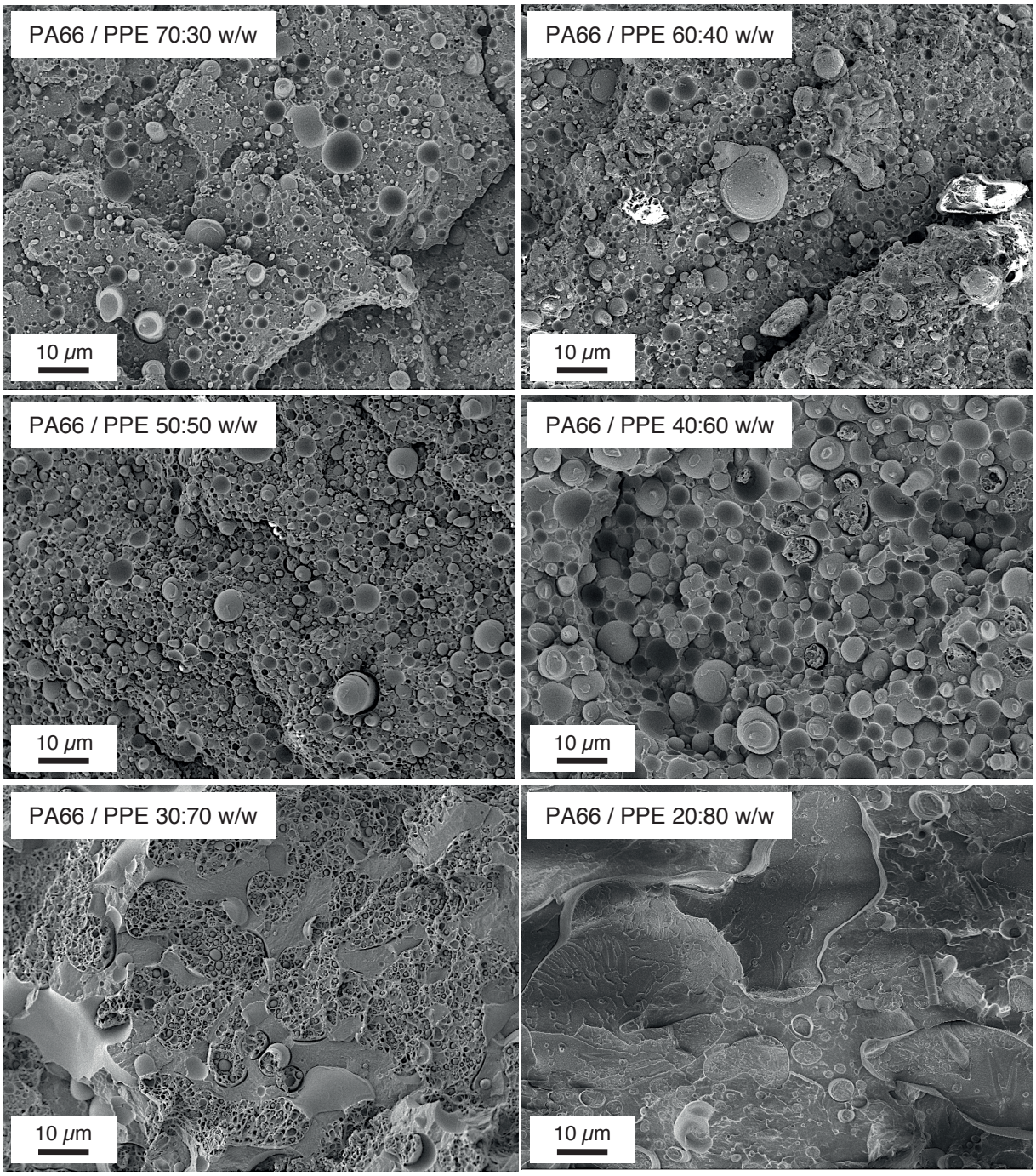

Figure 17 Cryo-fractured surfaces of binary PA66 / PPE blends with varying blend ratios from 70:30 to 20:80 w/w. From 70:30 to 40:60 w/w PA66 / PPE, latter is displayed as droplets in the PA66 matrix. At 30:70 w/w, the smooth structures represent PA66. At 20:80 w/w blend ratio, the large and irregular domains are identified as the PPE phase.

Indeed, the estimation by the Utracki model provides a good fit in the case of PA66 / PPE blends. At a blend ratio of 30:70 w/w, a co-continuous structure with spherical inclusion of PA66 in the PPE phases are visible. Further addition of PPE (20:80 w/w) results in a PPE matrix with irregularly shaped PA66 domains, indicating an incomplete phase transition toward a droplet-sea structure.

In terms of the possible application, it is desired to introduce as much PPE as possible as it lowers the thermal conductivity and water uptake and increases the dimensional and thermal stability. Nevertheless, it is strived to avoid a fully co-continuous structure or even PPE being the matrix phase, as it is less resistant to typical solvents, such as acetone or xylene. A blend ratio of 50:50 seems to give the best compromise in terms of overall properties and stable morphology.

6.1.2 Compatibilizer interactions with neat PA66 and neat PPE

This section will describe the interactions of the considered SMA-based compatibilizers with the individual blend components, namely PA66 and PPE. An emphasis will be placed on the miscibility of the compatibilizers in the blend polymers and their reactivity with neat PA66. SMA copolymers represent state-of-the-art compatibilizers, especially for PA6 / PPE blends [182,184,186,187], yet have not been investigated in more reactive PA66 / PPE blends. Where applicable, stated results will be supported by findings in the existing literature.

6.1.2.1 Interactions of SMAs with neat PPE

Several methods, such as optical or thermal analysis, can be applied to evaluate the miscibility of SMA copolymers with PPE. Regardless of the technique, mixing of the blend components either in solution or in the melt is mandatory. Having an intimate mixture of both polymers, necessary analysis can be performed afterwards. The most straightforward method is an optical observation of a PPE / SMA blend since both polymers are amorphous, *i.e.,* transparent. In case of miscibility, again, a transparent material is expected. In Figure 18, injection molded discs (with a thickness of 2 mm) of PPE blends with SMA4, SMA8, and SMA24 (82:18 w/w) are depicted.

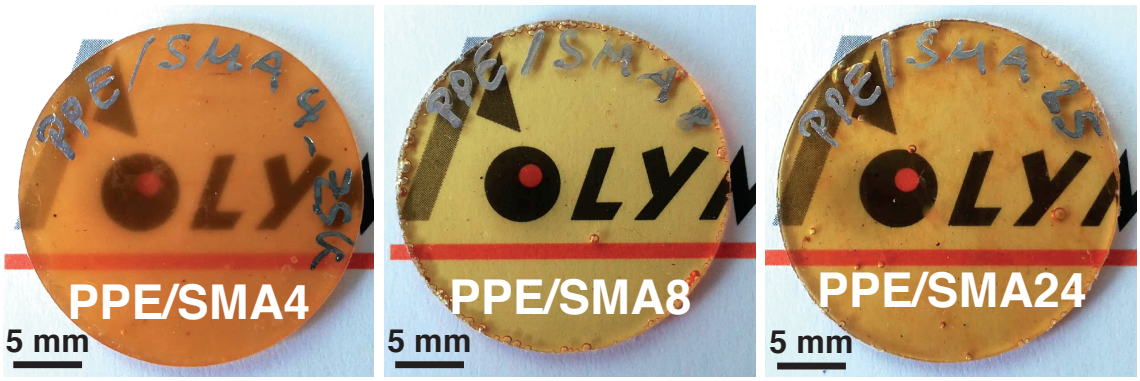

Figure 18 Injection molded discs (25 mm in diameter and 2 mm in thickness) of 82:18 w/w PPE and SMA4, SMA8, and SMA24, respectively.

Interestingly, all PPE / SMA combinations appear transparent, where only PPE / SMA4 reveals some turbidity, indicating immiscibility or a considerable difference in the refractive index (RI) of each of the polymers. To identify the true reason, further investigations are required.

Previous studies stated that SMA copolymers with a MA content greater than 8 wt% are immiscible with PPE [170,171]; therefore, it is expected that PPE / SMA24 is immiscible. To the best of our knowledge, no information was found in the literature in the case of PPE / SMA4, thus will be reported in this work for the first time. Focusing only on the MA content, both polymers (SMA4 and SMA8) should be compatible. Nevertheless, the unique structure of SMA4 (resulting from the third monomer N-phenyl maleimide) may alter the polarity in a way that it might be immiscible with PPE. So far, only limited information about this particular copolymer (SMA4) in blend systems is available. So far, it was only used together with SAN [281], as a compatibilizer for PC / ABS blends after further modification of its structure [282], and as a compatibilizer for PA6 / ABS blends in 3D printing [283].

To identify possible heterogeneities in the blends, TEM micrographs were prepared after staining the thin-sections, as seen in Figure 19, where ellipses indicate SMA domains.

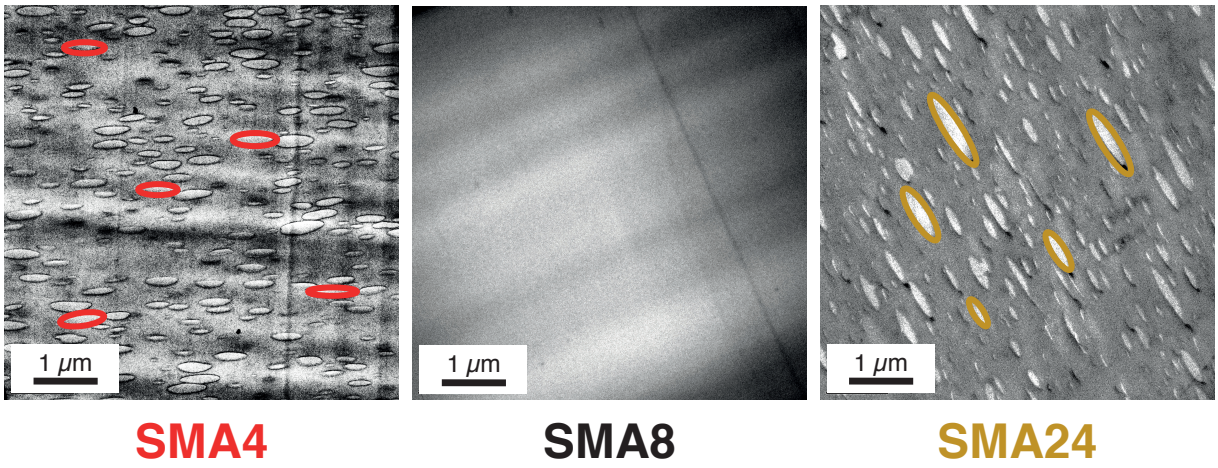

Figure 19 TEM micrographs of PPE blends (82:18 w/w) with SMA4, SMA8, and SMA24 after compounding, respectively. Ellipses indicate SMA domains.

As expected, the PPE / SMA8 is fully miscible, showing no phase separation. In contrast, PPE / SMA24 reveals distinct and elongated domains distributed all over the PPE matrix, ranging from 0.1 to 1.2 µm in length and 0.03 to 0.23 µm in width. As for the latter combination, PPE / SMA4 is also not miscible, with SMA4 droplets in a comparable size range of 0.1 to 0.7 µm in length and 0.05 to 0.22 µm in width. It is known that for heterogeneous systems, transparency can be achieved by either tuning the domain sizes of a dispersed phase far below the wavelength of incident light [284,285] or matching the refractive indexes (RIs) of both components with only minor deviations as of 0.01 to 0.001 [286,287]. As the domain sizes of SMA4 and SMA24 are relatively close to the wavelength of the incident light, a strong scattering of light is expected. The explanation of still having optical transparency can be given by comparison of the RI of PPE and SMA copolymers, given as 1.5750 and 1.5640, respectively [288]. Considering that the RI of SMA may vary depending on its structure, especially in SMA4, the RI difference between PPE and the SMAs lies in the range of a critical difference of 0.01 [200].

Besides the optical investigations, thermal analysis by the means of DSC can be applied to detect interactions on a molecular level. Upon miscibility of two polymers, it is known that the individual T_g signals coincide with their blend ratio [289]. In Figures 20 and 21, the temperature-dependent signals of the discrete polymers and the binary mixtures of PPE with SMA are plotted, respectively.

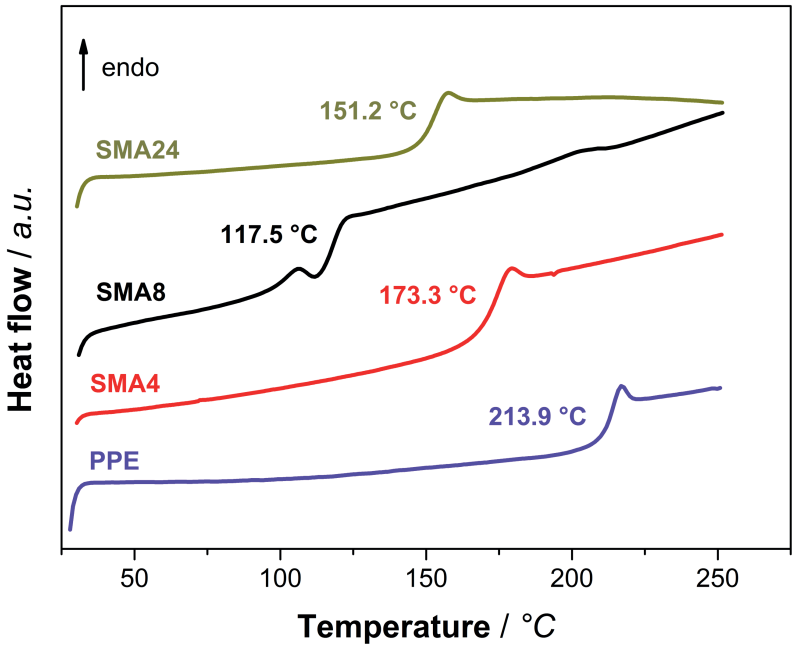

Figure 20 DSC thermograms showing the T_g of neat PPE and the neat SMA copolymers. For the sake of comparison, the curves are shifted vertically.

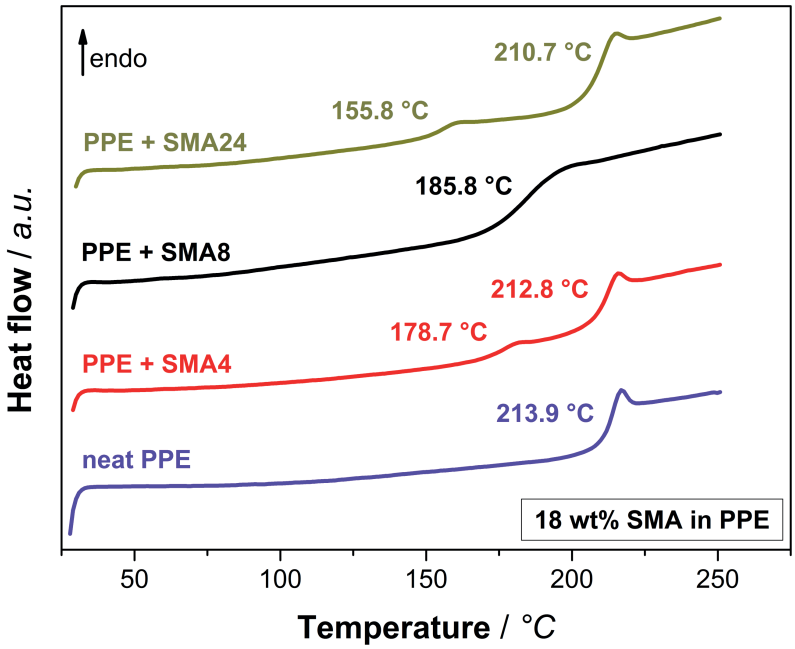

Figure 21 DSC thermograms showing the T_g of neat PPE and the binary blends of PPE and the corresponding SMA at a blend ratio of 82:18 w/w. For the sake of comparison, the curves are shifted vertically.

The DSC data can support the observations by optical analysis, showing that a single signal is only achieved for PPE / SMA8. The other two blends display the T_g signals of the individual components, all having a slight shift towards the other blend partner, indicating possible weak interactions. A linear dependency of the T_g is proposed for fully miscible polymer blends and is described by the Fox-Equation as shown in Equation 15 [290].

$$\frac{1}{T_g} = \frac{\omega_{PPE}}{T_{g\,PPE}} + \frac{\omega_{SMA}}{T_{g\,SMA}} \tag{15}$$

Where $\omega_{PPE,\,SMA}$ is the weight fraction of the PPE and SMA. Under consideration of the values for PPE and SMA8 in Figure 20, the T_g of the binary mixture at a weight ratio of 82:18 calculates as 186.4 °C, being in good agreement with the obtained value of 185.8 °C (Fig. 21).

6.1.2.2 Interactions of SMAs with neat PA66

Other than in PPE, SMAs were not reported to have a physical attraction to PA66. Instead, chemical reactions are found due to the high reactivity of anhydride and amine moieties present in SMA and PA66, respectively. The reactivity between both polymers can be tuned by the number of functional groups per polymer chain. Information on the molecular composition of the linear SMA copolymers are summarized in Table 4.

Table 4 Molecular information of SMA4, SMA8, and SMA24. All values other than M_w are calculated from MA contents given by the respective product information [c,d,e].

Molecular composition of SMA copolymers	SMA4	SMA8	SMA24
M_w [g/mol]	155.000	245.000	120.000
Chain length	intermediate	long	intermediate
MA content [wt%]	4.6	8.3	24
MA monomers per chain	73	207	294
Styrene monomers per chain	-	2157	875
MA / styrene ratio	1:-	1:9	1:3

The reactivity of SMA, *i.e.,* the amount of MA in the copolymer, can be described by various key figures, such as acid number (AN), MA content (as mass or molar fraction), or the molar ratio of the individual monomers. Latter can be calculated from the molecular weight of the monomers and the polymer unless the weight fraction of the components are known. For example, SMA8 having an MA content of 8.3 wt%, is composed of 207 MA and 2157 styrene monomers at the given average molecular weight, being equivalent to a monomer ratio of 1:9. In the case of SMA4, the number of MA monomers can be calculated as 73 per chain, a molar ratio however cannot be defined as the content of the third monomer present in SMA4 remains unknown. The linear chains of PA66 and SMA are transformed into graft copolymers (SMA-g-PA66) and partially cross-linked structures upon reaction [187,188]. A qualitative description of the SMA reactivity and the corresponding degree of graft formation can easily be given by shear rheological measurements, as shown in Figure 22.

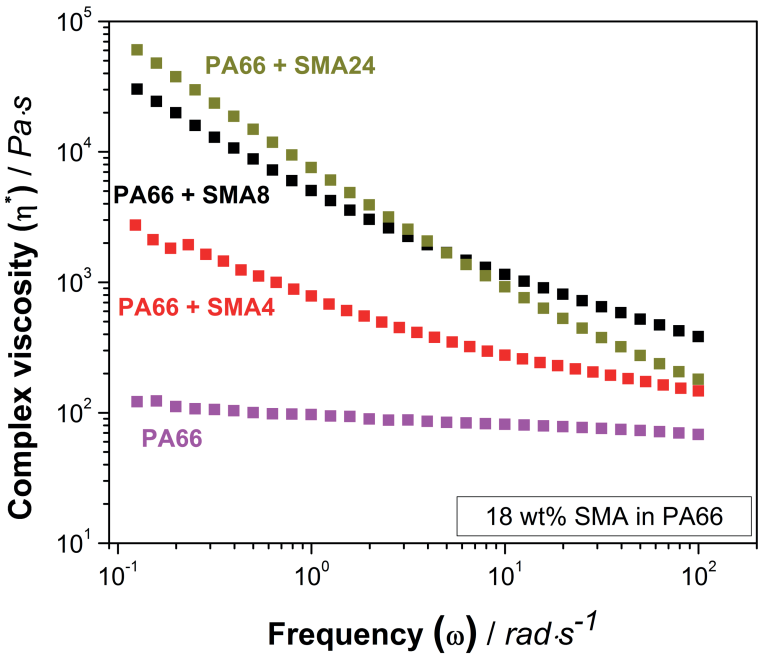

Figure 22 Complex shear viscosity (η^*) of neat PA66 and the binary PA66 / SMA blends at a ratio of 82:18 w/w.

Highly branched or cross-linked polymers have a linear response throughout the entire frequency range, comprised of very high viscosities at the lower frequency range, which is very

distinctive to the typical viscoelastic response [183,188]. At higher frequencies, the linearity for highly grafted or cross-linked polymers maintains, whereas linear or low-degree grafted polymers show an asymptotic response. The plateau region of the neat PA66 at lower ω is altered for all three SMAs, revealing the linear relationship (predominantly elastic behavior). An increase in the slope and overall viscosity up to a frequency of 10 rad·s^{-1} is observed in the order of SMA24 > SMA8 > SMA4, correlating well to their MA content, *i.e.,* reactivity.

As done for the binary blends of PPE and SMA (Fig. 19), the PA66 / SMA (82:18 w/w) morphologies were also investigated *via* TEM, as depicted in Figure 23. As expected, none of the SMAs are miscible with PA66 as phase separation is seen for all three blends. The domain sizes of SMA in PA66 follow an inverse trend regarding the MA content, having the smallest domains for PA66 / SMA24, as summarized in Table 5. This fact might indicate that SMA24 will more likely reside in the PA66 phase rather than in the PPE when considering the ternary blend systems, whereas the opposite is expected for the SMA4. The large domains of SMA4 imply that it may reside in the PPE phase more likely than in PA66. Considering the shapes of the SMA24, domains appear complex, having indistinct interfaces, typical for such a highly reactive SMA, and also having an increased interfacial thickness [188]. The interfaces become more distinct with decreasing MA content of SMA8 and SMA4, respectively [291].

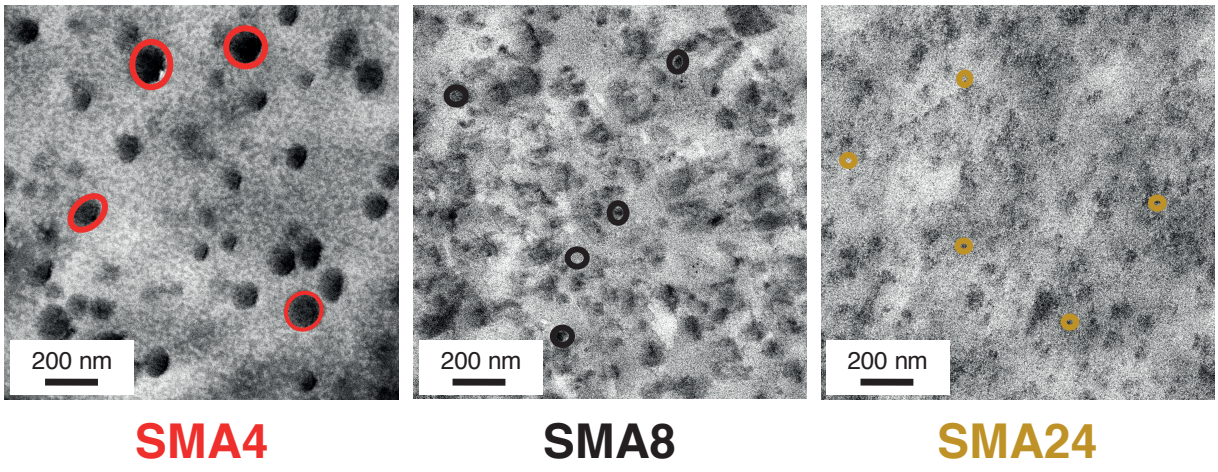

Figure 23 TEM micrographs of PA66 blends (82:18 w/w) with SMA4, SMA8, and SMA24 after compounding, respectively. SMA phases appear as black spots (highlighted in colored ellipses).

Table 5 Domain sizes of SMA4, SMA8, and SMA24 in PA66 and (18:82 w/w) and their state of the interface.

PA66 / SMA blends	SMA4	SMA8	SMA24
Range of domain sizes [nm]	55 – 160	30 – 100	10 – 70
Interface	distinct	intermediate	indistinct

6.1.3 Blending sequence of ternary PA66 / PPE / SMA blends

The compounding of a multi-component system is a compromise between reduction of process complexity (minimizing production steps, saving energy or resources, and limiting excessive thermal stress on the polymers) and getting the maximum output in terms of material performance (mechanical properties, morphology, and other relevant properties). The importance of investigating the blending sequence was testified for several compatibilized blend combinations, such as PC / PET [292], PA6 / ABS [247], PA6 / PC [293], PA6 / PPE [294], and PA66 / PPE [152]. The optimum blending order is discussed controversially in the mentioned examples, thus a clear statement is not established yet. Given this fact, the optimum blending sequence must be determined prior to the detailed investigations in the upcoming sections.

The best blending sequence is analyzed exemplarily on SMA24 compatibilized PA66 / PPE at a blend ratio of 50:50 w/w and a constant SMA24 content of 10 wt%. Besides the one-step blending labeled as ‘(PA66 / PPE / SMA24)’, two different two-step sequences, namely ‘(PA66 / SMA24) + PPE)’ and ‘(PPE / SMA24) + PA66)’ were considered, wherein SMA24 was first blended with PA66 or PPE, respectively. Selected properties of the blends are shown in Table 6 for the sake of better comparison.

Table 6 Performance of ternary PA66 / PPE / SMA24 (50:50:10 w/w) blends depending on the blending sequence.

Properties of PA66 / PPE / SMA24	(PA66 / SMA24) + PPE	(PPE / SMA24) + PA66	(PA66 / PPE / SMA24)
Young's modulus [MPa]	2660 ± 66	2720 ± 77	2710 ± 44
Tensile strength [MPa]	57.9 ± 3.9	55.4 ± 7.2	50.7 ± 6.3
Elongation at break [%]	2.5 ± 0.2	2.4 ± 0.2	1.6 ± 0.3
Thermal conductivity (λ) [W/m·K]	0.2028 ± 0.0002	0.2038 ± 0.0007	0.2030 ± 0.0006
Morphology	Co-continuous morphology without visual differences		

Expectedly, the properties of the blends did not vary considerably, as no differences in their morphologies could be detected. Nevertheless, significant changes in elongation at break, tensile strength, and thermal conductivity (λ) are achieved, where both two-step blends did perform best. Noticeable advantages are gained when SMA24 is first blended with PA66, as it provides the highest values combined with the narrowest standard deviations within this comparison.

In a two-step process, the SMA24 can thouroughly interact solely with the PA66 first, to create an equilibrium in the means of occurring reactions or orientation (phase separation). SMA24, having a high MA content, is most likely to reside in the PA66 phase in the ternary system. Thus, a pre-orientation in the first blending step is beneficial for the evolution of a stable morphology after the processing, resulting in a more homogeneous material response upon testing.

Based on the findings, a two-step blending sequence will be applied, wherein the SMAs are first mixed with PA66, followed by PPE.

6.1.4 Summary

In Chapter 6.1 it was aimed to gain knowledge on the behavior of the individual blend components, namely PA66, PPE, and SMA, more specifically in binary systems of PA66 + PPE, neat PPE + SMA, or neat PA66 + SMA.

The polymers used as PA66 / PPE reference blend face a large viscosity mismatch, resulting in a droplet-sea morphology with PPE droplets for a broad spectrum of the blend ratio. Once PPE reaches at least 70 wt%, a morphology shift is observed, where PA66 and PPE face co-continuity. Based on this fact and the desire to get an optimal balance between both polymers, a PA66 / PPE blend ratio in the range of 50:50 w/w seems most beneficial.

Neat PPE / SMA blends are prepared to gain knowledge about the miscibility of the individual SMAs in PPE. The findings confirm the information from the literature, that SMA8 – in contrast to SMA24 – is fully miscible in PPE. The miscibility was visualized by TEM and quantified by DSC analysis. The scientifically less known SMA4 was found immiscible in PPE, despite having only 4.6 wt% MA. A regular SMA copolymer with 4.6 wt% MA is expected to be compatible with PPE. It can be concluded that the n-phenyl maleimide monomer (third monomer aside from MA and styrene) in SMA4 significantly alters its polarity and causes the identified immiscibility.

All SMA copolymers are incompatible with PA66, yet differences in the morphology are found. SMA8 and SMA24 revealed relatively small domains with diffuse interfaces, whereas SMA4 featured distinct interfaces with the largest domain sizes within this comparison. Knowing this, the latter SMA seems to be the least compatible polymer in PA66. The reactivity of the SMAs is defined by their MA content and resulted in different rheological profiles of the binary blends, where SMA24 yielded the most significant changes due to excessive chain branching and even cross-linking to some extent. Based on these findings, it is expected that SMA24 is more likely to reside in the PA66 phase, SMA8 in the PPE phase, and SMA4 may be found equally distributed in both phases.

The optimal blending sequence to produce the ternary blends was investigated by using SMA24. It is seen that a two-step process with blending PA66 and SMA24 in the first step is the best solution regarding mechanical properties, having the highest values and narrowest standard deviations.

6.2 Influence of SMA type on PA66 / PPE blends

The compatibilization effect is frequently described by changes in the blend morphology and mechanical properties. In this section, the morphological changes will be shown and supported by rheological data. The mechanical performance will be described by tensile testing and subsequent fracture surface analysis. To do so, ternary blends of PA66 / PPE / SMA will be considered, having a constant PA66 / PPE ratio of 50:50 w/w and SMA4 or SMA8 or SMA24 contents varying from 1.25, 2.5, 5, 7.5 and 10 wt%. An overview of the SMA contents after the first and second blending steps and the total blend compositions are tabulated in Table 7.

Table 7 SMA contents in the blends of neat PA66 + SMA (first blending step) and in the ternary blends after the second mixing step, together with the absolute weight ratios of the ternary blend components.

SMA content [wt%] in PA66 / SMA	SMA content [wt%] in PA66 / PPE / SMA	PA66 / PPE / SMA weight ratios [%]
2.25	1.25	49.375:49.375:1.25
4.5	2.5	48.75:48.75:2.5
9	5	47.5:47.5:5
13.5	7.5	46.25:46.25:7.5
18	10	45:45:10

The goal of this chapter is to establish correlations between the interactions of the considered SMAs and the resulting material performance of the ternary PA66 / PPE / SMA blends. Finally, the best-performing SMA type will be selected for in-depth analysis by variation of the PA66 / PPE blend ratio. The performance will be judged as a combination of mechanical enhancement and degree of interfacial interaction.

It is noteworthy that major parts of the findings in this section are published as peer-reviewed article [195].

6.2.1 Influence on morphology

The morphology of immiscible polymer blends can be estimated by rheological measurements but is predominantly described by electron microscopic images, such as SEM or TEM. Latter is an absolute method giving information on the state of the material under ambient conditions. Nevertheless, it is of great interest to analyze and correlate the blend behavior in the melt to the resulting morphology after cooldown.

Indirect morphology determination by rheology

As the SMAs are first blended with PA66, followed by blending with PPE, the apparent morphology during mixing is expected to alter when compared to the PA66 / PPE reference. To understand the evolution of the rheological profile and corresponding blend morphology in the melt, different ratios of PA66 / SMA8 precursors (Table 7, left column) are chosen. to subsequently quantify the viscosity ratios of the precursors and PPE, as displayed in Figure 16 and Table 3. Oscillatory rheology results of PA66 / SMA8 binary blends are given in Figure 24.

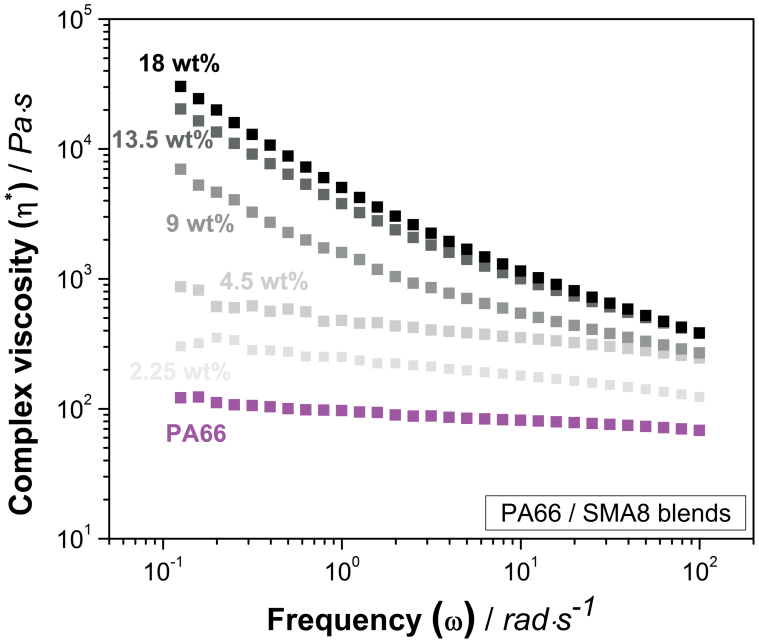

Figure 24 Complex shear viscosity (η^*) of neat PA66 and the binary PA66 / SMA8 blends at varying content of SMA8.

With the subsequent addition of SMA8 to PA66, the overall viscosity is significantly elevated already at the lowest content of 2.25 wt% SMA8. Despite a constant increase, below 9 wt%, no significant amount of graft copolymer formation can be detected yet. The frequency (ω) dependent viscosities obtained from Figure 24 are used to determine viscosity ratios (η_r) of mentioned PA66 / SMA8 blends and PPE, equivalent to the procedure provided in Table 5. The results at low and high ω (0.1 and 100 rad/s) are summarized in Table 8. Starting at a high shear rate and monotonously decreasing, values at 0.1 rad/s should allow to evaluate the last state of morphology just before freezing.

Table 8 Selected frequency (ω) dependent viscosity ratios (η_r) of PA66, binary PA66 / SMA8 blends with different SMA8 contents, and binary PA66 / SMA4 and SMA24 blends at 18 wt% SMA. All ratios are based on PPE, calculated by Equation 7.

Viscosity ratios (η_r) at frequency (ω) all ratios based on PPE	**0.1 rad/s**	**100 rad/s**
PA66	120	29
PA66 + 2.25 wt% SMA8	49	16
PA66 + 4.5 wt% SMA8	17	8
PA66 + 9 wt% SMA8	2.3	7.4
PA66 + 13.5 wt% SMA8	0.7	5
PA66 + 18 wt% SMA8	0.5	5
PA66 + 18 wt% SMA4	5.3	14
PA66 + 18 wt% SMA24	0.2	1

Expectedly, with increasing SMA8 content, ηr declines, which shows that at high ω, the ratio constantly remains above 1. According to Jordhamo *et al.* [94], all SMA8-based ternary blends should have a droplet-sea structure with PPE being the dispersed phase. Despite this theory, literature has even shown to shift the phase inversion region to values higher than 1, as proposed by Jordhamo, being dependent on the efficiency of mixing and sufficient reduction of the interfacial tension [295–297].

At low shear rates, however, η_r of the latter two SMA8 blends are below 1, meaning that the blend components PA66 / SMA8 and PPE are approximated in their corresponding viscosities. This observation might indicate the evolution of a co-continuous morphology for 50:50:7.5 and 50:50:10 PA66 / PPE / SMA8 ternary blends if other parameters such as interfacial tension, processing parameters, or diffusion of copolymers from one to the other polymer or the interface are neglected.

For SMA4 at 18 wt%, corresponding to the 50:50:10 PA66 / PPE / SMA4 blend, both values are far above equilibrium, and thus a droplet-sea morphology can be expected. For SMA24 at 18 wt%, corresponding to the 50:50:10 PA66 / PPE / SMA24 blend, both ratios are in the scope of a co-continuous morphology.

Direct morphology determination by transmission electron microscopy (TEM)

The complex interactions upon reactive blending may reveal a different behavior when solely rheological data is considered. By applying TEM, information from rheological investigations can be complemented by subsequent quantitative analysis. The morphology of 50:50 w/w PA66 / PPE 50:50 and ternary blends with 1.25 wt% SMA4, SMA8, and SMA24 are depicted in Figure 25.

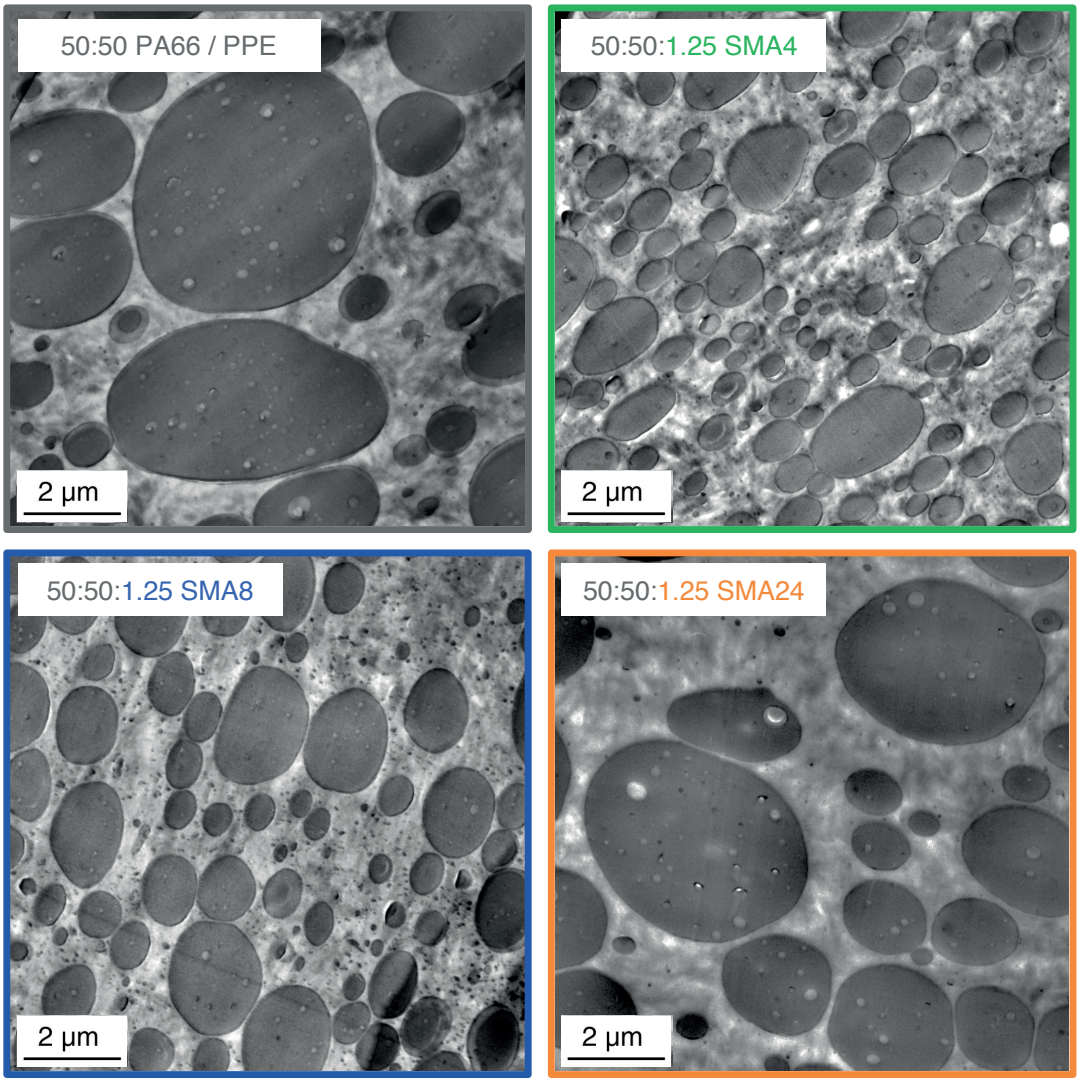

Figure 25 TEM micrographs of PA66 / PPE (50:50 w/w) and PA66 / PPE / SMA ternary blends with 1.25 wt% SMA4, SMA8, and SMA24. PPE domains appear as dark grey phases.

An image typical for immiscible and uncompatibilized blends is seen for the PA66 / PPE reference. The PPE is distributed in ellipsoidal domains in the PA66 matrix and shows only minor elongational deformation owing to its very high viscosity. For the same reason, a broad variation in the domain sizes is expected. In the case of successful compatibilization, usually, a reduction in domain sizes is expected [49,122,127]. Adding 1.25 wt% SMA4, the mentioned compatibilization effect, enabled by interfacial activity, can be seen clearly. The PPE domain sizes reduce significantly and appear more homogeneous. The same observations can be made in the case of 1.25 wt% SMA8, where the PPE is distributed even more uniformly.

An opposite trend can be observed upon adding 1.25 wt% of SMA24, whose morphology is similar to the uncompatibilized reference. This implies that SMA24 is not contributing to the compatibilization of both polymers. Given the high MA concentration and thus high polarity, SMA24 is expected to reside in the PA66 phase only and not migrate to the blend interface. Having a closer look, all SMA-containing blends reveal sub-micron-sized inclusions in the PA66 matrix, as indicated in Figure 26. Such nano-sized structures were also described to occur in other reactive blend systems containing SMA copolymers [146,291].

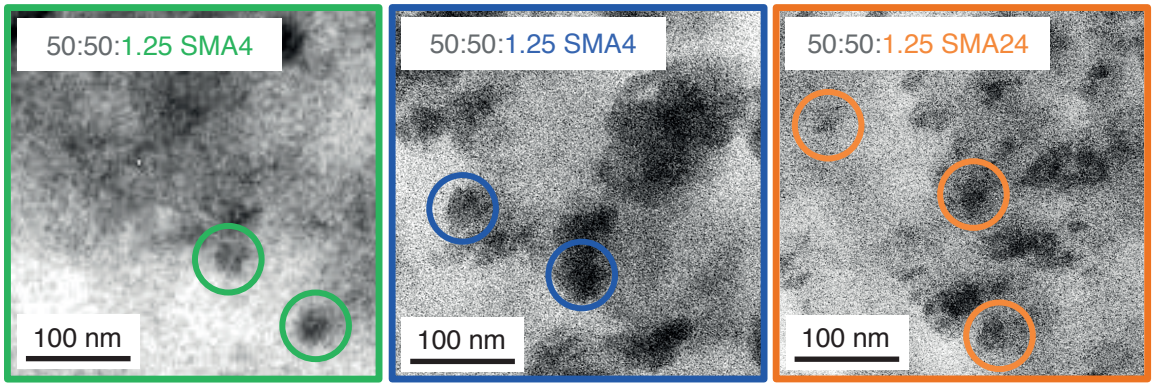

Figure 26 TEM micrographs of PA66 / PPE / SMA ternary blends with 1.25 wt% SMA4, SMA8 and SMA24 at higher magnifications.

In the reference blend, similar structures could be observed This allows to conclude that the inclusions either consist of unreacted SMA, reacted SMA copolymer micelles (SMA-g-PA66) [298], or latter having PPE in the core (swollen micelles). Comparing the micrographs in Figure 25 with those of in Figure 23, SMA4 appears different than it was in the binary 82:18 PA66 / SMA4 blend. The domain sizes are tiny, and the interfaces appear more diffuse. This structural change can be explained by its low reactivity and low content introduced in the ternary blend (1.25 wt%) compared to the binary blend with PA66 only (18 wt%). To support the qualitative observations, the domain size distributions of all mixtures are depicted in Figure 27.

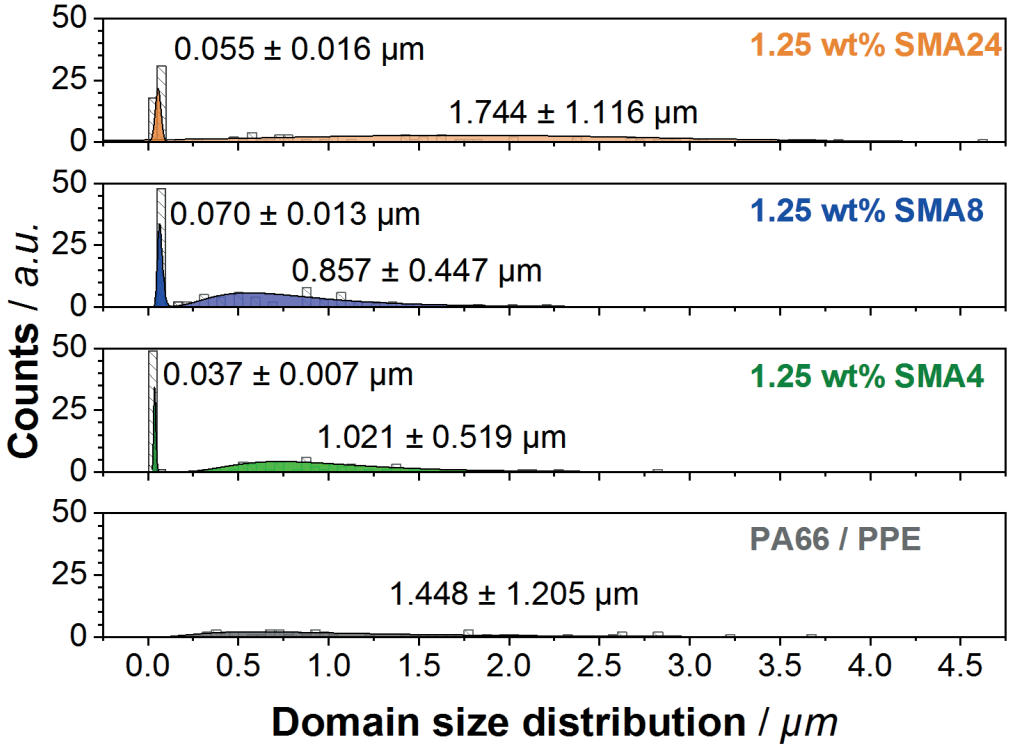

Figure 27 Domain size analysis of 50:50 w/w PA66 / PPE blends with 0 and 1.25 wt% SMA4, SMA8, and SMA24. The domains represent PPE (large fraction) and unreacted SMA, or SMA-g-PA66 micelles or latter swollen by PPE (small fractions).

As discussed, all blends containing SMA have a bimodal domain size distribution, where the larger fraction represents the PPE phase. Herein, blends with 1.25 wt% SMA4 and SMA8 indicate successful compatibilization. This is shown by a size reduction of the dispersed phase (PPE), also narrowing the size distribution, being most pronounced in the case of SMA8. Controversy, SMA24 leads to an increase in domain sizes. This finding confirms the assumption that SMA24 is not a suitable compatibilizer for PA66 / PPE, agreeing with observations for PA6 / PPE blends shown in the literature [56,299].

The nano-sized inclusions in the SMA4 ternary blends derive in size upon comparing with mentioned data in Table 5 (minimum 55 nm).

As all 1.25 wt% SMA blends maintain the droplet-sea morphology of the reference with only minor changes in shape and size of the PPE, it is of great interest to analyze the morphologies of the ternary blends with 10 wt% SMA as given in Figure 28.

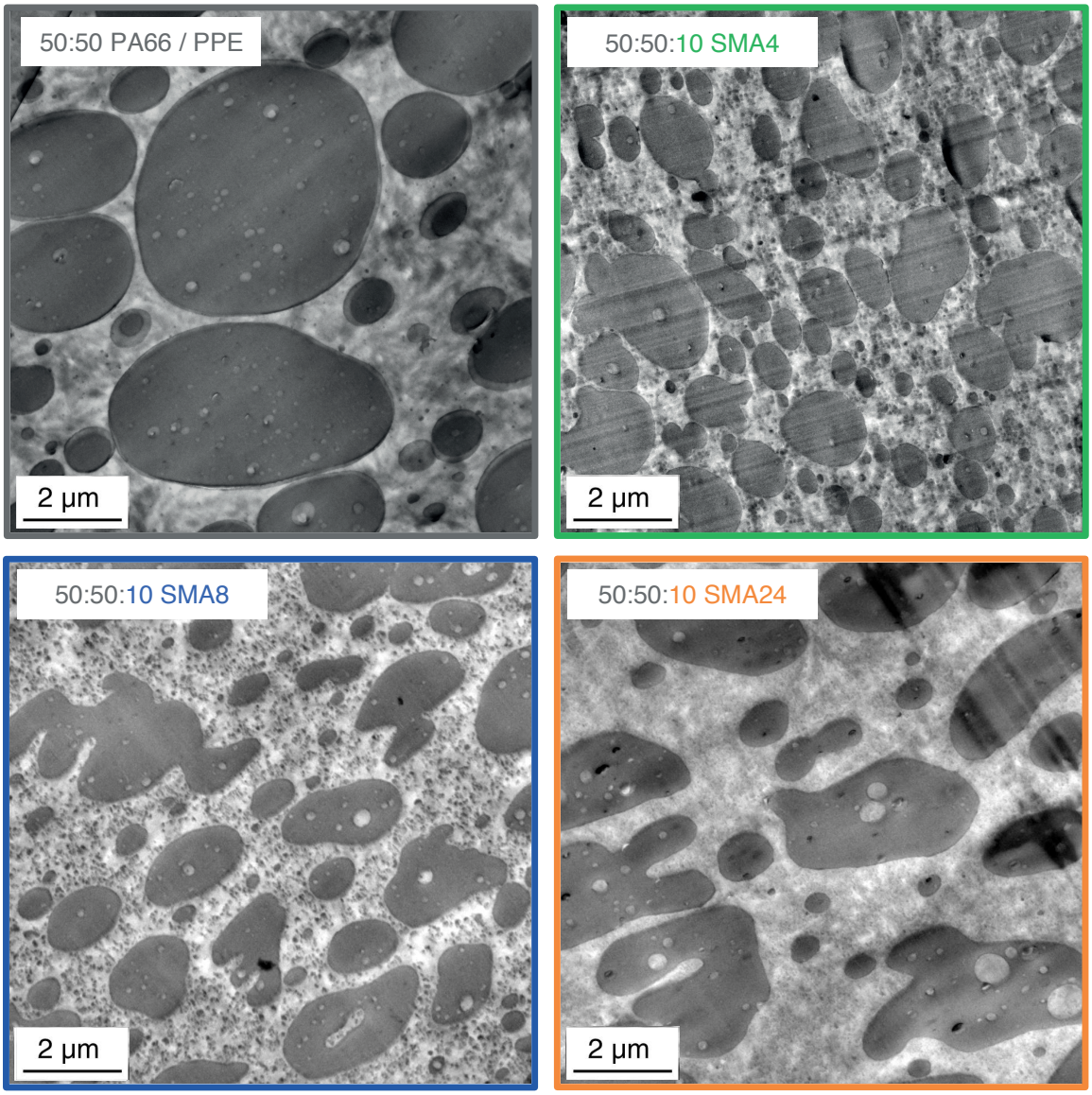

Figure 28 TEM micrographs of PA66 / PPE / SMA ternary blends with 10 wt% SMA4, SMA8, and SMA24. PPE domains appear as dark grey phases.

Even after adding 10 wt% SMA4 to the reference, a droplet-sea morphology is apparent; however, partial coalescence of the PPE domains is seen. In addition, a higher number of domains in the PA66 matrix are present, which also seem to be larger. Similar findings can be obtained upon adding 10 wt% SMA8 to the PA66 / PPE blend, yet the mentioned coalescence and the domain formation in the PA66 phase are more pronounced. The coalescence of the domains leads to irregularly shaped domains and indicates an ongoing but not completed phase transition, which is called dispersed-to-co-continuous transition (DCT) [297].

This observation is in good agreement with the previous rheological analysis. In the case of 10 wt% SMA24, the DCT is surpassed, resulting in a co-continuous morphology as anticipated by η_r values close to 1.

The coalescence of droplets is mainly enabled by the inclusion of reacted SMA within the PA66 phases (SMA-g-PA66), featuring an increase in viscosity of the PA66 phase and supported by a reduction of the interfacial tension. Both effects enable an efficient stress transfer from the matrix to the PPE domains at shear conditions apparent in the melt processing. This phenomenon contributes to further modification of the blend morphology, as illustrated in Figure 29.

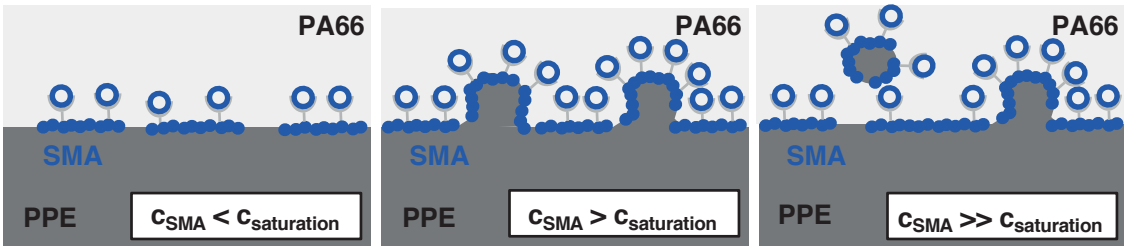

Figure 29 Schematic visualization of the nano-emulsion formation mechanism of PPE phases via surface roughening and subsequently pinching-off [200]. This mechanism is only valid for copolymers with miscibility in the dispersed phase, comprising a balanced polarity to reside at the interface (SMA8).

Reactive copolymers with an optimal polarity (here: SMA8) being miscible with the dispersed phase (here: PPE) reside at the interface until reaching a critical mass [255]. At this crucial point, the interface is saturated by SMA8, leading to a surface roughening of the PPE domains, followed by the so-called pinch-off effect upon further addition of the compatibilizer. The pinching-off of the dispersed phase results in nano-sized emulsions of PPE in the matrix, surrounded by the copolymer, similar to the concept of micelles [146,162,300]. This phenomenon should reveal a rise in the domain sizes included in the PA66 phase with an increasing amount of SMA. A quantitative description of the domain size distributions of all blends is given in Figure 30. For co-continuous morphologies, such an approach is not practicle, yet will be shown for 10 wt% of SMA24 for the sake of completeness.

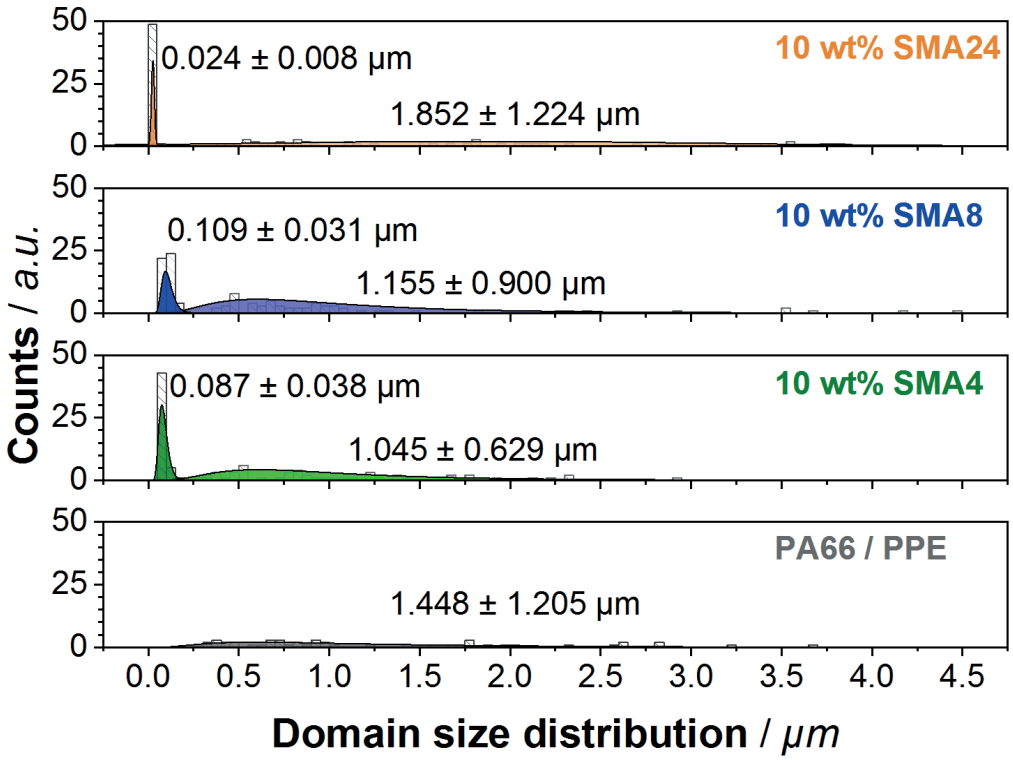

Figure 30 Domain size analysis of 50:50 w/w PA66 / PPE blends with 0 and 10 wt% SMA4, SMA8, and SMA24. The domains represent PPE (large fraction) and unreacted SMA, or SMA-g-PA66 micelles or latter swollen by PPE (small fractions).

Also, a bimodal domain distribution is found for 10 wt% SMA (Fig. 28). For all three ternary blends, the mean size and standard deviation of the PPE gets larger, supporting the microscopic analysis. As discussed in Chapter 6.1.2.1, SMA8 is the most compatible SMA with PPE; thus, firm surface roughening results in the most pronounced change (+30% compared to 1.25 wt% SMA8) within this comparison. Looking at the nano-sized domains, growth is a fact, upon comparing Figures 27 and 30, except for the highly incompatible SMA24. Despite the growing inclusions in the SMA4-containing blend, it is not an absolute proof of the existence of PPE inside the SMA4-g-PA66 micelles. According to Table 5, SMA4 forms domains in the range of 55 – 160 nm within PA66 (PA66 / SMA4 82:18 w/w). As the size range in Figure 30 is coherent, it is believed that reacted SMA4 domains are growing due to an increased content in the ternary blend. In contrast, the domain growth upon SMA8 addition can be attributed to an emulsifying effect by mentioned surface roughening and pinching-off.

The domains consisting of SMA8-g-PA66 micelles, swollen by PPE, reach up to 140 nm and clearly exceed the maximum of 100 nm, as stated in Table 5.

6.2.2 Influence on mechanical behavior under quasi-static load

The mechanical properties of polymer blends are highly dependent on the intrinsic properties of the constituents, morphology, interfacial interactions, preconditioning, and testing conditions. The combination of polymers showing a different behavior under stress (SMAs = brittle, PA66 = pseudo-ductile, PPE = ductile) will result in a complex interaction [224]. It is noteworthy that all specimens have been dried thoroughly to reduce exclude the effect of water absorption before testing, as PA66 is very sensitive to humidity. The Young's modulus (E), tensile strength (σ_M), and elongation at break (ε_B) of PA66 / PPE / SMA ternary blends are depicted in Figures 31, 32, and 33, respectively. The dashed lines are inserted as visual guidance and do not imply the actual development of values between two data points.

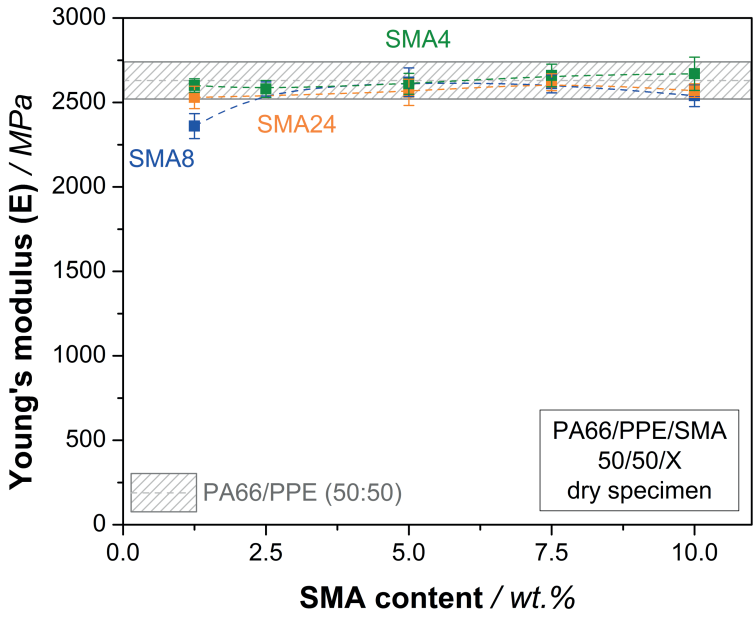

Figure 31 Young's modulus (E) of PA66 / PPE / SMA ternary blends with SMA4, SMA8, and SMA24 at varying SMA contents from 1.25 to 10 wt%. The grey bar represents the 50:50 w/w PA66 / PPE binary blend.

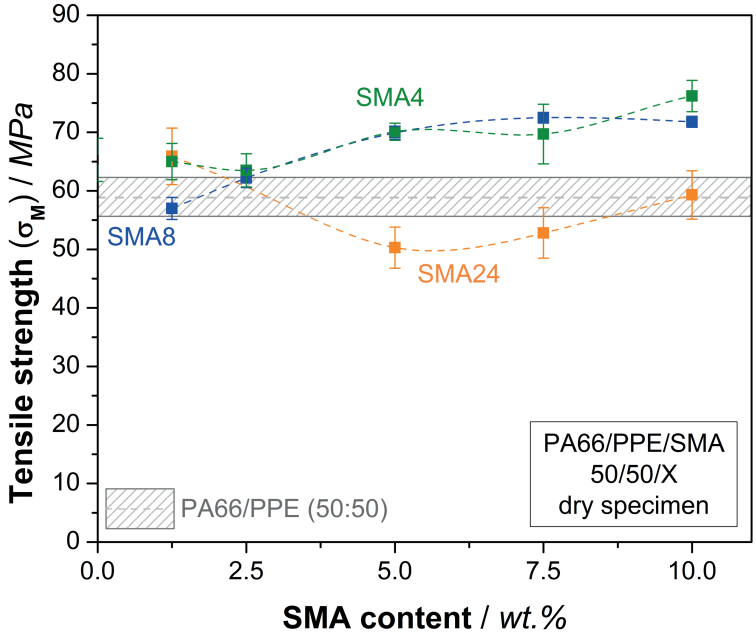

Figure 32 Tensile strength (σ_M) of PA66 / PPE / SMA ternary blends with SMA4, SMA8, and SMA24 at varying SMA contents from 1.25 to 10 wt%. The grey bar represents the 50:50 w/w PA66 / PPE binary blend.

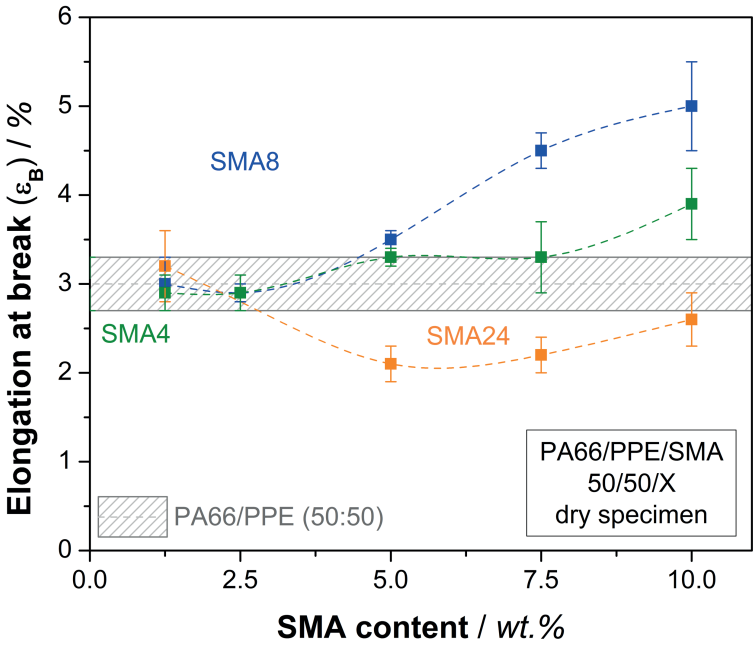

Figure 33 Elongation at break (ε_B) of PA66 / PPE / SMA ternary blends with SMA4, SMA8, and SMA24 at varying SMA contents from 1.25 to 10 wt%. The grey bar represents the 50:50 w/w PA66 / PPE binary blend.

Interestingly, all SMA blends incorporating 1.25 wt% SMA in the reference blend show a decrease in E. In the case of SMA8 and SMA24, this trend remains even up to a maximum addition of 10 wt% SMA. SMA4 recovers modulus from 5 wt% upwards and increases almost linearly, reaching a maximum at 10 wt% content. It can be assumed that all SMAs disrupt the intrinsic chemical connection between PA66 and PPE, inhibiting the transfer of elastic stress between the two phases to a certain extent. Given the interfacial activity of SMA8, it reveals the most substantial influence on E at 1.25 wt%. The relatively strong recovery at 2.5 wt% clearly justifies this argument. Despite all minor changes, all values remain comparable with the reference.

The influence of the SMAs on σ_M and ε_B are more pronounced compared to E. Nevertheless, a tendency to more heterogeneous behavior is seen for all SMAs with increasing content, expressed by larger scattering of the measured data. For SMA24, both properties follow the same trend, facing a significant decrease at 2.5 wt% addition. Further addition, up to 10 wt% results in a gradual incline up to the reference values. The initial drop can be attributed to the high amount of reactive maleic anhydride (MA), which reacts with the PA66 and does not allow the latter to form chemical bonds with PPE. The increase in values from 5 wt% is assumed to be a result of the changing morphology from droplet-sea to co-continuous, as indicated in Figures 25 and 28.

Ternary blends with SMA8 show the most substantial improvement within this comparison, reaching a maximum of σ_M at 7.5 wt% and ε_B at 10 wt%. This is expected to be an effect of a strong SMA-bridged interface build-up between the PA66 and PPE. The SMA4 blends exhibit a stepwise enhancement at 5 and 10 wt%, respectively. Here, it can be assumed that (un-)reacted SMA4 is able to migrate into the PPE phases during blending to plastify the PPE phase and gradually improve the interface between PA66 and PPE with increasing content. The maxima for both σ_M and ε_B can be found at 10 wt% of addition, even surpassing SMA8 in the former. The standard deviations, however, remain higher than those of SMA8, indicating a more heterogeneous material structure and mechanical behavior, respectively.

To gain a deeper insight into the deformation mechanism and to support the arguments mentioned above, the results of the fractographic analysis are displayed in Figures 34 and 35 for ternary blends with 1.25 and 10 wt% SMA, respectively.

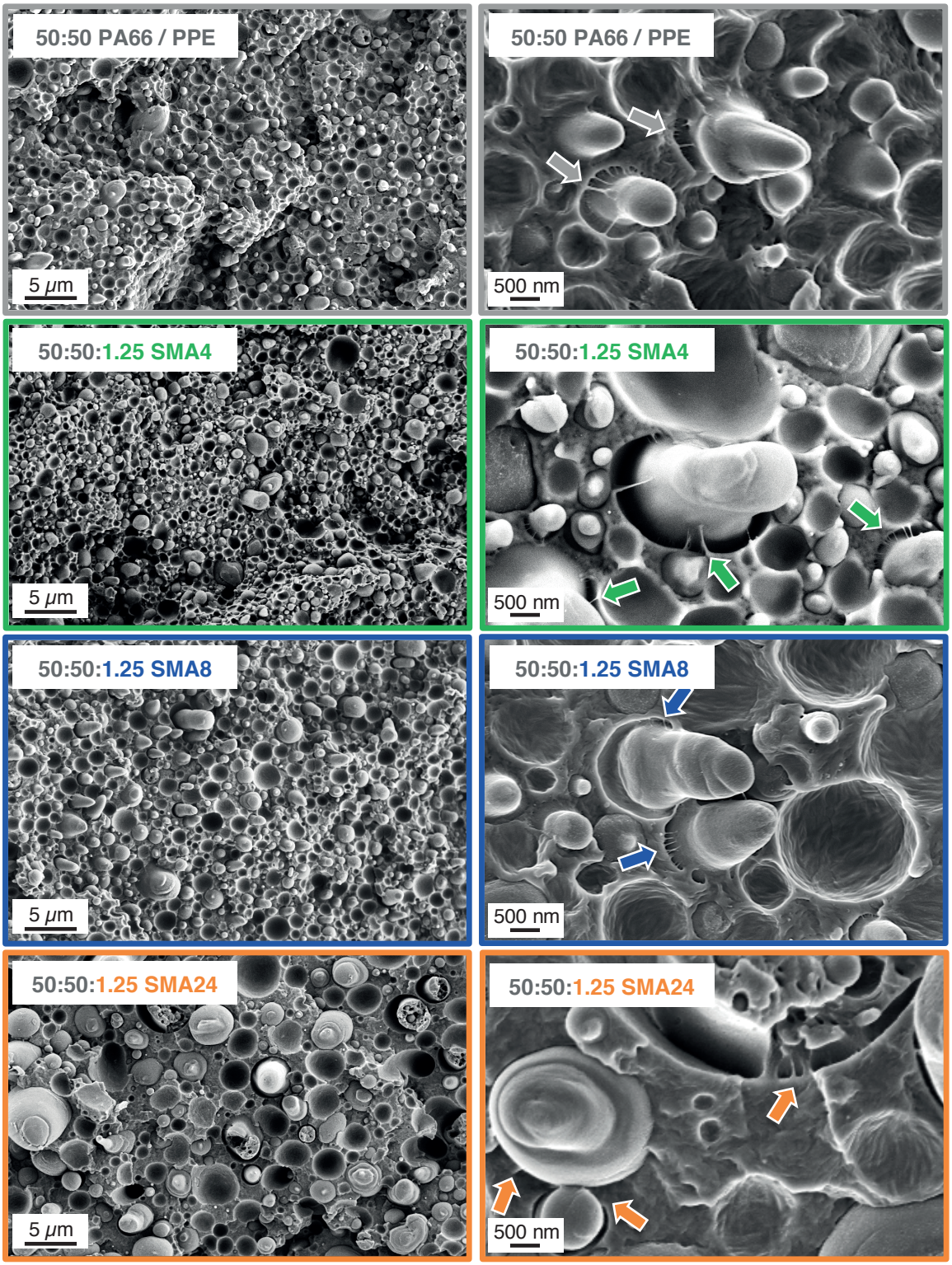

Figure 34 SEM images of fracture surfaces after tensile testing of 50:50 w/w PA66 / PPE reference and ternary blends with 1.25 wt% SMA4, SMA8, and SMA24 content. Higher magnifications with indicators on the right column.

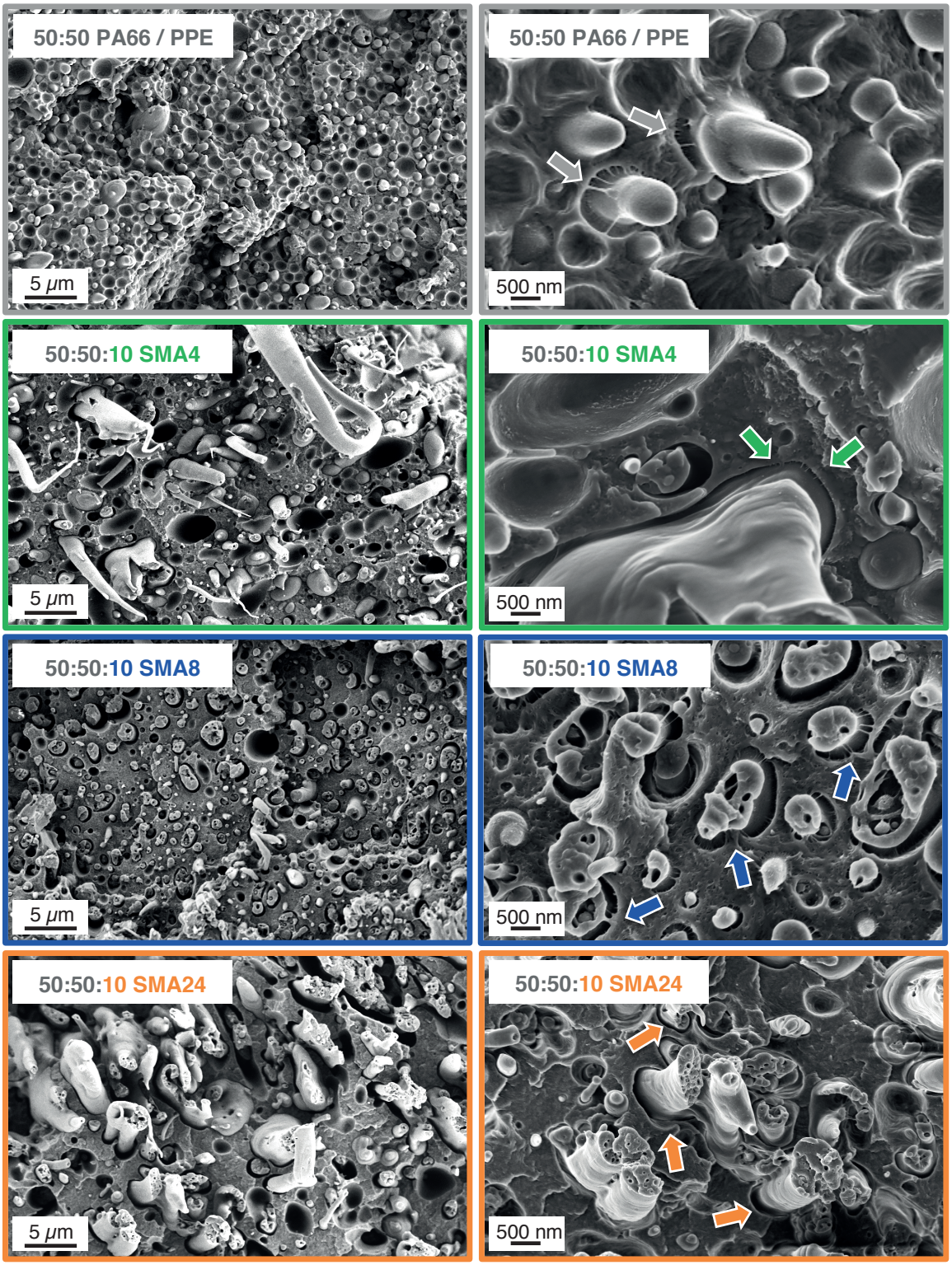

Figure 35 SEM images of fracture surfaces after tensile testing of 50:50 w/w PA66 / PPE reference and ternary blends with 10 wt% SMA4, SMA8, and SMA24 content. Higher magnifications with indicators on the right column.

The fracture surface of the reference is very rough and governed by strongly step-like deflected cracks. The PPE droplets reveal a minor degree of plastic deformation followed by a pull-out mechanism. The PA66 matrix shows a smooth fracture surface, *i.e.*, a typical brittle failure pattern, as it is known for its pseudo-ductility, especially in the dry state [225,226]. This PA66 behavior is valid for all blends discussed in the following.

At higher magnification, it can be seen that plastic deformation of PPE is enabled by crack bridging, given that PA66 (carboxyl moieties) and hydroxyl-terminated PPE undergo chemical bonding (esterification) upon melt-mixing [151]. Under stress, the chemically bound PA66-b-PPE block copolymers enable efficient local matrix deformation and help to reinforce the interface by fibrillation and mechanical interlocking.

At 1.25 wt% SMA, the morphology of the fracture surfaces of SMA4 and SMA8 are similar to the reference, even though SMA8 does not show as strong crack deflections as SMA4. In both cases, crack bridging and fibrillations at the interface are major mechanisms to enable the PPE deformation, although they are not as intense as for the reference. This indicates that the SMA4-g-PA66 and SMA8-g-PA66 copolymers compete with the intrinsically formed PA66-PPE bonds and negatively alter interfacial interaction. This can be seen as the leading cause of the absent reinforcing effect. In the case of 1.25 wt% SMA24, deformation of PPE is also observable together with fibrils. As stated earlier, SMA24 resides most likely in the PA66 phase and does not contribute to the interfacial activity at given content. By doing so, it does not interrupt the formation of bonds between PA66 and PPE.

The addition of 10 wt% SMA, however, results in very different deformation patterns for each of the ternary blends. SMA4 shows a relatively smooth fracture surface but an extreme PPE elongation of up to 25-times the size of an average PPE droplet (Fig. 30). As described in Chapter 6.1.2, SMA4 must mainly be residing in the PPE phase and incorporates a strong toughening effect. A high number of very fine fibrils can be observed at the blend interface. These fibrils, in interplay with the strong plastification, indicate sufficient stress transfer from the PA66 matrix to the PPE domains and subsequently increase the tensile strength. With 10 wt% of SMA8, the fracture surface becomes very rough with deep crack deflections.

Contrary to SMA4, almost no plastic deformation of PPE can be seen, allowing to conclude a cohesive-type of failure. A strong interfacial interaction, displayed by thick fibrillation in large number, overpowers PPE's deforming nature to improve the ternary blend behavior over the entire specimen homogeneously. 10 wt% of SMA24 results in a smooth fracture surface with intense plastic deformation of PPE. Even though no interface linkage could be observed, the co-continuous morphology of the blend allows the PPE to elongate due to an anchoring of the interconnected PPE phases [301]. The elongation of PPE does not fully compensate for the embrittlement of the PA66 phase, resulting in improved tensile behavior yet not exceeding the reference at any stage.

In summary, all three SMA types perform best at 10 wt% in the tensile test. SMA24, however, misses to surpass the performance of the binary reference due to a lack of interfacial activity. SMA4 and SMA8 significantly improve σ_M and ε_B, where SMA8 exhibits a better and most efficient interfacial enhancement. For this reason, SMA8 will be selected to investigate the influence of the PA66 / PPE blend ratio on morphological and mechanical properties in the following sections.

6.2.3 Summary

The goal of Chapter 6.2 was to establish fundamental correlations between different SMA interactions and the resulting morphological and mechanical properties of ternary PA66 / PPE / SMA blends at a constant PA66 / PPE ratio of 50:50 w/w. The findings from Chapter 6.1, *e.g.,* miscibility of SMAs in PPE and PA66, have successfully been correlated to the observations in this chapter.

A graphical summary of the SMA interactions within the PA66 / PPE blends is illustrated in Figure 36. For SMA4, significant parts reside in the PPE phases and provide interfacial strengthening to a certain extent (indicated in Fig. 36 by a thin interfacial layer). SMA8 has a high interfacial activity and thus is mainly found at any (newly created) interface between PA66 and PPE, improving the connection of mentioned blend components. SMA24 is exclusively found in the PA66 phase, forming micelles of itself and being absent from any blend interface.

Via TEM analysis of the ternary blends, it was shown that each SMA results in different morphological developments at a subsequent increase of their concentration from 1.25 to 10 wt%. In addition, this observation was successfully anticipated by rheological data. All SMAs enable a change in morphology from droplet-sea to co-continuous, however, at different concentration ranges. While SMA24 shows co-continuity at 10 wt%, SMA8 has a DCT and SMA4 remains as droplet-sea morphology at the same addition level. Also, each SMA results in a bimodal domain distribution in the PA66 matrix, where the large fraction is identified as the PPE phase, and the smaller fraction to (un-)reacted SMA phases to form grafted copolymers with PA66 and develop micellar structures. The domain sizes of the smaller fractions are coherent with the observations in Chapter 6.1 with one exception: upon the addition of SMA8, the domain sizes grow with increasing SMA8 content and exceed the reported range significantly (Table 5). Given this, it is postulated that PPE swells the SMA8-g-PA66 micelles. The mechanism of erosion (Figure 5, Mechanism 2) is enhanced by the interfacial activity of SMA8, leading to first surface roughening, followed by pinching-off.

In terms of mechanical properties, deformation behavior of blends also vary. While SMA4 blends rely on strong plasticization of PPE domains, enabled by selective location of SMA4 in the PPE, SMA8 blends reveal robust interfacial interactions through extensive chemical bonding. SMA24 blends are the least performing within this comparison, lacking interfacial interactions. A partial recovery of tensile properties is attributed to an anchoring effect given by the gyroidal (co-continuous) structure of the blend. However, it is not enough to surpass the reference properties at any concentration.

Overall, SMA4 and SMA8 yield in enhanced mechanical behavior. However, SMA4 tends to display a more considerable material heterogeneity, shown by larger standard deviations. This proves the fact that SMA8 creates the strongest interfaces between PA66 and PPE (highest elongation value), therefore SMA8 will be chosen for the following investigations.

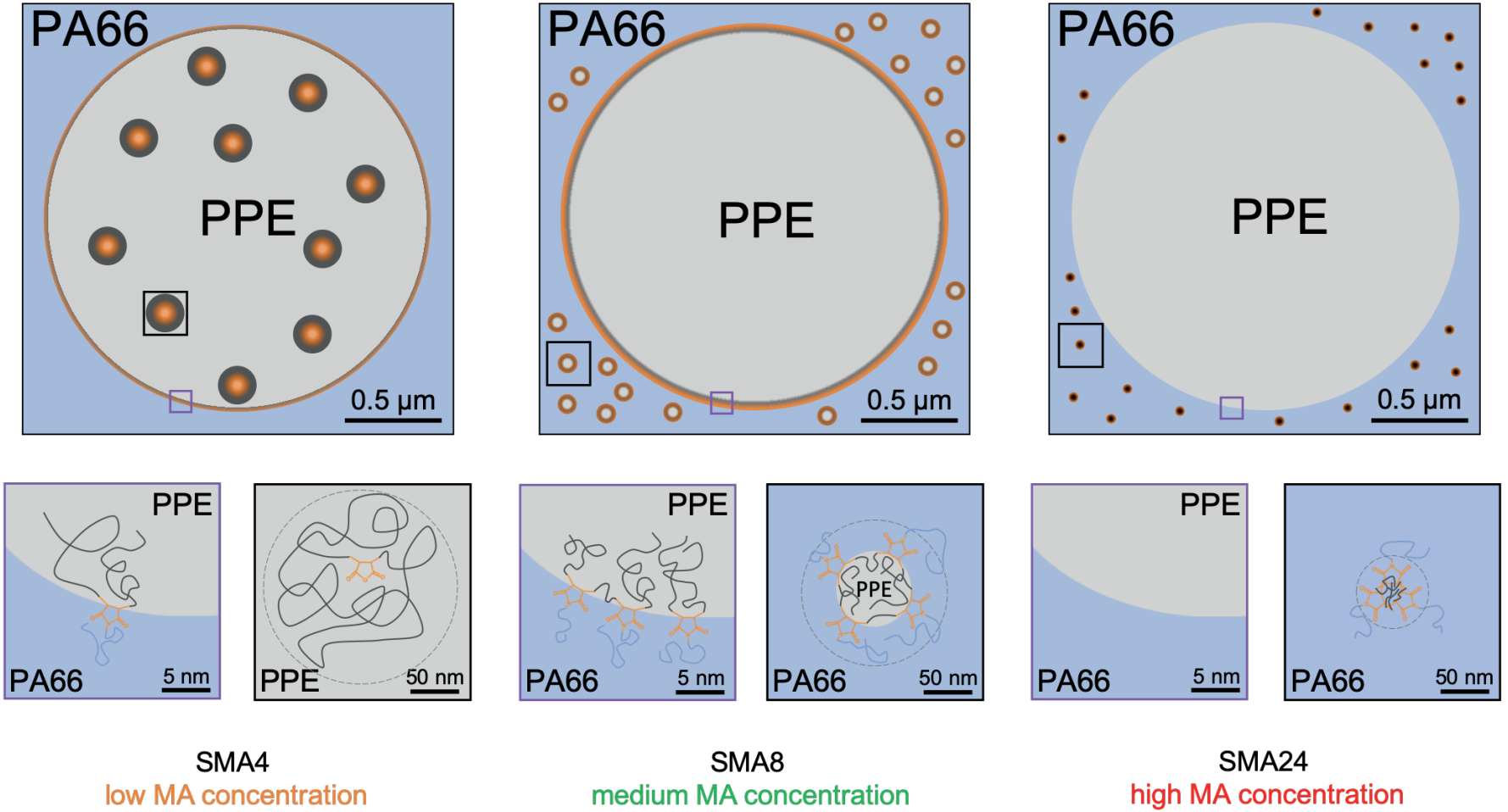

Figure 36 Schematic illustration of the interactions between SMA4 (left), SMA8 (center), and SMA24 (right) within the 50:50 w/w PA66 / PPE blend. On the top, the localization of each SMA in the blend, their sizes, and interfacial interactions are shown as an overview. Below, the interfacial interactions (purple frame) and the organization of the SMA copolymers in either PA66 or PPE (black frame) are given. PA66 polymer chains are illustrated in blue and polystyrene chains in black.

6.3 Influence of blend ratio on PA66 / PPE / SMA8 blends

The variation of the blend ratio is often described as the main factor in tuning the blend morphology and the resulting mechanical properties [296,302]. Also, the interaction of a compatibilizer enormously alters with changing blend ratio [194]. This section will discuss the morphological changes and correlate them to the mechanical performance under quasi-static tensile loading. The fracture mechanisms will be investigated by analysis of the fracture surfaces.

Ternary blends of PA66 / PPE / SMA8 will be used by variation of the PA66 / PPE blend ratio, namely 60:40 and 40:60 w/w. The SMA8 will be added at 2.5, 5, 7.5, and 10 wt%, respectively. The concentration of 1.25 wt% will not be considered, as only marginal changes in the material properties were detected in the previous section.

An overview of the SMA contents after the first and second blending steps and the total blend compositions for both blend ratios are tabulated in Table 9.

Table 9 SMA8 contents in the blends of neat PA66 + SMA8 (first blending step) and in the ternary blends after the second mixing step, together with the absolute weight ratios of the ternary blend components.

PA66 / PPE blend ratio	SMA content [wt%] in PA66 / SMA8	SMA content [wt%] in PA66 / PPE / SMA8	PA66 / PPE / SMA8 weight ratios [%]
60:40	4.1	2.5	58.5:39:2.5
	8.1	5	57:38:5
	11.9	7.5	55.5:37:7.5
	15.6	10	54:36:10
40:60	6.0	2.5	39:58.5:2.5
	11.6	5	38:57:5
	16.9	7.5	37:55.5:7.5
	21.7	10	36:54:10

This section aims to establish correlations between the interactions of SMA8 and the resulting material performance of the ternary PA66 / PPE / SMA blends upon alteration of the PA66 / PPE blend ratio. Finally, the ideal SMA8 concentration will be selected to be evaluated upon quasi-static (tensile) and dynamic (FCP) testing under dry and humid conditions. The performance will be judged according to the degree of improvement in tensile properties. It is noteworthy that major parts of the findings in this section are published as peer-reviewed article [196].

6.3.1 Influence on morphology

Analogous to the analysis in Chapter 6.2, the apparent blend structures will be identified via TEM measurements. The morphology of 60:40 (orange, left column) and 40:60 w/w (blue, right column) PA66 / PPE ternary blends with 0, 2.5, 5, and 10 wt% SMA8 are depicted in Figure 37. Looking at both binary blends, 60:40 and 40:60 w/w without SMA8, the effect of the blend ratio becomes very pronounced. As reported for 50:50 w/w binary mixture, also at 60:40 w/w PA66, the matrix phase possesses dispersed PPE, yet in a comparably lower size range. For the 40:60 w/w PA66 / PPE blend, a strong coalescence effect is evident, indicating an ongoing transition to co-continuity (dispersed-to-co-continuous transition (DCT)), with only a few distinct PPE domains not having coalesced.

Adding SMA8 to the binary blends, no significant change is seen for the 60:40 ternary blends, as all compositions remain in a droplet-sea structure. In the case of the 40:60 ternary blends, different observations can be made at each of the SMA8 concentrations. At 5 wt%, the amount of distinct PPE phases increases dramatically. In Chapter 6.2.1, the enhancement of the PA66 matrix viscosity due to SMA was already discussed and seen as the main reason for a morphology change given by a shift in the viscosity ratio of (PA66 / SMA) and PPE. However, the effect here is once more contrary to the observations stated before, supporting the assumption that SMA8 is highly interfacially active and inhibits coalescence effectively to a certain extent. At 10 wt%, a morphology transition to co-continuous becomes evident.

All SMA8-containing blends reveal nano-sized inclusions in the PA66 phase. To quantify the interplay between SMA8 content and blend ratio on the morphology, domain size distributions are depicted in Figures 38 and 39 for 60:40 and 40:60 w/w blends, respectively.

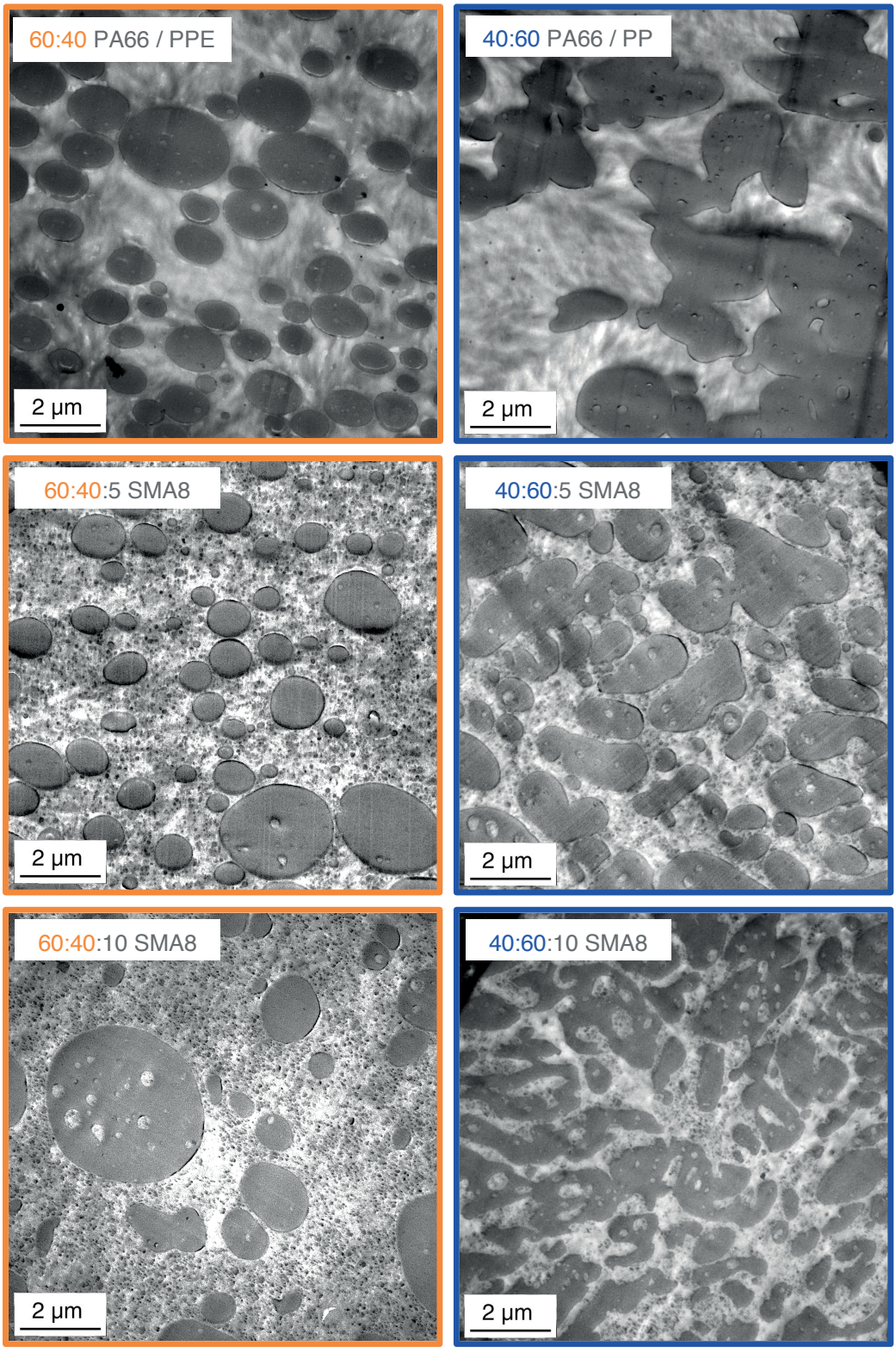

Figure 37 TEM micrographs of PA66 / PPE / SMA8 ternary blends with 60:40 (orange) and 40:60 (blue) PA66 / PPE ratio with 5 and 10 wt% SMA8. PPE domains appear as dark grey phases.

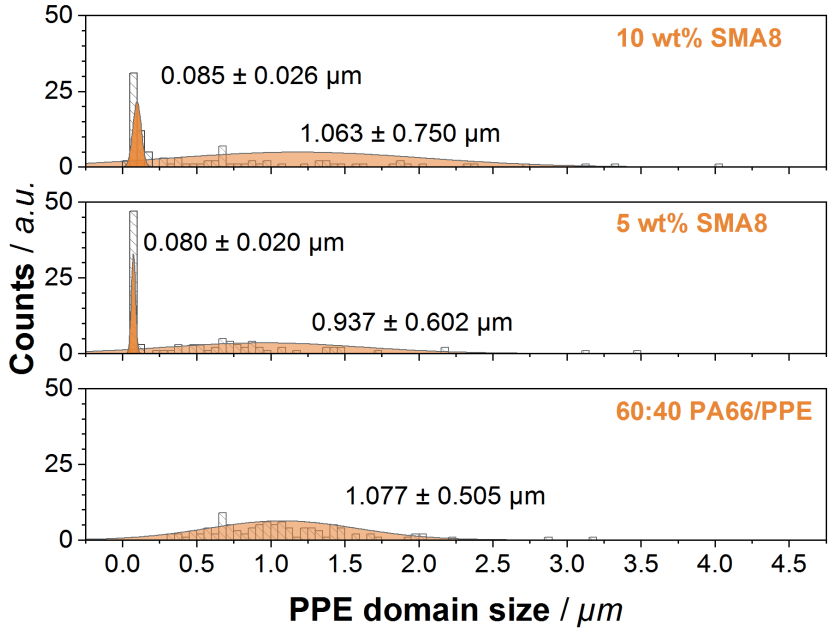

Figure 38 Domain size analysis of 60:40 w/w PA66 / PPE blends with 0, 5, and 10 wt% SMA8. The domains represent PPE (large fraction) and unreacted SMA8, or SMA8-g-PA66 micelles or latter swelled by PPE (small fractions).

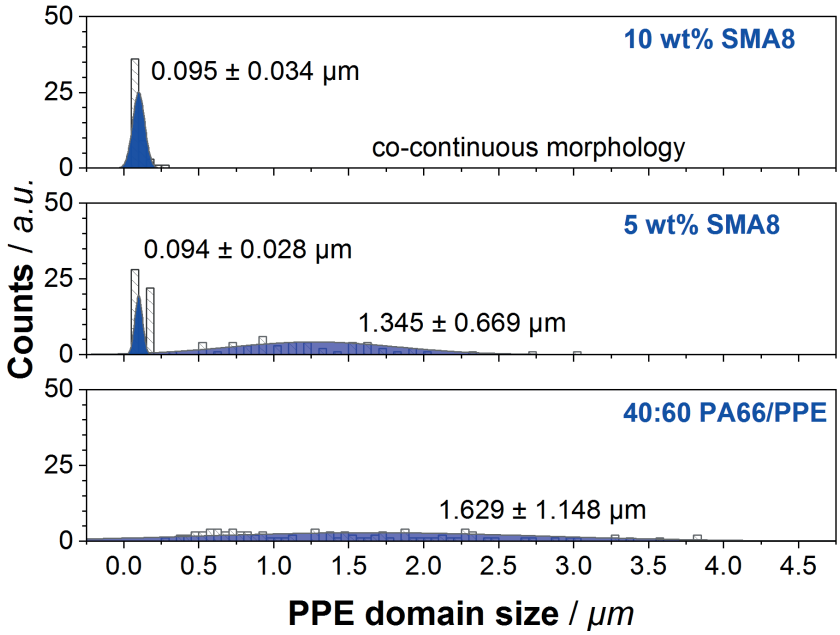

Figure 39 Domain size analysis of 40:60 w/w PA66 / PPE blends with 0, 5, and 10 wt% SMA8. The domains represent PPE (large fraction) and unreacted SMA8, or SMA8-g-PA66 micelles, or latter swelled by PPE (small fractions).

For 60:40 w/w blends, the PPE domain sizes remain somewhat stable, where first a reduction (5 wt%) and later a minimal coarsening to the range of the binary reference (10 wt%) is seen. Looking at the swollen micelles in the PA66 matrix, only a little difference can be seen from 5 to 10 wt% addition of SMA8, the latter having a more significant fraction of domains larger than 90 nm.

Even though one would expect continuous growth in size with growing SMA8 content, the reason for the stagnation can again be explained with the help of Figure 29. For constant processing parameters, blend ratio, and morphology, the dispersed phase volume (here: PPE) remains constant. With changing viscosity ratio, however, coalescence of PPE is favored and directly linked to a decrease in the total interfacial area between PA66 and PPE. A reduction in this area caused by the increasing content of SMA8 enables a more apparent saturation of the available interfaces. A greater surface area is generated with the help of excess SMA8, resulting in a comparable size range of the inclusions but a greater number of such within a given sample volume. Comparing the TEM images in Figure 37, the areal coverage by nano-domains is 2.2-times higher for 60:40:10 PA66 / PPE / SMA8 compared to the ternary blend with only 5 wt% SMA8.

In the case of 40:60 w/w blends, an apparent reduction of PPE domain sizes reflects the inhibition of coalescence when 5 wt% SMA8 is added, explaining the efficient compatibilization mechanism as mentioned earlier. At higher SMA8 contents (40:60:10 PA66 / PPE / SMA8), a co-continuous morphology is obtained which does not allow a comparison of domain sizes anymore. The micelle sizes of the blends with 5 to 10 wt% SMA8 only differ minimally, where 40:60:5 PA66 / PPE / SMA8 possesses a domain in the size of 45 – 197 nm, whereas 60:40:10 PA66 / PPE / SMA8 displays a range between 55 – 217 nm. Also, a reduction of overall available interfacial area is given here, as gyroidal structures have a reduced interface compared to droplet-sea morphologies [303].

The theory of copolymer micelles swollen by PPE can also be proven for 60:40 and 40:60 w/w blend ratios, as both ternary blends reach domain sizes of more than 160 nm at 10 wt% SMA8 addition, again exceeding the maximum values stated for 82:18 w/w PA66 / SMA8 in Table 5.

6.3.2 Influence on mechanical behavior under quasi-static load

The mechanical properties of polymer blends are significantly affectedby changing blend ratios [158,296,302]. For PA66 / PPE blends, very few examples exist in the literature discussing the effect of blend ratios in the presence of a compatibilizer, namely PPE-g-MA [51,65] and very recently HIPS-g-MA [194]. In terms of tensile properties, two of the mentioned studies attribute the best performance to the highest considered PA66 content, whereas one states the best results for 60:40 and 40:60 w/w blend ratios. Given this, it is of high interest to investigate the tensile properties depending on blend ratio and SMA8 content.

It is noteworthy that all specimens have been dried thoroughly to reduce further complexity before testing, as PA66 is very sensitive to humidity. The Young's modulus (E), tensile strength (σ_M), and elongation at break (ε_B) of PA66 / PPE / SMA ternary blends are depicted in Figure 40, 41, and 42, respectively. The dashed lines are inserted as visual guidance and do not imply the actual development of values between two data points. Orange and blue-filled rectangulars represent the corresponding reference values for the 60:40 and 40:60 w/w binary blends.

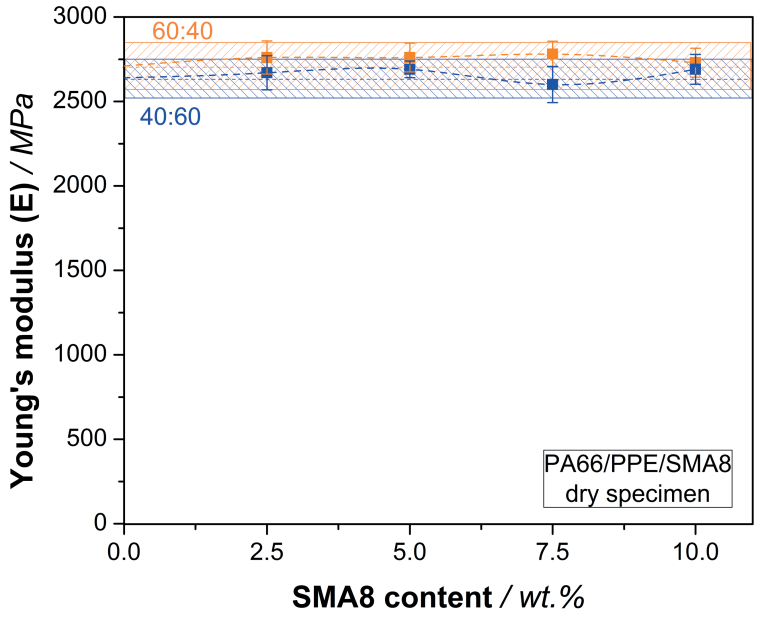

Figure 40 Young's modulus (E) of 60:40 and 40:60 w/w PA66 / PPE / SMA ternary blends with SMA8 at varying SMA contents from 2.5 to 10 wt%. The orange and blue bar represents the 60:40 and 40:60 w/w PA66 / PPE binary blend.

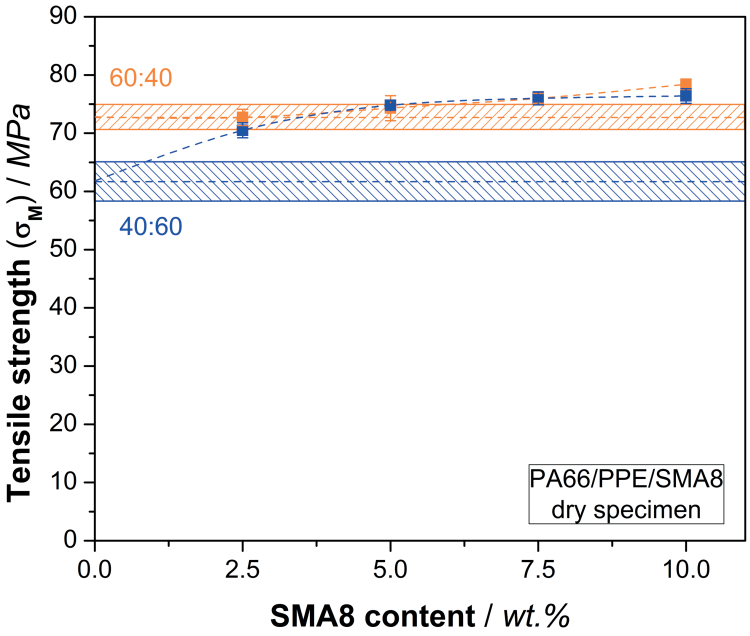

Figure 41 Tensile strength (σ_M) of 60:40 and 40:60 w/w PA66 / PPE / SMA ternary blends with SMA8 at varying SMA contents from 2.5 to 10 wt%. The orange and blue bar represents the 60:40 and 40:60 w/w PA66 / PPE binary blend.

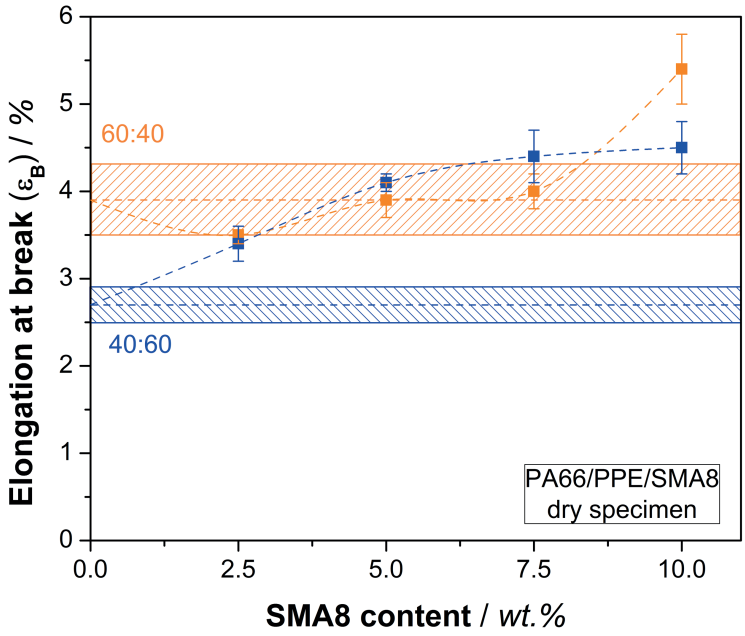

Figure 42 Elongation at break (ε_B) of 60:40 and 40:60 w/w PA66 / PPE / SMA ternary blends with SMA8 at varying SMA contents from 2.5 to 10 wt%. The orange and blue bar represents the 60:40 and 40:60 w/w PA66 / PPE binary blend.

In terms of E (Fig.40), the 60:40 w/w PA66 / PPE reference leads to a higher value than the 40:60 w/w equivalent. This relation remains same throughout all SMA contents, although the differences are marginal. These data agree with the observations with 50:50 w/w blends in the previous section, where SMA8 does not contribute to a change in E. The relation between 60:40 and 40:60 w/w found for E is also valid for σ_M and ε_B, where the first demonstrates higher values than the latter. Nevertheless, upon the addition of SMA8, very different data development is observable.

Considering σ_M (Fig. 41), the 60:40 w/w blend displays a steady and almost linear incline to reach its' peak for 10 wt% of SMA8 addition (+7.7% compared to the binary reference). On a relative basis, the growth of the 50:50 w/w blend with 10 wt% SMA was +10.0% compared to its reference without SMA8. In the case of the 40:60 w/w blends, a strong initial increase is seen for 2.5 wt% SMA8, followed by an asymptotic development to also reach a maximum at 10 wt% SMA8 (+23.6%). The relative improvement in σ_M seems to directly relate to a rising PPE amount in the blend.

Looking at ε_B (Fig. 41), the 60:40 w/w blend reveals an initial drop in the value at the lowest SMA8 content (also seen for the 50:50 w/w blends) of 2.5 wt%, followed by a recovery to the reference value at 5 wt% SMA. Finally, a significant improvement to a maximum at 10 wt% SMA8 addition is observed. Despite the high mean value, the standard deviations of these blends become steadily larger with increasing SMA8 content. This morphological heterogeneity is an effect of the coarsening droplet size of PPE in the PA66 matrix (Fig. 37 and 38), resulting in more inconsistent material behavior throughout the sample when exposed to stress. This can be stated as a general observation regardless of the SMA type or PA66 / PPE blend ratio used in this work. For the 40:60 w/w blends, a significant linear increase can be seen up to 5 wt% SMA8, followed by an asymptotic development to also reach a maximum at 10 wt% SMA8, in line with the progress for σ_M. The relative improvement in ε_B also follows the same blend ratio-related trend, having the least pronounced enhancements at the lowest PPE amounts (60:40 w/w PA66 / PPE blends).

In summary, the blends with 10 wt% SMA8 perform best in tensile tests, regardless of the blend ratio (also valid for 50:50 w/w PA66 / PPE). Given this, 10 wt% can confidently be selected as most suitable SMA 8 content for further investigations.

To gain a deeper understanding of the deformation mechanism and to support the arguments mentioned previously, the results of the fractographic investigation for 60:40 and 40:60 w/w PA66 / PPE is indicated in Figure 43 and 44, respectively. Both blend ratios including 0, 5, and 10 wt% SMA8 are discussed.

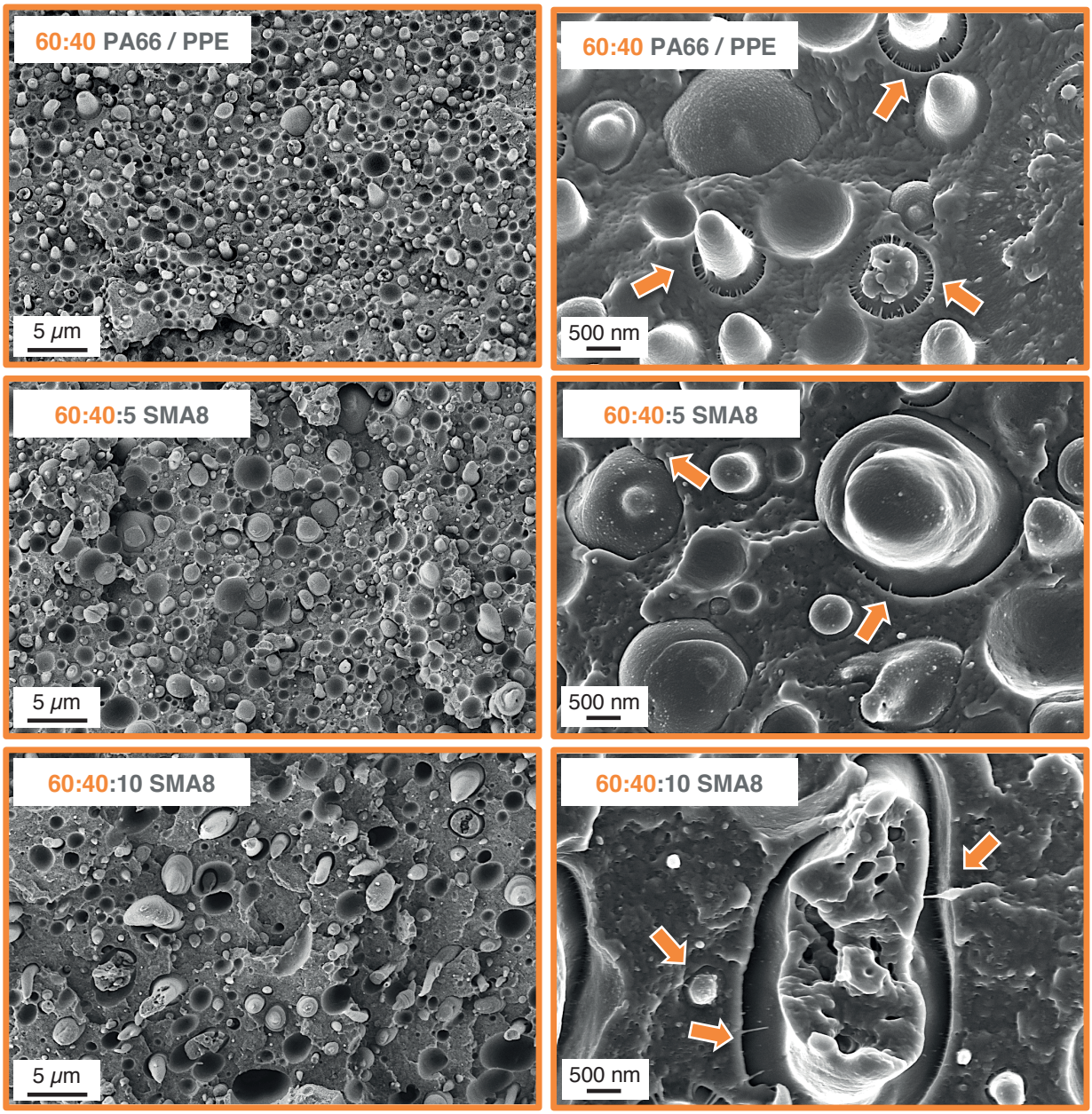

Figure 43 SEM images of fracture surfaces of 60:40 w/w PA66 / PPE reference and ternary blends with 5 and 10 wt% SMA8 after tensile testing. Higher magnifications with indicators are present on the right column.

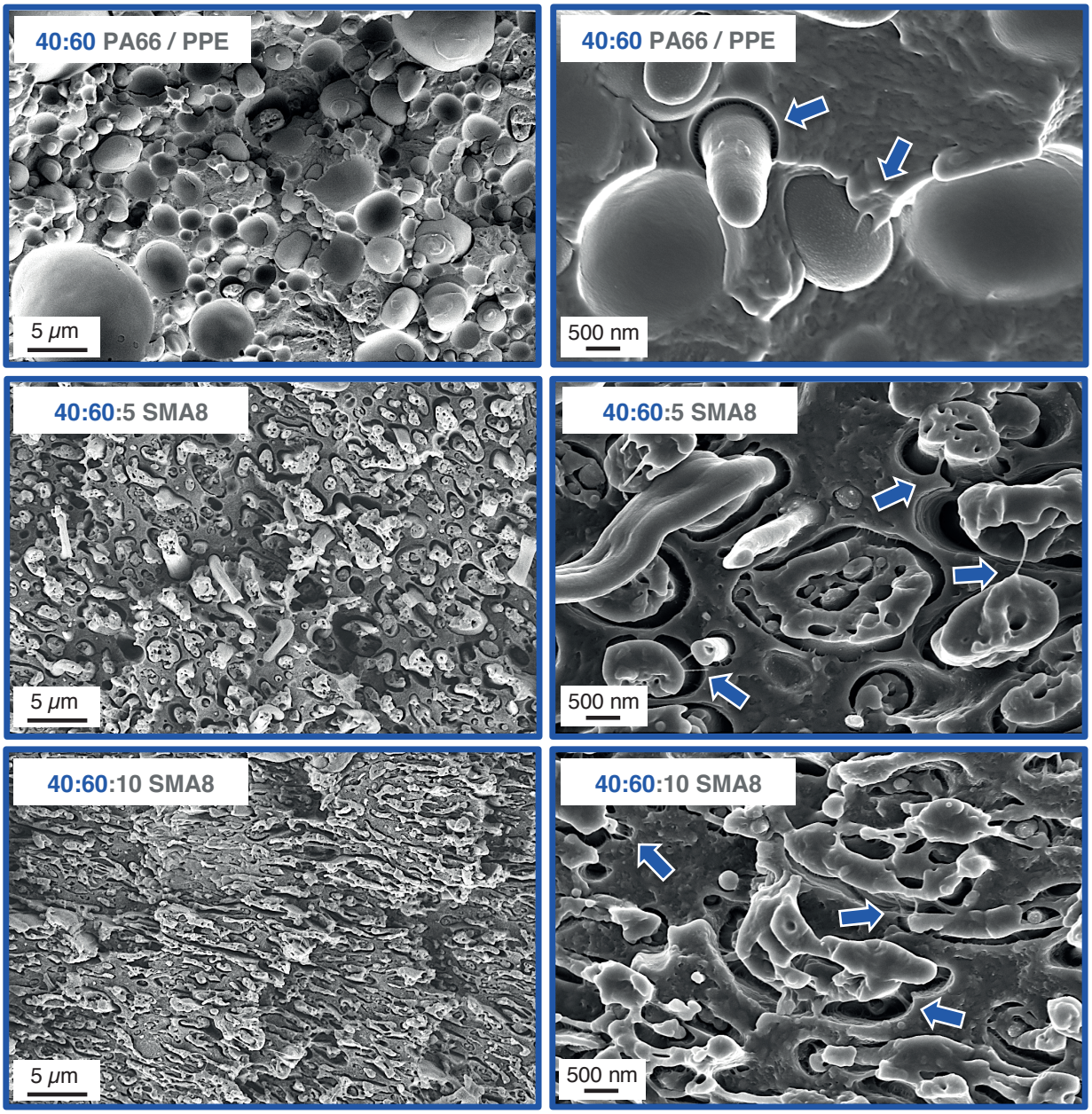

Figure 44 SEM images of fracture surfaces of 40:60 w/w PA66 / PPE reference and ternary blends with 5 and 10 wt% SMA8 after tensile testing. Higher magnifications with indicators are present on the right column.

The 60:40 w/w PA66 / PPE reference (Fig. 43) shows a relatively smooth fracture surface with a low degree of crack deflections. The dry state and notch-sensitivity of PA66 feature brittle failure with negligible plastic deformation. The PPE domains are sporadically elongated, but mainly pull-outs are evident. The smooth cavity surfaces indicate a weak stress transfer between the two phases.

Local matrix fibrillations can be observed at higher magnification wherever elongated PPE domains are found. This is because of the intrinsic covalent bonding between PA66 and PPE, creating linear PA66-b-PPE copolymers [151]. This crack bridging mechanism is expressed stronger than the 50:50 w/w equivalent seen in Figure 35, meaning that the degree of interfacial enhancement is directly linked to the PA66 amount (carboxylic acid moieties).

Adding 5 wt% SMA8 gives rise to a similar fracture surface but has more crack deflections. Looking closer, the elongation of PPE domains is comparable, if not a little less expressed compared to the reference. The difference is seen at the blend interfaces, with a lower degree of crack bridging with very short fibrils. As discussed in Chapter 6.2.2, replacing the direct bonds between PA66 and PPE with SMA8-g-PA66 compatibilizer copolymers leads to a woarsening or stagnating mechanical performance until this interfacial reorganization is completed (at higher SMA contents).

The fracture surface at 10 wt% SMA8 content, governed by an increased number of crack deflections, is rougher. With the increasing depth of these step-like deformations, PPE elongation also appears more prominent. A strengthening of the interface is visible by crack deflections originating from the blend interfaces (upper two arrows) up to a level where even cohesive failure of PPE domains is enabled. The improved stress transfer is rewarded by both increasing σ_M and ε_B. Interestingly, the previously discussed nano-micelles can also be seen in the SEM images for 5 and 10 w% SMA8, pronounced by bright spherical inclusions within the PA66 phases.

The fracture surface of the 40:60 w/w PA66 / PPE binary blend (Fig. 44) appears rougher than the 60:40 equivalent, mainly governed by debonding of the broadly dispersed PPE domains (at a very low level of elongation) and low-degree crack deflections. The level of interfacial interactions can be concluded as more deficient compared to the 60:40 w/w binary reference.

Upon addition of 5 wt% SMA8, the fracture surface changes significantly. Given the morphology transition, the PPE phases appear in smaller structures where the majority is highly elongated. Profound steps strongly express apparent crack deflections. At higher magnification, the coexistence of cohesively failed PPE phases and extended domains (up to 5-times in size) are seen. These result in a mixed deformation mechanism, replacing the less stress-consuming pull-outs.

The fibrils located at the interfaces also elongate strongly, proving the enhancement of interfacial interaction. Besides the matrix deformations, interparticle bridging of PPE domains is observed in PA / PPE systems for the very first time. The interparticle bridges (fibrils) are located between two PPE domains in proximity, with a very thin layer of PA66 matrix (with compatibilizer copolymers) in between.

With a further increase of SMA8 to a content of 10 wt%, a co-continuous morphology with very fine structures is evident, in which very strong step-like crack deflections govern the surface. The interlocking mechanism in such morphologies is very efficient in stress absorption and lead to in strongly improved tensile properties. At higher magnification, the multiple deformation mechanisms can be defined, starting from micro-crack deflections, local matrix deformation by fibrillation, followed by partial elongation, and subsequently the cohesive failure of PPE enhanced by anchoring of the phases. As stated for the 60:40 blends, nano-emulsions can also be seen in the 40:60 w/w blends whenever SMA8 is added.

In conclusion, the best tensile properties could be achieved for both PA66 / PPE blend ratios, 60:40 and 40:60 w/w, at an SMA8 content of 10 wt%. Despite the better properties of the 60:40 binary blend, the 40:60 blend revealed the most efficient interaction with SMA8 (greater relative improvements), closing the gap already at only 2.5 wt% of compatibilizer. The 60:40 binary blends' higher energy dissipation is justified by having moderate crack deflections, along with debonding and pull-outs of PPE domains, as the underlying deformation mechanisms. The more vital interaction of 40:60 blends with SMA8 results in an elevated level of crack deflections and PPE elongation, debonding, and anchoring by the co-continuous structure.

6.3.3 Summary

The goal of Chapter 6.3 was to understand the role of the PA66 / PPE blend ratio, namely 60:40 and 40:60 w/w, on the morphology development and the resulting mechanical properties thereof. The findings from the previous Chapters 6.1 and 6.2, e. g. SMA8-g-PA66 micelles with PPE cores, has successfully been correlated to the observations in this section.

Via TEM analysis of the ternary blends, it was shown that at each blend ratio, the evolution of morphology differed with and without the addition of SMA8 from 2.5 to 10 wt%. While the overall morphology did not change for the 60:40 w/w ternary blends (all droplet-sea), the 40:60 blends varied from coalesced droplet-sea to droplet-sea and finally reached co-continuity upon 0 to 2.5 and 10 wt% SMA8 addition, respectively. The inhibition of coalescence could be addressed to the strong interfacial orientation of SMA8 and its' reacted species with PA66.

In both blend ratios with SMA8, a bimodal domain distribution was evident. The larger fractions are attributed to PPE polymer and the smaller particles to either unreacted SMA8, SMA8-g-PA66 micelles, or the latter with PPE cores. As stated in Chapter 6.2, the theory of swollen nano-micelles was again successfully proven by nano-domain sizes significantly above values expressed in the PA66 / SMA8 binary systems (Table 5). Additionally, the domain sizes correlated to the PPE amount in the blends, growing with increasing PPE content.

To have a complete picture of the morphological changes of PA66 / PPE / SMA8 blends, information discussed in all previous sections is consolidated within a ternary phase diagram as depicted in Figure 45.

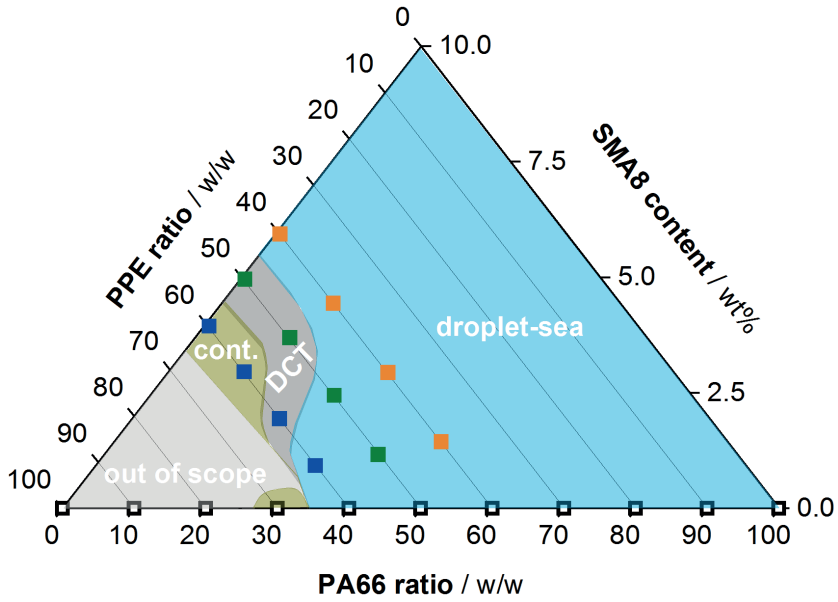

Figure 45 Ternary phase diagram of PA66 / PPE / SMA8 blends at varying PA66 / PPE blend ratio and SMA8 content. All rectangular represent measured data: PA66 / PPE binary blends (white with black edges), 60:40 PA66 / PPE (orange), 50:50 PA66 / PPE (green), and 40:60 w/w PA66 / PPE (blue). Filled areas represent droplet-sea (blue), dispersed-to-co-continuous transition (DCT, dark grey), co-continuous (cont., dark yellow). The light grey zone is undefined, as it is out of the scope of this research.

Regarding tensile properties, the fundamental deformation mechanism is predetermined by SMA8; however, altering the availability of PPE (blend ratio) and a change in morphology lead to different observations. Generally stated, the interactions of SMA8 with the blend increase with higher PPE or lower PA66 amounts (40:60 w/w PA66 / PPE). A small quantity of SMA8 (2.5 wt%) enables mentioned blend ratio to eliminate the disadvantageous mechanical properties at the binary level without SMA8 when compared to the 60:40 w/w equivalent. The deformation mechanisms, despite being similar in type, do differ in intensity when comparing both blend ratios. Main micro-mechanisms are found as plastic deformation of PPE by interfacial tearing, followed by crack bridging by matrix fibrillation and cohesive failure of PPE. Latter is excessively observed at co-continuous morphology (40:60:10 PA66 / PPE / SMA8), enabled by the interconnected nature, allowing an anchoring effect.

Multiple stated developments draw a conclusion that a droplet-sea structure is beneficial over a co-continuous morphology, as found in all 60:40 w/w blends and 40:60:2.5 PA66 / PPE / SMA8. Regardless of the morphology, the SMA8 content remains the most critical factor for improvements, giving rise to the best performance in both blend ratios at 10 wt%. Given this fact, a constant SMA8 content of 10 wt% will be considered for the following investigations.

An overview summarizing the tensile properties of all considered blend ratios is shown in Table 10.

Table 10 Consolidated tensile properties of SMA8-compatibilized PA66 / PPE blends at 60:40, 50:50, and 40:60 w/w blend ratio. The highest values of each category (E, σ_M, and ε_B) within a one blend ratio are highlighted in bold.

	Young's modulus (E) [MPa]			**Tensile strength (σ_M) [MPa]**			**Elongation at break (ε_B) [%]**		
SMA8 [wt%]	**60:40**	**50:50**	**40:60**	**60:40**	**50:50**	**40:60**	**60:40**	**50:50**	**40:60**
0	2710 ±135	**2630 ±110**	2640 ±114	72.8 ±2.9	65.3 ±3.7	61.8 ±3.3	3.9 ±0.4	3.0 ±0.3	2.7 ±0.2
2.5	2760 ±98	2580 ±42	2670 ±101	72.7 ±1.4	62.2 ±1.7	70.5 ±1.3	3.5 ±0.1	2.9 ±0.1	3.4 ±0.2
5	2760 ±85	2620 ±85	**2690 ±49**	74.3 ±0.7	69.9 ±1.2	74.8 ±0.7	3.9 ±0.2	3.5 ±0.1	4.1 ±0.1
7.5	**2780 ±76**	2610 ±53	2600 ±107	76.0 ±0.8	**72.5 ±0.9**	76.0 ±1.1	4.0 ±0.2	4.5 ±0.2	4.4 ±0.3
10	2730 ±85	2540 ±65	**2690 ±88**	**78.4 ±0.9**	71.8 ±0.9	**76.4 ±1.3**	**5.4 ±0.4**	**5.0 ±0.5**	**4.5 ±0.3**

Apart from E of the 50:50 w/w blends, all tensile values reach their maximum at the higher end of the SMA8 contents examined, independent of the blend ratio. Given this, the statements above support that an addition of 10 wt% SMA8 is the most promising candidate for the upcoming investigations.

6.4 Influence of humidity on PA66 / PPE / SMA8 Blends

Polymer conditioning (drying or humidifying) before processing or testing is a key parameter, especially when handling polymers prone to significant humidity uptake, such as polyamides. Performing tests, the state of moisture must be defined sharply to provide reliable and reproducible results [199].

When comparing or blending polymers having different sensitivity to water, such as PA66, PPE, and SMA, the most convenient strategy is to have all polymers in the dry state as done in this work. Latter two polymers are hydrophobic and do not absorb noticeable concentrations of water, and therefore can be used as purchased [304,305]. Despite the convenience in comparability, conditioning of materials *via* vacuum-drying is far apart from the realistic conditions which these materials face at their targeted end application. Therefore, conditioning of samples ideally at an equilibrium state of temperature and humidity becomes necessary. However, it may take up to several months in case of simple storage in standard atmosphere (23°C and 50% relative humidity) [306]. Given this fact, all PA66-containing blends will undergo the conditioning protocol described in DIN EN ISO 1110 and will be tested subsequently at an absolute water content of approximately 1 wt%, labeled as 'cond.'.

In this chapter, the changes in material performance will be investigated by comparing dried and conditioned states. Tensile toughness data will be extracted from the findings obtained in the previous sections and complemented by tensile toughness data in conditioned state. After a basic analysis of the quasi-static tensile toughness, an in-depth examination of the resistance in dynamic fatigue crack propagation (FCP) will be performed and supplemented by an analysis of the fracture surfaces in both conditioning states. Binary and ternary blends of PA66 / PPE and SMA8 (10 wt%) will be considered for the investigations, as shown in Table 11.

Table 11 Overview of all binary PA66 / PPE and ternary PA66 / PPE / SMA8 blends examined in this chapter.

PA66 / PPE blend ratio (w/w)	SMA8 [wt%]	Sample condition
60:40	0	Dry (< 0.2 wt% H_2O)
50:50	10	Cond. (~ 1 wt% H_2O)
40:60		

The goal of this chapter is to gain a deeper understanding of the interfacial interactions between the blend constituents and the resulting mechanical properties upon quasi-static (tensile) and dynamic (FCP) testing thereof. Additionally, the influence of humidity will be highlighted and correlated to apparent changes in the deformation mechanisms.

6.4.1 Influence on mechanical behavior under quasi-static load (tensile)

Despite the general knowledge of humidity-dependent polyamide (PA) properties, the number of investigations targeting the effect of moisture in PA-based blends on tensile properties is limited [307–310]. Nevertheless, all agree on the fact that an increasing level of humidity allows a more ductile deformation of the PA. Being blended with a brittle polymer, an existing ductility mismatch might be dramatically altered by the introduction of humidity and thus is of great academic interest.

Tensile toughness (U_T), also referred to as deformation energy, is calculated by applying Equation 16 to the obtained stress-strain curves:

$$U_T = \int_0^{\varepsilon_B} \sigma \cdot d\varepsilon \, [\frac{J}{m^3}] \tag{16}$$

where ε_B is strain at break, σ is tensile stress, and ε is tensile strain.

The U_T of dry and conditioned binary PA66 / PPE blends at varying blend ratios and ternary mixtures thereof with 10 wt% SMA8 are depicted in Figure 46.

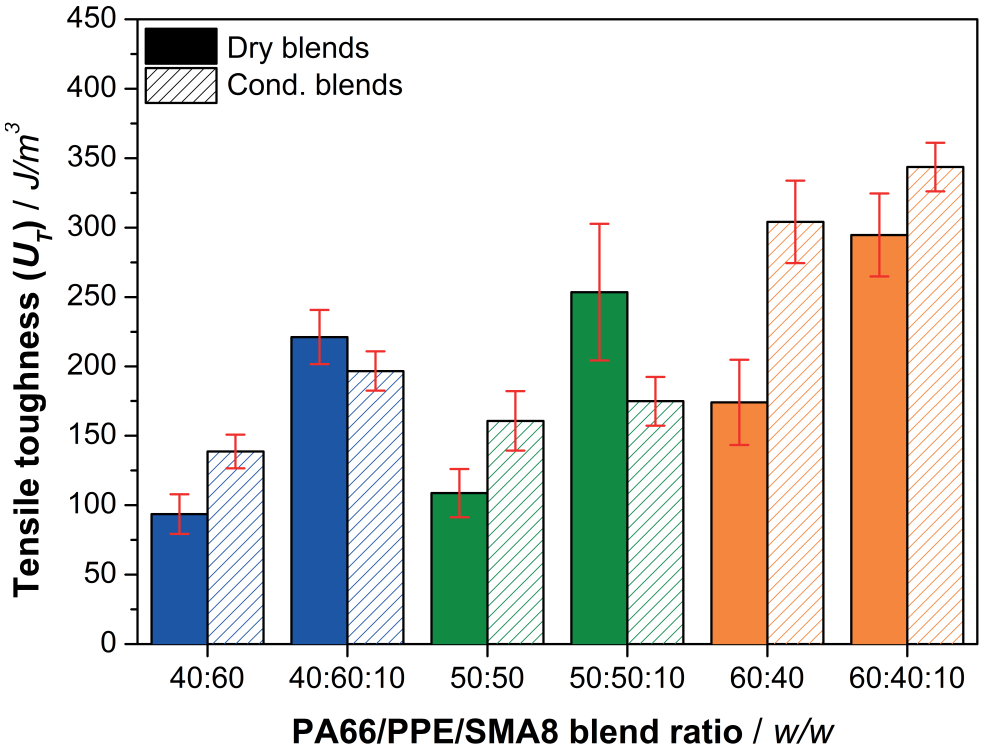

Figure 46 Dry (solid bars) and conditioned (patterned bars) tensile toughness (U_T) of binary PA66 / PPE blends at varying ratios and ternary blends thereof with 10 wt% SMA8.

As discussed in the previous sections, adding SMA8 improves tensile strength (σ_M) and elongation at break (ε_B) of the materials in a dry state at any blend ratio considered. Expectedly, U_T also shows an increase at all blend ratios upon the addition of 10 wt% SMA8. In the conditioned state, the addition of SMA8 again leads to improved toughness values, yet not as significant as in the dry condition, indicating that the introduced SMA8 interferes with the gain of ductility of the PA66 phases to some extent. Comparing dry and conditioned blends at constant blend ratio and SMA8 content, two pairs, namely 40:60:10 and 50:50:10, show a controversial behavior. Toughness is reduced upon moisture uptake, caused by a dramatic reduction in σ_M combined with no improvement in ε_B values. The latter case is unexpected at first sight; considering the blend morphologies in Figures 28 and 37, however, provides a good explanation. The morphology of both blends is derived from the droplet-sea structure of 60:40:10, having a co-continuous organization for 40:60:10 and a dispersed-to-co-continuous transition (DCT) for 50:50:10 PA66 / PPE / SMA8. The interpenetrating nature of the blend phases in co-continuity, combined with the larger nano-domains in the PA66 phase, restrain the

plastic deformation of the PA66, not allowing to elevate the elongation and thus, toughness above the level of a dry specimen.

In summary, SMA8 improves the toughness of all blends compared to the binary equivalents in both dry and conditioned states. The most decisive improvements upon conditioning the materials are achieved at a PA66 / PPE blend ratio of 60:40 with and without SMA8. The 40:60:10 and 50:50:10 blends reveal a lower toughness in a conditioned state, compared to their dry equivalents, due to changes in their respective morphologies towards co-continuity.

6.4.2 Influence on mechanical behavior under dynamic load (FCP)

To create an understanding of the deformation behavior of complex (ternary) blend structures, fatigue crack propagation (FCP) tests have proven to be one of the most potent methods, as different crack propagation rates result in different responses in the respective phases [158,202,227,265]. From there, other responses of the individual blend constituents can be observed and described as deformation depends directly on the loading time.

In this chapter, the FCP results will be addressed in two parts: first, materials in the dry state, followed by conditioned materials in the second. In each part, the results will be discussed by an evaluation of the curve shapes and relative shifts, together with their respective key metrics. The metrics of relevance are the threshold stress intensity factor (ΔK_{th}), the slope of the Paris-Erdogan regime (m), and critical stress intensity factor (ΔK_{cr}) extracted from regions I-III. SEM analysis will be performed individually for regions I and III (threshold and critical region) and compared to the different blend compositions to understand underlying deformation and fracture mechanisms.

FCP of blends at dry state

The FCP behavior of dry PA66 / PPE binary blends and their equivalent ternary blends with 10 wt% SMA8 are compared in Figure 47. Additionally, the characteristic values extracted from regions I-III (ΔK_{th}, m, and ΔK_{cr}) are summarized in Figure 48.

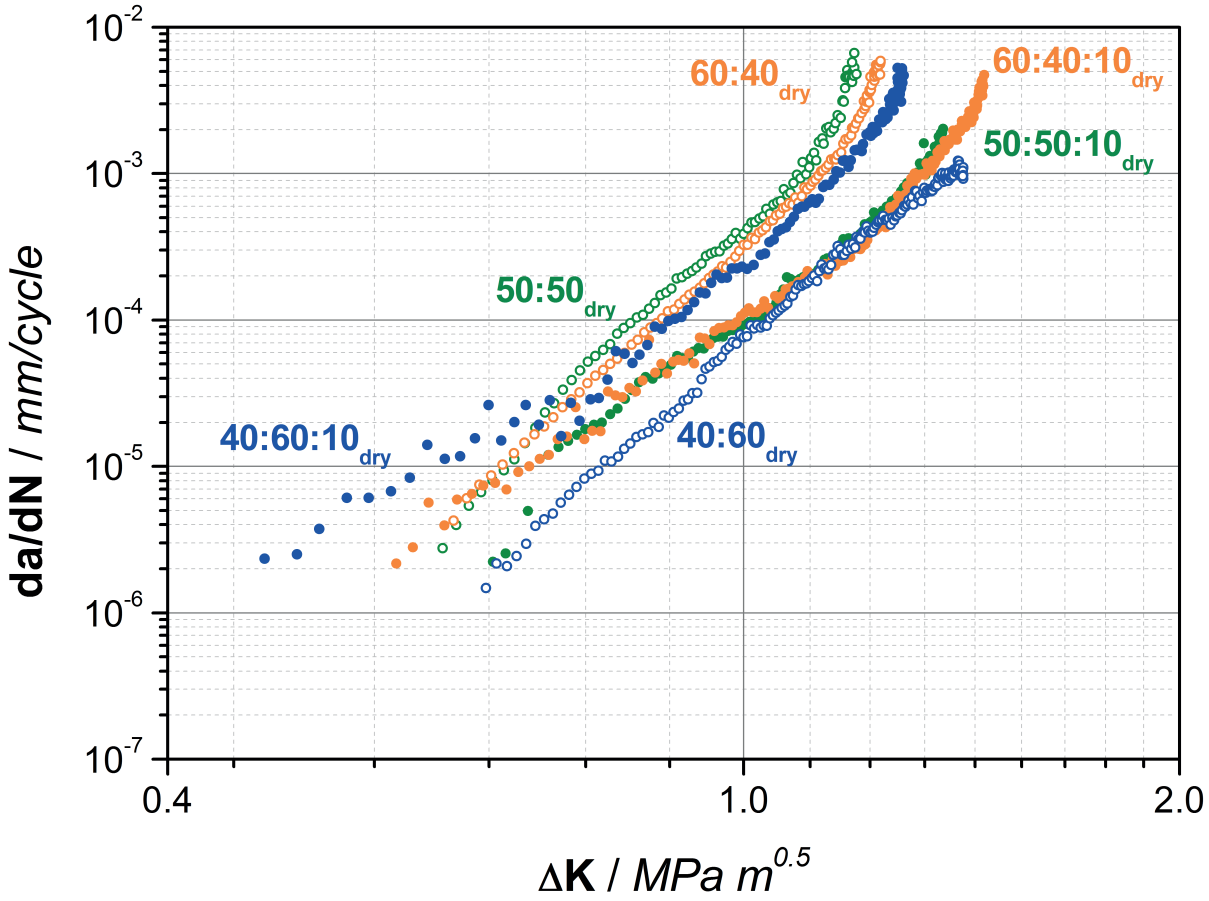

Figure 47 FCP behavior of dry PA66 / PPE binary blends (open circles) and ternary mixtures thereof with 10 wt% SMA8 (solid circles).

In the qualitative comparison of the binary blends (Fig. 47, orange, green, and blue open circles), the 40:60 w/w PA66 / PPE blend is the most resistant material against crack propagation, as the entire curve is shifted to higher ΔK when compared to the other two binary blends. Although 60:40 seems to have an improved behavior over 50:50 at regions II and III, it is in the range of experimental scattering, typically seen in da/dN [266,311]. Compared to the tensile performance seen in Table 10, a correlation by PA66 content is not possible here.

In terms of ternary blends (solid orange, green, and blue circles), the FCP behavior of the 40:60 PA66 / PPE blend ratio again deviates from the findings in the previous chapters, as seen by the significant shift in the curve to the left. The 60:40:10 and 50:50:10 ternary blends meet the expectations well by having a right shift in a similar degree. One common observation for all blends is the reduction of slopes in region II upon adding 10 wt% SMA8, indicating a

strengthening of the blend interfaces and thus, reducing the crack propagation speed effectively. While the values for regions I and III, namely ΔK_{th} and ΔK_{cr}, are easily distinguishable, the slope in region II requires a closer look. Therefore, the average values of *m* are given in Figure 48, together with ΔK_{th} and ΔK_{cr}.

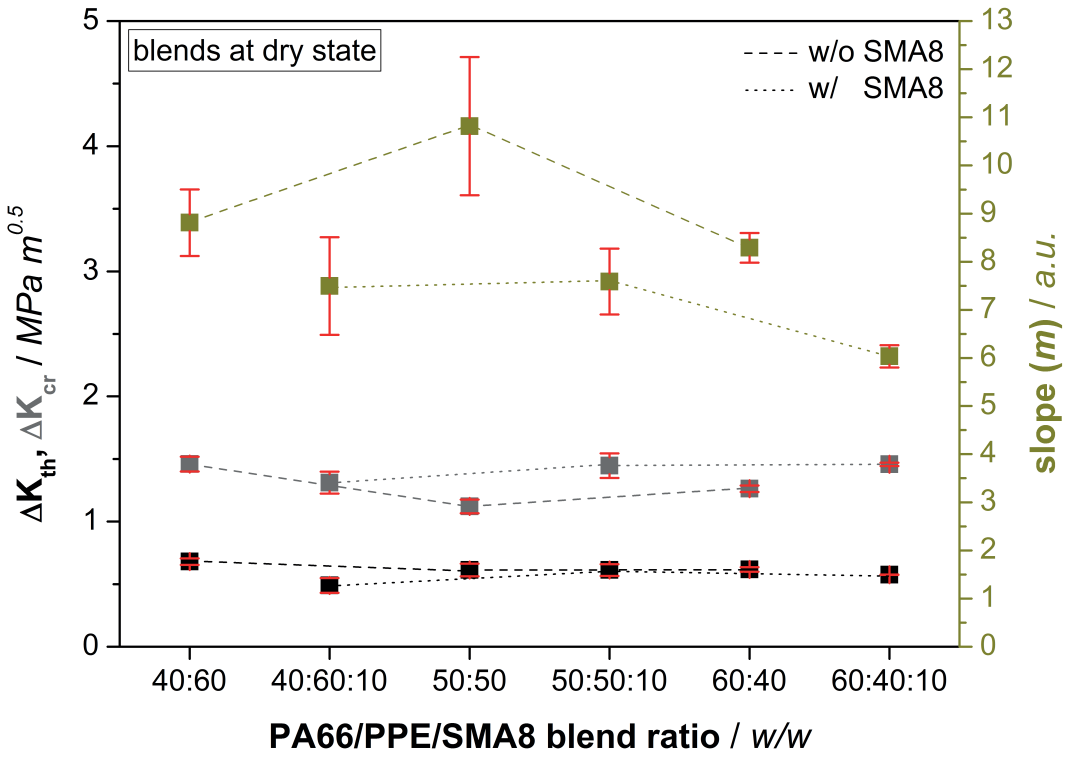

Figure 48 FCP values extracted from the curves in Figure 47 at their respective regions I-III, namely ΔK_{th}, *m,* and ΔK_{cr}.

As anticipated from the curves, the slopes of all blend ratios drop upon the addition of 10 wt% SMA8, translating into a higher resistance for cyclic loads in the stable crack growth region II. Surprisingly, the slope of the 50:50 w/w binary blend reveals the highest value and the most significant deviation. At the same time, the best relative improvement with -43% is also found for this blend. A clear trend of material behavior is not apparent from both figures shown so far. Therefore, fractographic analysis combined with the knowledge of morphological from previous chapters becomes crucial. In Figures 49-53, the fracture surfaces of all blends in regions I and III state are given in the dry state.

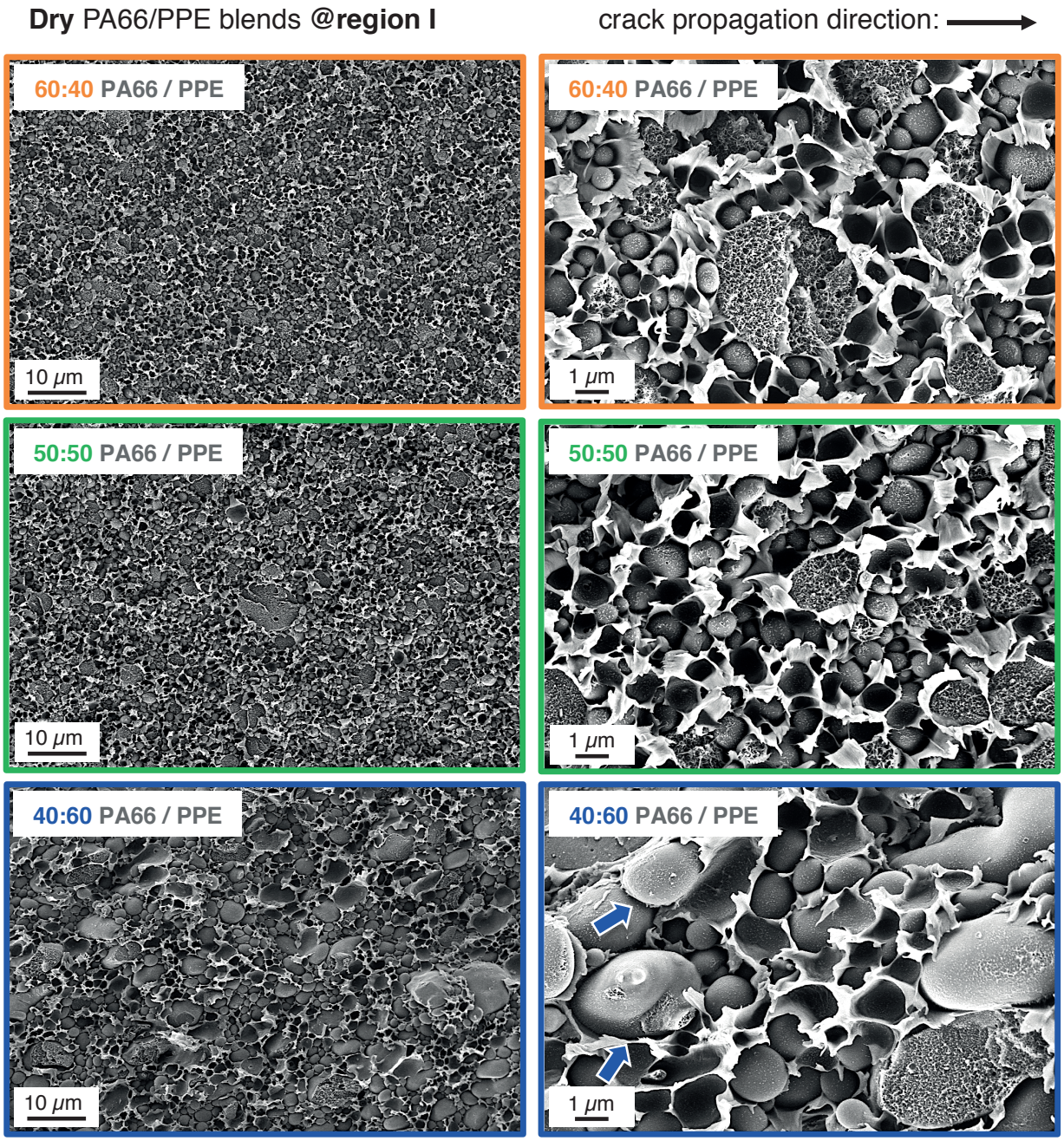

Figure 49 SEM fracture surfaces of FCP tested 60:40, 50:50, and 40:60 w/w PA66 / PPE binary blends (from top to bottom) with respect to da/dN region I at different magnifications (left to right). All considered materials are tested in a dry state. The cracks propagate from left to right. The arrows indicate existing elongated PPE domains.

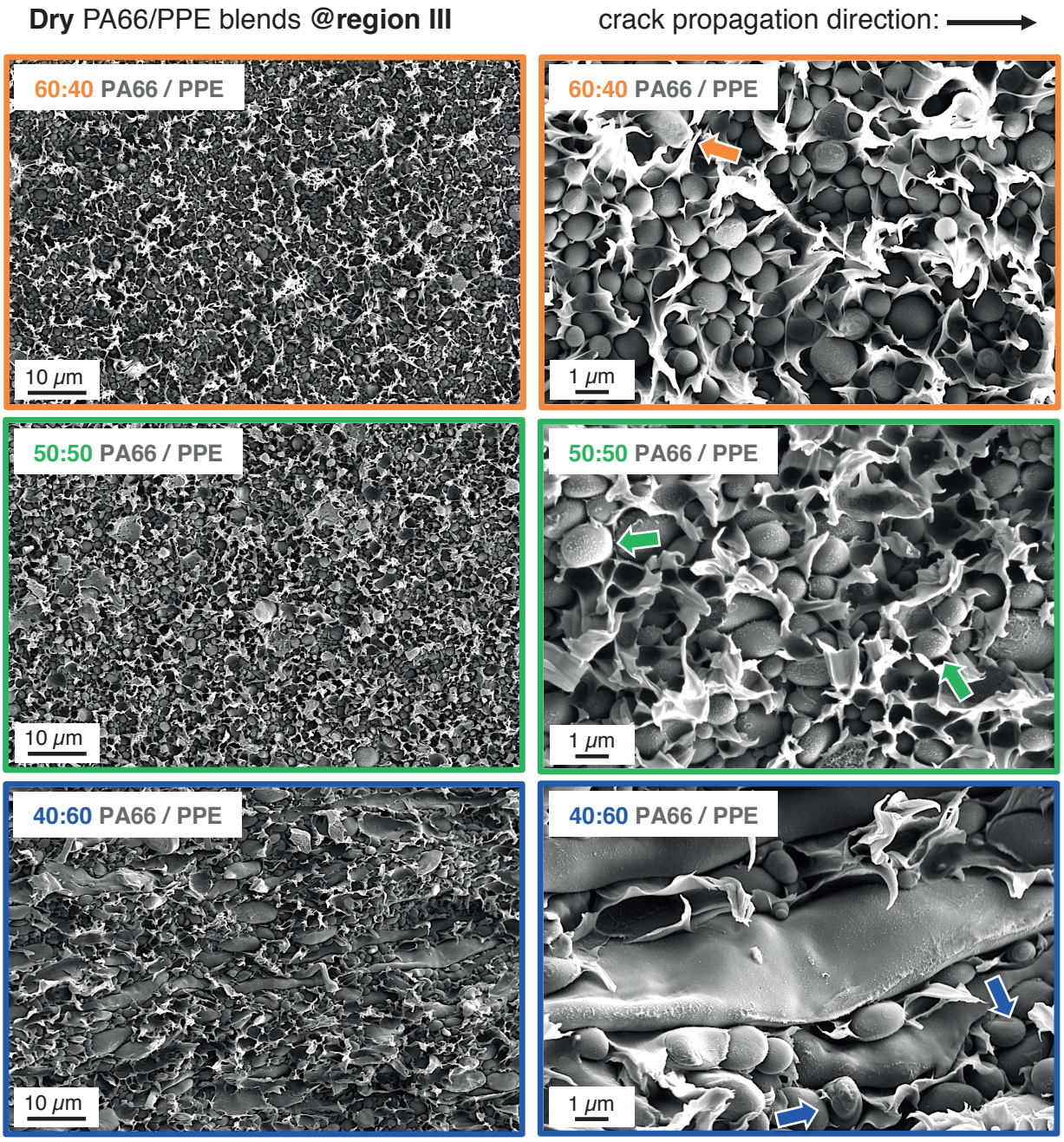

Figure 50 SEM fracture surfaces of FCP tested 60:40, 50:50, and 40:60 w/w PA66 / PPE binary blends (from top to bottom) with respect to da/dN region III at different magnifications (left to right). All considered materials are tested in a dry state. The cracks propagate from left to right. The arrows indicate existing elongated PPE domains.

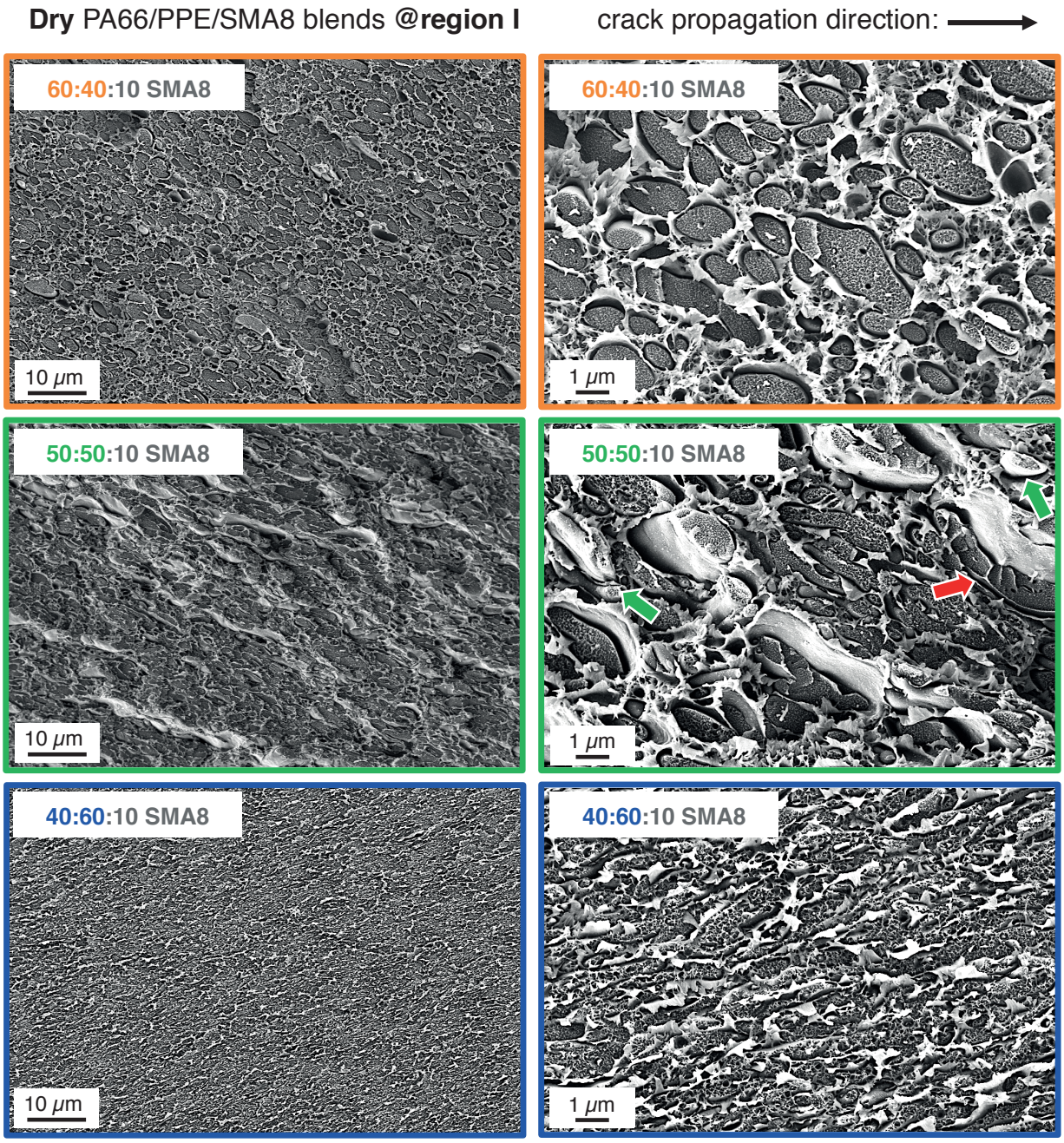

Figure 51 SEM fracture surfaces of FCP tested 60:40:10, 50:50:10, and 40:60:10 w/w PA66 / PPE / SMA8 ternary blends (from top to bottom) with respect to da/dN region I at different magnifications (left to right). All considered materials are tested in a dry state. The cracks propagate from left to right. The green arrows indicate existing elongated PPE domains. The red arrow shows severe crack initiation and deflection at the PA66-PPE interphase.

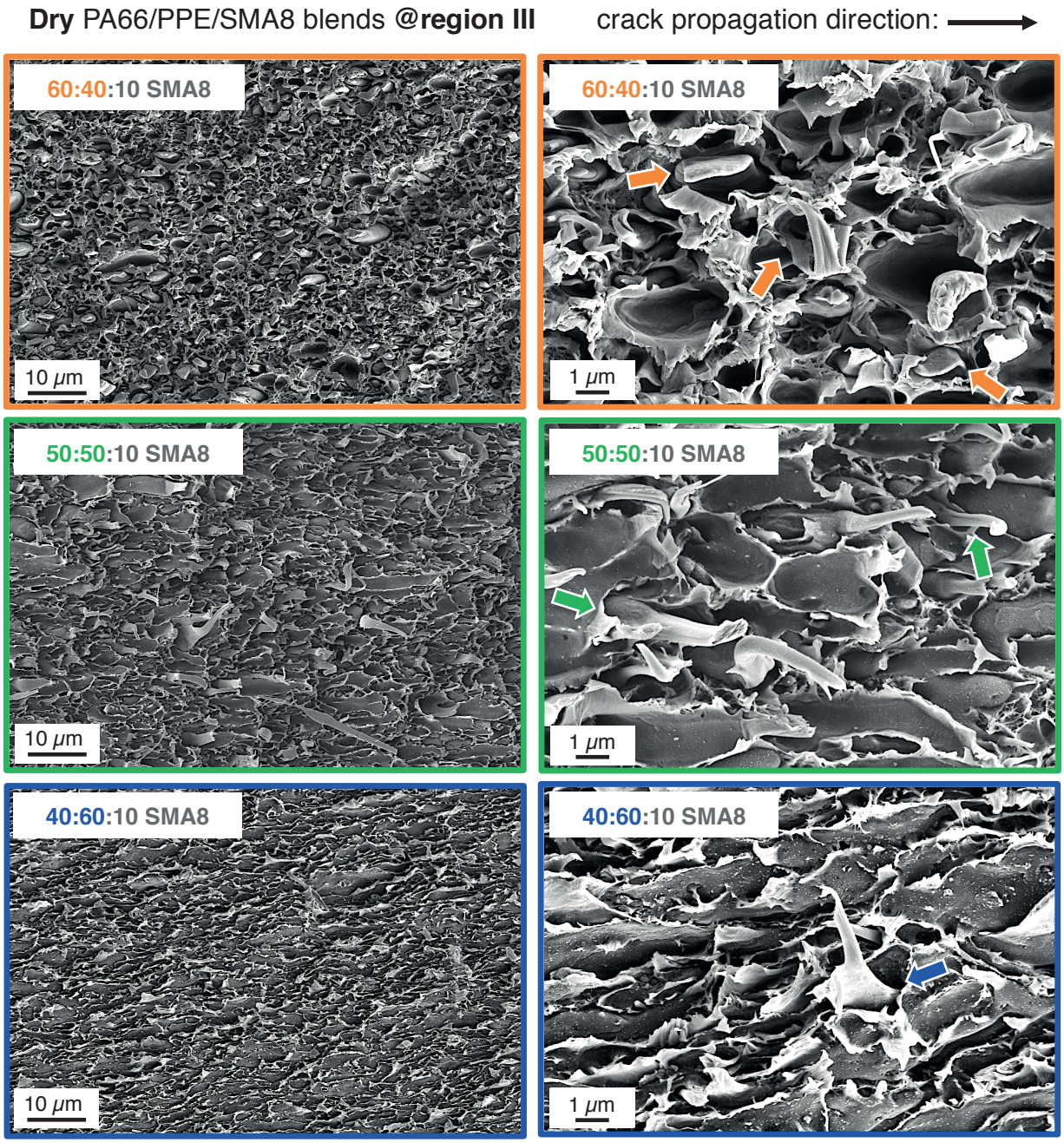

Figure 52 SEM fracture surfaces of FCP tested 60:40:10, 50:50:10, and 40:60:10 w/w PA66 / PPE / SMA8 ternary blends (from top to bottom) with respect to da/dN region III at different magnifications (left to right). All considered materials are tested in a dry state. The cracks propagate from left to right. The arrows indicate existing elongated PPE domains.

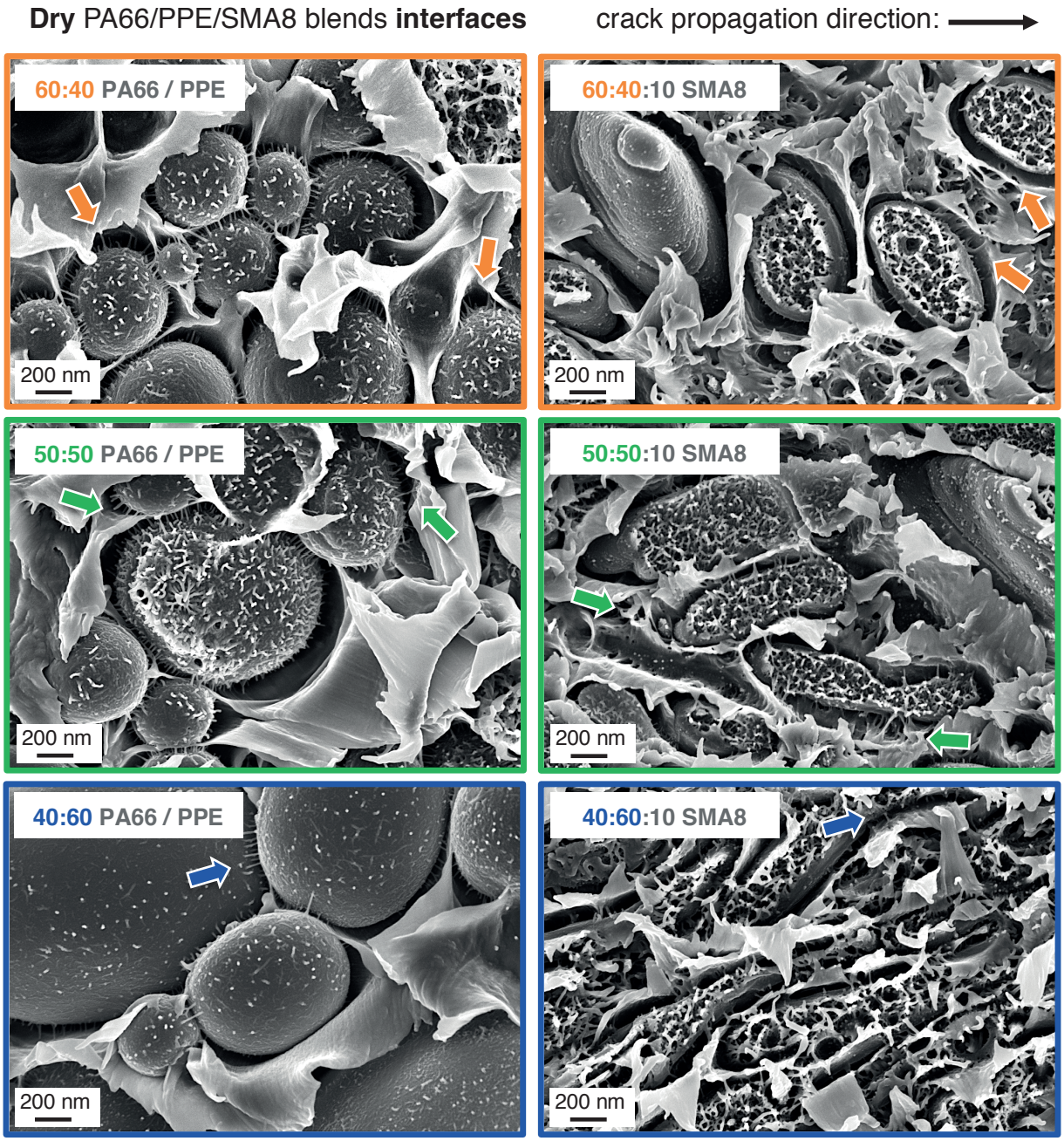

Figure 53 SEM fracture surfaces of FCP tested 60:40, 50:50, and 40:60 w/w PA66 / PPE binary blends (left column) and ternary blends thereof (right column) at very high magnification. All considered materials are tested in a dry state. The cracks propagate from left to right. The arrows indicate unruptured elongated interfacial fibrillations.

Figures 49 and 50 show the region I and III fracture surfaces of binary PA66 / PPE blends in the dry state, respectively. Looking at the binary blends in region I (Fig. 49, left column), all show a smooth fracture surface with minimal and evenly distributed agitation, indicating a brittle-type fracture on the macroscopic scale. Herein, 40:60 PA66 / PPE stands out with step-like crack deflections. This rougher surface can readily be linked with the significantly better da/dN curve. At higher magnification (Fig. 49, right column), information on the deformation mechanisms within the individual blend components can be gained. The most apparent observations are the growing PPE domain sizes and a reduction of cohesively fractured PPE domains with increasing PPE content in the blend. Interestingly, the PPE domains tend to fracture cohesively only for larger domain sizes with > 1 µm. Also, a higher degree of elongation is found for PA66, *i.e.,* ductile behavior, compared to PPE in all three cases.

The 40:60 w/w blend reveals severe cavitation, tearing (elongated domains as indicated by arrows), and pull-out of PPE. In very few cases of PPE fracture, massive crazing is the primary deformation mechanism for PPE. The residue structures can be attributed to crazing by apparent nano-voids and ruptured fibrils, as illustrated in Figure 10. The PA66 mainly displays elongated lamellar ligaments perpendicular to the crack direction as a residue of shear deformation zones (yielding) [228]. In the case of the other two blends, the tearing of PPE is less pronounced. In exchange for less plastic deformation of PPE, the degree of cohesively fractured PPE domains increases with increasing PA66 content. This observation indicates an improved interfacial stress transfer [223]. The surface of fractured PPE phases is governed by nano-voids and ruptured fibrils as residues of the crazing mechanism; however, they appear to be bigger than the 40:60 PA66 / PPE blend. With increasing stress and time, nano-voids and fibrils face coalescence and thus, become larger in their lateral dimension [202]. This means that the PPE domains in 60:40 and 50:50 PA66 / PPE did fail at a later stage than 40:60, supporting the statements of higher interfacial strength with increasing PA66 content.

Additionally, this aligns with the results and fracture surface discussions of the quasi-static loaded blends in Chapters 6.2 and 6.3. However, the better performance of the 40:60 w/w blend seems to originate from the coalesced droplet-sea morphology (Fig. 37), providing very large domains. These domains most likely exceed the plastic zone size and act as efficient barriers to the propagating crack, leading to crack deflections. The deflection paired with the stronger PPE domain tearing gives rise to a higher stress absorption level [263].

The interfacial interactions of all three binary blends are shown in highly-magnified images shown in Figure 53 (left column). The intrinsic interfacial interaction of binary mixtures is seen in great detail, as documented in the previous chapters. In all blends, the PPE domains and respective cavities are governed by PA66-b-PPE copolymer fibrils at a diameter of approx. 30 nm, acting as crack bridges and stress transfer centers. Unruptured fibrillations are indicated by the arrows in the respective images. As mentioned above, the increased ability of stress transfer is enabled by more vital interfacial interaction, displayed by the higher fibril density for higher PA66 content blends.

Looking at binary blends in region III (Fig. 50, left column), all show an increasingly agitated fracture surface compared to the region I. At higher magnification (Fig. 50, right column), the absence of cohesively ruptured PPE domains is most noticeable for all blends. The increased stress intensity prevents the cracks from propagating through PPE domains. The plastic deformation of PA66 also is more pronounced in all three cases compared to the state in region I, indicating that either PPE is not as responsive to higher stresses or the blend interface fails to transfer stresses efficiently. The 60:40 and 50:50 PA66 / PPE blends show a limited number of elongated PPE domains. In the case of the 40:60 blend, a very distinctive observation can be made. Extraordinarily long lamellae-type PPE domains are found, reaching dimensions of up to 48 µm in length and 6 µm in width, oriented in injection direction (same as crack propagation direction). In the case of the other blend ratios, PPE domains of only up to 10 µm are observed. Such large structures explain the outstanding FCP behavior of 40:60 PA66 / PPE, as anticipated in the discussion in region I. Structures bigger than the plastic zone size are frequently described as very efficient in energy absorption at higher propagation rates by significantly deflecting, blunting, pinning, or branching the propagating crack [80,111,220,261,312,313].

Finally, the fracture surfaces of PA66 / PPE / SMA8 ternary blends are examined, as depicted in Figures 51 and 52 for regions I and III, together with highly-magnified images in Figure 53 (right column). In Figure 51, the overview fractographs (left column) already support the different behaviors of the measured curves (Fig. 47) very distinctly by showing roughened fracture surfaces for 60:40:10 and 50:50:10 PA66 / PPE / SMA8 in comparison to the respective binary blend references. Controversially, the fracture surface of 40:60:10 w/w smoothened, showing evenly distributed features. These features indicate a brittle type of failure coming from the more plastically deformed binary reference (40:60 PA66 / PPE). Despite the differences, all three blends exhibit a brittle failure on the macroscopic scale.

Looking closer (Fig. 51, right column), very different fracture behaviors can be identified compared to the binary blends and within the comparison of the ternary mixtures in the region I. The tortuous fracture surfaces of 60:40:10 and 50:50:10 interestingly possess different deformation mechanisms, although they are very close in their absolute FCP values. As stated in the binary blend discussion, a higher PA66 content gives rise to an improved interfacial interaction of the PA66 and PPE, also in the presence of SMA8. Given this, the crack in the 60:40:10 blend does not propagate through the blend interface but through the matrix and having a robust interface also the PPE domains. This leads to a cohesive breakage of the latter with almost no tearing of PPE droplets. Cavitation and debonding of PPE domains, despite to a lower extent, contributes to the overall energy absorption of the material. From a micro-mechanical perspective, again, massive crazing is found as the dominant mechanism for the PPE phase, whereas PA66 shows high plastic deformation, enabled by crazing and shear yielding. Despite shear yielding or bands being the most prominent micro-mechanisms, crazing of PA66 polymers is also described in the literature [314]. Nano-sized voids are clear indicators of this mechanism (Fig. 53, right column), most likely initiated by rigid (PPE swollen) SMA8-g-PA66 micelles in the PA66 phases, as reported to be present (Chapters 6.2 and 6.3).

In the case of 50:50:10 PA66 / PPE / SMA8, the DCT morphology gives rise to various deformation mechanisms (Fig. 51, right column). The strongly expressed step-like deformations are caused by interfacial debonding. This mechanism coexists with cohesively failed PPE domains as reported for 60:40:10. Elongated PPE domains are also present, as indicated by the green arrow. On a macroscopic scale, the crack propagation can be summarized as interface dominated, initiated in the matrix phase, and transferred to the PPE phase by

sufficient interfacial bonding strength. Such local stress transfer zones are found in the fracture image, as indicated by the red arrow. High local stress concentrations are evident at the PA66-PPE interface, at which, after debonding, the stress is transferred to the PPE phase, resulting in the initiation and deflection of micro cracks.

The 40:60:10 ternary blend has, by far, the lowest ΔK_{th} value within this comparison (Fig. 47). At higher magnification (Fig. 51, right column), the given features are comparable to the 60:40:10 blend, where a cohesive failure of PPE domains is very prominent. Nevertheless, significant differences are, firstly, the morphology (co-continuous) and the domain size range of the PPE phase. The PPE phases seem highly oriented in the injection and crack propagation direction and possess a width of < 1 µm. Additionally, The PA66 phase appears to have undergone a higher degree of plastic deformation, expressed by a greater length of ruptured lamellae. A closer look into the blend's fracture surface in Figure 53 (right column) reveals very thin and highly elongated PA66 phases, with larger nano-voids and ruptured craze fibrils in the PPE. The blend interfaces are strongly debonded and show a significantly lower number of interfacial crack bridges compared to 60:40:10 and 50:50:10 PA66 / PPE / SMA8.

In Figure 52, ternary blend fracture surfaces in region III are depicted. The increased stress intensity factor leads to a higher severity in the deformation of the blends, providing more extensive visual details than in region I. All three blends show step-like crack deflections paired with a significant amount of PPE debonding and pull-out, increasing with increasing PPE content. The higher ΔK alters the crack propagation mechanism to be more interfacially oriented, also seen for the binary blends (Fig. 50). This shows that the blend interface is the most sensitive part of the blends at higher stress levels. Nevertheless, high plastic deformation of PA66 and PPE phases conclude a strengthened interface compared to the binary blends for 60:40:10 and 50:50:10 PA66 / PPE / SMA8 (Fig. 52, right column).

In the case of 40:60:10, the PA66 phase tends to have a higher degree of elongation, but alongside significantly weakened interfaces with almost absent PPE deformations. For 50:50:10, also smooth cavities of pulled-out PPE phases are present; however, a considerable fraction of highly elongated PPE domains prove a good interfacial stress transfer even in this critical failure environment. Nano-voids and residues of craze fibrils are still observable. The elongation of the PA66 phase seems to be at a very low degree, which is linkable to the DCT

morphology close to co-continuity, which is already indicated in the 40:60 binary blend and the ternary blend equivalent. With this, enabling plastic deformation of PPE seems to be the critical factor in increasing the FCP resistance in the ternary blend materials. This effect can be encountered in 60:40:10 PA66 / PPE / SMA8 to an even greater extent. Here, PA66 and PPE show elevated plastic deformation behaviors owing to the droplet-sea structure and the development of the most robust interfacial bonding within this comparison, also proven by tensile measurements.

In summary, three major factors influencing FCP in dry state most have been identified, namely PA66 content, blend morphology, and SMA8 compatibilizer. Increasing the PA66 content intensifies interactions with PPE and SMA8 due to the greater number of available reactive groups, resulting in improved interfacial strength. In terms of morphology, a droplet-sea structure tends to be beneficial over a co-continuous organization of the blend phases. However, the appearance of very large domains can alter this tendency in favor of the material with having larger structures, as found for 40:60 PA66 / PPE in the binary blend comparison. The use of SMA8 compatibilizer improves the materials at the blend interfaces and in the PA66 phases by forming nano-sized inclusions, as shown in Figure 26. The beneficial effect of a high concentration of tiny rigid particles on da/dN behavior is well described in the literature [228,315,316].

FCP on blends at conditioned state

The FCP behavior of wet PA66 / PPE binary blends and their equivalent ternary blends with 10 wt% SMA8 are compared in Figure 54. Additionally, the characteristic values extracted from regions I-III (ΔK_{th}, m, and ΔK_{cr}) are summarized in Figure 55.

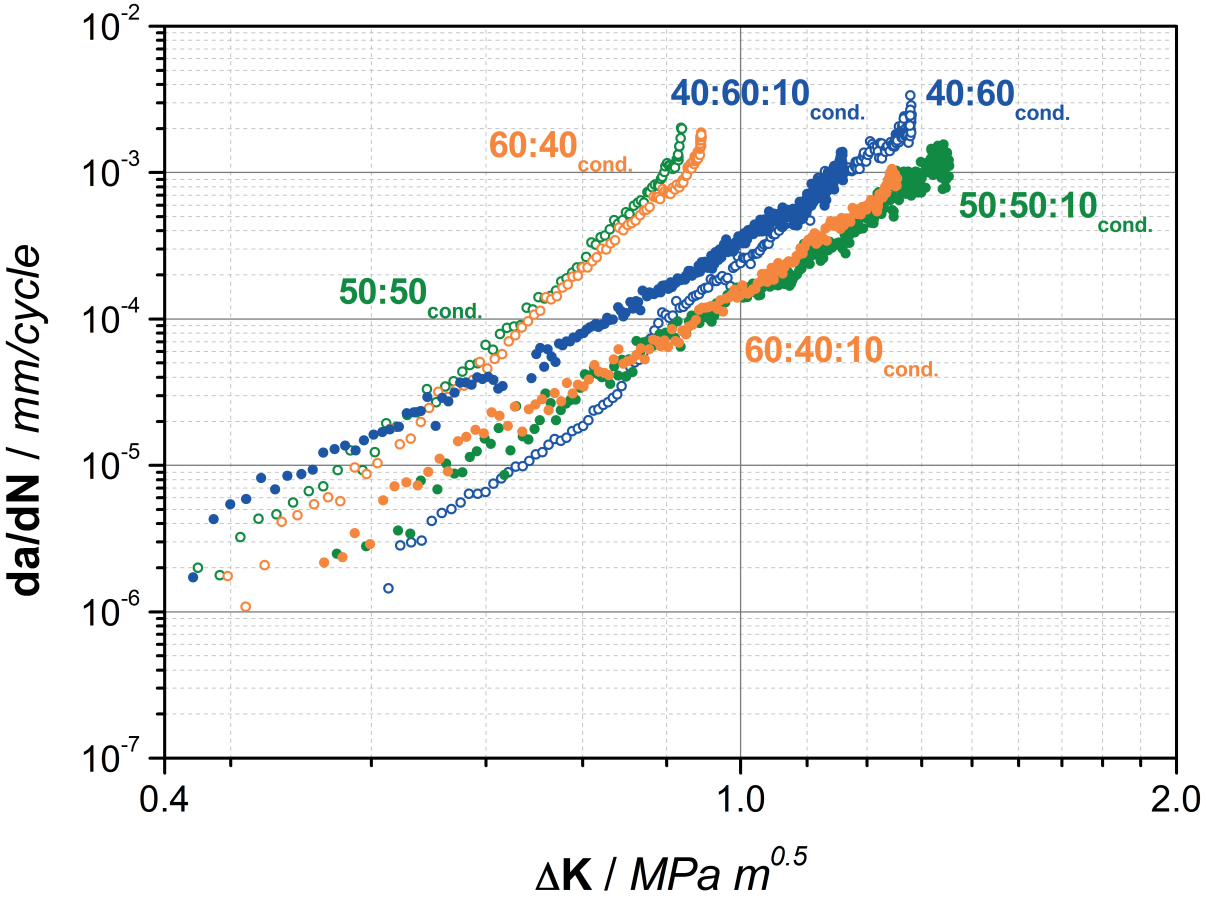

Figure 54 FCP behavior of conditioned PA66 / PPE binary blends (open circles) and ternary blends thereof with 10 wt% SMA8 (solid circles).

Upon qualitative comparison of the binary blends (Fig. 54, orange, green, and blue open circles), a plot similar to the dry state is seen (Fig. 47). All values of the 40:60 blend are shifted to higher ΔK, showing a significantly better performance compared to 60:40 and 50:50 PA66 / PPE. Latter two are comparable considering experimental scattering, although the blend ratio of 60:40 seems to perform marginally better in regions I and III.

In the case of ternary blends (solid orange, green, and blue circles), adding 10 wt% SMA8 to the 40:60 mixture has a detrimental effect in regions I and III. Apart from this, a significantly smaller slope than the binary reference is visible. Again, in the two other blend ratios (60:40:10 and 50:50:10 w/w), an overall right-shift combined with a less steep slope is evident compared to the binary references. Here, the latter blend ratio has higher ΔK values before reaching the critical fracture region. As stated, all three ternary blends have a superior FCP behavior in region II. For a better evaluation of differences in the characteristic values, average ΔK_{th}, m, and ΔK_{cr} data are plotted in Figure 55.

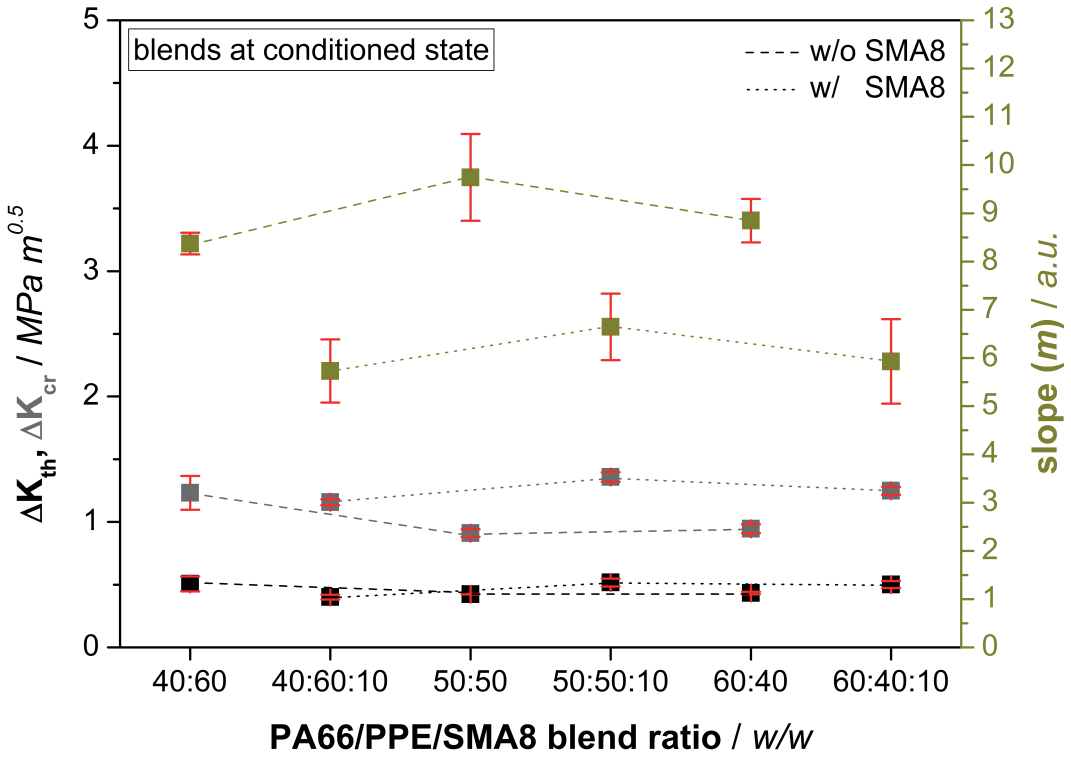

Figure 55 FCP values extracted from the curves in Figure 54 at their respective regions I-III, namely ΔK_{th}, m, and ΔK_{cr}.

As observed in the curves, all slopes (m) experience a significant reduction upon the existence of SMA8, which proves the higher resistance of FCP in region II. Again, the slope of the 50:50 binary blend is the highest, consistent with the observation in the dry state. Also, the best relative improvement is found for the same blend ratio when SMA8 is added (-47%).

Comparing the values of conditioned binary blends with the respective values in the dry state, an unfavorable FCP behavior becomes evident for all three blend ratios. While *m* tends to be improved, lower ΔK_{th} and ΔK_{cr} are obtained upon introducing humidity, where first is most pronounced with up to -42% in the case of 60:40:10, having the highest PA66 content. This reduction of FCP resistance is in good alignment with the literature, as described by Bretz *et al.* [271] for neat PA66. At water contents of up to 2 wt%, tightly-bound H_2O molecules bridge the hydrogen bonds and thus, plasticize the crystalline phases locally.

Interestingly, the changes upon conditioning of ternary PA66 / PPE / SMA8 blends are not as dramatic as in the binary mixtures. For all three blends, an improvement in *m* (lowered positive slopes) is found with a maximum of -29% for the 40:60:10 blend. In contrast, ΔK_{th} and ΔK_{cr} exacerbate marginally. The detrimental effect of humidity is most pronounced in the threshold region with up to -22% for the 40:60:10 blend. SMA8, present in the PA66 phases as nano-emulsion, is believed to initiate a premature failure of PA66. Nevertheless, it can be concluded that SMA8 is capable of suppressing the negative effect of humidity in the materials, especially in the higher end of stress intensities. This suppression is a positive attribute, helping to improve the sensitivity of PA66 / PPE blends against humidity, fluctuating strongly in the application as thermal breaks in modern door and window frames.

To understand the changes within the considered materials upon compatibilizing and increasing stress intensity factor, fracture surfaces of all blends at conditioned state are depicted in Figures 56-60.

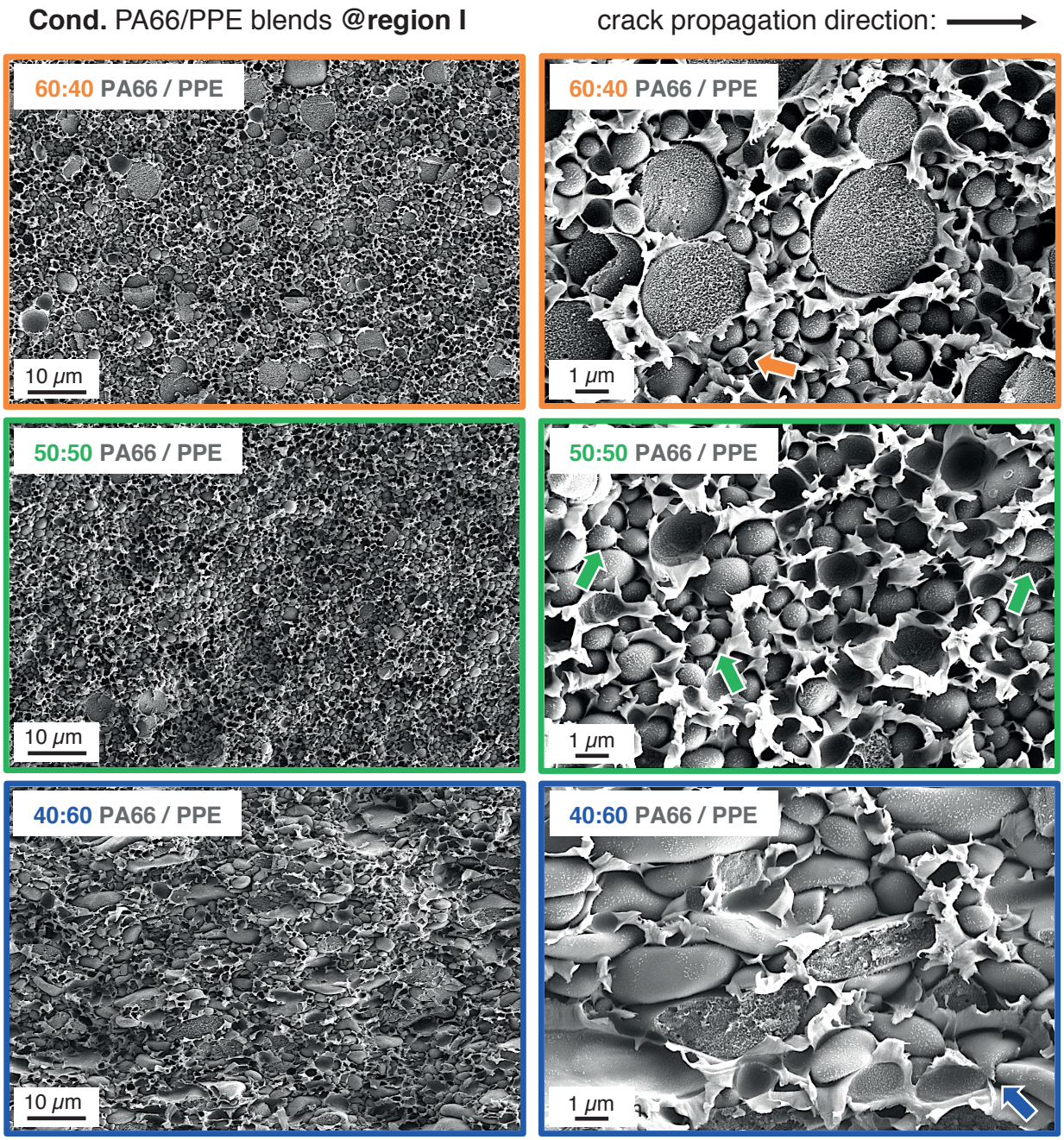

Figure 56 SEM fracture surfaces of FCP tested 60:40, 50:50, and 40:60 w/w PA66 / PPE binary blends (from top to bottom) with respect to da/dN region I at different magnifications (left to right). All considered materials are tested in a conditioned state. The cracks propagate from left to right. The arrows indicate existing elongated PPE domains.

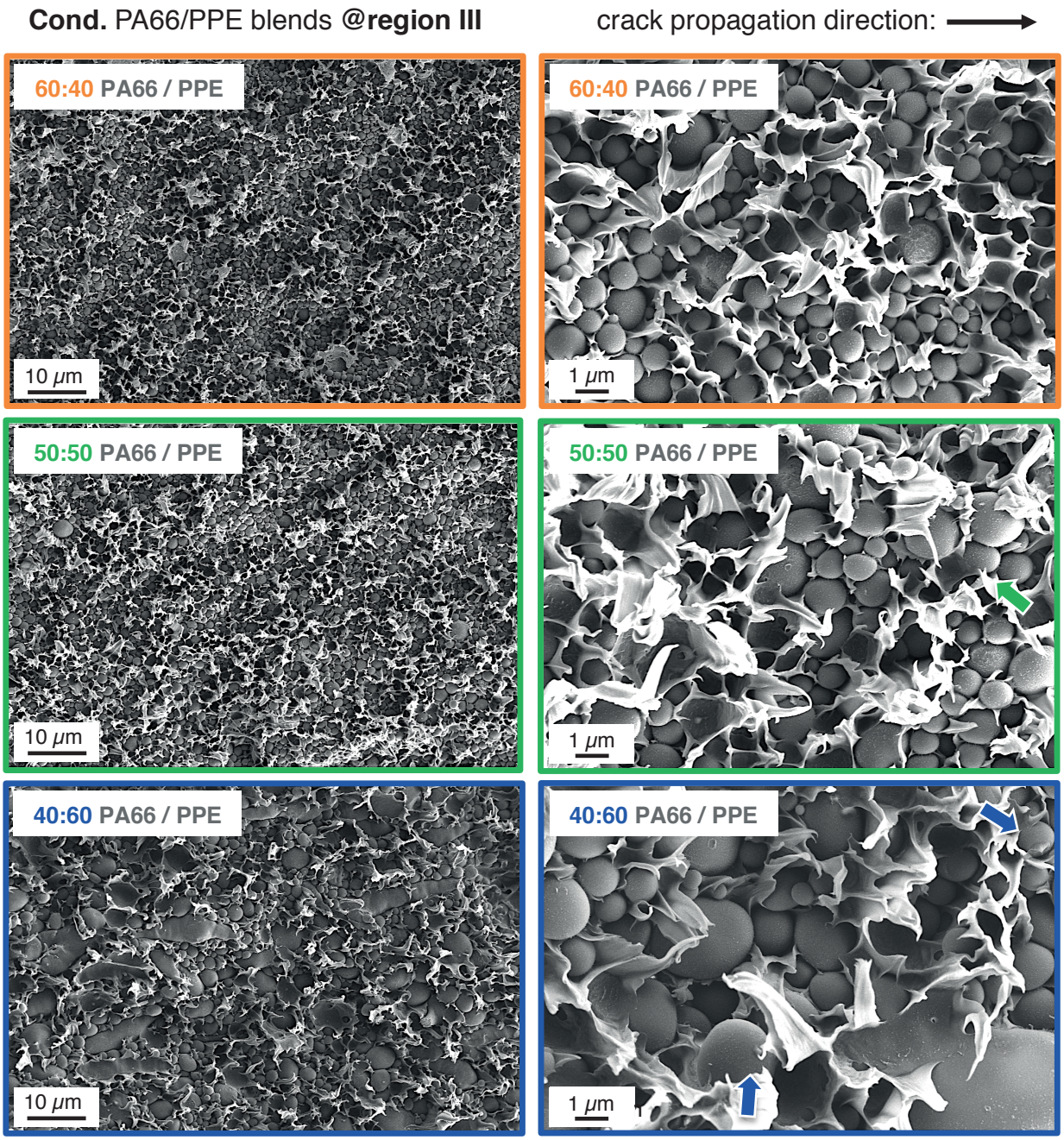

Figure 57 SEM fracture surfaces of FCP tested 60:40, 50:50, and 40:60 w/w PA66 / PPE binary blends (from top to bottom) with respect to da/dN region III at different magnifications (left to right). All considered materials are tested in a conditioned state. The cracks propagate from left to right. The arrows indicate existing elongated PPE domains.

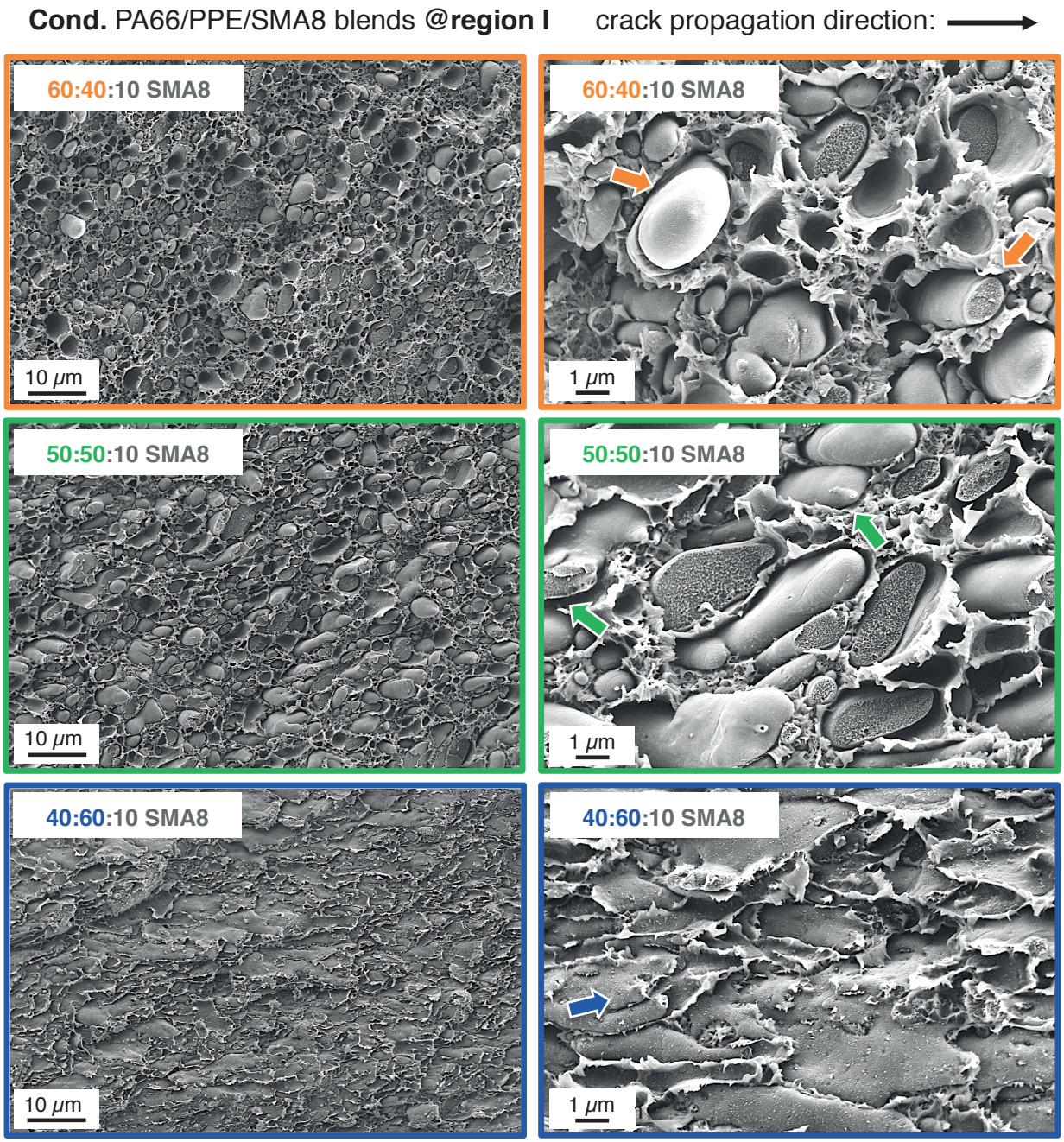

Figure 58 SEM fracture surfaces of FCP tested 60:40:10, 50:50:10, and 40:60:10 w/w PA66 / PPE / SMA8 ternary blends (from top to bottom) with respect to da/dN region I, at different magnifications (left to right). All considered materials are tested in a conditioned state. The cracks propagate from left to right. The arrows indicate existing elongated PPE domains.

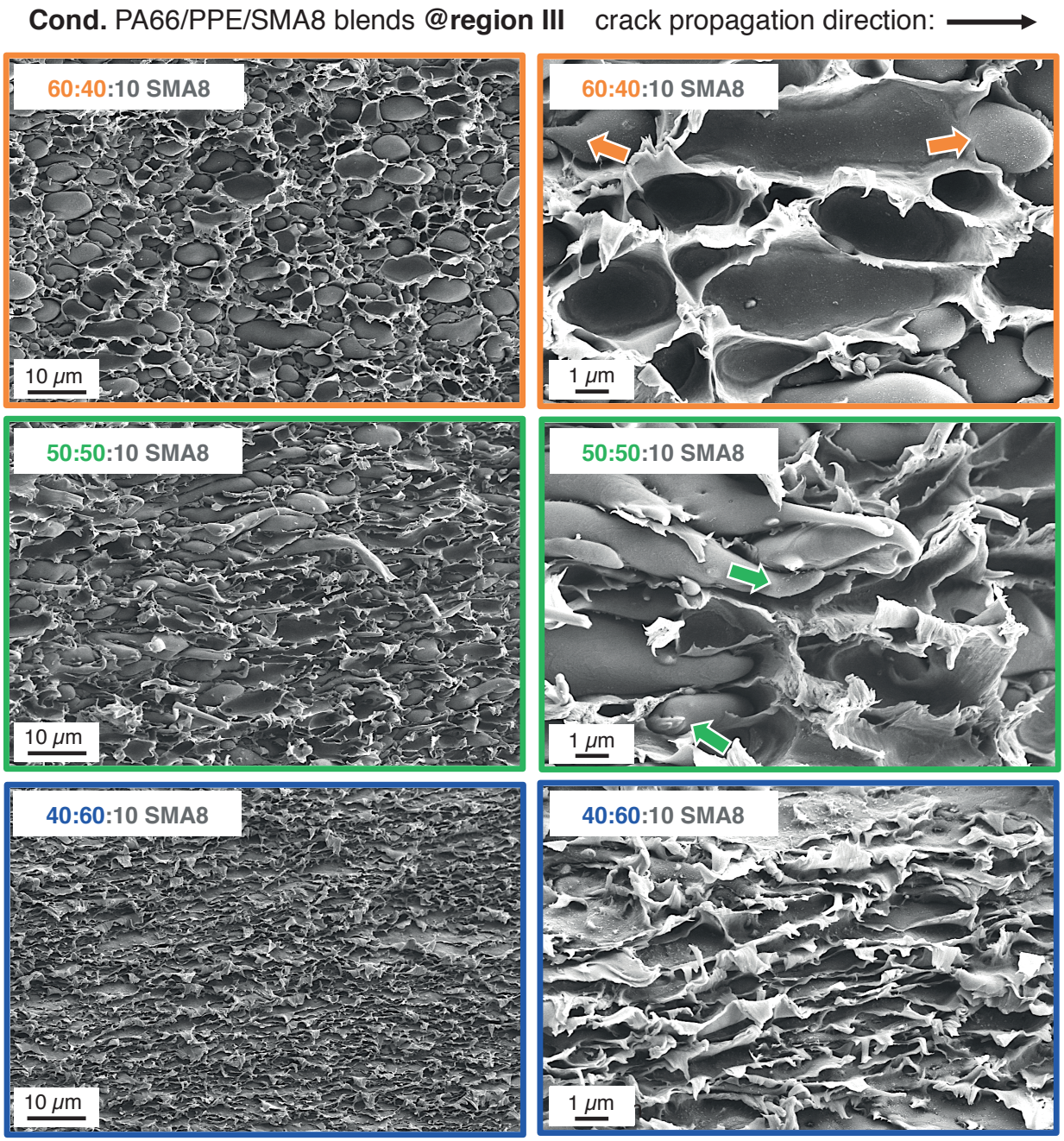

Figure 59 SEM fracture surfaces of FCP tested 60:40:10, 50:50:10, and 40:60:10 w/w PA66 / PPE / SMA8 ternary blends (from top to bottom) with respect to da/dN region III at different magnifications (left to right). All considered materials are tested in a conditioned state. The cracks propagate from left to right. The arrows indicate existing elongated PPE domains.

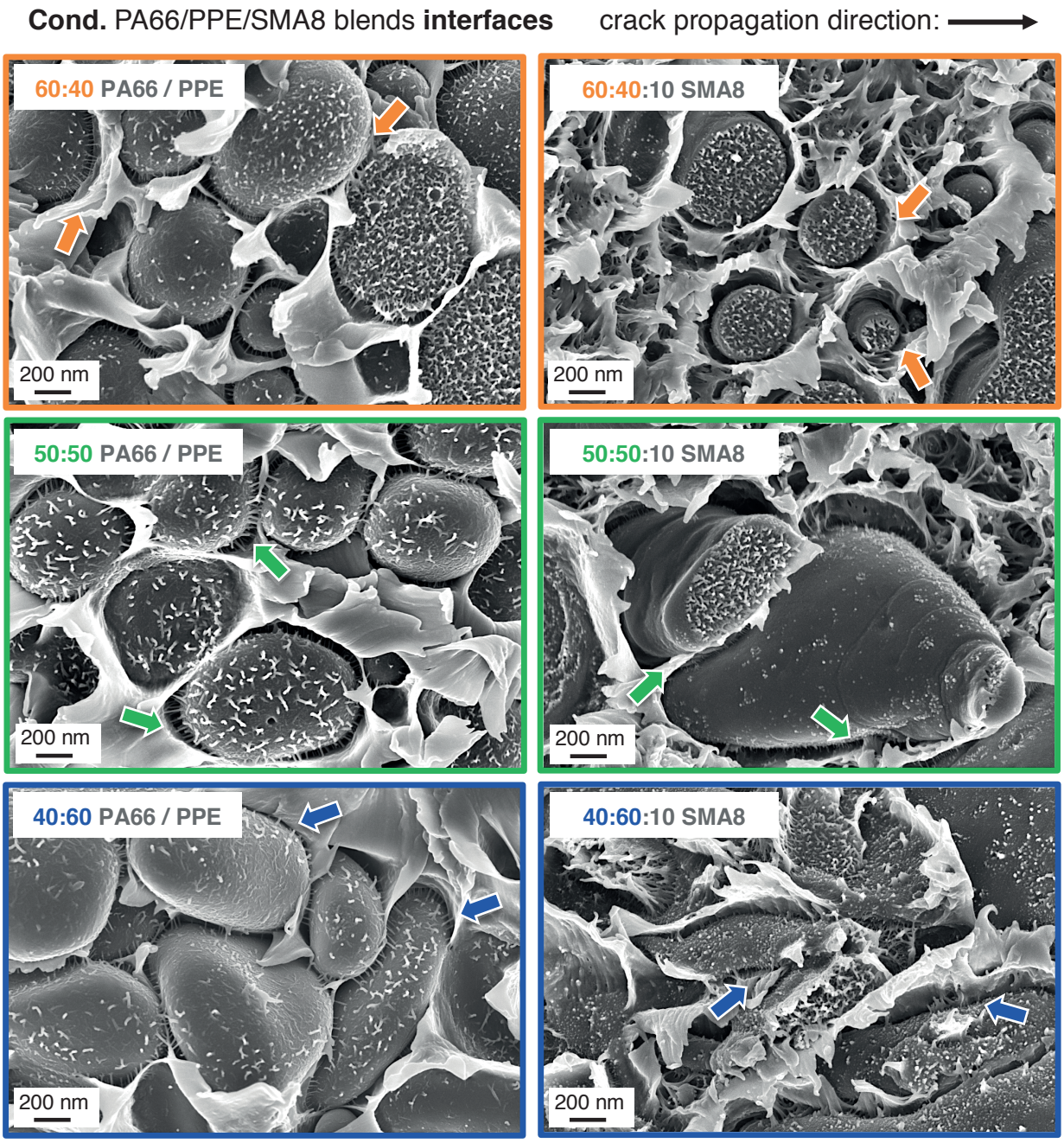

Figure 60 SEM fracture surfaces of FCP tested 60:40, 50:50, and 40:60 w/w PA66 / PPE binary blends (left column) and ternary blends thereof (right column) at very high magnification. All considered materials are tested in a conditioned state. The cracks propagate from left to right. The arrows indicate unruptured elongated interfacial fibrillations.

In Figures 56 and 57, fracture surfaces of the binary PA66 / PPE blends in regions I and III are given in a conditioned state, together with highly-magnified images to highlight local interfacial structures in Figure 60 (left column).

In region I, homogeneous fracture surfaces are seen for 60:40 and 50:50 blends, whereas 40:60 reveals more vigorous agitation by step-like deformations (Fig. 56, left column). From this, a brittle-type fracture behavior can be derived for all three blends, with 40:60 having the highest energy absorption capability, as reflected in the curves in Figure 54. This relation is similar to the behavior of the blends at the dry state. In the images at higher magnification (Fig. 56, right column), all three blends feature the exact deformation mechanism for PA66 as in the dry state, identified as homogeneous deformation zones (yielding). The plasticization of PA66 does not translate into larger lamellae as expected. This behavior indicates that the crack must be propagating preferably through the blend interfaces. Looking at the PPE domains, cavitation, limited tearing (indicated by arrows), and pull-out are mainly found, whereas the latter decreases with increasing PPE content. Again, these observations align with the findings for binary blends in region I at the dry stage.

In the case of 60:40 PA66 / PPE, elongation of PPE domains is very limited. Also, cohesively-failed PPE domains are only visible for the droplets bigger than 3 µm and partially in smaller domains (< 1 µm), as displayed in Figure 60 (left column). The 50:50 w/w blend reveals a larger degree of PPE tearing; however, in exchange for lessened cohesive failure of these domains, compared to 60:40. At the highly-magnified images in Figure 60, very long and thick fibrils and residues of such are seen compared to 60:40, although clearly less in terms of the number. It can be assumed that this difference is the main driver for PPE tearing. However, tearing of PPE is the initial state of cohesively failed domains and therefore does not enable an improved FCP behavior. At greater magnification, the 40:60 blend shows the highest degree of plastic deformation of PPE and lowest degree of cohesive failure within this comparison. The coalesced morphology and the occurring larger domains provide an effective barrier for crack propagation, leading to micro-crack deflections.

Overall, the very smooth PPE surfaces and cavities in PA66 indicate a weakened interfacial strength, with PA66 being plasticized by H_2O. Despite this plasticization, the lamellar ligaments have a comparable degree of elongation to the dry state materials in Figure 49. This means that

the blend interfaces most likely are the weakest links in the materials to enable such interface-dominated fracture, regardless of the blend ratio. Additionally, the contribution of morphology again has a more significant effect than the interfacial bonding strength, clearly higher for 50:50 and 60:40 PA66 / PPE, respectively.

For the binary blends in region III (Fig. 57, left column), slightly roughened fracture surfaces compared to the equivalents in the region I are noticeable, looking almost the same as the surfaces of dry binary blends in region III. A closer look (Fig. 57, right column) reveals that cavitation and pull-out of PPE domains are central deformation mechanisms, whereas elongation of PPE droplets has almost diminished. Only for 50:50 and 40:60 PA66 / PPE such tearing could be identified. Most noticeable is the higher rate of plastic deformation of the PA66 matrix seen in all three blends, expressed by highly-drawn lamellar and fibrillar ligaments compared to region I. This observation is in line with the findings in the dry state and can be attributed to the natural response of PA66 to environments of increased stress. A very distinctive observation again is the appearance of substantial PPE domains in the 40:60 w/w blend. These coalesced PPE domains were described in the dry state to be the main contributor to the resulting FCP properties of this blend, being the best within the comparison of binary mixtures. The same trend applies to the conditioned blends and shows that the domain sizes must still be significantly larger than the plastic zone size, although the latter is expected to grow.

Lastly, fracture surfaces of ternary PA66 / PPE / SMA8 blend in the conditioned state are investigated, as shown in Figures 58 and 59 for regions I and III, respectively. Highly-magnified images provide information on local interfacial interactions in Figure 60 (right column).

The fractographs of the ternary blends in region I (Fig.58) indicate rough fracture surfaces, in which 60:40:10 and 50:50:10 PA66 / PPE / SMA8 are more agitated than their binary blend equivalents, all showing brittle-type failure. Compared to the binary blends in Figure 51, a controversial observation can be made in the case of 40:60:10 w/w, having a smoother fracture surface with SMA8. The morphological overviews of the fracture surfaces already represent the obtained FCP curves well, where 40:60:10 PA66 / PPE / SMA8 has the lowest ΔK_{th} value. In contrast, the other ternary blends are at a higher level (Fig. 54 and 55).

A closer look (Fig. 58, right column) reveals very similar deformation characteristics for 60:40:10 and 50:50:10. Both are governed by a significant number of PPE cavitation, tearing, and subsequently debonding. This coexists with an intermediate degree of cohesive failure, displayed by the residues of massive crazing. The PA66 matrix in both blends seems to have a similar drawing rate of the visible lamellar ligaments. The rigid (PPE swollen) SMA8-g-PA66 micelles in the PA66 phase appear to initiate the matrix deformation, as seen by the small cavities in Figure 60. These micelles create localized stress centers, most likely triggering a crazing-type failure of the PA66 matrix, followed by shear yielding. The crazing mechanism might cause a premature failure of the pseudo-ductile PA66. Unexpectedly, the plasticization of PA66 does not translate into enlarged ligaments, which is a sign of weakened interfacial strength when compared to the ternary blends in the dry state, same as for the binary blends. The second indicator of this weakness is the reduction in the number of cohesively ruptured PPE domains. In the dry state, the PA66 matrix was able to transfer the stress more effectively through the interface, to cause a cohesive rupture of PPE with almost no tearing of the droplets (Fig. 51).

A similar trend is seen for the 40:60:10 blend, where cohesive failure in the dry state turned into an interface-driven crack propagation with significantly reduced energy absorption. The fracture surface features no cohesive PPE failure but a minimal degree of tearing. Only at very high magnification (Fig. 60) rupture of PPE can be observed in sizes of about 200 nm. The level of PA66 deformation appears comparable to the other blend ratios, allowing to neglect the effect of blend morphology on the fracture behavior of PA66 in the conditioned state. It can be concluded that PA66 and its' copolymers (SMA8-g-PA66) at the blend interfaces reveal enhanced chain mobility. Due to this fact, the lowered yield strength of the chains leads to premature rupture at low-stress cyclic loads present in the region I. A comparison of the interfaces in the dry and conditioned state in Figures 53 and 60 reflects this assumption by a significantly weakened interfacial crack bridging.

To investigate the effect of higher cyclic stresses, the morphology of the fracture surfaces of conditioned ternary blends are given in Figure 59 for region III. For all three blends, a roughened fracture is seen, governed by strong plastic deformation of PA66. However, the degree of PA66 deformation seems comparable to the binary equivalents and the ternary blend at dry state in region III, in the case of 60:40:10 and 50:50 mixtures. For 40:60:10, the

development of thin and highly-elongated PA66 lamellae is evident. The very smooth surfaces of PPE domains and PA66 cavities indicate an interface-dominated crack propagation, as reported earlier for the conditioned binary blends and dry ternary blends in region III. Nevertheless, very different underlying failure mechanisms are found in each of the three ternary blends and require an individual discussion.

The tortuous fracture surface of 60:40:10 PA66 / PPE / SMA8 is governed by cavitation, tearing, and severe debonding of the PPE domains. The cavitation and debonding mechanisms seem to be very efficient in the absorption of energy, giving rise to a ΔK_{cr} value comparable but not as good as the dry ternary blend. A lower degree of PPE tearing explains this slight loss in ΔK_{cr} very well, caused by the plasticized and thus weaker blend interface. In the case of the 50:50:10 blend, all the mechanisms mentioned earlier exist, too. However, a more efficient tearing is found and justifies the better performance in the da/dN test compared to 60:40:10 w/w. The PPE domains show intense plastic deformation (yielding) and subsequently crazing only at the cohesively ruptured ends. The observations here align with the blend's failure mechanisms in the dry state. The slightly lower ΔK_{cr} also is a consequence of lowered interfacial strength caused by the interfacial plasticization.

In the case of 40:60:10 PA66 / PPE / SMA8, the crack also propagates through the interface. However, no plastic deformation of PPE is observable. The PPE surfaces are very smooth and do not show very long ruptured fibril residues, indicating a facile propagation of the crack. Compared to the equivalent in the dry state, the PA66 deformation by shear yielding appears more pronounced. The co-continuous structure allows the PA66 to elongate stronger, enabled by a mechanical anchoring mechanism, as also discussed in the tensile tests in Chapter 6.3. Nevertheless, the ability of SMA8 to improve interfacial strength is insufficient to compensate for the effect of morphological changes having very thin co-continuous blend phases.

In summary, all blends face deterioration upon conditioning, regardless of the blend ratio or the existence of the SMA8 compatibilizer. Plasticization is identified as a key influence causing weakened interfacial structures. Additionally, cavitation of (PPE-swollen) SMA8-g-PA66 nano-domains leads to premature failure of PA66. Nevertheless, a higher PA66 content allows a more vital interaction, as stated in the dry state. Another major driving factor is again identified to be the blend morphology. Here, the droplet-sea and DCT morphology of 60:40:10

and 50:50:10 perform better than the co-continuous 40:60:10 blend. Lastly, the introduction of SMA8 not only alters the morphology of the blends but also improves the interfacial strength impressively, which helps to suppress the loss of FCP resistance, especially at higher ends of stress intensity, as given in region III.

6.4.3 Summary

The goal of Chapter 6.4 was to gain a deeper understanding of the interfacial interactions between blend constituents and the resulting mechanical properties in quasi-static (tensile) and dynamic (FCP) testing. Here, the influence of varying H_2O content on changes in the deformation mechanisms was of particular interest. A correlation between findings from all previous sections and this chapter's obtained data was established.

In terms of toughness under quasi-static loading (U_T), three general trends were found related to the introduction of SMA8, blend ratio, and humidity level. Regardless of the last two parameters, SMA8 helped to improve U_T in any case compared to the binary equivalents. Secondly, higher ratios of PA66 gave rise to better U_T values without exception. Thirdly, different responses to humidity in binary and ternary blends have been detected. In the binary blends, increasing U_T was found upon introducing moisture (~ 1 wt% H_2O). As only PA66 is affected by humidity, the effect is enhanced with increasing PA66 content. The humidity plasticizes the PA66 phases by bridging the existing hydrogen bonds between the polymer chains. This gives rise to a lowered stress uptake but simultaneously significantly enhances strain behavior, leveraging the toughness. In the ternary blends, this effect could only be found in the PA66-rich 60:40:10 w/w blend. In the other two cases, a reduction of U_T was seen, being linked to the change in their morphology from dispersed-to-co-continuous (DCT) to co-continuous for 50:50:10 and 40:60:10 PA66 / PPE / SMA8, respectively.

Regarding fatigue crack propagation (FCP) properties, the blends revealed very different responses depending on their state of conditioning. Neglecting the influence of humidity, general trends were identified, which are: 1) for binary blends, 40:60 PA66 / PPE always performs best; 2) the blends at 60:40 PA66 / PPE ratio, both binary and ternary have a very similar FCP resistance; 3) The use of SMA8 deteriorates the properties of 40:60:10 significantly; 4) SMA8 improves the interfacial strength of all blends. Regarding the first, very

large PPE domains were found in at least two dimensions, which is the driver for the exceptional FCP resistance. Concerning the second, the 50:50 PA66 / PPE blend ratio-based binary and ternary blends were identified as closer to 60:40 than to the 40:60 blend ratio in terms of morphology, although in ternary systems, 50:50:10 (DCT) did derive from a droplet-sea structure as reported for 60:40:10 PA66 / PPE / SMA8. Third, SMA8 altered the 40:60 w/w blend morphology from coalesced droplet-sea with coarse domain distribution to a very finely and homogeneously structured co-continuous morphology. Fourth, SMA8 was described as highly-active in the interface between PA66 and PPE in all previous sections. Also, SMA8 can increase the interfacial adhesion by very pronounced crack bridging, shown by intense fibrillations. Additionally, the nano-sized inclusions in the PA66 helped to improve the matrix, as in the concept of rigid nanoparticle toughening [228,315,316].

In the conditioned state, all blends, binary and ternary, encountered a reduction in FCP resistance. On the binary level, a left-shift of the curves was observed, whereas, on the ternary level, the shift was not as monotonic. While a substantial improvement in region II was present, expressed by a lowered slope (*m*), the threshold (region I) was strongly shifted to lower values. At critical stress level (region III), the left-shift appeared to be relatively low. Premature failure of the PA66 phases has been identified as the lead cause of deteriorated threshold values enabled by SMA8-g-PA66 nano-domains within the PA66. The rigid domains cavitate and initiate a crack formation in PA66 by crazing. Aside from this, higher PA66 contents allow better interfacial interaction and, with that, better FCP results.

After all, the size of existing structures is the most crucial factor, as shown in the 40:60 w/w blends very impressively. While the binary 40:60 PA66 / PPE with its' large domains performed best, the ternary blend with 10 wt% SMA8 performed worst in both, dry and wet states. The ideal blend can be described as an SMA8-containing ternary mixture with a droplet-sea morphology, having some degree of larger PPE domains distributed in the PA66 matrix.

An overview summarizing the FCP properties of all blend ratios at dry and conditioned state is visible in Table 12.

Table 12 Consolidated FCP data of SMA8-compatibilized PA66 / PPE blends at 60:40, 50:50, and 40:60 w/w blend ratio in dry and humid conditions.

	Threshold stress intensity factor (ΔK_{th}) [MPa•m$^{0.5}$]		**Slope of linear regime (m) [mm/cycle]**		**Critical stress intensity factor (ΔK_{cr}) [MPa•m$^{0.5}$]**	
	Dry	Cond.	Dry	Cond.	Dry	Cond.
60:40	0.62 ± 0.02	0.43 ± 0.01	8.29 ± 0.31	8.85 ± 0.45	1.26 ± 0.03	0.95 ± 0.04
60:40:10	0.58 ± 0.01	0.50 ± 0.03	6.04 ± 0.23	5.93 ± 0.88	1.46 ± 0.01	1.25 ± 0.03
50:50	0.61 ± 0.05	0.42 ± 0.01	10.82 ± 1.44	9.74 ± 0.90	1.12 ± 0.06	0.91 ± 0.03
50:50:10	0.61 ± 0.05	0.52 ± 0.03	7.59 ± 0.68	6.65 ± 0.69	1.45 ± 0.10	1.36 ± 0.04
40:60	0.68 ± 0.03	0.51 ± 0.06	8.81 ± 0.69	8.37 ± 0.22	1.46 ± 0.06	1.23 ± 0.14
40:60:10	0.49 ± 0.06	0.40 ± 0.02	7.50 ± 1.01	5.79 ± 0.66	1.31 ± 0.09	1.16 ± 0.02

7 Summary

PA-based PPE blends have been identified to have great potential in several applications, such as automotive exterior parts or thermal breaks in modern windows and door frames. SMA copolymers have experienced great academic interest to compatibilize the blends; however, PPE in combination with PA66 has not been studied in detail. The main objective of this thesis was to create structure-property relationships for SMA-compatibilized PA66 / PPE blends. These relationships were used to identify an optimal blend composition with maximum improved properties suitable for applications such as thermal breaks. The immiscible PA66 / PPE blend gives rise to macro phase separation, depending on the weight ratio. Given the vast viscosity difference (PPE very high; PA66 low), the system forms a stable droplet-sea structure with a PA66 matrix up to 60 wt PPE. At 70 wt%, a continuous structure of both polymers is found. Different SMA types with varying maleic anhydride (MA) concentration and structure reveal different interactions with the individual blend polymers. Other than SMA4 and SMA 24, complete miscibility between PPE and SMA8 is seen. In PA66, however, all SMA types are immiscible but react with the PA66 strongly with increasing MA concentration and forming nano-sized droplets.

SMA8 is defined as an ideal candidate for reactivity with PA66 and miscibility in PPE, leading to an efficient localization at the blend interface. Regarding morphology, SMA4 blends remain as droplet-sea structures even at 10 wt% addition in the 50:50 w/w PA66 / PPE blend. SMA8 displays a disperse-to-co-continuous morphology (DCT) at 10 wt%, whereas SMA24 completed the transition to have full co-continuity. All SMA copolymers show nano-sized inclusions in the PA66 phase, similar to the binary PA66 / SMA blends. Yet, SMA8 inclusions differ in size compared to the binary system proving the existence of swollen SMA8-g-PA66 copolymers with PPE cores. The interfacial activity of SMA8 improved the mechanical properties most effectively, resulting in the best tensile properties. This enhancement is attributed to a superior interfacial interaction displayed by an extensive crack bridging mechanism, proven by unruptured fibrillations and plastic deformation of PPE. Differences in blend morphology and mechanical properties also depend on the ratio of PA66 / PPE. Higher PA66 content (60:40 w/w) stabilizes the droplet-sea morphology, even at 10 wt% SMA8, whereas 40:60 PA66 / PPE reaches full co-continuity at the highest SMA8 content of 10 wt%.

The nano-emulsions in PA66 have also been identified to correlate with the PPE content, where larger emulsions are found with increasing PPE amount. The mechanical properties are directly related to the PA66 content, increasing with increasing PA66. The droplet-sea morphology again provides the best mechanical performance in tensile tests. Same as for 50:50 blend ratio, an SMA8 addition of 10 wt% results in best tensile properties.

The sensitivity of PA66 to humidity requires investigating blend properties not only in a dry state (< 0.2 wt% H_2O) but also in a conditioned state (~ 1.0 wt% H_2O), being closer to targeted applicating facing fluctuating atmospheric influences. The quasi-static toughness of binary blends reveals a direct dependence on PA66, declining with decreasing PA66 ratio. This dependence does not alter upon conditioning of the binary blends, where H_2O plasticizes PA66. The H_2O is interfering with the hydrogen bonds between PA66 chains, causing a reduction of stress absorption at the simultaneous improvement of strain behavior. This effect in the ternary blends is only observed in the 60:40:10 PA66 / PPE / SMA8 with a droplet-sea morphology. In the other two blends, the change in morphology significantly influences the quasi-static toughness, resulting in lowered values upon conditioning. Under cyclic loading, the effect of morphology again overrules the positive influence of higher PA66 contents. The existence of very large PPE domains (~ 50 µm) in the binary 40:60 w/w blend results in best fatigue crack propagation (FCP) values irrespective of the moisture level of the materials. The conditioning of both binary and ternary blends gives rise to a lower FCP performance by the mentioned plasticization effect of the PA66 phase. The use of SMA8, however, suppresses the detrimental effect of introduced humidity in the materials, especially in the region of critical crack propagation (higher end of stress intensity). The suppression, combined with an improved slope (m) in region II, is attributed to the enhancement of the blend interfaces, justified by substantial crack bridging and thus, stress transfer between the blend phases.

Summarizing all findings, a blend composition of 60:40:10 PA66 / PPE / SMA8 provides the best mechanical performance in quasi-static and dynamic loadings, combined with a droplet-sea morphology. While the improvement in mechanical resistance provides more flexibility in the product design, the morphology guarantees high stability to thermal and chemical stresses.

8 Zusammenfassung

PA / PPE-Blends haben aus industrieller Sicht ein großes Potenzial in verschiedensten Anwendungen, wie z.B. in Fahrzeuganbauteilen oder Wärmedämmstegen in modernen Fensterrahmen gezeigt. Aufgrund der Unverträglichkeit von PA und PPE ist es jedoch zwingend notwendig einen Verträglichkeitsvermittler einzusetzen, welcher die mechanischen Eigenschaften des Blendsystems wesentlich beeinflusst. Insbesondere SMA-Copolymere zeigten sich in der akademischen Literatur als vielseitig einsetzbar. In Verbindung mit PA66 und PPE wurden vereinzelte, jedoch keine systematischen Untersuchungen veröffentlicht. Das Hauptziel dieser Arbeit war es deshalb, Struktur-Eigenschafts-Beziehungen für SMA-kompatibilisierte PA66 / PPE-Mischungen herzustellen. Mithilfe dieser Beziehungen sollte eine optimale Mischungszusammensetzung mit maximal verbesserten Eigenschaften ermittelt werden.

Die Unverträglichkeit der PA66 / PPE-Mischung führt zur Phasenseparation auf makroskopischer Ebene, welche in ihrer Form stark vom Gewichtsverhältnis beider Polymere abhängt. Angesichts des großen Viskositätsunterschieds (PPE sehr hoch, PA66 niedrig) bildet das System bis zu 60 Gew.-% PPE eine stabile Tröpfchenmorphologie aus, bei der PPE verteilt in einer PA66-Matrix vorliegt. Die Tröpfchen variieren je nach PPE-Gehalt in ihrer Form und Größe. Bei 70 Gew.-% PPE wird eine Morphologieänderung hin zu einer co-kontinuierlichen Struktur der beiden Polymere vorgefunden.

SMA-Copolymere werden hauptsächlich der molekularen Masse und dem Maleinsäureanhydrid (MA)-Gehalt unterschieden. Die Wechselwirkung zwischen unterschiedlichen SMA-Typen und den Blendpolymeren stellt eine wichtige Basisinformation dar, um darauffolgend richtige Schlüsse ziehen zu können. Von den drei untersuchten SMAs wurde nur bei SMA8 eine vollständige Mischbarkeit in PPE festgestellt. In PA66 hingegen sind alle drei SMA-Typen nicht mischbar, wechselwirken aber mit zunehmendem MA-Gehalt zunehmend stark mit dem PA66. Alle SMAs liegen als nanoskalige Tröpfchen im PA66 vor. Das SMA8 erwies sich als idealen Verträglichkeitsvermittler, da sowohl eine Mischbarkeit in PPE, als auch eine balancierte Reaktivität mit PA66 ermittelt wurde. Dieses ausgewogene

Verhalten führte dazu, dass SMA8 vorwiegend an den Grenzflächen zwischen PA66 und PPE vorgefunden wurde.

Die Morphologie der Blends zeigte erneut deutliche Unterschiede in Abhängigkeit des SMA-Typs festgestellt. Die Tröpfchenmorphologie der PA66 / PPE Blends blieb über die gesamte Konzentrationsreihe von SMA4 unverändert, während mit SMA8 ein Übergang zu einer co-kontinuierlichen Struktur bei 10 Gew.-% vorlag. Dieser Übergang wurde mit SMA24 schon bei 7,5 Gew.-% festgestellt und bei 10 Gew.-% in Form einer vollständigen co-Kontinuität abgeschlossen. Alle SMA-Typen führten wie schon in den binären PA66 / SMA Mischungen erneut zu nanoskaligen Einschlüssen. Unter Verwendung von SMA8 wurden Domänen mit deutlicher Abweichung in ihrer Größe beobachtet. Diese Veränderung konnte auf eine Quellung der SMA8-g-PA66 Copolymer-Mizellen durch PPE zurückgeführt werden. Diese erhöhte Grenzflächenaktivität von SMA8 zeigte sich auch in Bezug auf die zugmechanischen Eigenschaften als vorteilhaft, womit die höchsten Messerwerte erzielt werden konnten. Diese Verbesserung wurde durch einen ausgeprägten Rissüberbrückungsmechanismus ermöglicht, gekennzeichnet durch ein teilweise intaktes Netzwerk an fibrillaren Strukturen und einer ausgeprägten plastischen Verformung der PPE-Phasen.

Diese beschriebenen Wechselwirkungen zwischen Morphologie und den mechanischen Eigenschaften hängen auch stark vom Mischungsverhältnis der beiden Polymere PA66 und PPE ab. Während ein hoher PA66-Anteil (60:40 m/m) die Tröpfchenmorphologie stets beibehielt, wurde bei 40:60 PA66 / PPE eine co-kontinuierliche Anordnung ab 10 Gew.-% SMA8 vorgefunden. Zudem wurde nachgewiesen, dass die Nanoemulsionen in der PA66-Phase mit dem PPE-Gehalt korrelieren, wobei mit zunehmendem PPE-Anteil größere Emulsionsteilchen gefunden wurden. Die mechanischen Eigenschaften stehen in direktem Zusammenhang mit dem PA66 und nehmen mit steigendem PA66-Gehalt zu. Die Tröpfchenmorphologie ermöglichte wiederum die besten mechanischen Kenndaten in den Zugversuchen (60:40 PA66 / PPE). Wie beim Mischungsverhältnis 50:50 führt auch hier ein SMA8-Zusatz von 10 Gew.-% zu den besten Zugeigenschaften.

Durch das feuchteabhängige Materialverhalten von PA66 ist eine Untersuchung der mechanischen Eigenschaften nicht nur im trockenen (< 0,2 Gew.-% H_2O), sondern auch im konditionierten Zustand (~ 1,0 Gew.-% H_2O) essentiell. Grund hierfür ist die Anwendung

dieser Materialien in Umgebungen schwankender Temperatur und Feuchtigkeit, wie z.B. Wärmedämmstege in modernen Aluminiumfenstern oder in Automobilanbauteilen.

Die quasistatische Zähigkeit der binären Blends zeigte eine direkte Abhängigkeit vom PA66, welche mit abnehmendem PA66-Anteil abnimmt. Dieses Muster änderte sich auch durch vorherige Konditionierung der Mischungen nicht. Das H_2O schwächt die Wasserstoffbrückenbindungen zwischen den PA66-Ketten, was zu einer Verringerung der Festigkeit bei gleichzeitiger Verbesserung des Dehnungsverhaltens führt. Dieser Effekt wurde bei den ternären Blends nur bei 60:40:10 PA66 / PPE / SMA8 mit einer Tröpfchenmorphologie beobachtet. Bei den anderen beiden Mischungsverhältnissen beeinflusste die Änderung der Morphologie die quasistatische Zähigkeit weitaus stärker, was sich durch deutlich reduzierte Messwerte bei vorher konditionierten Proben kenntlich machte.

Unter zyklischer Beanspruchung überwog der Morphologie-Effekt wiederum dem positiven Einfluss des höheren PA66-Gehalts. Das Vorhandensein sehr großer PPE-Domänen (~ 50 µm) in der binären 40:60 PA66 / PPE Mischung führte – unabhängig vom Feuchtigkeitsgehalt der Materialien – zu den besten Werten in Ermüdungsrissausbreitungsversuchen (FCP). Die Konditionierung sowohl der binären als auch der ternären Mischungen führte durch den erwähnten Plastifizierungseffekt der PA66-Phase zu einer geringeren FCP-Leistung. Mit Verwendung des SMA8 konnten in allen Mischungen nachteilige Auswirkungen der eingebrachten Feuchtigkeit, insbesondere im Bereich der kritischen Rissausbreitung (höheres Ende der Spannungsintensität), kompensiert werden. Gleichzeitig wurde auch eine Verbesserung in der Steigung (m) in Region II festgestellt. Alle diese Effekte wurden auf die Optimierung der Grenzflächen zurückgeführt, welche durch starke Rissüberbrückungs- und damit Spannungsübertragungs-Mechanismen zwischen den Blend-Phasen begründet ist.

Zusammenfassend lässt sich sagen, dass eine Blendzusammensetzung von 60:40:10 PA66 / PPE / SMA8 die besten mechanischen Eigenschaften sowohl bei quasistatischen, als auch dynamischen Belastungen in Verbindung mit einer Tröpfchenmorphologie zeigte. Während die Verbesserung der Widerstandsfähigkeit unter mechanischer Belastung mehr Freiheiten bei der Produktgestaltung ermöglicht, garantiert die gegebene Tröpfchenmorphologie eine ausgewiesene Stabilität gegenüber thermischen und chemischen Belastungen.

9 Outlook

SMA copolymers are already known for many years in academia and industry. The use as a compatibilizer for PA-based blends was mentioned in 1988 for the first time [317]. Although studied intensively in various PA-based blends together with PPE, a systematic analysis of (im-)miscible SMAs (SMA8 and SMA24) for PA66 / PPE blends have only been performed by the author of this thesis. Based on SMA, new polymers by adding n-phenyl maleimide (Styrene-maleic anhydride-n-phenyl maleimide terpolymer) have been investigated since the 90s [281,282,318,319]. Despite the commercial existence of such terpolymers, only two publications are found to have used such as a blend compatibilizer, namely PC / ABS [117] and PA6 / ABS in 3D printing [283]. This thesis has shown that, even though not miscible in PPE, the SMA terpolymer (SMA4) gave rise to excellent mechanical properties, being close to the best performing SMA8 (Chapter 6.2). This fact creates an interest in studying this type of compatibilizer further. The commercial availability of such terpolymers is limited to two companies, namely Denka and Polyscope, which offer one and five grades, respectively. Selected properties of the terpolymers are listed in Table 13. Unfortunately, the manufacturers do not fully disclose information on the molecular composition of the terpolymers, thus requiring extensive analysis to obtain such data [319].

Interestingly, Polyscope offers terpolymers in very close molecular weight ranges, making it very attractive for a systematic scientific investigation within PA66 / PPE blends. Higher n-phenyl maleimide monomer contents lead to higher glass transition temperatures and thermal stabilities [282]. With this, the thermal resistance of the resulting blends can also be part of future investigations.

Table 13 Selected properties of commercial SMA terpolymers [f,g]. Monomer contents of Xiran® IZ1018M and Xiran® IZ0721M have been calculated from molar ratios given in the references for better comparison.

			Polyscope			Denka
	Xiran® IZ1018M	Xiran® IZ0721M	Xibond® 315	Xibond® 330	Xibond® 370	Denka IP MS-CP
Molecular weight (M_w) [kg/mol]	145	135	155	155	150	-
Anhydride content [wt%]	11.4	7.4	1.8	5.3	7.2	-
Styrene content [wt%]	77.0	71.7	-	-	-	-
N-phenyl maleimide content [wt%]	11.6	12.6	-	-	-	-
Glass transition temperature (T_g) [°C]	175	178	180	180	175	196

10 Bibliography

[1] Miyata, K., Christie, R.J., Kataoka, K., Polymeric micelles for nano-scale drug delivery. *React. Funct. Polym.* **2011**, 71, 227–234. doi:10.1016/j.reactfunctpolym.2010.10.009

[2] Xin, H., Reid, O.G., Ren, G., Kim, F.S., Ginger, D.S., Jenekhe, S.A., Polymer Nanowire/Fullerene Bulk Heterojunction Solar Cells: How Nanostructure Determines Photovoltaic Properties. *ACS Nano*. **2010**, 4, 1861–1872. doi:10.1021/nn9014906

[3] Schacher, F.H., Rupar, P.A., Manners, I., Functional Block Copolymers: Nanostructured Materials with Emerging Applications. *Angew. Chemie Int. Ed.* **2012**, 51, 7898–7921. doi:10.1002/anie.201200310

[4] Tang, Z., He, C., Tian, H., Ding, J., Hsiao, B.S., Chu, B., Chen, X., Polymeric nanostructured materials for biomedical applications. *Prog. Polym. Sci.* **2016**, 60, 86–128. doi:10.1016/j.progpolymsci.2016.05.005

[5] Stuart, M.A.C., Huck, W.T.S., Genzer, J., Müller, M., Ober, C., Stamm, M., Sukhorukov, G.B., Szleifer, I., Tsukruk, V. V., Urban, M., Winnik, F., Zauscher, S., Luzinov, I., Minko, S., Emerging applications of stimuli-responsive polymer materials. *Nat. Mater.* **2010**, 9, 101–113. doi:10.1038/nmat2614

[6] Zhu, W., Bartos, P.J.M., Porro, A., Application of nanotechnology in construction. *Mater. Struct.* **2004**, 37, 649–658. doi:10.1007/BF02483294

[7] Okolieocha, C., Beckert, F., Herling, M., Breu, J., Mülhaupt, R., Altstädt, V., Preparation of microcellular low-density PMMA nanocomposite foams: Influence of different fillers on the mechanical, rheological and cell morphological properties. *Compos. Sci. Technol.* **2015**, 118, 108–116. doi:10.1016/j.compscitech.2015.08.016

[8] Handge, U.A., Hedicke-Höchstötter, K., Altstädt, V., Composites of polyamide 6 and silicate nanotubes of the mineral halloysite: Influence of molecular weight on thermal, mechanical and rheological properties. *Polymer.* **2010**, 51, 2690–2699. doi:10.1016/j.polymer.2010.04.041

[9] Kausar, A., Rafique, I., Muhammad, B., Aerospace Application of Polymer Nanocomposite with Carbon Nanotube, Graphite, Graphene Oxide, and Nanoclay. *Polym. Plast. Technol. Eng.* **2017**, 56, 1438–1456. doi:10.1080/03602559.2016.1276594

[10] Bull, S.J., Multifunctional polymer nanocomposites for industrial applications, in: P.J. Brown, K. Stevens (Eds.), Nanofibers Nanotechnol. Text., Elsevier, **2007**: pp. 256–280. doi:10.1533/9781845693732.2.256

[11] Zhao, X., Lv, L., Pan, B., Zhang, W., Zhang, S., Zhang, Q., Polymer-supported nanocomposites for environmental application: A review. *Chem. Eng. J.* **2011**, 170, 381–394. doi:10.1016/j.cej.2011.02.071

[12] Garcés, J.M., Moll, D.J., Bicerano, J., Fibiger, R., McLeod, D.G., Polymeric Nanocomposites for Automotive Applications. *Adv. Mater.* **2000**, 12, 1835–1839. doi:10.1002/1521-4095(200012)12:23<1835::AID-ADMA1835>3.0.CO;2-T

[13] Müller, A.H.E., Schmidt, H.-W., Complex Macromolecular Systems I, Springer Berlin Heidelberg, **2010**, ISBN:978-3-642-12875-2. doi:10.1007/978-3-642-12876-9

[14] Robeson, L.M., Applications of polymer blends: Emphasis on recent advances. *Polym. Eng. Sci.* **1984**, 24, 587–597. doi:10.1002/pen.760240810

[15] Ploypetchara, N., Suppakul, P., Atong, D., Pechyen, C., Blend of Polypropylene/Poly(lactic acid) for Medical Packaging Application: Physicochemical, Thermal, Mechanical, and Barrier Properties. *Energy Procedia*. **2014**, 56, 201–210. doi:10.1016/j.egypro.2014.07.150

[16] Pivsa-Art, W., Pavasupree, S., O-Charoen, N., Insuan, U., Jailak, P., Pivsa-Art, S., Preparation of Polymer Blends Between Poly (L-Lactic Acid), Poly (Butylene Succinate-Co-Adipate) and Poly (Butylene Adipate-Co-Terephthalate) for Blow Film Industrial Application. *Energy Procedia*. **2011**, 9, 581–588. doi:10.1016/j.egypro.2011.09.068

[17] Verma, A., Budiyal, L., Sanjay, M.R., Siengchin, S., Processing and characterization analysis of pyrolyzed oil rubber (from waste tires)-epoxy polymer blend composite for lightweight structures and coatings applications. *Polym. Eng. Sci.* **2019**, 59, 2041–2051. doi:10.1002/pen.25204

[18] Kuncser, V., Miu, L., Size Effects in Nanostructures, Springer Berlin Heidelberg, **2014**, ISBN:978-3-662-44478-8. doi:10.1007/978-3-662-44479-5

[19] Gleiter, H., Nanostructured materials: basic concepts and microstructure. *Acta Mater.* **2000**, 48, 1–29. doi:10.1016/S1359-6454(99)00285-2

[20] Wang, J., Huang, Z., Duan, H., Yu, S., Feng, X., Wang, G., Zhang, W., Wang, T., Surface stress effect in mechanics of nanostructured materials. *Acta Mech. Solida Sin.* **2011**, 24, 52–82. doi:10.1016/S0894-9166(11)60009-8

[21] Kryszewski, M., Gałęski, A., Martuscelli, E., Polymer Blends, Springer US, **1984**, ISBN:978-1-4899-1833-8. doi:10.1007/978-1-4899-1831-4

[22] Wang, K., Chen, F., Li, Z., Fu, Q., Control of the hierarchical structure of polymer articles via "structuring" processing. *Prog. Polym. Sci.* **2014**, 39, 891–920. doi:10.1016/j.progpolymsci.2013.05.012

[23] Yang, Z., Nollenberger, K., Albers, J., Craig, D., Qi, S., Microstructure of an Immiscible Polymer Blend and Its Stabilization Effect on Amorphous Solid Dispersions. *Mol. Pharm.* **2013**, 10, 2767–2780. doi:10.1021/mp400209w

[24] Ciardelli, F., Penczek, S., Modification and Blending of Synthetic and Natural Macromolecules, Springer Netherlands, Dordrecht, **2004**, ISBN:978-1-4020-2733-8. doi:10.1007/978-1-4020-2735-2

[25] Cummins, C., Lundy, R., Walsh, J.J., Ponsinet, V., Fleury, G., Morris, M.A., Enabling future nanomanufacturing through block copolymer self-assembly: A review. *Nano Today*. **2020**, 35, 100936. doi:10.1016/j.nantod.2020.100936

[26] Kim, J.K., Yang, S.Y., Lee, Y., Kim, Y., Functional nanomaterials based on block copolymer self-assembly. *Prog. Polym. Sci.* **2010**, 35, 1325–1349. doi:10.1016/j.progpolymsci.2010.06.002

[27] Yan, Q., Zhao, Y., Block copolymer self-assembly controlled by the "green" gas stimulus of carbon dioxide. *Chem. Commun.* **2014**, 50, 11631–11641. doi:10.1039/C4CC03412K

[28] Yan, L.-T., Popp, N., Ghosh, S.-K., Böker, A., Self-Assembly of Janus Nanoparticles in Diblock Copolymers. *ACS Nano*. **2010**, 4, 913–920. doi:10.1021/nn901739v

[29] Ott, H., Abetz, V., Altstädt, V., Thomann, Y., Pfau, A., Comparative study of a block copolymer morphology by transmission electron microscopy and scanning force microscopy. *J. Microsc.* **2002**, 205, 106–108. doi:10.1046/j.0022-2720.2001.00975.x

[30] Li, N., Nikoubashman, A., Panagiotopoulos, A.Z., Self-Assembly of Polymer Blends and Nanoparticles through Rapid Solvent Exchange. *Langmuir*. **2019**, 35, 3780–3789. doi:10.1021/acs.langmuir.8b04197

[31] Xu, G.-K., Feng, X.-Q., Li, Y., Self-Assembled Nanostructures of Homopolymer and Diblock Copolymer Blends in a Selective Solvent. *J. Phys. Chem. B*. **2010**, 114, 1257–1263. doi:10.1021/jp908823h

[32] Kim, S.H., Misner, M.J., Russell, T.P., Solvent-Induced Ordering in Thin Film Diblock Copolymer/Homopolymer Mixtures. *Adv. Mater.* **2004**, 16, 2119–2123. doi:10.1002/adma.200306577

[33] Kim, J.Y., Jin, H.M., Jeong, S.-J., Chang, T., Kim, B.H., Cha, S.K., Kim, J.S., Shin, D.O., Choi, J.Y., Kim, J.H., Yang, G.G., Jeon, S., Lee, Y.-G., Kim, K.M., Shin, J., Kim, S.O., Bimodal phase separated block copolymer/homopolymer blends self-assembly for hierarchical porous metal nanomesh electrodes. *Nanoscale*. **2018**, 10, 100–108. doi:10.1039/C7NR07178G

[34] Elbert, B., Wagner, D., Tailor-Made for Special Cases. *Kunststoffe Int.* **2015**, 52–55

[35] Nießner, N., Breiner, U., Grefenstein, A., Material Class with Wide Application: Styrene Polymers. *Kunststoffe Int.* **2001**, 104–106

[36] Gahleitner, M., Tranninger, C., Doshev, P., Heterophasic copolymers of polypropylene: Development, design principles, and future challenges. *J. Appl. Polym. Sci.* **2013**, 130, 3028–3037. doi:10.1002/app.39626

[37] Kloos, F., Strouk, H., Uebe, R., Heufer, G., Untersuchung praxisrelevanter Eigenschaften von PP-Blends. *Angew. Makromol. Chemie*. **1991**, 185, 97–108. doi:10.1002/apmc.1991.051850110

[38] Paulik, C., Gahleitner, M., Neißl, W., Weiche, zähelastische PP-Copolymere. *Kunststoffe*. **1996**, 97–100

[39] Han, C.D., Rheology and Processing of Polymeric Materials: Volume 2: Polymer Processing, Oxford University Press, **2006**, ISBN:9780195187830. doi:10.1093/oso/9780195187830.001.0001

[40] An, F.-Z., Wang, Z.-W., Hu, J., Gao, X.-Q., Shen, K.-Z., Deng, C., Morphology Control Technologies of Polymeric Materials During Processing. *Macromol. Mater. Eng.* **2014**, 299, 400–423. doi:10.1002/mame.201300216

[41] Huang, H.-X., Jiang, G., Li, X.-J., Development of Polymer Blend Morphology along an Extruder with Different Screw Geometries. *Int. Polym. Process.* **2008**, 23, 47–54. doi:10.3139/217.2019

[42] Lee, J.K., Han, C.D., Evolution of polymer blend morphology during compounding in a twin-screw extruder. *Polymer.* **2000**, 41, 1799–1815. doi:10.1016/S0032-3861(99)00325-0

[43] Yang, J., Phase Morphology and Orientation Development of Polymer Blends in Melt Processing, The University of Akron, **2008**

[44] Li, H., Sundararaj, U., Morphology Development of Polymer Blends in Extruder: The Effects of Compatibilization and Rotation Rate. *Macromol. Chem. Phys.* **2009**, 210, 852–863. doi:10.1002/macp.200800543

[45] Kamal, M.R., Garmabi, H., Hozhabr, S., Arghyris, L., The development of laminar morphology during extrusion of polymer blends. *Polym. Eng. Sci.* **1995**, 35, 41–51. doi:10.1002/pen.760350107

[46] García-Masabet, V., Santana Pérez, O., Cailloux, J., Abt, T., Sánchez-Soto, M., Carrasco, F., Maspoch, M.L., PLA/PA Bio-Blends: Induced Morphology by Extrusion. *Polymers.* **2019**, 12, 10. doi:10.3390/polym12010010

[47] Bärwinkel, S., Seidel, A., Hobeika, S., Hufen, R., Mörl, M., Altstädt, V., Morphology Formation in PC/ABS Blends during Thermal Processing and the Effect of the Viscosity Ratio of Blend Partners. *Materials.* **2016**, 9, 659. doi:10.3390/ma9080659

[48] Ran, J., Lai, X., Li, H., Zeng, X., Remarkable enhancement of mechanical and tribological properties of polyamide 46/polyphenylene oxide alloy by polyurethane-coated carbon fiber. *High Perform. Polym.* **2019**, 31, 1122–1131. doi:10.1177/0954008319827639

[49] Cao, Y., Zhang, J., Feng, J., Wu, P., Compatibilization of Immiscible Polymer Blends Using Graphene Oxide Sheets. *ACS Nano*. **2011**, 5, 5920–5927. doi:10.1021/nn201717a

[50] Lee, M., Son, K., Kim, J., Kim, D., Min, B.H., Kim, J.H., Effect of PA6T on morphology and electrical conductivity in PA66/PA6T/PPE/multiwalled carbon nanotube nanocomposites. *Compos. Sci. Technol.* **2018**, 164, 260–266. doi:10.1016/j.compscitech.2018.05.049

[51] Li, W., Yao, Z., Yao, R., Li, X., Liu, S., Effect of pre-irradiation PPO-grafted maleic anhydride on structure and properties of PPO-g-MAH/PA66 blends. *Radiat. Eff. Defects Solids*. **2014**, 169, 344–352. doi:10.1080/10420150.2013.865622

[52] Campbell, J.R., Hobbs, S.Y., Shea, T.J., Watkins, V.H., Poly(Phenylene oxide)/polyamide blends via reactive extrusion. *Polym. Eng. Sci.* **1990**, 30, 1056–1062. doi:10.1002/pen.760301709

[53] Ghidoni, D., Bencini, E., Nocci, R., Compatibilizing PPE and PA6 with nitro-phthalimide derivatives. *J. Mater. Sci.* **1996**, 31, 95–101. doi:10.1007/BF00355132

[54] Ghidoni, D., Fasulo, G.C., Cecchele, D., Merlotti, M., Sterzi, G., Nocci, R., A study on compatibilization of AES/PA6 blends. *J. Mater. Sci.* **1993**, 28, 4119–4128. doi:10.1007/BF00351242

[55] Jo, W.H., Park, C.D., Lee, M.S., Preparation of functionalized polystyrene by reactive extrusion and its blend with polyamide 6. *Polymer.* **1996**, 37, 1709–1714. doi:10.1016/0032-3861(96)83723-2

[56] Tol, R.T., Mathot, V.B.F., Groeninckx, G., Confined crystallization phenomena in immiscible polymer blends with dispersed micro- and nanometer sized PA6 droplets, part 2: reactively compatibilized PS/PA6 and (PPE/PS)/PA6 blends. *Polymer.* **2005**, 46, 383–396. doi:10.1016/j.polymer.2004.10.070

[57] Harrats, C., Dedecker, K., Groeninckx, G., Jérôme, R., Reactively and physically compatibilized immiscible polymer blends: stability of the copolymer at the interface. *Macromol. Symp.* **2003**, 198, 183–196. doi:10.1002/masy.200350816

[58] Wu, Y., Shi, Y., Zhu, L., Shentu, B., Weng, Z., Joint Effect of Compatibilizer and Organo-Montmorillonite on Compatibilization of Polyamide-6/Poly(phenylene oxide) Blend: Morphology and Properties. *Polym. Plast. Technol. Eng.* **2015**, 54, 682–690. doi:10.1080/03602559.2014.979498

[59] Bastian, M., Plastifizierung und Morphologieentwicklung von Polymerblends in Doppelschnecken-Extrudern, Universität Paderborn, **2000**

[60] Bastian, M., Melting of Polymer Blends in Co-rotating Twin Screw Extruders. *Int. Polym. Process.* **2001**, 16, 124–130. doi:10.3139/217.1632

[61] Heindl, M., Einfluss von Dehnströmungen auf die Morphologieausbildung in Polymerblends, Universität Erlangen-Nürnberg, **2005**

[62] Baer, E., Advanced Polymers. *Sci. Am.* **1986**, 255, 178–190. doi:10.1038/scientificamerican1086-178

[63] Weber, M., Polymer blends: materials with versatile properties. *Macromol. Symp.* **2001**, 163, 235–250. doi:10.1002/1521-3900(200101)163:1<235::AID-MASY235>3.0.CO;2-3

[64] Brannock, G.R., Barlow, J.W., Paul, D.R., Blends of styrene/maleic anhydride copolymers with polymethacrylates. *J. Polym. Sci. Part B Polym. Phys.* **1991**, 29, 413–429. doi:10.1002/polb.1991.090290404

[65] Yang, K., Xin, C., Huang, Y., Jiang, L., He, Y., Effects of extensional flow on properties of polyamide-66/poly(2,6-dimethyl-1,4-phenylene oxide) blends: A study of morphology, mechanical properties, and rheology. *Polym. Eng. Sci.* **2016**, 57, 1090–1098. doi:10.1002/pen.24484

[66] Graebling, D., Muller, R., Palierne, J.F., Linear viscoelastic behavior of some incompatible polymer blends in the melt. Interpretation of data with a model of emulsion of viscoelastic liquids. *Macromolecules*. **1993**, 26, 320–329. doi:10.1021/ma00054a011

[67] Carson, S.O., Maia, J.M., Covas, J.A., A New Extensional Mixing Element for Improved Dispersive Mixing in Twin-Screw Extrusion, Part 2: Experimental Validation for Immiscible Polymer Blends. *Adv. Polym. Technol.* **2018**, 37, 167–175. doi:10.1002/adv.21653

[68] Alemán, J. V., Chadwick, A. V., He, J., Hess, M., Horie, K., Jones, R.G., Kratochvíl, P., Meisel, I., Mita, I., Moad, G., Penczek, S., Stepto, R.F.T., Definitions of terms relating to the structure and processing of sols, gels, networks, and inorganic-organic hybrid materials (IUPAC Recommendations 2007). *Pure Appl. Chem.* **2007**, 79, 1801–1829. doi:10.1351/pac200779101801

[69] Subramanian, M.N., Polymer Blends: Thermodynamics, in: Polym. Blends Compos., John Wiley & Sons, Inc., **2017**: pp. 153–168. doi:10.1002/9781119383581.ch6

[70] Robeson, L.M., Polymer Blends, Carl Hanser Verlag GmbH & Co. KG, **2007**, ISBN:978-3-446-22569-5. doi:10.3139/9783446436503

[71] Gooch, J.W., Flory-Huggins Theory, in: Encycl. Dict. Polym., Springer New York, New York, NY, **2011**: pp. 315–315. doi:10.1007/978-1-4419-6247-8_5128

[72] Young, N.P., Balsara, N.P., Flory–Huggins Equation, in: Encycl. Polym. Nanomater., Springer Berlin Heidelberg, Berlin, Heidelberg, **2014**: pp. 1–7. doi:10.1007/978-3-642-36199-9_79-1

[73] Horváth, Z., Gyarmati, B., Menyhárd, A., Doshev, P., Gahleitner, M., Varga, J., Pukánszky, B., The role of solubility and critical temperatures for the efficiency of sorbitol clarifiers in polypropylene. *RSC Adv.* **2014**, 4, 19737–19745. doi:10.1039/C4RA01917B

[74] Utracki, L.A., Wilkie, C.A., Polymer Blends Handbook, Springer Netherlands, **2014**, ISBN:978-94-007-6063-9. doi:10.1007/978-94-007-6064-6

[75] Scott, C., Macosko, C.W., Morphology development during the initial stages of polymer-polymer blending. *Polymer.* **1995**, 36, 461–470. doi:10.1016/0032-3861(95)91554-K

[76] Macosko, C.W., Morphology development and control in immiscible polymer blends. *Macromol. Symp.* **2000**, 149, 171–184. doi:10.1002/1521-3900(200001)149:1<171::AID-MASY171>3.0.CO;2-8

[77] Liu, Z., Deng, Y., Han, Y., Chen, M., Sun, S., Cao, C., Zhou, C., Zhang, H., Toughening of Polyamide-6 with a Maleic Anhydride Functionalized Acrylonitrile-Styrene-Butyl Acrylate Copolymer. *Ind. Eng. Chem. Res.* **2012**, 51, 9235–9240. doi:10.1021/ie202960q

[78] Akkapeddi, M.K., Commercial Polymer Blends, in: Polym. Blends Handb., Springer Netherlands, **2014**: pp. 1733–1883. doi:10.1007/978-94-007-6064-6_22

[79] Kalarikkal, R.K.M.S.T.N., Micro and Nano Fibrillar Composites (MFCs and NFCs) from Polymer Blends, Elsevier, **2017**, ISBN:9780081019917. doi:10.1016/C2016-0-01649-2

[80] Charef, H., Sabu, T., Groeninckx, G., Micro- and Nanostructured Multiphase Polymer Blend Systems, CRC Press, **2005**, ISBN:9780429115486. doi:10.1201/9781420026542

[81] Hoseini, A.H.A., Arjmand, M., Sundararaj, U., Trifkovic, M., Tunable electrical conductivity of polystyrene/polyamide-6/carbon nanotube blend nanocomposites via control of morphology and nanofiller localization. *Eur. Polym. J.* **2017**, 95, 418–429. doi:10.1016/j.eurpolymj.2017.08.037

[82] Fina, A., Han, Z., Saracco, G., Gross, U., Mainil, M., Morphology and conduction properties of graphite-filled immiscible PVDF/PPgMA blends. *Polym. Adv. Technol.* **2012**, 23, 1572–1579. doi:10.1002/pat.3031

[83] Zou, H., Wang, K., Zhang, Q., Fu, Q., A change of phase morphology in poly(p-phenylene sulfide)/polyamide 66 blends induced by adding multi-walled carbon nanotubes. *Polymer.* **2006**, 47, 7821–7826. doi:10.1016/j.polymer.2006.09.008

[84] Taylor, G.I., The formation of emulsions in definable fields of flow. *Proc. R. Soc. London. Ser. A, Contain. Pap. a Math. Phys. Character*. **1934**, 146, 501–523. doi:10.1098/rspa.1934.0169

[85] Grace, H.P., Dispersion Phenomena in High Viscosity Immiscible Fluid Systems and Application of Static Mixers as Dispersion Devices in such Systems. *Chem. Eng. Commun.* **1982**, 14, 225–277. doi:10.1080/00986448208911047

[86] Anastasiadis, S.H., Gancarz, I., Koberstein, J.T., Interfacial tension of immiscible polymer blends: temperature and molecular weight dependence. *Macromolecules*. **1988**, 21, 2980–2987. doi:10.1021/ma00188a015

[87] Yang, J., White, J.L., Jiang, Q., Phase morphology development in a low interfacial tension immiscible polyolefin blend during die extrusion and melt spinning. *Polym. Eng. Sci.* **2010**, 50, 1969–1977. doi:10.1002/pen.21726

[88] Elemans, P.H.M., Janssen, J.M.H., Meijer, H.E.H., The measurement of interfacial tension in polymer/polymer systems: The breaking thread method. *J. Rheol.* **1990**, 34, 1311–1325. doi:10.1122/1.550087

[89] Palierne, J.F., Linear rheology of viscoelastic emulsions with interfacial tension. *Rheol. Acta*. **1990**, 29, 204–214. doi:10.1007/BF01331356

[90] Taylor, G.I., The viscosity of a fluid containing small drops of another fluid. *Proc. R. Soc. London. Ser. A, Contain. Pap. a Math. Phys. Character*. **1932**, 138, 41–48. doi:10.1098/rspa.1932.0169

[91] Utracki, L.A., Shi, Z.H., Development of polymer blend morphology during compounding in a twin-screw extruder. Part I: Droplet dispersion and coalescence-a review. *Polym. Eng. Sci.* **1992**, 32, 1824–1833. doi:10.1002/pen.760322405

[92] Puyvelde, P.V. Van, Moldenaers, P., Rheology and Morphology Development in Immiscible Polymer Blends, in: Rheol. Rev., **2005**: pp. 101–145. doi:10.1002/9781118892756.ch19

[93] Ruckdäschel, H., Micro- and nanostructured polymmer blends - Processing, properties and foaming behaviour, Universität Bayreuth, **2008**

[94] Jordhamo, G.M., Manson, J.A., Sperling, L.H., Phase continuity and inversion in polymer blends and simultaneous interpenetrating networks. *Polym. Eng. Sci.* **1986**, 26, 517–524. doi:10.1002/pen.760260802

[95] Utracki, L.A., On the viscosity-concentration dependence of immiscible polymer blends. *J. Rheol.* **1991**, 35, 1615–1637. doi:10.1122/1.550248

[96] Avgeropoulos, G.N., Weissert, F.C., Biddison, P.H., Böhm, G.G.A., Heterogeneous Blends of Polymers. Rheology and Morphology. *Rubber Chem. Technol.* **1976**, 49, 93–104. doi:10.5254/1.3534954

[97] Chen, T.H., Su, A.C., Morphology of poly(p-phenylene sulfide)polyethylene blends. *Polymer.* **1993**, 34, 4826–4831. doi:10.1016/0032-3861(93)90004-T

[98] Yu, W., Zhou, C., Inoue, T., A coalescence mechanism for the coarsening behavior of polymer blends during a quiescent annealing process. I. Monodispersed particle system. *J. Polym. Sci. Part B Polym. Phys.* **2000**, 38, 2378–2389. doi:10.1002/1099-0488(20000915)38:18<2378::AID-POLB50>3.0.CO;2-I

[99] Mirabella, F.M., Barley, J.S., Ostwald ripening in immiscible polyolefin blends. *J. Polym. Sci. Part B Polym. Phys.* **1995**, 33, 2281–2287. doi:10.1002/polb.1995.090331613

[100] Fortelny, I., Zivny, A., Juza, J., Coarsening of the phase structure in immiscible polymer blends. Coalescence or ostwald ripening?. *J. Polym. Sci. Part B Polym. Phys.* **1999**, 37, 181–187. doi:10.1002/(SICI)1099-0488(19990201)37:3<181::AID-POLB1>3.0.CO;2-I

[101] Imre, B., Pukánszky, B., Compatibilization in bio-based and biodegradable polymer blends. *Eur. Polym. J.* **2013**, 49, 1215–1233. doi:10.1016/j.eurpolymj.2013.01.019

[102] Yang, X., Song, J., Wang, H., Lin, Q., Jin, X., Yang, X., Li, Y., Reactive Comb Polymer Compatibilized Immiscible PVDF/PLLA Blends: Effects of the Main Chain Structure of Compatibilizer. *Polymers.* **2020**, 12, 526. doi:10.3390/polym12030526

[103] Tselios, C., Bikiaris, D., Maslis, V., Panayiotou, C., In situ compatibilization of polypropylene–polyethylene blends: a thermomechanical and spectroscopic study. *Polymer.* **1998**, 39, 6807–6817. doi:10.1016/S0032-3861(98)00132-3

[104] Osswald, T.A., Menges, G., Material Science of Polymers for Engineers, in: Mater. Sci. Polym. Eng., Carl Hanser Verlag GmbH & Co. KG, **2012**. doi:10.3139/9781569905241.fm

[105] Gaylord, N.G., Compatibilizing Agents: Structure and Function in Polyblends. *J. Macromol. Sci. Part A - Chem.* **1989**, 26, 1211–1229. doi:10.1080/00222338908052043

[106] Koning, C.; Van Duin, M.; Pagnoulle, C.; Jérôme, R., Strategies for compatibilization of polymer blends. *Prog. Polym. Sci.* **1998**, 23, 707–757. doi:10.1016/S0079-6700(97)00054-3

[107] Kulshreshtha, A.K., Vasile, C., Handbook of Polymer Blends and Composites, Smithers Rapra Publishing, **2002**, ISBN:1859572499.

[108] Giustiniani, A., Drenckhan, W., Poulard, C., Interfacial tension of reactive, liquid interfaces and its consequences. *Adv. Colloid Interface Sci.* **2017**, 247, 185–197. doi:10.1016/j.cis.2017.07.017

[109] Macosko, C.W., Guégan, P., Khandpur, A.K., Nakayama, A., Marechal, P., Inoue, T., Compatibilizers for Melt Blending: Premade Block Copolymers. *Macromolecules*. **1996**, 29, 5590–5598. doi:10.1021/ma9602482

[110] Moad, G., The synthesis of polyolefin graft copolymers by reactive extrusion. *Prog. Polym. Sci.* **1999**, 24, 81–142

[111] Collyer, A.A., Rubber Toughened Engineering Plastics, Springer Netherlands, **1994**, ISBN:978-94-010-4549-0. doi:10.1007/978-94-011-1260-4

[112] Scheirs, J., Priddy, D.B., Modern Styrenic Polymers: Polystyrenes and Styrenic Copolymers, John Wiley & Sons, Ltd, **2003**, ISBN:0471497525. doi:10.1002/0470867213

[113] Janssen, L.P.B.M., Reactive Extrusion Systems, CRC Press, **2004**, ISBN:9780429215018. doi:10.1201/9780203014172

[114] Al-Malaika, S., Reactive Modifiers for Polymers, Springer Netherlands, **1997**, ISBN:978-94-010-7148-2. doi:10.1007/978-94-009-1449-0

[115] Sun, Y.J., Hu, G.H., Lambla, M., Kotlar, H.K., In situ compatibilization of polypropylene and poly(butylene terephthalate) polymer blends by one-step reactive extrusion. *Polymer.* **1996**, 37, 4119–4127. doi:10.1016/0032-3861(96)00229-7

[116] Hale, W., Keskkula, H., Paul, D.R., Compatibilization of PBT–ABS blends compatibilized by methyl methacrylate–glycidyl methacrylate–ethyl acrylate terpolymers. *Polymer.* **1999**, 40, 365–377. doi:10.1016/S0032-3861(98)00575-8

[117] Lim, J.C., Cho, K.Y., Park, J.-K., Weld line characteristics of PC/ABS blend. II. Effect of reactive compatibilizer. *J. Appl. Polym. Sci.* **2008**, 108, 3632–3643. doi:10.1002/app.27316

[118] Peng, Y., Guo, W., Zhu, P., Wu, C., Structures and properties of ternary blends of recycled poly(ethylene terephthalate)/bisphenol-A polycarbonate/(E/nBA/GMA). *J. Appl. Polym. Sci.* **2008**, 109, 483–491. doi:10.1002/app.27348

[119] Bouilloux, A., Ernst, B., Lobbrecht, A., Muller, R., Rheological and morphological study of the phase inversion in reactive polymer blends. *Polymer.* **1997**, 38, 4775–4783. doi:10.1016/S0032-3861(97)00001-3

[120] Hu, G.-H., Flat, J.-J., Lambla, M., Exchange and free radical grafting reactions in reactive extrusion. *Makromol. Chemie. Macromol. Symp.* **1993**, 75, 137–157. doi:10.1002/masy.19930750113

[121] Li, Y., Shimizu, H., Novel morphologies of poly(phenylene oxide) (PPO)/polyamide 6 (PA6) blend nanocomposites. *Polymer.* **2004**, 45, 7381–7388. doi:10.1016/j.polymer.2004.09.018

[122] Lin, H.-M., Behera, K., Yadav, M., Chiu, F.-C., Polyamide 6/Poly(vinylidene fluoride) Blend-Based Nanocomposites with Enhanced Rigidity: Selective Localization of Carbon Nanotube and Organoclay. *Polymers.* **2020**, 12, 184. doi:10.3390/polym12010184

[123] Salzano de Luna, M., Filippone, G., Effects of nanoparticles on the morphology of immiscible polymer blends – Challenges and opportunities. *Eur. Polym. J.* **2016**, 79, 198–218. doi:10.1016/j.eurpolymj.2016.02.023

[124] Schmelz, J., Pirner, D., Krekhova, M., Ruhland, T.M., Schmalz, H., Interfacial activity of patchy worm-like micelles. *Soft Matter*. **2013**, 9, 11173–11177. doi:10.1039/c3sm51914g

[125] Parpaite, T., Otazaghine, B., Caro, A.S., Taguet, A., Sonnier, R., Lopez-Cuesta, J.M., Janus hybrid silica/polymer nanoparticles as effective compatibilizing agents for polystyrene/polyamide-6 melted blends. *Polymer.* **2016**, 90, 34–44. doi:10.1016/j.polymer.2016.02.044

[126] Poggi, E., Gohy, J.-F., Janus particles: from synthesis to application. *Colloid Polym. Sci.* **2017**, 295, 2083–2108. doi:10.1007/s00396-017-4192-8

[127] Bahrami, R., Löbling, T.I., Gröschel, A.H., Schmalz, H., Müller, A.H.E., Altstädt, V., The impact of Janus nanoparticles on the compatibilization of immiscible polymer blends under technologically relevant conditions. *ACS Nano*. **2014**, 8, 10048–10056. doi:10.1021/nn502662p

[128] Bahrami, R., Löbling, T.I., Schmalz, H., Müller, A.H.E., Altstädt, V., Micromechanics of "raspberry" morphology in PPE/SAN polymer blends compatibilized with linear ABC triblock terpolymers. *Polymer*. **2015**, 80, 52–63. doi:10.1016/j.polymer.2015.10.039

[129] Arboleda-Clemente, L., García-Fonte, X., Abad, M.-J., Ares-Pernas, A., Role of rheology in tunning thermal conductivity of polyamide 12/polyamide 6 composites with a segregated multiwalled carbon nanotube network. *J. Compos. Mater.* **2018**, 52, 2549–2557. doi:10.1177/0021998317749715

[130] Mun, S.C., Kim, M., Lee, C.S., Lee, M.H., Son, Y., Park, O.O., Preferential positioning of γ-ray treated multi-walled carbon nanotubes in polyamide 6,6/poly(p-phenylene ether) blends. *Macromol. Res.* **2013**, 21, 356–361. doi:10.1007/s13233-013-1041-6

[131] Lee, J.Y., Choi, K.H., Hwang, J., Sung, M., Kim, J.E., Park, B.J., Kim, J.W., Janus amphiphilic nanoplatelets as smart colloid surfactants with complementary face-to-face interactions. *Chem. Commun.* **2020**, 56, 6031–6034. doi:10.1039/D0CC02231D

[132] Weiss, S., Hirsemann, D., Biersack, B., Ziadeh, M., Müller, A.H.E., Breu, J., Hybrid Janus particles based on polymer-modified kaolinite. *Polymer.* **2013**, 54, 1388–1396. doi:10.1016/j.polymer.2012.12.041

[133] Bubmann, T., Seidel, A., Altstädt, V., Transparent PC/PMMA Blends Via Reactive Compatibilization in a Twin-Screw Extruder. *Polymers.* **2019**, 11, 2070. doi:10.3390/polym11122070

[134] Li, R., Zhang, X., Zhou, L., Dong, J., Wang, D., In situ compatibilization of polypropylene/polystyrene blend by controlled degradation and reactive extrusion. *J. Appl. Polym. Sci.* **2008**, NA-NA. doi:10.1002/app.29118

[135] Xie, H.-Q., Xu, J., Zhou, S., Polymer blends with two kinds of elastomeric ionomers. *Polymer.* **1991**, 32, 95–102. doi:10.1016/0032-3861(91)90568-4

[136] Burattini, S., Greenland, B.W., Merino, D.H., Weng, W., Seppala, J., Colquhoun, H.M., Hayes, W., Mackay, M.E., Hamley, I.W., Rowan, S.J., A Healable Supramolecular Polymer Blend Based on Aromatic π–π Stacking and Hydrogen-Bonding Interactions. *J. Am. Chem. Soc.* **2010**, 132, 12051–12058. doi:10.1021/ja104446r

[137] Wu, Y., Zhang, H., Shentu, B., Weng, Z., Preparation of Poly(phenylene oxide)/Polyamide-6 Nanocomposites with High Tensile Strength and Excellent Impact Performance. *Ind. Eng. Chem. Res.* **2015**, 54, 5870–5875. doi:10.1021/acs.iecr.5b01041

[138] Cai, X., Li, B., Pan, Y., Wu, G., Morphology evolution of immiscible polymer blends as directed by nanoparticle self-agglomeration. *Polymer.* **2012**, 53, 259–266. doi:10.1016/j.polymer.2011.11.032

[139] Fenouillot, F., Cassagnau, P., Majesté, J.C., Uneven distribution of nanoparticles in immiscible fluids: Morphology development in polymer blends. *Polymer.* **2009**, 50, 1333–1350. doi:10.1016/j.polymer.2008.12.029

[140] Zhang, J., Grzybowski, B.A., Granick, S., Janus Particle Synthesis, Assembly, and Application. *Langmuir*. **2017**, 33, 6964–6977. doi:10.1021/acs.langmuir.7b01123

[141] Galloway, J.A., Jeon, H.K., Bell, J.R., Macosko, C.W., Block copolymer compatibilization of cocontinuous polymer blends. *Polymer.* **2005**, 46, 183–191. doi:10.1016/j.polymer.2004.10.061

[142] Anastasiadis, S.H., Gancarz, I., Koberstein, J.T., Compatibilizing effect of block copolymers added to the polymer/polymer interface. *Macromolecules*. **1989**, 22, 1449–1453. doi:10.1021/ma00193a074

[143] Tao, F., Nysten, B., Baudouin, A.-C., Thomassin, J.-M., Vuluga, D., Detrembleur, C., Bailly, C., Influence of nanoparticle–polymer interactions on the apparent migration behaviour of carbon nanotubes in an immiscible polymer blend. *Polymer.* **2011**, 52, 4798–4805. doi:10.1016/j.polymer.2011.08.035

[144] Kietzke, T., Neher, D., Landfester, K., Montenegro, R., Güntner, R., Scherf, U., Novel approaches to polymer blends based on polymer nanoparticles. *Nat. Mater.* **2003**, 2, 408–412. doi:10.1038/nmat889

[145] Salehiyan, R., Ray, S.S., Tuning the Conductivity of Nanocomposites through Nanoparticle Migration and Interface Crossing in Immiscible Polymer Blends: A Review on Fundamental Understanding. *Macromol. Mater. Eng.* **2019**, 304, 1800431. doi:10.1002/mame.201800431

[146] Jeon, H.K., Feist, B.J., Koh, S.B., Chang, K., Macosko, C.W., Dion, R.P., Reactively formed block and graft copolymers as compatibilizers for polyamide 66/PS blends. *Polymer.* **2004**, 45, 197–206. doi:10.1016/j.polymer.2003.10.099

[147] Park, I., Barlow, J.W., Paul, D.R., The in situ reactive compatibilization of nylon-6/polystyrene blends using anhydride functionalized polystyrenes. *J. Polym. Sci. Part B Polym. Phys.* **1992**, 30, 1021–1033. doi:10.1002/polb.1992.090300910

[148] Li, B., Zhang, Y., Bai, X., Wang, S., Ji, J., Effect of PPO-g-MA on structures and properties of PPO/PA6/short glass fiber composites. *J. Polym. Sci. Part B Polym. Phys.* **2009**, 47, 2188–2197. doi:10.1002/polb.21815

[149] Zhang, Y.T., Li, Y., Li, L., Qu, X.W., New Reactive Compatibilizer B Preparation and its Application in Polystyrene Ether/Nylon 66 Alloy. *Adv. Mater. Res.* **2011**, 413, 449–453. doi:10.4028/www.scientific.net/AMR.413.449

[150] Kolařík, J., Fambri, L., Šlouf, M., Konečný, D., Heterogeneous polyamide 66/syndiotactic polystyrene blends: Phase structure and thermal and mechanical properties. *J. Appl. Polym. Sci.* **2005**, 96, 673–684. doi:10.1002/app.21496

[151] Moyses, S., Ramakrishnan, V., Lietzau, C., Bajaj, P., The effect of in situ-formed copolymers on the morphology of reactive poly(phenylene ether)/poly(amide-6) blends. *J. Polym. Sci.* **2020**, 58, 1262–1275. doi:10.1002/pol.20200017

[152] Son, Y., Lee, S., One Step Method for Fabrication of PPO/PA-66/Elastomer Blends. *Polym. Bull.* **2006**, 56, 267–273. doi:10.1007/s00289-005-0473-3

[153] Musa, O.M., Handbook of Maleic Anhydride Based Materials, Springer International Publishing, **2016**, ISBN:978-3-319-29453-7. doi:10.1007/978-3-319-29454-4

[154] Chanda, M., Roy, S.K., Industrial Polymers, Specialty Polymers, and Their Applications, CRC Press, **2008**, ISBN:9781420080599. doi:10.1201/9781420080599

[155] Maier, R.D., Handbuch Kunststoff Additive, Carl Hanser Verlag GmbH & Co. KG, **2016**, ISBN:978-3-446-22352-3. doi:10.3139/9783446432918

[156] Liu, W.-B., Kuo, W.-F., Chiang, C.-J., Chang, F.-C., In situ compatibilization of PBT/PPO blends. *Eur. Polym. J.* **1996**, 32, 91–99. doi:10.1016/0014-3057(95)00115-8

[157] Chen, R.S., Ab Ghani, M.H., Salleh, M.N., Ahmad, S., Gan, S., Influence of Blend Composition and Compatibilizer on Mechanical and Morphological Properties of Recycled HDPE/PET Blends. *Mater. Sci. Appl.* **2014**, 05, 943–952. doi:10.4236/msa.2014.513096

[158] Handge, U.A., Galeski, A., Kim, S.C., Dijkstra, D.J., Götz, C., Fischer, F., Lim, G.T., Altstädt, V., Gabriel, C., Weber, M., Steininger, H., Melt processing, mechanical, and fatigue crack propagation properties of reactively compatibilized blends of polyamide 6 and acrylonitrile-butadiene-styrene copolymer. *J. Appl. Polym. Sci.* **2012**, 124, 740–754. doi:10.1002/app.35055

[159] Kudva, R.A., Keskkula, H., Paul, D.R., Properties of compatibilized nylon 6/ABS blends: Part I. Effect of ABS type. *Polymer.* **2000**, 41, 239–258. doi:10.1016/S0032-3861(99)00106-8

[160] Weber, M., Heckmann, W., Goeldel, A., Styrenics/polyamide-blends - Reactive blending and properties. *Macromol. Symp.* **2006**, 233, 1–10. doi:10.1002/masy.200690003

[161] Dedecker, K., Groenickx, G., Inoue, T., Reactive compatibilization of A /(B / C) polymer blends: part 3 Quantitative analysis of the interfacial thickness and the interfacial tension. *Polymer.* **1998**, 39, 5001–5010

[162] Yu, C., Shi, D., Wang, J., Shi, H., Jiang, T., Yang, Y., Hu, G.-H., Li, R.K.Y., Effect of a dual compatibilizer on the formation of co-continuous morphology of immiscible polymer blends. *Mater. Des.* **2016**, 107, 171–177. doi:10.1016/j.matdes.2016.06.044

[163] Choi, J.-H., Kim, H.-G., Han, D.-H., Lim, J.-C., Oh, D.-H., Min, K.-E., Effect of processing conditions on compatibility of nylon 6/polystyrene blend. *J. Appl. Polym. Sci.* **2006**, 101, 1–7. doi:10.1002/app.22081

[164] Kim, D.K., Song, K.H., Koo, C.M., Hong, S.M., Chae, D.W., Characterization of compatibilized blends of nylon 66/poly(2,6-dimethyl-1,4-phenylene ether)/high-impact polystyrene filled with phosphinate-based flame retardants: Mechanical property, rheological behavior, and flame retardancy. *J. Fire Sci.* **2015**, 33, 339–357. doi:10.1177/0734904115595993

[165] Moore, E.R., Properties of styrene-maleic anhydride copolymers. *Ind. Eng. Chem. Prod. Res. Dev.* **1986**, 25, 315–321. doi:10.1021/i300022a033

[166] Rätzsch, M., Alternating maleic anhydride copolymers. *Prog. Polym. Sci.* **1988**, 13, 277–337. doi:10.1016/0079-6700(88)90001-9

[167] Gan, P.P., Paul, D.R., Phase behavior of blends of styrene/maleic anhydride copolymers. *J. Appl. Polym. Sci.* **1994**, 54, 317–331. doi:10.1002/app.1994.070540306

[168] Fang, H., Mighri, F., Ajji, A., Miscibility characterization of SMA/SAN and SMA/PMMA blends by differential scanning calorimetry and fluorescence techniques. *J. Appl. Polym. Sci.* **2007**, 105, 2955–2962. doi:10.1002/app.26460

[169] Chen, J.J., Lin, W.S., Lin, F.L., Tong, T.S., Blends of Styrene-Maleic Anhydride Copolymer with ABS, Technomic Publishing, **1989**, ISBN:9781315136899

[170] Fried, J.R., Hanna, G.A., Studies of poly(2,6-dimethyl-1,4-phenylene oxide blends): I. Copolymers of styrene and maleic anhydride. *Polym. Eng. Sci.* **1982**, 22, 705–718. doi:10.1002/pen.760221110

[171] Witteler, H., Lieser, G., Droescher, M., Compatibility of poly[oxy(2,6-dimethyl-l,4-phenylene)] and styrene/maleic anhydride copolymers. *Makromol. Chem., Rapid Commun.* **1993**, 14, 401–403. doi:10.1002/marc.1993.030140706

[172] Chen, Z., Pei, J., Li, R., Study of the Preparation and Dielectric Property of PP/SMA/PVDF Blend Material. *Appl. Sci.* **2017**, 7, 389. doi:10.3390/app7040389

[173] Zhou, J.C., Gao, J., Wang, S.H., Lin, S.X., Huang, J., Xu, L.L., Effect of compatibilizer on the strength of ABS/PMMA blends. *IOP Conf. Ser. Mater. Sci. Eng.* **2014**, 62, 012030. doi:10.1088/1757-899X/62/1/012030

[174] Cassu, S.N., Felisberti, M.I., Polystyrene and polyester polyurethane elastomer blends compatibilized by SMA. *J. Appl. Polym. Sci.* **2004**, 93, 2297–2304. doi:10.1002/app.20790

[175] Ju, M.Y., Chang, F.C., Compatibilization of PET/PS blends through SMA and PMPI dual compatibilizers. *Polymer.* **2000**, 41, 1719–1730. doi:10.1016/S0032-3861(99)00355-9

[176] Basu, D., Banerjee, A., Determination of optimum compatibilizer (SMA) concentration for PBT/ABS (70/30) blend using tensile strength data. *J. Appl. Polym. Sci.* **1997**, 64, 1485–1487. doi:10.1002/(SICI)1097-4628(19970523)64:8<1485::AID-APP5>3.0.CO;2-D

[177] Majumdar, B., Keskkula, H., Paul, D., Morphology of nylon 6/ABS blends compatibilized by a styrene/maleic anhydride copolymer. *Polymer.* **1994**, 35, 3164–3172. doi:10.1016/0032-3861(94)90117-1

[178] Misra, A., Sawhney, G., Kumar, R.A., Structure and properties of compatibilized blends of polyamide-6 and ABS. *J. Appl. Polym. Sci.* **1993**, 50, 1179–1186. doi:10.1002/app.1993.070500708

[179] Guo, J.B., Zhang, K.Z., Qin, S.H., Morphology and Mechanical Properties of PA6/ABS Blends. *Adv. Mater. Res.* **2012**, 535–537, 2600–2605. doi:10.4028/www.scientific.net/AMR.535-537.2600

[180] Tol, R.T., Mathot, V.B.F., Groeninckx, G., Confined crystallization phenomena in immiscible polymer blends with dispersed micro – and nanometer sized PA6 droplets, part 1: uncompatibilized PS/PA6, (PPE/PS)/PA6 and PPE/PA6 blends. *Polymer.* **2005**, 46, 369–382. doi:10.1016/j.polymer.2004.10.085

[181] Lu, C., Gao, X., Yang, D., Cao, Q., Huang, X., Liu, J., Zhang, Y., Flame retardancy of polystyrene/nylon-6 blends with dispersion of clay at the interface. *Polym. Degrad. Stab.* **2014**, 107, 10–20. doi:10.1016/j.polymdegradstab.2014.04.028

[182] Dedecker, K., Groeninckx, G., Reactive compatibilization of the polyamide 6/poly(phenylene oxide) blend by means of styrene-maleic anhydride copolymer. *J. Appl. Polym. Sci.* **1999**, 73, 889–898. doi:10.1002/(SICI)1097-4628(19990808)73:6<889::AID-APP5>3.0.CO;2-S

[183] Tol, R., Groeninckx, G., Vinckier, I., Moldenaers, P., Mewis, J., Phase morphology and stability of co-continuous (PPE/PS)/PA6 and PS/PA6 blends: effect of rheology and reactive compatibilization. *Polymer.* **2004**, 45, 2587–2601. doi:10.1016/j.polymer.2003.12.072

[184] Guo, Z., Shen, Y., Fang, Z., Compatibilization of polyamide 6/poly(2,6-dimethyl-1,4-phenylene oxide) blends by poly(styrene-co-maleic anhydride). *J. Polym. Eng.* **2014**, 34, 193–199. doi:10.1515/polyeng-2013-0163

[185] Chiou, K.-C., Chang, F.-C., Mai, Y.-W., Impact specific essential work of fracture of compatibilized polyamide-6 (PA6)/poly(phenylene ether) (PPE) blends. *Polym. Eng. Sci.* **2001**, 41, 1007–1018. doi:10.1002/pen.10802

[186] Wang, S., Li, B., Zhang, Y., Compatibilization of poly(2,6-dimethyl-1,4-phenylene oxide)/polyamide 6 blends with styrene-maleic anhydride copolymer: Mechanical properties, morphology, crystallization, and melting behavior. *J. Appl. Polym. Sci.* **2010**, 118, 3545–3551. doi:10.1002/app.32730

[187] Chiang, C.-R., Chang, F.-C., Polymer blends of polyamide-6 (PA6) and poly(phenylene oxide) (PPO) compatibilized by styrene-maleic anhydride (SMA) copolymer. *Polymer.* **1997**, 38, 4807–4817. doi:10.1016/S0032-3861(96)00015-8

[188] Van Duin, M., Aussems, M., Borggreve, R.J.M., Graft formation and chain scission in blends of polyamide-6 and -6.6 with maleic anhydride containing polymers. *J. Polym. Sci. Part A Polym. Chem.* **1998**, 36, 179–188. doi:10.1002/(SICI)1099-0518(19980115)36:1<179::AID-POLA22>3.0.CO;2-F

[189] Jo, W.H., Kim, H.C., Morphology and Rheological Properties of Poly(phenylene ether) and Polyamide-6 with a Compatibilizer. *Int. J. Polym. Mater.* **1993**, 21, 37–44. doi:10.1080/00914039308048510

[190] Chiou, K.-C., Wu, S.-C., Wu, H.-D., Chang, F.-C., Compatibilization and elastomer toughening of polyamide-6 (PA6)/poly(phenylene ether) (PPE) blends. *J. Appl. Polym. Sci.* **1999**, 74, 23–32. doi:10.1002/(SICI)1097-4628(19991003)74:1<23::AID-APP3>3.0.CO;2-U

[191] Bhatia, Q.S., Burrell, M.C., Chera, J.J., XPS surface studies of injection-molded poly(phenylene ether)/nylon 6,6 and poly(phenylene ether)/HIPS blends. *J. Appl. Polym. Sci.* **1992**, 46, 1915–1925. doi:10.1002/app.1992.070461104

[192] Tanaka, K., Nakayama, K., Influence of drying condition on dynamic viscoelastic properties of immiscible blend of polyamide and poly (phenylene ether). *Adv. Compos. Mater.* **1996**, 5, 169–183. doi:10.1163/156855196X00220

[193] Kim, D.K., Lee, A.S., Baek, B.K., Song, K.H., Hong, S.M., Koo, C.M., PPE/Nylon 66 Blends with High Mechanical Toughness and Flame Retardancy. *Macromol. Res.* **2020**, 28, 103–109. doi:10.1007/s13233-020-8022-3

[194] Zhang, Z., Cai, K., Liu, S., Guo, W., Zhang, B., Yang, M., Liu, W., The effect of HIPS-g-MAH on the mechanical properties of PA66/PPO alloy. *Polym. Bull.* **2022**, 79, 7939–7951. doi:10.1007/s00289-021-03897-2

[195] Aksit, A., Menzel, T., Aksit, M., Altstädt, V., Properties of Styrene–Maleic Anhydride Copolymer Compatibilized Polyamide 66/Poly (Phenylene Ether) Blends: Effect of Maleic Anhydride Concentration and Copolymer Content. *Materials.* **2020**, 13, 1237. doi:10.3390/ma13051237

[196] Aksit, A., Geis, N., Aksit, M., Altstädt, V., Properties of Styrene-Maleic Anhydride Copolymer Compatibilized Polyamide 66/Poly (Phenylene Ether) Blends: Effect of Blend Ratio and Compatibilizer Content. *Materials.* **2020**, 13, 3400. doi:10.3390/ma13153400

[197] Paul, D.R., Bucknall, C.B., Polymer Blends: Formulation and Performance, Wiley, **2000**, ISBN:9780471248255

[198] Creton, C., Kramer, E.J., Hui, C.Y., Brown, H.R., Failure mechanisms of polymer interfaces reinforced with block copolymers. *Macromolecules*. **1992**, 25, 3075–3088. doi:10.1021/ma00038a010

[199] Jia, N., Kagan, V.A., Mechanical Performance of Polyamides with Influence of Moisture and Temperature – Accurate Evaluation and Better Understanding, in: Plast. Fail. Anal. Prev., Elsevier, **2001**: pp. 95–104. doi:10.1016/B978-188420792-1.50014-7

[200] Isayev, A.I., Encyclopedia of Polymer Blends, Wiley-VCH Verlag GmbH & Co. KGaA, **2010**, ISBN:9783527805204. doi:10.1002/9783527805204

[201] Münstedt, H., Rheological and Morphological Properties of Dispersed Polymeric Materials, Carl Hanser Verlag GmbH & Co. KG, **2016**, ISBN:978-1-56990-607-1. doi:10.3139/9781569906088

[202] Michler, G.H., Baltá-Calleja, F.J., Nano- and Micromechanics of Polymers, Carl Hanser Verlag GmbH & Co. KG, **2012**, ISBN:978-3-446-42767-9. doi:10.3139/9783446428447

[203] Sarkissova, M., Harrats, C., Groeninckx, G., Thomas, S., Design and characterisation of microfibrillar reinforced composite materials based on PET/PA12 blends. *Compos. Part A Appl. Sci. Manuf.* **2004**, 35, 489–499. doi:10.1016/j.compositesa.2003.09.025

[204] Hussein, M., Effects of strain rate and temperature on the mechanical behavior of carbon black reinforced elastomers based on butyl rubber and high molecular weight polyethylene. *Results Phys.* **2018**, 9, 511–517. doi:10.1016/j.rinp.2018.02.043

[205] Chiu, H., Hwung, D., Study on poly(2,6-dimethyl-1,4-phenylene oxide)/SBS triblock copolymer blends. *Angew. Makromol. Chemie*. **1994**, 214, 153–167. doi:10.1002/apmc.1994.052140114

[206] Howe, D. V, Wolkowicz, M.D., Structure-property relationships in polyamide/acrylonitrile-butadiene-styrene (ABS) blends. *Polym. Eng. Sci.* **1987**, 27, 1582–1590. doi:10.1002/pen.760272104

[207] Jeziorska, R., Abramowicz, A., Szadkowska, A., Pasnik, A., Spasowka, E., Poly(phenylene oxide) and Renewable Polyamide 11 Blends Compatibilized by Ethylene- n -Octene Copolymer. *J. Renew. Mater.* **2018**, 6, 772–783. doi:10.7569/JRM.2018.634114

[208] Donald, A.M., The effect of temperature on crazing mechanisms in polystyrene. *J. Mater. Sci.* **1985**, 20, 2630–2638. doi:10.1007/BF00556095

[209] Socrate, S., Boyce, M.C., Lazzeri, A., A micromechanical model for multiple crazing in high impact polystyrene. *Mech. Mater.* **2001**, 33, 155–175. doi:10.1016/S0167-6636(00)00068-5

[210] Bucknall, C.B., Quantitative approaches to particle cavitation, shear yielding, and crazing in rubber-toughened polymers. *J. Polym. Sci. Part B Polym. Phys.* **2007**, 45, 1399–1409. doi:10.1002/polb.21171

[211] Gross, D., Seelig, T., Bruchmechanik, Springer Berlin Heidelberg, **2016**, ISBN:978-3-662-46736-7. doi:10.1007/978-3-662-46737-4

[212] Grellmann, W., Langer, B., Deformation and Fracture Behaviour of Polymers, Springer Berlin Heidelberg, Berlin, Heidelberg, **2001**, ISBN:978-3-642-07453-0. doi:10.1007/978-3-662-04556-5

[213] Lalande, L., Plummer, C.J.G., Månson, J.-A.E., Gérard, P., Microdeformation mechanisms in rubber toughened PMMA and PMMA-based copolymers. *Eng. Fract. Mech.* **2006**, 73, 2413–2426. doi:10.1016/j.engfracmech.2006.05.014

[214] Fischer, B., Ziadeh, M., Pfaff, A., Breu, J., Altstädt, V., Impact of large aspect ratio, shear-stiff, mica-like clay on mechanical behaviour of PMMA/clay nanocomposites. *Polymer.* **2012**, 53, 3230–3237. doi:10.1016/j.polymer.2012.04.055

[215] Keskkula, H., Schwarz, M., Paul, D.R., Examination of failure in rubber toughened polystyrene. *Polymer.* **1986**, 27, 211–216. doi:10.1016/0032-3861(86)90328-9

[216] Grellmann, W., Langer, B., Deformation and Fracture Behaviour of Polymer Materials, Springer International Publishing, Cham, **2017**, ISBN:978-3-319-41877-3. doi:10.1007/978-3-319-41879-7

[217] González-Velázquez, J.L., Mechanical Behavior and Fracture of Engineering Materials, Springer International Publishing, **2020**, ISBN:978-3-030-29240-9. doi:10.1007/978-3-030-29241-6

[218] Wu, S., Control of intrinsic brittleness and toughness of polymers and blends by chemical structure: A review. *Polym. Int.* **1992**, 29, 229–247. doi:10.1002/pi.4990290313

[219] Wu, S., Chain structure, phase morphology, and toughness relationships in polymers and blends. *Polym. Eng. Sci.* **1990**, 30, 753–761. doi:10.1002/pen.760301302

[220] Argon, A.S., The Physics of Deformation and Fracture of Polymers, Cambridge University Press, **2013**, ISBN:9781139033046. doi:10.1017/CBO9781139033046

[221] Bowden, P.B., Young, R.J., Deformation mechanisms in crystalline polymers. *J. Mater. Sci.* **1974**, 9, 2034–2051. doi:10.1007/BF00540553

[222] Butler, M.F., Donald, A.M., Ryan, A.J., Time resolved simultaneous small- and wide-angle X-ray scattering during polyethylene deformation—II. Cold drawing of linear polyethylene. *Polymer.* **1998**, 39, 39–52. doi:10.1016/S0032-3861(97)00226-7

[223] Sue, H.J., Yee, A.F., Toughening mechanisms in a multi-phase alloy of nylon 6,6/polyphenylene oxide. *J. Mater. Sci.* **1989**, 24, 1447–1457. doi:10.1007/BF02397085

[224] Hobbs, S.Y., Dekkers, M.E.J., Deformation mechanisms in toughened poly(phenylene oxide)-polyamide blends. *J. Mater. Sci.* **1989**, 24, 1316–1322. doi:10.1007/BF02397065

[225] Takano, M., Nielsen, L.E., The notch sensitivity of polymeric materials. *J. Appl. Polym. Sci.* **1976**, 20, 2193–2207. doi:10.1002/app.1976.070200814

[226] Prabhakaran, R., Nair, E.M.S., Sinha, P.K., Notch sensitivity of polymers. *J. Appl. Polym. Sci.* **1978**, 22, 3011–3020. doi:10.1002/app.1978.070221026

[227] Bureau, M.N., Di Francesco, E., Denault, J., Dickson, J.I., Mechanical behavior of injection-molded polystyrene/polyethylene blends: fracture toughness vs. fatigue crack propagation. *Polym. Eng. Sci.* **1999**, 39, 1119–1129. doi:10.1002/pen.11499

[228] Bellemare, S.C., Bureau, M.N., Denault, J., Dickson, J.I., Fatigue crack initiation and propagation in polyamide-6 and in polyamide-6 nanocomposites. *Polym. Compos.* **2004**, 25, 433–441. doi:10.1002/pc.20036

[229] González-Velázquez, J.L., Fractography and Failure Analysis, Springer International Publishing, **2018**, ISBN:978-3-319-76650-8. doi:10.1007/978-3-319-76651-5

[230] Thomas, S., Groeninckx, G., Nylon 6 / Ethylene Propylene Rubber (EPM) Blends : Phase Morphology Development during Processing and Comparison with Literature Data. *J. Appl. Polym. Sci.* **1999**, 71, 1405–1429

[231] Tjong, S.C., Ke, Y.C., Fracture toughening behavior and mechanical properties of polyphenylene oxide/high-impact polystyrene blends. *Polym. Eng. Sci.* **1996**, 36, 2626–2633. doi:10.1002/pen.10662

[232] Liu, J., Sue, H.-J., Thompson, Z.J., Bates, F.S., Dettloff, M., Jacob, G., Verghese, N., Pham, H., Nanocavitation in Self-Assembled Amphiphilic Block Copolymer-Modified Epoxy. *Macromolecules*. **2008**, 41, 7616–7624. doi:10.1021/ma801037q

[233] Li, T., Zhang, J., Schneiderman, D.K., Francis, L.F., Bates, F.S., Toughening Glassy Poly(lactide) with Block Copolymer Micelles. *ACS Macro Lett.* **2016**, 5, 359–364. doi:10.1021/acsmacrolett.6b00063

[234] Lang, R.W., Manson, J.A., Hertzberg, R.W., Effect of short glass fibers and particulate fillers on fatigue crack propagation in polyamides. *Polym. Eng. Sci.* **1982**, 22, 982–987. doi:10.1002/pen.760221513

[235] Esmaeillou, B., Ferreira, P., Bellenger, V., Tcharkhtchi, A., Fatigue behavior of polyamide 66/glass fiber under various kinds of applied load. *Polym. Compos.* **2012**, 33, 540–547. doi:10.1002/pc.22185

[236] Wyzgoski, M.G., Novak, G.E., Fatigue fracture of nylon polymers - Part II Effect of glass-fibre reinforcement. *J. Mater. Sci.* **1991**, 26, 6314–6324. doi:10.1007/BF02387810

[237] Parker, D.S., Sue, H.-J., Huang, J., Yee, A.F., Toughening mechanisms in core-shell rubber modified polycarbonate. *Polymer.* **1990**, 31, 2267–2277. doi:10.1016/0032-3861(90)90312-M

[238] Lim, S.-H., Dasari, A., Yu, Z.-Z., Mai, Y.-W., Liu, S., Yong, M.S., Fracture toughness of nylon 6/organoclay/elastomer nanocomposites. *Compos. Sci. Technol.* **2007**, 67, 2914–2923. doi:10.1016/j.compscitech.2007.05.007

[239] Harmia, T., Friedrich, K., Fracture toughness and failure mechanisms in unreinforced and long-glass-fibre-reinforced PA66/PP blends. *Compos. Sci. Technol.* **1995**, 53, 423–430. doi:10.1016/0266-3538(95)00031-3

[240] Xu, X.Y., Sun, S.L., Chen, Z.C., Zhang, H.X., Toughening of polyamide 6 with a maleic anhydride functionalized acrylonitrile–butadiene–styrene copolymer. *J. Appl. Polym. Sci.* **2008**, 109, 2482–2490. doi:10.1002/app.28238

[241] Yang, H., Cao, X., Ma, Y., An, J., Ke, Y., Liu, X., Wang, F., Effect of maleic anhydride grafted polybutadiene on the compatibility of polyamide 66/acrylonitrile-butadiene-styrene copolymer blend. *Polym. Eng. Sci.* **2012**, 52, 481–488. doi:10.1002/pen.22105

[242] Ke, Z., Shi, D., Yin, J., Li, R.K.Y., Mai, Y.-W., Facile Method of Preparing Supertough Polyamide 6 with Low Rubber Content. *Macromolecules*. **2008**, 41, 7264–7267. doi:10.1021/ma800495t

[243] Kelnar, I., Stephan, M., Jakisch, L., Fortelný, I., Reactive blending of nylon 6 and modified poly(styrene-co-maleic anhydride); influence of poly(styrene-co-maleic anhydride) modification by fatty amine onto blend properties. *J. Appl. Polym. Sci.* **1997**, 66, 555–562. doi:10.1002/(SICI)1097-4628(19971017)66:3<555::AID-APP17>3.0.CO;2-U

[244] Yin, B., Li, L., Zhou, Y., Gong, L., Yang, M., Xie, B., Largely improved impact toughness of PA6/EPDM-g-MA/HDPE ternary blends: The role of core–shell particles formed in melt processing on preventing micro-crack propagation. *Polymer.* **2013**, 54, 1938–1947. doi:10.1016/j.polymer.2013.02.001

[245] Wu, G., Zhang, K., Takagi, K., Sano, H., Yui, H., Rubber-toughened polyamide-6 with a low thermal expansion coefficient: effect of preferential distribution of rubber and inorganic filler. *Polym. Int.* **2016**, 65, 102–108. doi:10.1002/pi.5036

[246] Bohn, C.C., Manning, S.C., Moore, R.B., Comparison of carboxylated and maleated polypropylene as reactive compatibilizers in polypropylene/polyamide-6,6 blends. *J. Appl. Polym. Sci.* **2001**, 79, 2398–2407. doi:10.1002/1097-4628(20010328)79:13<2398::AID-APP1047>3.0.CO;2-3

[247] Castro, L.D.C., Oliveira, A.D., Kersch, M., Altstädt, V., Pessan, L.A., Effects of mixing protocol on morphology and properties of PA6/ABS blends compatibilized with MMA-MA. *J. Appl. Polym. Sci.* **2016**, 133, 1–8. doi:10.1002/app.43612

[248] Otterson, D.M., Kim, B.H., Lavengood, R.E., The effect of compatibilizer level on the mechanical properties of a nylon 6/ABS polymer blend. *J. Mater. Sci.* **1991**, 26, 1478–1484. doi:10.1007/BF00544656

[249] Richard, H.A., Sander, M., Ermüdungsrisse, Vieweg+Teubner Verlag, **2012**, ISBN:978-3-8348-1594-1. doi:10.1007/978-3-8348-8663-7

[250] Irwin, G.R., Analysis of Stresses and Strains Near the End of a Crack Traversing a Plate. *J. Appl. Mech.* **1957**, 24, 361–364. doi:10.1115/1.4011547

[251] Rice, J.R., Mechanics of crack tip deformation and extension by fatigue. Fatigue Crack Propagation, in: ASTM STP 415, American Society for Testing and Materials, **1976**: pp. 247–309

[252] Hertzberg, R.W., Manson, J.A., Fatigue of Engineering Plastics, Academic Press, **1980**, ISBN:9780123435507

[253] Hertzberg, R.W., Manson, J.A., Skibo, M., Frequency sensitivity of fatigue processes in polymeric solids. *Polym. Eng. Sci.* **1975**, 15, 252–260. doi:10.1002/pen.760150404

[254] Koster, C., Altstädt, V., Kausch, H.H., Cantwell, W.J., Split rate fatigue propagation in polymer blends. *Polym. Bull.* **1995**, 34, 243–248. doi:10.1007/BF00316402

[255] Bahrami, R., Fracture Mechanics of Nanostructured Polymer Blends with Janus Particles, Universität Bayreuth, **2018**

[256] Paris, P., Erdogan, F., A Critical Analysis of Crack Propagation Laws. *J. Basic Eng.* **1963**, 85, 528–533. doi:10.1115/1.3656900

[257] Buehler, M.J., Abraham, F.F., Gao, H., Hyperelasticity governs dynamic fracture at a critical length scale. *Nature*. **2003**, 426, 141–146. doi:10.1038/nature02096

[258] Manson, J.A., Hertzberg, R.W., Kim, S.L., Wu, W.C., Fatigue Crack Propagation in Polycarbonate, American Chemical Society, **1976**. doi:10.1021/ba-1976-0154.ch013

[259] Kim, S.L., Skibo, M., Manson, J.A., Hertzberg, R.W., Fatigue crack propagation in poly(methyl methacrylate): Effect of molecular weight and internal plasticization. *Polym. Eng. Sci.* **1977**, 17, 194–203. doi:10.1002/pen.760170308

[260] Hertzberg, R.W., Skibo, M.D., Manson, J.A., Fatigue crack propagation in polyacetal. *J. Mater. Sci.* **1978**, 13, 1038–1044. doi:10.1007/BF00544699

[261] Altstädt, V., The Influence of Molecular Variables on Fatigue Resistance in Stress Cracking Environments, in: H.-H. Kausch (Ed.), Intrinsic Mol. Mobil. Toughness Polym. II, Springer Berlin Heidelberg, **2005**: pp. 105–152. doi:10.1007/b136975

[262] Bakis, G., Kothmann, M.H., Zeiler, R., Brückner, A., Ziadeh, M., Breu, J., Altstädt, V., Influence of size, aspect ratio and shear stiffness of nanoclays on the fatigue crack propagation behavior of their epoxy nanocomposites. *Polymer.* **2018**, 158, 372–380. doi:10.1016/j.polymer.2018.10.008

[263] Bureau, M.N., Dickson, J.I., Denault, J., Fatigue propagation behaviour of polystyrene/polyethylene blends. *J. Mater. Sci.* **1998**, 33, 1405–1419. doi:10.1023/A:1004379121319

[264] Fang, Q.Z., Wang, T.J., Li, H.M., "Tail" phenomenon and fatigue crack propagation of PC/ABS alloy. *Polym. Degrad. Stab.* **2008**, 93, 281–290. doi:10.1016/j.polymdegradstab.2007.09.002

[265] Ruckdaschel, H., Fischer, F., Altstadt, V., Muller, A.H.E., OS4-1-3 Fatigue crack growth behavior of multiphase blends. *Abstr. ATEM Int. Conf. Adv. Technol. Exp. Mech. Asian Conf. Exp. Mech.* **2007**, 2007.6, _OS4-1-3-1-_OS4-1-3-7. doi:10.1299/jsmeatem.2007.6._OS4-1-3-1

[266] Wyzgoski, M.G., Novak, G.E., Fatigue-resistant nylon alloys. *J. Appl. Polym. Sci.* **1994**, 51, 873–885. doi:10.1002/app.1994.070510510

[267] Baschek, G., Hartwig, G., Zahradnik, F., Effect of water absorption in polymers at low and high temperatures. *Polymer.* **1999**, 40, 3433–3441. doi:10.1016/S0032-3861(98)00560-6

[268] Bianchi, R., Chiavacci, P., Vosa, R., Guerra, G., Effect of moisture on the crystallization behavior of PET from the quenched amorphous phase. *J. Appl. Polym. Sci.* **1991**, 43, 1087–1089. doi:10.1002/app.1991.070430608

[269] Qiuling Wang, Springer, G.S., Moisture Absorption and Fracture Toughness of PEEK Polymer and Graphite Fiber Reinforced PEEK. *J. Compos. Mater.* **1989**, 23, 434–447. doi:10.1177/002199838902300501

[270] Papir, Y.S., Kapur, S., Rogers, C.E., Baer, E., Effect of orientation, anisotropy, and water on the relaxation behavior of nylon 6 from 4.2 to 300°K. *J. Polym. Sci. Part A-2 Polym. Phys.* **1972**, 10, 1305–1319. doi:10.1002/pol.1972.160100710

[271] Bretz, P.E., Hertzberg, R.W., Manson, J.A., Fatigue crack propagation in crystalline polymers: effect of moisture in nylon 66. *J. Mater. Sci.* **1979**, 14, 2482–2492. doi:10.1007/BF00737039

[272] Rajeesh, K.R., Gnanamoorthy, R., Velmurugan, R., Effect of humidity on the indentation hardness and flexural fatigue behavior of polyamide 6 nanocomposite. *Mater. Sci. Eng. A*. **2010**, 527, 2826–2830. doi:10.1016/j.msea.2010.01.070

[273] Parodi, E., Peters, G.W.M., Govaert, L.E., Prediction of plasticity-controlled failure in polyamide 6: Influence of temperature and relative humidity. *J. Appl. Polym. Sci.* **2018**, 135, 45942. doi:10.1002/app.45942

[274] Hassan, A., Rahman, N.A., Yahya, R., Moisture absorption effect on thermal, dynamic mechanical and mechanical properties of injection-molded short glass-fiber/polyamide 6,6 composites. *Fibers Polym.* **2012**, 13, 899–906. doi:10.1007/s12221-012-0899-9

[275] Bretz, P.E., Hertzberg, R.W., Manson, J.A., Influence of absorbed moisture on fatigue crack propagation behaviour in polyamides - Part 1 Macroscopic response. *J. Mater. Sci.* **1981**, 16, 2061–2069. doi:10.1007/BF00542365

[276] Murthy, N.S., Hydrogen bonding, mobility, and structural transitions in aliphatic polyamides. *J. Polym. Sci. Part B Polym. Phys.* **2006**, 44, 1763–1782. doi:10.1002/polb.20833

[277] Chen, H., Zhu, S., Maia, J., Phase Control of Polyamide 6 via Extension-Dominated Polymer Blend Reactive Extrusion. *Polym. Eng. Sci.* **2020**, 60, 1019–1028. doi:10.1002/pen.25357

[278] Saxena, A., Hudak, S.J., Review and extension of compliance information for common crack growth specimens. *Int. J. Fract.* **1978**, 14, 453–468. doi:10.1007/BF01390468

[279] Wu, S., Formation of dispersed phase in incompatible polymer blends: Interfacial and rheological effects. *Polym. Eng. Sci.* **1987**, 27, 335–343. doi:10.1002/pen.760270506

[280] Chiang, C., Chang, F., Polymer blends of polyamide-6 and poly(phenylene oxide) compatibilized by styrene-co-glycidyl methacrylate. *J. Appl. Polym. Sci.* **1996**, 61, 2411–2421. doi:10.1002/(SICI)1097-4628(19960926)61:13<2411::AID-APP21>3.0.CO;2-5

[281] Ahn, T.O., Lee, S.-S., Park, L.S., Jeong, H.M., Miscibility of partially imidized styrene-maleic anhydride copolymers with styrene-acrylonitrile copolymers. *Polymer.* **1995**, 36, 4347–4350. doi:10.1016/0032-3861(95)92233-5

[282] Mou, Y.L., Xia, W., Wang, Z., Zheng, D., Synthesis and Characterization of Styrene, Maleic Anhydride and N-phenyl Maleimide Tripolymer, in: Proc. 2nd Annu. Int. Conf. Adv. Mater. Eng. (AME 2016), Atlantis Press, Paris, France, **2016**: pp. 1110–1115. doi:10.2991/ame-16.2016.180

[283] Spreeman, M.E., Stretz, H.A., Dadmun, M.D., Role of compatibilizer in 3D printing of polymer blends. *Addit. Manuf.* **2019**, 27, 267–277. doi:10.1016/j.addma.2019.03.009

[284] Schulz, H., Burtscher, P., Mädler, L., Correlating filler transparency with inorganic/polymer composite transparency. *Compos. Part A Appl. Sci. Manuf.* **2007**, 38, 2451–2459. doi:10.1016/j.compositesa.2007.08.006

[285] Loste, J., Lopez-Cuesta, J.-M., Billon, L., Garay, H., Save, M., Transparent polymer nanocomposites: An overview on their synthesis and advanced properties. *Prog. Polym. Sci.* **2019**, 89, 133–158. doi:10.1016/j.progpolymsci.2018.10.003

[286] Biangardi, H.J., Sturm, H., Kostersitz, G., Transparente Polymere Mehrphasensysteme. *Angew. Makromol. Chemie*. **1990**, 183, 221–241. doi:10.1002/apmc.1990.051830112

[287] Wildner, W., Drummer, D., Light scattering of glass-particle filled matrices with similar refractive index. *J. Compos. Mater.* **2018**, 52, 4231–4246. doi:10.1177/0021998318778889

[288] Gooch, J.W., Encyclopedic Dictionary of Polymers, Springer New York, **2011**, ISBN:978-1-4419-6246-1. doi:10.1007/978-1-4419-6247-8

[289] Thomas, S., Grohens, Y., Jyotishkumar, P., Characterization of Polymer Blends - Miscibility, Morphology and Interfaces, Wiley-VCH Verlag GmbH & Co. KGaA, **2014**, ISBN:9783527645602. doi:10.1002/9783527645602

[290] Fox, T.G., Influence of Diluent and of Copolymer Composition on the Glass Temperature of a Polymer System. *Bull. Am. Phys. Scoiety*. **1956**, 1, 123

[291] Dedecker, K., Groeninckx, G., Interfacial Graft Copolymer Formation during Reactive Melt Blending of Polyamide 6 and Styrene− Maleic Anhydride Copolymers. *Macromolecules*. **1999**, 2472–2479. doi:10.1021/ma980642v

[292] Wu, J., Xue, P., Mai, Y.-W., Effect of blending sequence on the morphology and impact toughness of poly(ethylene terephthalate)/polycarbonate blends. *Polym. Eng. Sci.* **2000**, 40, 786–797. doi:10.1002/pen.11208

[293] Wang, Q., Jiang, Y., Li, L., Wang, P., Yang, Q., Li, G., Mechanical Properties, Rheology, and Crystallization of Epoxy-Resin-Compatibilized Polyamide 6/Polycarbonate Blends: Effect of Mixing Sequences. *J. Macromol. Sci. Part B*. **2012**, 51, 96–108. doi:10.1080/00222348.2011.565273

[294] Chiang, C.-R., Chang, F.-C., Polymer blends of polyamide-6 (PA6) and poly (phenylene ether) (PPE) compatibilized by a multifunctional epoxy coupler. *J. Polym. Sci. Part B Polym. Phys.* **1998**, 36, 1805–1819. doi:10.1002/(SICI)1099-0488(199808)36:11<1805::AID-POLB2>3.0.CO;2-P

[295] Favis, B., Chalifoux, J., Influence of composition on the morphology of polypropylene/polycarbonate blends. *Polymer.* **1988**, 29, 1761–1767. doi:10.1016/0032-3861(88)90388-6

[296] Everaert, V., Aerts, L., Groeninckx, G., Phase morphology development in immiscible PP/(PS/PPE) blends influence of the melt-viscosity ratio and blend composition. *Polymer.* **1999**, 40, 6627–6644. doi:10.1016/S0032-3861(99)00048-8

[297] You, W., Yu, W., Control of the dispersed-to-continuous transition in polymer blends by viscoelastic asymmetry. *Polymer.* **2018**, 134, 254–262. doi:10.1016/j.polymer.2017.11.074

[298] Visakh, P.M., Markovic, G., Pasquin, D., Recent Developments in Polymer Macro, Micro and Nano Blends, Elsevier, **2017**, ISBN:9780081004081. doi:10.1016/C2014-0-03998-6

[299] Kelnar, I., Stephan, M., Jakisch, L., Janata, M., Fortelný, I., Compatibilization of PA6/PPO blend with carboxylated poly(styrene) compounds. *J. Appl. Polym. Sci.* **2001**, 80, 2273–2280. doi:10.1002/app.1332

[300] Pan, L., Chiba, T., Inoue, T., Reactive blending of polyamide with polyethylene: pull-out of in situ-formed graft copolymer. *Polymer.* **2001**, 42, 8825–8831. doi:10.1016/S0032-3861(01)00441-4

[301] Pötschke, P., Paul, D.R., Formation of Co-continuous Structures in Melt-Mixed Immiscible Polymer Blends. *J. Macromol. Sci. Part C Polym. Rev.* **2003**, 43, 87–141. doi:10.1081/MC-120018022

[302] Komalan, C., George, K.E., Kumar, P.A.S., Varughese, K.T., Thomas, S., Dynamic mechanical analysis of binary and ternary polymer blends based on nylon copolymer/EPDM rubber and EPM grafted maleic anhydride compatibilizer. *Express Polym. Lett.* **2007**, 1, 641–653. doi:10.3144/expresspolymlett.2007.88

[303] Charfeddine, I., Majesté, J.C., Carrot, C., Lhost, O., A model for the prediction of the morphology of immiscible blends of polymers. *Polymer.* **2020**, 193, 122334. doi:10.1016/j.polymer.2020.122334

[304] Dörr, J.M., Scheidelaar, S., Koorengevel, M.C., Dominguez, J.J., Schäfer, M., van Walree, C.A., Killian, J.A., The styrene–maleic acid copolymer: a versatile tool in membrane research. *Eur. Biophys. J.* **2016**, 45, 3–21. doi:10.1007/s00249-015-1093-y

[305] Peters, E., Poly(phenylene ether) Based Amphiphilic Block Copolymers. *Polymers.* **2017**, 9, 433. doi:10.3390/polym9090433

[306] Sayer, S., Mechanical Performance of Polyamid 66 and Influence of Glass Fiber Content on Moisture Absorption. *Mater. Test.* **2014**, 56, 325–330. doi:10.3139/120.110563

[307] Do, V.-T., Nguyen-Tran, H.-D., Chun, D.-M., Effect of polypropylene on the mechanical properties and water absorption of carbon-fiber-reinforced-polyamide-6/polypropylene composite. *Compos. Struct.* **2016**, 150, 240–245. doi:10.1016/j.compstruct.2016.05.011

[308] Aparna, S., Purnima, D., Adusumalli, R.B., Effect of Compatibilizer on the Properties of Polyamide 6 Blend Based Carbon Fiber Reinforced Composites. *Fibers Polym.* **2018**, 19, 1335–1346. doi:10.1007/s12221-018-1009-4

[309] Handge, U.A., Sailer, C., Steininger, H., Weber, M., Scholtyssek, S., Seydewitz, V., Michler, G.H., Micromechanical processes and failure phenomena in reactively compatibilized blends of polyamide 6 and styrenic polymers. I. Polyamide 6/acrylonitrile- butadiene-styrene copolymer blends. *J. Appl. Polym. Sci.* **2009**, 112, 1658–1669. doi:10.1002/app.29566

[310] Handge, U.A., Sailer, C., Steininger, H., Weber, M., Scholtyssek, S., Seydewitz, V., Michler, G.H., Micromechanical processes and failure phenomena in reactively compatibilized blends of polyamide 6 and styrenic polymers. II. Polyamide 6/styrene-acrylonitrile copolymer blends. *J. Appl. Polym. Sci.* **2010**, 115, 2529–2539. doi:10.1002/app.31270

[311] Fang, Q.Z., Wang, T.J., Li, H.M., Overload effect on the fatigue crack propagation of PC/ABS alloy. *Polymer.* **2007**, 48, 6691–6706. doi:10.1016/j.polymer.2007.08.048

[312] Thomas, S., Joseph, K., Malhotra, S.K., Goda, K., Polymer Composites, Wiley-VCH Verlag GmbH & Co. KGaA, **2012**, ISBN:9783527645213. doi:10.1002/9783527645213

[313] Kothmann, M.H., Bakis, G., Zeiler, R., Ziadeh, M., Breu, J., Altstädt, V., Fatigue Crack Growth Behaviour of Epoxy Nanocomposites-Influence of Particle Geometry, in: Deformation and Fracture Behaviour of Polymer Materials, Springer Cham, **2017**: pp. 23–32. doi:10.1007/978-3-319-41879-7_2

[314] Friedrich, K., Crazes and shear bands in semi-crystalline thermoplastics, in: Crazing Polym., Springer-Verlag, Berlin/Heidelberg, **2005**: pp. 225–274. doi:10.1007/BFb0024059

[315] Michler, G.H., von Schmeling, H.-H.K.-B., The physics and micro-mechanics of nano-voids and nano-particles in polymer combinations. *Polymer.* **2013**, 54, 3131–3144. doi:10.1016/j.polymer.2013.03.035

[316] Kothmann, M.H., Zeiler, R., Rios de Anda, A., Brückner, A., Altstädt, V., Fatigue crack propagation behaviour of epoxy resins modified with silica-nanoparticles. *Polymer.* **2015**, 60, 157–163. doi:10.1016/j.polymer.2015.01.036

[317] Chen, C.C., Fontan, E., Min, K., White, J.L., An investigation of instability of phase morphology of blends of nylons with polyethylenes and polystyrenes and effects of compatibilizing agents. *Polym. Eng. Sci.* **1988**, 28, 69–80. doi:10.1002/pen.760280203

[318] Florjańczyk, Z., Krawiec, W., Such, K., A study of the relative reactivity of maleic anhydride and some maleimides in free radical copolymerization and terpolymerization. *J. Polym. Sci. Part A Polym. Chem.* **1990**, 28, 795–801. doi:10.1002/pola.1990.080280408

[319] Lee, S.-S., Ahn, T.O., Direct polymer reaction of poly(styrene-co-maleic anhydride): Polymeric imidization. *J. Appl. Polym. Sci.* **1999**, 71, 1187–1196. doi:10.1002/(SICI)1097-4628(19990214)71:7<1187::AID-APP17>3.0.CO;2-N

11 Other sources

a. Alumil Aluminium Industry S.A., hinged window frame systems [online]. [Accessed on: 22.01.2023]. Available under: https://www.alumil.com/docs/default-source/knowledgebase/pre-qualification-files/supreme/uae/pre-qualification-s(d)77.pdf?sfvrsn=16a3c823_6

b SABIC, Noryl GTX resins. [online]. [Accessed on: 22.01.2023]. Available under: https://www.sabic.com/en/products/specialties/noryl-resins/noryl-gtx-resin

c LUSTRAN® SMA 245, product data sheet. [online]. [Accessed on: 22.01.2023]. Available under: https://omnexus.specialchem.com/product/t-ineos-lustran-sma-245

d XIBOND® 120, product data sheet. [online]. [Accessed on: 22.01.2023]. Available under: https://www.palmerholland.com/All-Products/XIBOND-120

e XIBOND® 315, product data sheet. [online]. [Accessed on: 22.01.2023]. Available under: https://www.palmerholland.com/All-Products/XIBOND-315

f SpecialChem S.A., Polyscope product list. [online]. [Accessed on: 22.01.2023]. Available under: https://polymer-additives.specialchem.com/selectors?q=polyscope

g Denka, Denka IP product data sheet. [online]. [Accessed on: 22.01.2023]. Available under: https://www.denka.co.jp/eng/product/detail_00018/

Curriculum Vitae

Personal data	Alper Aksit born on Jan/14/1990 in Stuttgart	
Marital status	Married	
Nationality	Turkish	
Education	2000 - 2006	Rilke-Realschule, Stuttgart O-Level „Mittlere Reife“ (1.8)
	2009 - 2010	TO-Stuttgart, Stuttgart Degree: A-Level „Fachhochschulreife“ (1.8)
	2010 - 2014	University of Applied Sciences Esslingen B.Sc. in Chemical Engineering/ Color and Coatings (1.8)
	2013 - 2013	Kettering University, Flint, Michigan, USA Study abroad exchange program
	2014 - 2017	University of Bayreuth M.Sc. in Polymer Science (1.3)
	2016 - 2017	Hong Kong University of Science and Technology (HKUST), Hong Kong, China Scientific internship
	2014 - 2017	University of Bayreuth Elite study program „Macromolecular Science“ (1.3)
	2021 - 2022	Collège des Ingénieurs MBA in Management and Technology (1.3)
Professional experience	2022 - 2023	Marketing Manager Compounds & Circular Plastics, Evonik Operations GmbH
	2017 - 2021	Scientific Staff, Polymer Engineering, University of Bayreuth
	2006 - 2009	Apprenticeship as chemical technician „Chemikant“, Sika Deutschland GmbH, Stuttgart (1.7)

Publications

Reviewed Publications:

A. Aksit, T. Menzel, M. Aksit, V. Altstädt

Properties of Styrene–Maleic Anhydride Copolymer Compatibilized Polyamide 66/Poly (Phenylene Ether) Blends: Effect of Maleic Anhydride Concentration and Copolymer Content

Materials 13(5), 1237, 2020

A. Aksit, N. Geis, M. Aksit, V. Altstädt

Properties of Styrene-Maleic Anhydride Copolymer compatibilized Polyamide 66/Poly (phenylene ether) Blends: Effect of Blend Ratio and Compatibilizer Content

Materials 13(15), 3400, 2020

M. Aksit, S. Gröschel, U. Kuhn, A. Aksit, K. Kreger, H.-W. Schmidt, V. Altstädt

Low-Density Polybutylene Terephthalate Foams with Enhanced Compressive Strength via a Reactive-Extrusion Process

Polymers 12(9), 2021, 2020

G. Bakis, J.-F. Wendel, R. Zeiler, A. Aksit, M. Häublein, M. Demleitner, J. Benra, S. Forero, W. Schütz, V. Altstädt

Mechanical properties of the carbon nanotube modified epoxy-carbon fiber unidirectional prepreg laminates

Polymers 13(5), 770, 2021

Conference Contributions:

A. Aksit, V. Altstädt

Morphology and tensile properties of PA66/PPE blends: Effects of SMA content and MA concentration

Oral presentation: PPS Europe-Africa 2019 Regional Conference (PPS2019), Pretoria, South Africa, 2019

V. Altstädt, A. Aksit

Microplastic – lifecycle, biological effects and challenging solutions

Oral presentation: PPS-35, Cesme, Turkey, 2019